Engineering of Self-healing Adhesives and Polymeric Sensors with Stretchable Applications

by

Sunghyun Nam

A dissertation submitted in partial fulfillment
of the requirements for the degree of
Doctor of Philosophy
(Macromolecular Science and Engineering)
in the University of Michigan
2020

Doctoral Committee:

Professor L. Jay Guo, Chair
Professor Jinsang Kim
Professor Katsuo Kurabayashi
Professor Mark Meyerhoff

Sunghyun Nam
shnam@umich.edu
ORCID iD: 0000-0002-1217-3481

To my family: your love made this possible

Acknowledgments

It is with great pleasure that I shine a light on the heroes behind this thesis. First and foremost, I must express my very profound gratitude to my advisor, Prof. L. Jay Guo for providing me with unfailing support and continuous encouragement throughout my years of study. Without his support, the entire process of researching and writing this thesis would not have been possible. No words are sufficient to express my indebtedness for four years of Prof. Guo's guidance, input, and collaboration.

I would next like to thank my committee members, Prof. Jinsang Kim, Prof. Katsuo Kurabayashi, and Prof. Mark Meyerhoff for sharing their invaluable wisdom and comments throughout this study.

I would also like to acknowledge all current and past Guo group members: Dr. Chengang Ji, Dr. Ashwin Panday, Dr. Jinhwan Lee, Dr. Taehwa Lee, Dr. Taehee Jang, Dr. Sangeon Lee, Dr. Cheng Zhang, Dr. Long Chen, Dr. Xi Chen, Dr. Qingyu Cui, Dr. Saurabh Acharya, Dr. Kyungheon Kim, Dr. Sungho Lee, Yeonjoon Cheong, Yongbum Park, Changyeong Jeong, Kaito Yamada, Suneel Joglekar, Weijie Feng, and Yichun Chang for their kindness and assistance. And with great fondness, I thank our SHA project members, Boonjae Jang, Jennie Paik, and Jiajie Li for their kindness and

participation during my study and project. The stars aligned for me to have such gracious colleagues.

I have also had the luck to make great friends beyond the laboratory. To Alex Kim, Min Jang, Dr. Chan Cheong, Boyoung Kim, Jason Lee, and Seungmi Moon, Daseul Yang, Taeyong Ahn, and all others who made the cold winters of Michigan more bearable with their warm affection and open arms. I extend my best wishes of love, fortune, and health.

Above all, and this bears repeating, my journey is made possible only with my family: the daily sacrifice endured by my loving wife Yujung, and the onslaught of giggles, hugs, and kisses of my kids Hyunjun and Hyeyoon. You three are the wind beneath my wings.

Table of Contents

List of Figures

List of Tables

List of Appendices

Abstract

An ultra-fast self-healing adhesive (SHA) has been developed based on a reversible network of dynamic metal−ligand interactions which is strategically manipulated by activation energy control. The amorphous structure with a low glass transition temperature (T_g) induced by the formation of zinc-poly(vinyl alcohol) (PVA) complexes enables this polymer to be autonomously healed under ambient conditions without any intervention after mechanically damaged. The mechanical and electrical properties of the SHAs can be tuned by varying the metal/ligand ratio as well as an amount of water within materials. This dynamic coordination bond-mediated elastomer exhibits not only an excellent adhesion property to a variety of substrates but also a mechanically superior deformability compared to conventional elastomers being exploited for stretchable electronics.

It is also demonstrated that novel stretchable ammonia (NH_3) vapor sensor based on polymer electrolytes can be prepared and this system is extensively investigated. The presented sensor, comprised of the plasticized PVA electrolyte with glycerol, exceeds the performance of conventional SWCNT-based NH_3 sensors in terms of sensitivity, recovery time, and stretchability. This stretchable chemical sensor has the advantage of easy fabrication, low cost, convenient scale-up and reliable sensing performances. In

addition to the high sensitivity and stretchability, a remarkable selectivity for discriminating NH_3 from different chemicals including water has also been observed for this new sensor. From our knowledge so far, this thesis work is the first attempt to develop a stretchable NH_3 vapor sensor based on polymer electrolytes. With new materials and mechanisms, our polymeric sensors are promising as commercially viable and alternative NH_3 sensors in the field of robotics and wearable electronics.

Chapter 1

Introduction

1.1 Introduction to stretchable electronics

Flexible electronics has been investigated in a wide range of applications, such as flexible transistors, smart sensors, artificial skins, flexible energy harvesting and storage devices, and rollable displays [1-6]. Flexible electronics are desirable due to their key advantages including high flexibility, low-cost manufacturing such as ink-jet printing, slot-dye coating, and roll-to-roll processing [7-11]. However, flexible electronics also exhibit a limitation which makes them incompatible to large deformation processes including bending, twisting, and stretching. Furthermore, some flexible electronics exploited as a wearable device face challenges for a high deformable capability when integrated with curvilinear surfaces such as human skin, as illustrated in Figure 1.1. For this reason, stretchable electronics have recently emerged [12]. Stretchable electronics is a technology that builds conventional electronic circuits on top of a stretchable substrate or fabricates new structures indicating stretchable behavior. Over the past decade, stretchable electronics have been attracting intensive attention due to their promising

applications in many areas where electronic devices undergo large deformation and form intimate contact with human skins.

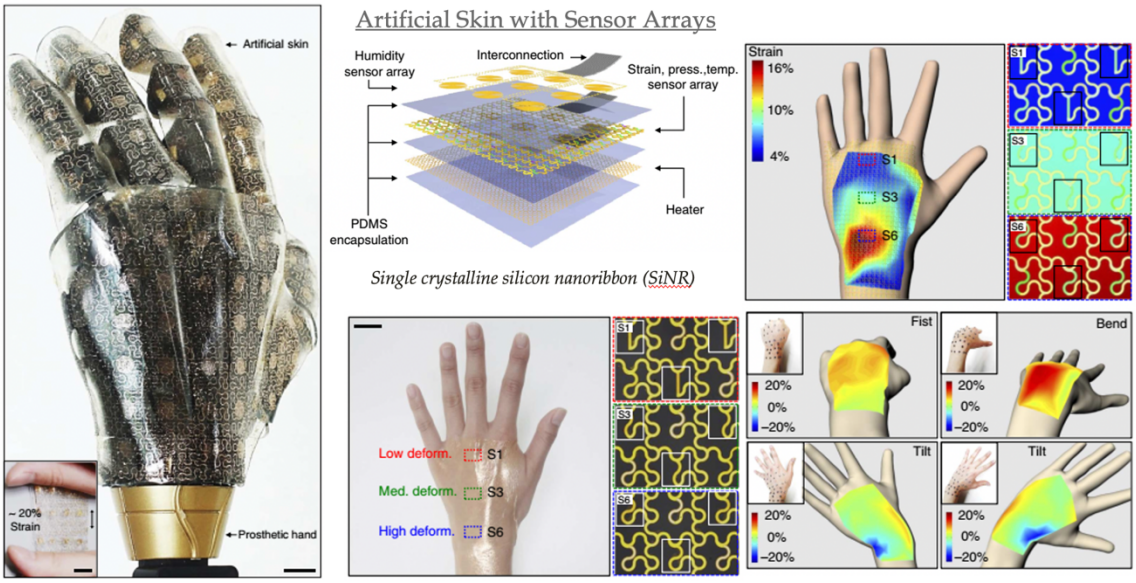

Figure 1.1 Artificial skin integrated with stretchable sensor arrays ([99] J. Kim *et al.*, Stretchable silicon nanoribbon electronics for skin prosthesis, *Nat. Commun.* **5**, 5747, 2014).

1.2 Stretchable sensors

Tremendous achievements have been made in the area of stretchable sensors to enable electronic devices capable of detecting various external stimuli, including pressure, chemicals, and biological species [13-18]. Kim et al. reported a diagnostic and therapeutic stretchable sensor working at the epicardium and it is able to measure temperature, strain, electrophysiological signals and physical contact [19]. A stretchable strain sensor comprised of two arrays of platinum-coated polymer nanofibers and

mounted on PDMS was studied contact [20]. A stretchable temperature sensor based on elastically buckled film have also been made onto an elastomeric substrate [21].

In other respects, an application of electronic skin based on stretchable polymers was investigated [22]. Furthermore, novel high-k dielectric materials were studied by introducing high-k inorganic nanoparticles into the elastomer [23-24]. In addition, a stretchable pressure sensor based on microstructured PDMS has also been employed as a stretchable dielectric layer [25]. Interestingly, pressure sensors mimicking human skin were also reported by using stretchable SWNT electrodes [26-27]. By integrating these sensors mentioned above, wearable sensing systems with mechanically soft assemblies comprised of nanoscale materials were studied, as shown in Figure 1.2 [202].

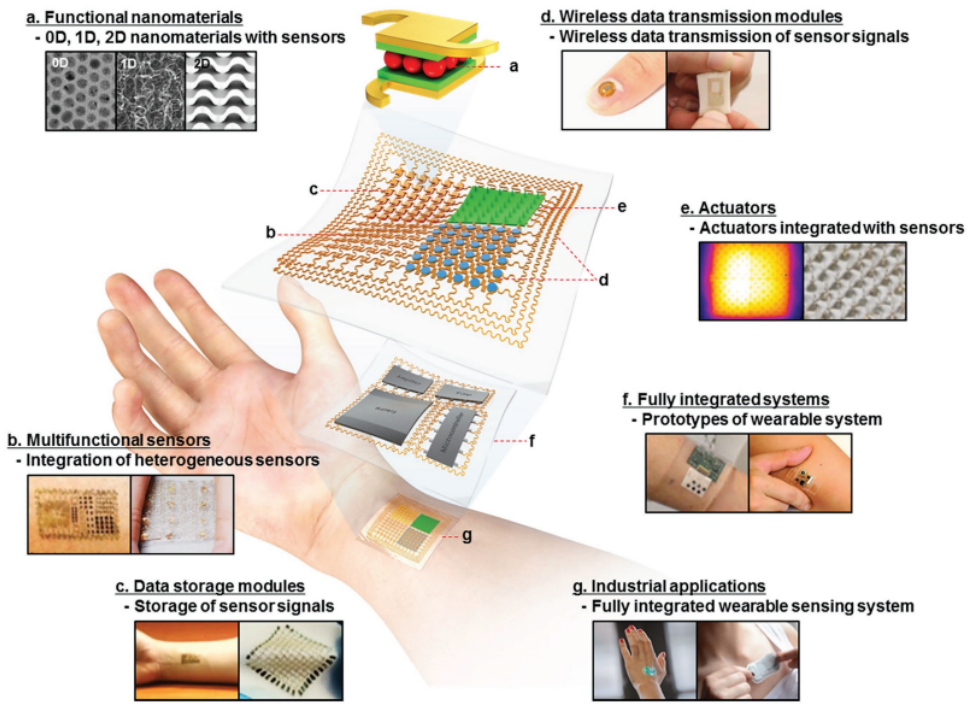

Figure 1.2 Wearable sensing systems based on stretchable and flexible sensors ([202] Y. Lee *et al.*, Wearable sensing systems with mechanically soft assemblies of nanoscale materials, *Adv. Mater. Technol.* **2**, 1700053, 2017).

1.3 Stretchable materials

The most indispensable requisite for achieving the stretchable electronics is to secure highly stretchable materials which is compliant to large deformation. Many electronic devices are fabricated on silicon or polymeric substrates such as polyethylene terephthalate (PET) and/or polyimide. However, these substrates are not adequate for stretchable electronics due to their rigidity. Recently, polydimethylsiloxane (PDMS) has extensively been used as a substrate in testing of stretchable electronics. Some studies on the film transfer technique that thin films coated onto silicon can be transferred to PDMS substrates were reported [28-29]. As a different technique for the fabrication of stretchable device, structured PDMS formed by relieving the strain was used as a stretchable substrate [30-31].

In addition to PDMS, polyurethane (PU) and Ecoflex were studied as other stretchable substrates. A stretchable strain sensor based on carbon nanotube (CNT) formed on a PU substrate was reported [32]. On an Ecoflex substrate, silver nanowires (AgNWs) based strain sensor with a high stretchability was also studied [33]. Furthermore, a stretchable LED array has been fabricated on an Ecoflex substrate [34].

It is noted that most of the stretchable materials are vulnerable to mechanical damage such as crack and fracture under large deformation. V. Vijay et al. studied the compatibility between sensing materials and stretchable substrates [35]. According to their study, both cracks and delamination were observed in PEDOT:PSS film deposited on PDMS, PMMA, and nitrile rubber as substrates under less than 5 % strain. However, no mechanical damage was observed in PEDOT:PSS films on a SEBS substrate at the same strains. They investigated that PEDOT:PSS/SEBS can tolerate up to 28% strain

with no discernible cracks as determined by scanning electron microscopy (SEM) and atomic force microscopy (AFM). Therefore, the goal of this dissertation work is to develop novel stretchable materials enduring mechanical fractures, that otherwise can self-heal when damaged without any interventions at room temperature.

In addition to polymers as a stretchable substrate, the sensing materials should possess the compliant properties to various deformations. For this reason, many of nanoscale materials categorized into 0D, 1D, and 2D based on their dimension or shape are being exploited as a sensing material for stretchable sensors. Table 1 represents the advantages and disadvantages of nanomaterials and their assembly methods.

	0D	***1D***	***2D***
Structure	• Nanoparticle	• Nanorod • Nanowire • Nanofiber	• Nanosheet
Advantages	• Electrical tunneling • High surface to volume ratio	• High aspect ratio • Complex networks	• High flexibility • Uniform crystallinity • Transparency
Disadvantages	• Hard to form network • Easy to aggregate in high T	• Non-uniform spatial arrangement • High roughness compared to 2D materials	• Low surface area to volume ratio
Assembly method	• Langmuir Blodgett • Electrodeposition • Blending • Spin coating	• Blending • Spin coating • Electrospinning • Molding • Spraying	• Exfoliation • Transfer printing

Table 1 Comparison of nanoscale materials categorized into 0D, 1D and 2D as a sensing material for stretchable electronics.

In addition to polymers as a stretchable substrate, the sensing materials should possess the compliant properties to various deformations. For this reason, many of nanoscale materials categorized into 0D, 1D, and 2D based on their dimension or shape are being exploited as a sensing material for stretchable sensors. Table 1 represents the advantages and disadvantages of nanomaterials and their assembly methods. Figure 1.3 illustrates a variety of stretchable and wearable sensors based on nanoscale materials which are capable of detecting various external stimuli, including pressure, chemicals, and biological species.

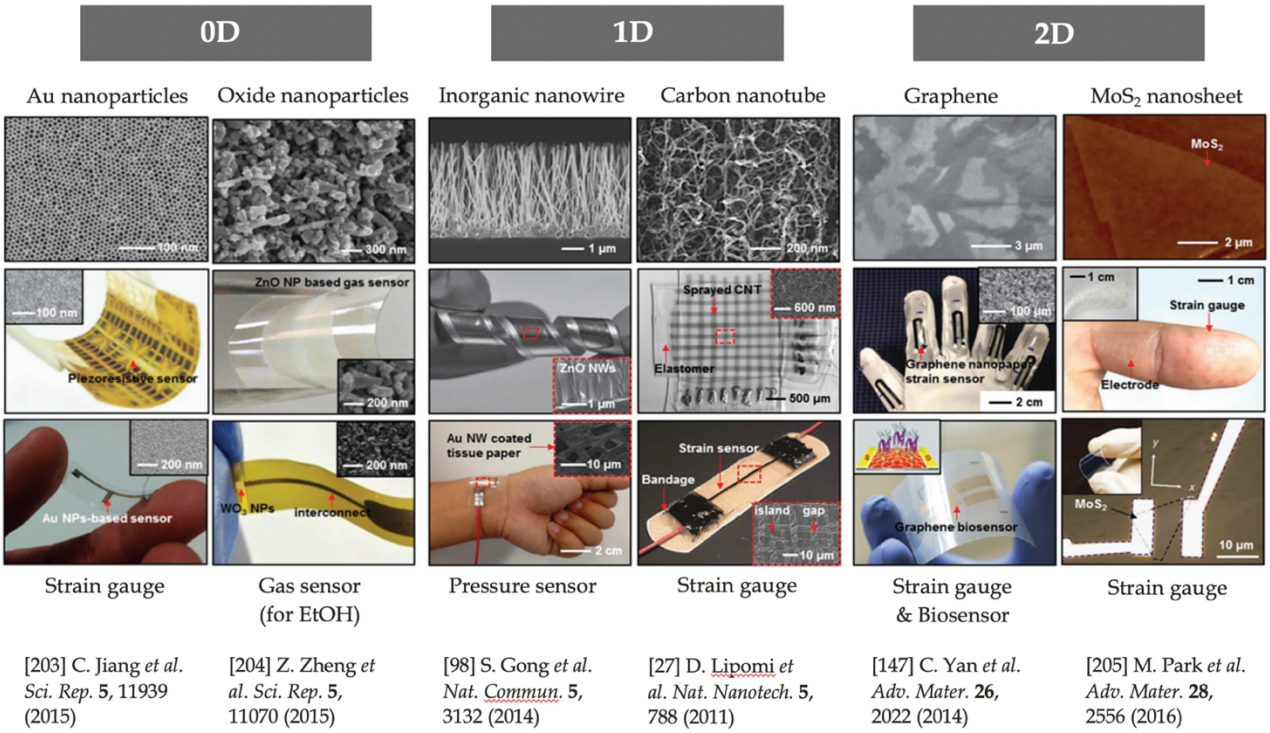

Figure 1.3 A variety of stretchable and wearable sensors based on 0D, 1D, and 2D nanoscale materials which are capable of detecting various external stimuli, including pressure, chemicals, and biological species [27, 98, 147, 203-205].

1.4 Self-healing materials

When faced with the predicament of mechanical fractures in biological systems, most of biological tissue offers a smart function of self-healing. Soft biomaterials, such as human skin, have the ability to self-repair when damaged. After wounds heal, the skin is able to retain its innate sensing functionalities. This process is initiated by chemical signals such as inflammation. The signals lead to wound closure and matrix remodeling. The ability to self-heal after mechanical damage could enhance significantly the lifetime of materials, thereby reducing both material disposal and cost. In a similar strategy, synthetic self-healing polymers are able to repair themselves and recover functionalities despite being subjected to mechanical damage, as shown in Figure 1.4. Recently, self-healing materials have been demonstrated to have attractive applications towards electrical conductors [36-37], functional surfaces [38], and electronic skin [39] with enhanced lifetime and durability. The self-healing feature is particularly desirable for stretchable electronics because the lifetimes of many stretchable devices are limited by the similar dilemma of mechanical fractures over the repeated stretching process [40].

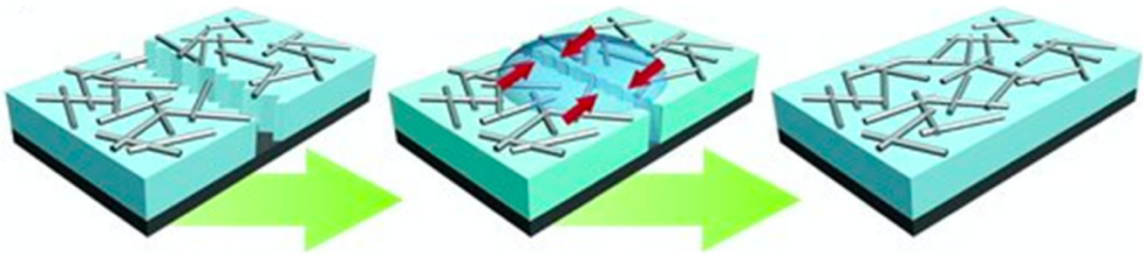

Figure 1.4 Schematic illustration of the self-healing conductor using polyelectrolyte multilayers coated with silver nanowires ([206] S. J. Benight *et al.*, Stretchable and self-healing polymers and devices for electronic skin, *Progress in Polymer Science* **38**, 1961, 2013).

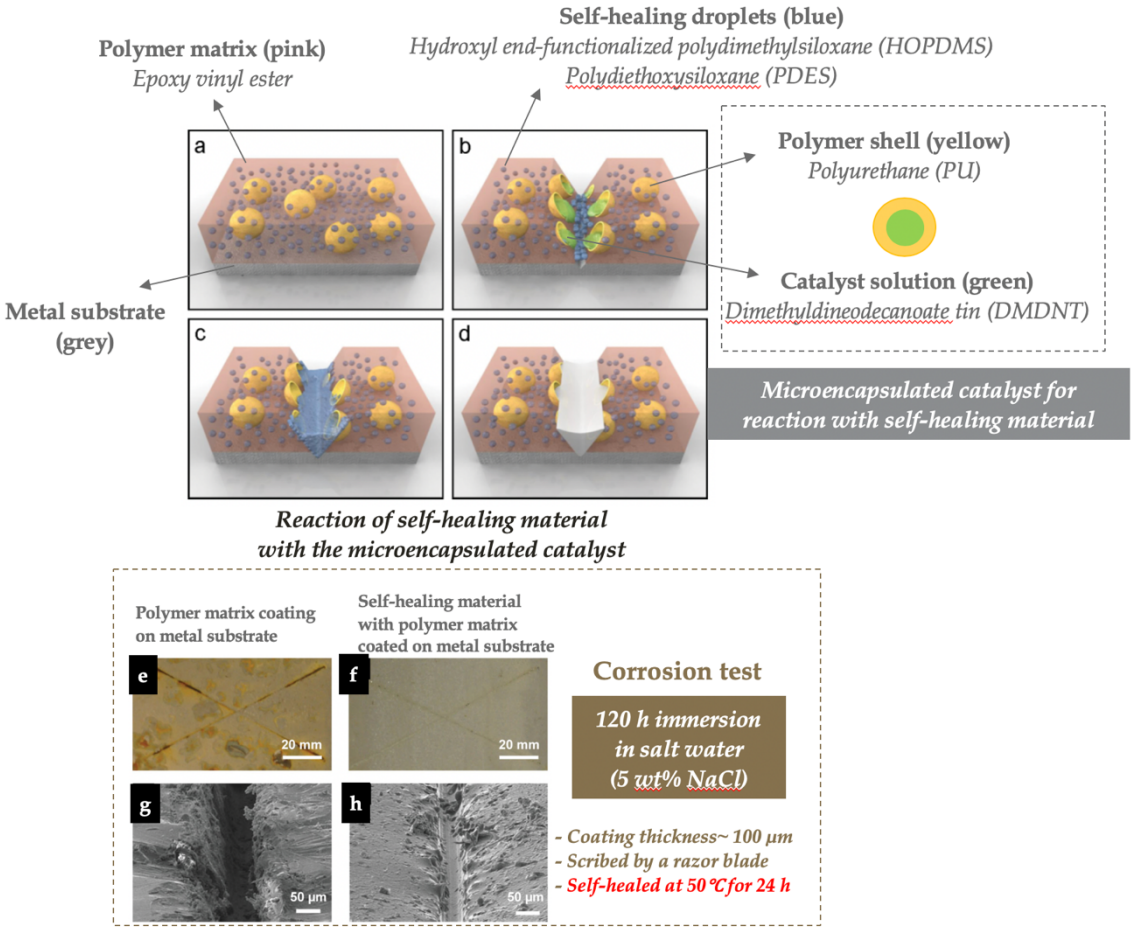

Figure 1.5 Schematic representations of self-healing process of the primitive self-healing polymer (a-d) and corrosion test (e-h). (a) Self-healing coating containing microencapsulated catalyst (yellow) and phase-separated healing agent droplets (blue) in a matrix (light orange) on a metallic substrate (grey). (b) Damage to the coating layer releases catalyst (green) and healing agent (blue). (c) Mixing of healing agent and catalyst in the damaged region. (d) Damage healed by cross-linked PDMS, protecting the substrate from the environment. (e) Control sample, consisting of the epoxy vinyl ester matrix and adhesion promoter, and (f) Self-healing coating, consisting of matrix, adhesion promoter, microencapsulated catalyst, and phase-separated PDMS healing agent. (g,h) SEM images of the scribed region of the control coating (g) and the self-healing coating after healing (h) ([47] S. H. Cho *et al.*, Self-healing polymer coatings, *Adv. Mater.* **21**, 645, 2009).

The primitive self-healing material had a complicated structure comprised of polymer matrix, self-healing agent, and microencapsulated catalyst to accelerate a self-healing reaction when the material is critically damaged, as illustrated in Figure 1.5 [47].

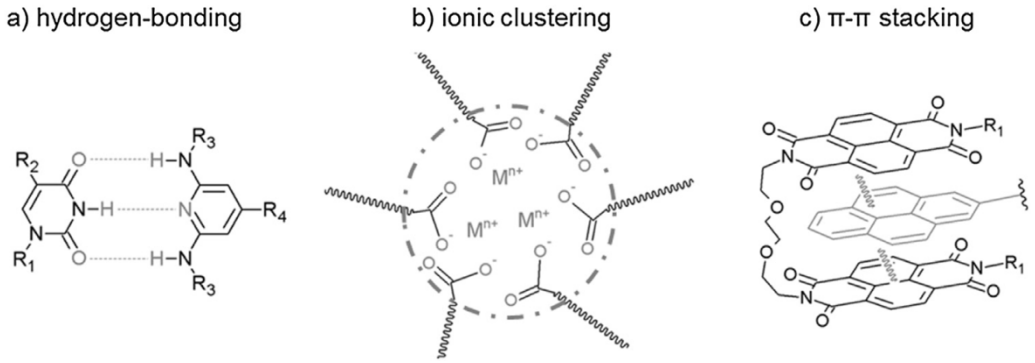

Figure 1.6 Schematic non-covalent network formation strategies to induce a dynamic bond; (a) Hydrogen-bonding between pyrimidin base residues. (b) Ionomers with anionic charged polymer chains and positive counter metal ions. (c) π-π stacking of π-electron rich pyrenyl units with electron poor π systems ([207] K. Urdl *et al.*, Self-healing of densely crosslinked thermoset polymers - a critical review, *Progress in Organic Coatings* **104**, 232, 2017).

However, a wide variety of self-healing materials have been investigating ever since many research groups focused on developing a spontaneous self-healing material. Various mechanisms of self-healing have been reported by researchers working on systems of self-repair by mimicking human skin and biological tissues. According to the previously reported mechanisms, self-healing could be triggered by chemical, crosslinking, chain entanglement of polymers, luminescence, morphological organization, shape memory, temperature, UV, water, and so forth. However, autonomous self-healing materials that can be repaired without any interventions when damaged have been developed by inducing a dynamic and sacrificial bond such as hydrogen bond,

coordination bond, ionic crosslinking, and π-π stacking, as shown in Figure 1.6 [207]. In this thesis work, ultra-fast self-healing polymer based on metal-ligand interactions has been investigated.

1.5 Stretchable and self-healing electronics

Recently, self-healing materials have attracted increasing attention in the field of flexible electronics. Haick and co-workers reported a self-healing flexible sensing platform by dispersing metal particles in polyurethane diol as self-healing electrode [41]. J. Hur et al. studied the self-healing conductive hydrogel by polymerizing pyrrole in agarose solution [42]. Bao and co-workers demonstrated a self-healing electronic sensor skin based on a nanostructured μNi particles-supramolecular organic composite, as shown in Figure 1.7 [43]. However, these self-healing electronic devices had limited stretchability of less than 100 % strain. For this reason, nowadays, highly stretchable hydrogels have been extensively studied by focusing on ionic conductors due to their remarkable piezoelectric effect under high stretching states and excellent transparency [44]. Specifically, conductive hydrogels are promising materials for the application of ionic skin, bioelectrodes, and biosensors due to a biocompatibility resulting from the high amount of water being retained within hydrogels [45]. Therefore, it is of great interest to fabricate highly stretchable self-healing strain sensor by combining the advantages of both biocompatible hydrogels and electronic conductors for applications in robotics, human motion detection, entertainment, health-monitoring, medical diagnosis, chemical detection, etc.

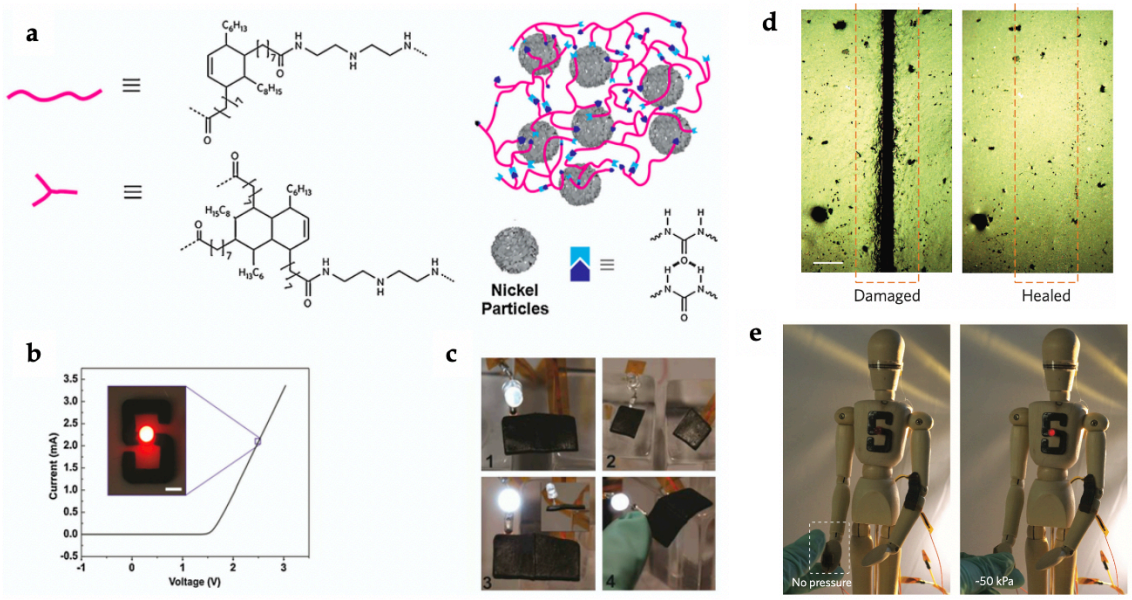

Figure 1.7 Self-healing conductor based on a composite of self-healing polymer and metal particles. (a) Illustration of the self-healing composite. Pink lines represent linear and branched polymers that form the randomly branched network; blue and purple shapes represent urea groups at the ends of the branched polymers that form the primary hydrogen bonds between the polymer chains. (b) A current–voltage curve of a commercial LED using self-healing electrically conductive composite wire molded into an 'S' shape. (c) Healed film being flexed to show its mechanical strength and flexibility after only 5 min of healing at room temperature. (d) Optical microscope image of damaged sample and complete scar healing for 31 vol% μNi composite. Scale bar, 1 mm. (e) Tactile sensor circuit demonstration. LED intensity responds as a function of increasing tactile pressure ([43] B. C-K. Tee *et al.*, An electrically and mechanically self-healing composite with pressure- and flexion-sensitive properties for electronic skin applications, *Nat. Nanotechnol.* **7**, 825, 2012).

1.6 Sticktronics

With the exciting development of Internet of Things (IoT), the ability to endow the surface of existing objects with desired electronic features has been attractive. The

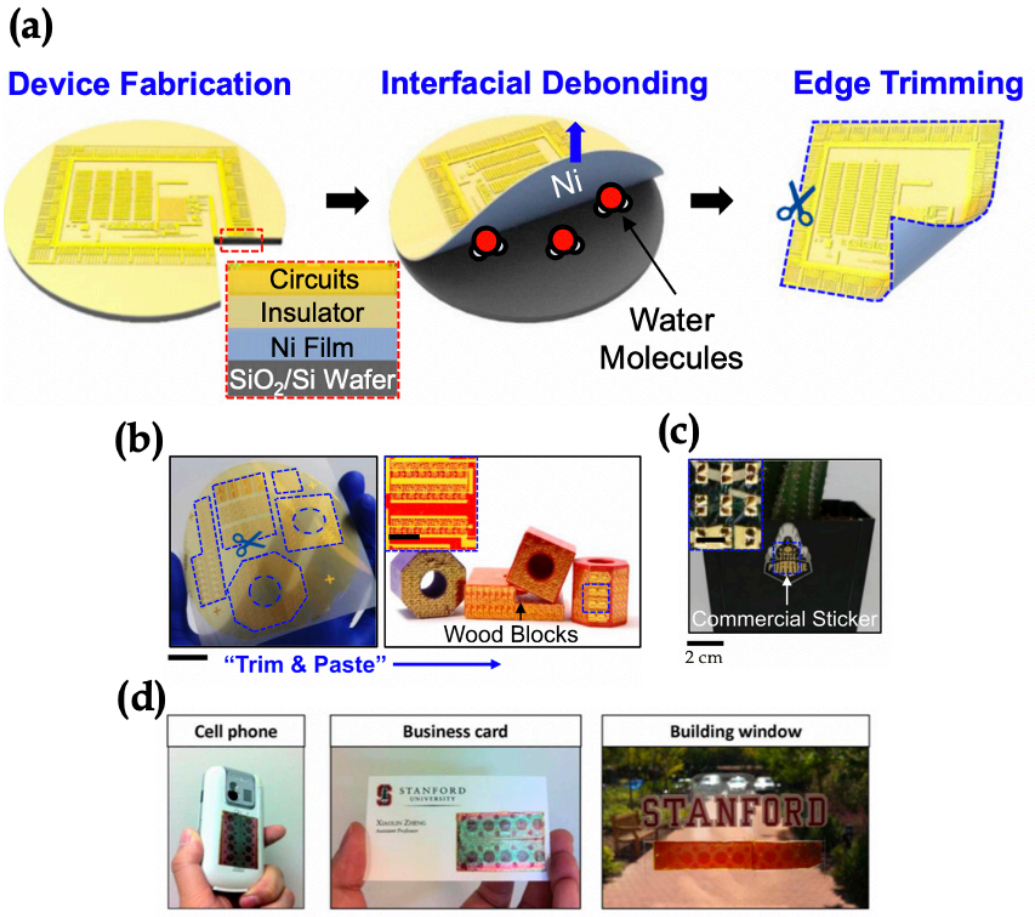

Figure 1.8 Schematic illustrations of the concept of sticktronics (sticker + electronics). (a) Schematic illustrations of key steps for physically liberating a thin-film nanoelectronics from its fabrication SiO2/Si wafer in water. The Inset shows a cross-sectional illustration. (b) Optical images of arrays of liberated thin-film capacitors on a thermally releasable tape (Left) and after pasted on the surface of commercial wooden blocks with right fits (Right). (Scale bar: 2 cm.) The Inset shows a magnified view of the transferred devices. (c) Optical image of arrays of liberated temperature sensors pasted on the surface of a commercial flowerpot with a commercial sticker. (Scale bar: 2 cm.) The Inset shows a magnified view of the transferred sensor arrays. (Scale bar: 2 mm.) (d) Optical images of liberated thin-film solar cells on cell phone (left), business card (middle), and building window (right) ([46] D. S. Wie *et al.*, Wafer-recyclable, environment-friendly transfer printing for large-scale thin-film nanoelectronics, *PNAS* **115**, 7236, 2018).

sticktronics (sticker + electronics) enables that the realization of high-performance thin-film electronics on arbitrary places including cell phone, business card, and building window, as shown in Figure 1.8 [46]. The physically liberated thin-film nanoelectronics peeled off from the original substrate such as silicon can be then pasted onto arbitrary places of interest, thereby endowing the particular surface with desirable add-on electronic features. These arbitrary objects are previously inaccessible due to the incompatibility issues with the existing device fabrication facilities. Therefore, the peel-and-stick process provides a simple way for integrating desirable electronic devices into buildings, clothes, home appliances, furniture, bath tiles, metals, human skins, and many other nonconventional substrates. However, state-of-art sticktronics are exploiting commercially available adhesives involving thermal release tape and/or stickers. Therefore, malleable electronic materials having a re-bondable, adjustable, and long-term adhesion could be promising as a candidate material for sticktronics. In this thesis work, it is demonstrated that the structural design strategy that serves as a versatile method for polymers to prepare efficient self-healing adhesives (SHAs) is applicable to sticktronics.

1.7 Goal of research

The aim of this dissertation work is to develop stretchable electronics based on the self-healing polymers designed to enable spontaneous repair of the mechanical damage and thus increase the lifetime of the stretchable devices. The self-healing strategy is highly desirable for stretchable electronics because the lifetimes of many stretchable sensors are limited by the dilemma of mechanical fractures under large deformation. To

achieve this goal, strong metal-ligand binding sites are placed within the polymer ligand by adding zinc ions, which results in highly dynamic metal-ligand interactions. This motif of spontaneous self-healing based on the dynamic coordination bond has been demonstrated by the presence of an amorphous structure in novel self-healing polymers with a low T_g to enable polymer mobility. The dynamic bonds can readily break and re-bond, which is favorable for energy dissipation under stretching and self-healing on being damaged. In the meantime, the metal ions still present near the ligands by the strong interactions, which allows a rapid self-association. In addition, we also demonstrate a practical potential of self-healing polymers as a self-healing adhesive (SHA). Cracks and damage in the adhesive joint during cycling can be healed spontaneously by the dynamic coordination bonding adhesive used. Therefore, the SHA would open up a new opportunity for many applications of self-healing materials.

On the basis of the merits of our novel self-healing polymers, they have great potential in stretchable and flexible electronics. This thesis includes investigations of the stretchable and self-healable strain sensors based on metal-ligand complexed self-healing polymers. As a different application of stretchable electronics, research on development of a stretchable chemical sensor, which is capable of detecting ammonia (NH_3) vapors, is also described. Sensitivity and recovery times that are ten times higher and faster than state-of-art ammonia sensors made from SWCNTs have been observed.

1.8 Organization of thesis

The organization of the thesis is as follows: Chapter 2 introduces ultra-fast and autonomous self-healing polymers base on the metal-ligand interactions. As major findings, we demonstrate the correlation of activation energy of self-healing materials and self-healing efficiency. The kinetic model describing the effect of moisture within materials on the self-healing ability has been established. Some potential applications of novel self-healing polymer – self-healing adhesives, anti-scratching coatings, interlaying materials for laminated safety glass, pressure sensitive adhesives (PSAs), and energy absorbing materials – have been demonstrated in this chapter.

Chapter 3 describes the stretchable and self-healable strain sensors based on metal-ligand complexed self-healing adhesive (SHA). The SHA-based wearable sensor can be attached directly on the skin in order to accurately detect complex human motions. Furthermore, the composite-type strain sensor comprised of the SHA associated with AgNWs indicates a dramatic improvement of the gauge factor, rendering it to be worked from small strain to extreme strain. With high stretchability, predictable responses, autonomous self-healing ability, and ease of processing, the applications of SHA-based sensor can be extended to pressure sensing, health monitoring, medical diagnosis, soft robotics, and artificial skin.

Chapter 4 demonstrates a stretchable chemical sensor, which is capable of detecting ammonia (NH_3) vapors. Sensitivity and recovery times that are ten times higher and faster than state-of-art ammonia sensors made from SWCNTs are obtained. The flexible polymer electrolyte-based NH_3 sensor studied in this present work will provide

new opening insights to create commercially available and cost-effective chemical sensors.

Chapter 5 summarizes all of the work done so far and discusses the further works to be done and prospects for stretchable electronics along with self-healing materials.

Chapter 2

Ultra-fast Self-healing Adhesives via Activation Energy Controlled Metal-Ligand Interactions

2.1 Introduction

2.1.1 Self-healing materials

Self-healing is referred to as the ability of a material to recover its original shape or structure upon mechanical damage. Human skin has been known as a natural material for the perfectly spontaneous self-healing. Recently, self-healing materials are under intense development because self-healing ability would improve the lifetime, recyclability, durability, energy efficiency, and safety of synthetic materials. According to the study of the National Association of Corrosion Engineers (NACE) International, the worldwide corrosion authority, the global cost of corrosion is estimated to be $2.5 trillion per year, which is equivalent to 3.4% of the global GDP (2013). By using available corrosion control solutions, it is estimated that savings of between 15 and 35% of the cost of corrosion could be realized; i.e., between $375 and $875 billion annually on a global basis. For this reason, self-healing materials with the tremendous potential to prolong the lifetime of materials have been emerged.

The primitive self-healing polymer was comprised of the fluidic self-healing catalyst covered by the microencapsulation dispersed into polymer matrix [47]. The structural complexity and restricted self-healing area within materials in early studies give rise to the necessity of autonomous self-healing materials which are capable of repairing themselves when mechanically damaged or chemically corroded. Recently, many synthetic materials with self-healing capabilities are highly desirable for applications involving self-healing conductors [48], self-healing sensors [41], and self-healing coatings [38]. A variety of self-healing strategies have been studied for polymeric systems. Conventionally, self-healing polymers make use of hydrogen bonds [39], dynamic covalent bonds [49], ion-dipole interactions [50], disulfide bonds [51], liquid metal interactions [52], and even the incorporation of healing agents [53] as the healing motifs.

Metal−ligand complexes are promising candidates as a trigger to induce an effective self-healing due to the reversible and dynamic nature of coordination bonds between metal and ligand under ambient condition. The reversible metal-ligand interactions are based on the ability of metal ions repeating the association and dissociation from the ligands. Several self-healing polymers have been reported by using reversible metal−ligand interactions triggered by external energy such as light [54] or heat [55] as well as the spontaneous polymer without any interventions [56] in order to induce the self-healing. Table 2.1 represents the comparison of the coordination bond with the covalent bond based on two molecular models, $H_3N \rightarrow BH_3$ and H_3C-BH_3. The arrow means the donation of lone-pair electron form nitrogen to boron in order to form the coordination bond. As shown in Table 2.1, the coordination bond has a smaller

rupture energy, longer bond distance, and larger dipole moment than those of the covalent bond. The strength of the coordination bond is one third that of the covalent bond. The bond length of the coordination bond is 10% larger than that of the covalent bond. Theoretically estimated dipole moment of $H_3N\rightarrow BH_3$ should be 8D when electrons equally paired. Therefore, the dipole moment of 5.22D shown in Table 2 exhibits that electrons are asymmetrically paired, in other words, the electron pair remains more closely associated with the donor than with the acceptor atom. Based on the molecular orbitals analysis, the coordination bond is accompanied by transfer of 20% electrons from N to B [201]. Therefore, the coordination bond is more desirable to make materials to be self-healed than the covalent bond which requires a high energy for breaking and reformation when damaged.

	Covalent Bond	Coordination Bond
Molecules	$H_3C\text{-}CH_3$	$H_3N\rightarrow BH_3$
Rupture enthalpy (ΔH_{dis}) at 298K [kcal/mol]	89.8	31.1
Bond distance [Å]	1.533	1.658
Dipole moment	0	5.22D

Table 2 Comparison of coordination bond with covalent bond in terms of structure, rupture enthalpy, bond distance, and dipole moment [201].

In this dissertation work, to realize a spontaneous self-healing polymer having simple fabrication procedures and free to organic solvents, we have been investigating a highly dynamic metal-ligand interaction, zinc-poly(vinyl alcohol) (Zn-PVA), as the healing trigger. PVA is a water-soluble polymer that has many excellent characteristics

such as film forming property and high bonding strength as well as harmless, anti-static and biodegradable properties. It can be used as a raw material for applications in the field of coating, adhesive agent, surfactant, emulsifier, dispersants, and films [57]. In addition, self-healing PVA hydrogels based on their hydrogen bonds as a self-healing motif were investigated [58]. However, these PVA hydrogels that just depend on the hydrogen bonds required a high concentration of raw material (35 wt% of PVA) to induce self-healing and long self-healing time from at least a few hours through several days.

Zinc(II) is known as a metal ion showing a fast ligand exchange and a reversible metal-ligand interaction [59]. According to this study, zinc ions can readily transfer between ligands showing the mechanism of association and dissociation. This active transfer ability of zinc ions is capable of forming a dynamic coordination bond under optimized conditions for material preparation. In addition to the characteristics of metal ion, the mobility of polymer chains as a ligand should be taken account into a significant requirement for the dynamic bonds. Some of the previous work that involved metal-ligand interactions for self-healing materials have conceptualized the mobility of polymer chains for the dynamic bonds by lowering a glass transition temperature (T_g) of polymer matrix [56]. D. Mozhdehi et al. has also argued that the metal-ligand complexes could be formed in the soft matrix region having a low T_g within polymer to achieve the autonomous self-healing [60]. However, this is not sufficient to describe the dynamic nature of metal-ligand complex based self-healing polymers.

Here we demonstrate the water effect on the self-healing property by placing the dynamic zinc ions to hydroxyl groups of poly(vinyl alcohol) (PVA) as a ligand. Particularly provided were ultra-fast self-healing via activation energy controlled metal-

ligand interactions studied in this dissertation. This self-healable polymer with the physical crosslinking formed via freezing-thawing process has been complexed with zinc ion which is able to generate Zn-PVA complexes contributing to the autonomous self-healing property as well as Zn-water complexes inhibiting materials from healing. It is known that self-healing polymers based on metal-ligand complexes are less affected by the moisture, whereas the hydrogen bonding mediated self-healing polymers are significantly sensitive to the moisture [56]. However, zinc ions could readily form the complex with water molecules, which results in the reduction in self-healing efficiency of materials. Therefore, we have investigated the effect of water on the activation energy which contributes to self-healing efficiency in the viewpoint of kinetics.

2.1.2 Self-healing adhesive (SHA)

Here, we introduce self-healing adhesive (SHA) that is a derivative of self-healing materials with practical potential for re-bondable and durable adhesion. This SHA with an adjustable and repeatable adhesion could repair the adhesive joints and heal autonomously cracks after being damaged. Specifically, as a special class of polymeric adhesives, pressure sensitive adhesive (PSA) with self-healing ability has attracted much attention. The PSA has been widely exploited to laminate optical films stacked on display panels in the field of liquid crystal displays (LCDs) and organic light emitting diodes (OLEDs). It is a kind of quasi-reversible adhesive, which is able to adhere to different substrates when pressure is applied. The PSA has a viscoelastic property with a low glass transition temperature, thus sustaining permanently tacky and soft characteristics. As the stretchable and foldable displays are gradually emerging to the market, those areas would

require different types of PSAs with self-healing ability and superior stretchability to conventional PSAs. We demonstrate herein that novel SHA exhibits an adjustable adhesive property required as PSA as well as excellent durability such as energy absorbing ability and chemical stability.

We also demonstrated special applications of SHA towards stretchable and wearable sensors. The SHA based on the metal-ligand interactions and activation energy adjustment surpasses conventional elastomers such as poly(dimethylsiloxane) (PDMS) in the aspect of stretchability. Moreover, the SHA exhibits an electrically conductive property without an addition of conducting substances. It is known that most stretchable electronic devices that are soft and conformable have relied heavily (over 90 %) on a PDMS as the elastomeric substrate [61]. Y. Rao et al. studied on self-healing crosslinked polymers via metal-ligand coordination bonds [62]. They induced metal-ligand complexes by using PDMS associated with bipyridine and metal salts such as Fe^{2+} and Zn^{2+} resulting in the autonomous and stretchable self-healing materials. However, some intrinsic drawbacks of PDMS exhibiting a limited stretchability (< 200 % strain) and a poor adhesion to human skin limit practical applications of ultra-stretchable and wearable electronics. Furthermore, it is not adequate for devices requiring a crack resistance and long-term lifetime due to the lack of self-healing ability after being damaged. More importantly, many materials for stretchable electronics has been extremely restricted for eco-friendly and skin attachable applications because they are dissolved by organic solvents. Consequently, we demonstrate stretchable and wearable sensors based on the SHA, exhibiting an excellent stretchability over 1,000 % strain as well as a remarkable safety which is harmless when attached to human skins.

Herein, ultra-fast and autonomous self-healing polymers based on the coordination bonds associated with metal-ligand complexes are demonstrated. Specifically, a self-healing adhesive (SHA) has been introduced as a practical application of self-healing materials. We describe a design concept of SHA that takes advantage of the systematic approach in adjusting the self-healing efficiency in terms of the activation energy. Novel SHA may include crosslinked polymer networks comprising Zn-PVA complexes, providing the reversible and dynamic bond for the self-healing. These Zn-PVA complexes coexist in the SHA competing with significant amounts of Zn-H_2O complexes inhibiting ultra-fast self-healing. Therefore, the structural design strategy to form the desirable Zn-PVA complexes may serve as a versatile method for polymers enabling autonomous self-healing and very high stretchability. We demonstrate the kinetic approach to attest our hypothesis that the control of activation energy supports to increase the preferable Zn-PVA complexes, while the inhibitive Zn-H_2O complexes could be suppressed via dehumidification process. Furthermore, we envision the application of SHA towards re-bondable and adjustable PSAs as well as self-healing wearable sensors associated with good stretchability and electrically conductive properties.

2.2 Experimental methods

In the present work, ultra-fast self-healing adhesives (SHAs) based on Zn-PVA complexes were basically obtained by a freezing-thawing method [63]. 10 g of PVA (Sigma-Aldrich, M_w ~ 89,000 g/mol, > 99% hydrolysis) was dissolved in 100 ml of

deionized water while vigorously stirring it with a magnetic bar at 90 ℃ for 1 hour and then the mixed solution was cooled to room temperature. For metal-ligand complexation, zinc nitrate hexahydrate, $Zn(NO_3)_2 \cdot 6H_2O$, was chosen as the Zn^{2+} source due to its good solubility with water as well as thermal stability in the solid state. Zinc nitrate hexahydrate (Sigma-Aldrich, purum p.a., crystallized > 99% grade, $M_w \sim 297.49$ g/mol) was added into 10 wt% PVA solution prepared with molar ratios (N_{PVA}:N_{Zn}) of 10:1, 10:1.5, 10:2, 10:2.5, and 10:3 followed by additional mixing using a magnetic bar at 25 ℃ for 1 hour. Each of these as-prepared homogeneous aqueous solutions were poured into a polycarbonate petri-dish of desired dimension and then frozen in a refrigerator at −15 °C for 24 hours. The fully frozen samples were thawed out at room temperature for 3 hours. This freezing-thawing process was repeated to three cycles, resulting in the formation of Zn-PVA complexed hydrogels. Finally, we prepared several sets of the same samples as ones prepared via aforementioned procedures. In order to investigate the effect of heat on self-healing, self-healing times for some sets of samples were evaluated upon heating at 30, 40, 50, and 60℃ compared to room temperature. Likewise, we have put other sets of samples into a desiccator to remove residual water existing within Zn-PVA complexes. These dehumidified samples were prepared to analyze the effect of moisture on self-healing efficiency. The observed humidity and temperature inside the desiccator were 17 ± 2 %RH and 22 ± 1 ℃, respectively. The self-healing time was evaluated by measuring a time showing the elongation of 200 % without any fractures in healed region of each sample when self-recovered under given conditions.

2.3 Results and discussion

2.3.1 Visual observation of self-healing polymers

Figure 2.1 shows visual observations of features for SHAs in comparing relative amounts of a transition metal ion, zinc, and a ligand of PVA after three cycles of freezing-thawing. The ratios range from a ratio of moles of PVA (N_{PVA}) to moles of zinc ions (Zn^{2+}) (N_{zn}) of 10:0 up to 10:3. Whereas the pristine PVA hydrogel without adding zinc ions to polymer is visually opaque, the Zn-PVA complexed hydrogels become gradually transparent as the molar ratio of zinc to PVA (N_{Zn}/N_{PVA}) increases, as shown in Figure 2.1. For example, a ratio of N_{PVA}:N_{Zn} of 10:2 or greater appears to start having transparency. This can be attributed to the steric hindrance of zinc ions forming the coordination bond with the hydroxyl groups of PVA, thus preventing PVA from being crosslinked via physical crosslinking during the freezing-thawing cycles.

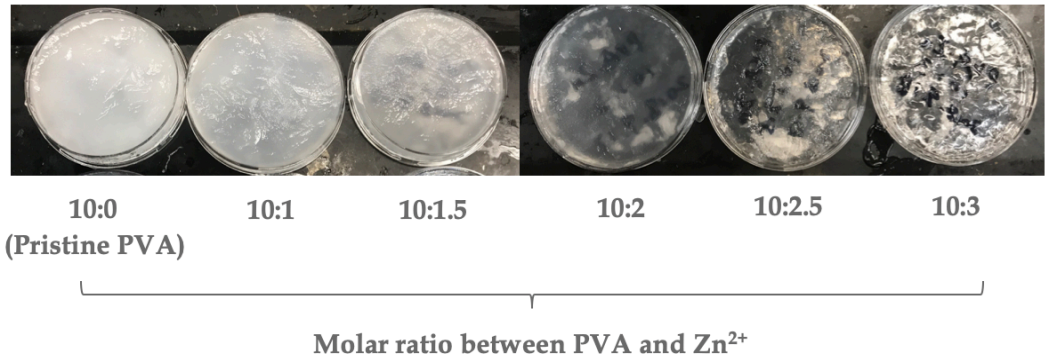

Figure 2.1 Visual observation of features for self-healing polymers in terms of respective amounts of a transition metal ion, here zinc, and a ligand of poly(vinyl alcohol) (PVA). More specifically, self-healing hydrogels based on Zn-PVA complexes via freezing-thawing process over 3 cycles are shown.

It has been widely accepted that the gelation phenomenon is a result of formation of network in which PVA crystallites work as junction points. Nambu et al. studied that aqueous PVA solution is highly gelled when the "repeated freezing-and-thawing" method was applied [64]. Aqueous PVA solution was first frozen and then the frozen state was released at a low temperature above 0 ℃. With increasing the number of freezing-thawing cycle, a rubber-like elasticity with water resistance in the resultant gel increases, whereas the inherent stickiness caused by the original solution decreases. It is generally known that the physical crosslinking of PVA hydrogels is formed by the local recrystallization via folding of PVA backbone chains mediated by the intramolecular and intermolecular hydrogen bond between hydroxyl groups of PVA during freezing-thawing process.

F. Yokoyama explained this phenomenon on the basis of micro-phase separation that may occur in the PVA-water system during freezing [65]. They suggested a structural model for the highly elastic PVA hydrogel which is prepared by the repeated freezing and melting, as shown in Figure 2.2. The model shows that the hydrogel is composed of the following three kinds of phases: water phases or solution phases with a very low concentration of PVA, which in the frozen gel correspond to the crystal phases of ice; amorphous phases, in which every PVA chain is associated with water; PVA crystal phases, which restrain gross mobility of the amorphous chains. It is suggested that a very large fraction of water is the bulk water or free water. Here, it is unquestionable that water molecules which are classified into the category of free water are directly related to the formation of ice crystal phases. This isolated bulk water phase (equal to ice crystal phase) can be called the PVA-poor phase, as seen in Figure 2.2. However, bound

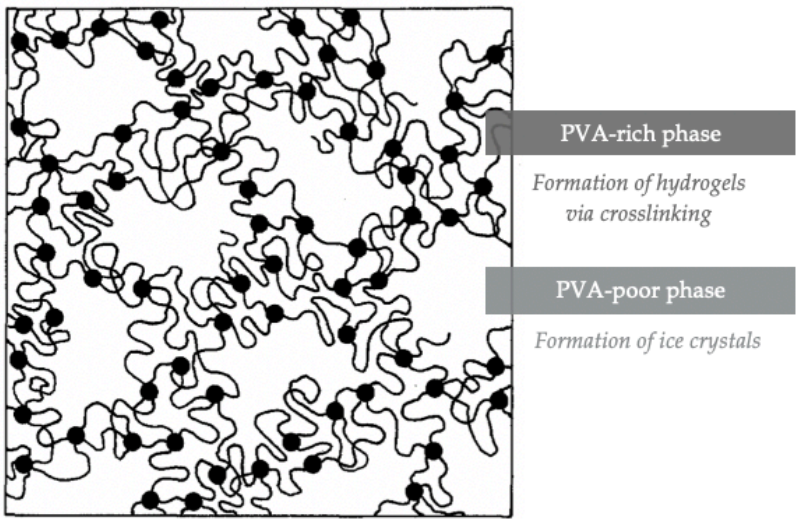

Figure 2.2 Schematic representation of structural model of PVA hydrogel prepared by the "repeated freezing and thawing". Solid circles represent PVA crystallites as a junction point for physical crosslinking ([65] F. Yokoyama *et al.*, Morphology and structure of highly elastic poly(vinyl alcohol) hydrogel prepared by repeated freezing-and-melting, *Colloid & Polymer Sci.* **264**, 595, 1986).

water as the different category of water interacts strongly with the polymer molecules forming PVA-rich phases. It is expected that polymer chains as impurity will be rejected from the growing ice crystals whenever the PVA-water system is frozen. Thus, with the freezing cycle number, the concentration of PVA in the PVA-rich solution phases increases, while that in the PVA-poor solution phases decreases. Then, the denser domains from the PVA-rich phases begins to be built up by segregation at ice grain boundaries. Consequently, the formation of the PVA crystallites which act as the junction points is much facilitated in the segregated phases and the gelation is much enhanced.

For this reason, the original PVA hydrogel (N_{PVA}:N_{Zn}=10:0) exhibits visually cloudy and almost non-transparent appearance, as shown in Figure 2.1. However, owing

to a strong metal-ligand interaction between zinc ions and hydroxyl groups in PVA chains, a large amount of amorphous chains could remain in the SHAs as shown in Figure 2.3. With the addition of zinc ions to PVA, metal-ligand complexations begin to interfere with the chain folding between PVA backbone chains due to the steric hindrance of zinc ions and the reduction in the formation of hydrogen bonds. Therefore, Visual observation of optical transparency shown in Figure 2.1 is taken into account to estimate a change of crosslinking density during the formation process. As a result, the formation of PVA crystalline phases could be restricted by the metal-ligand complexes, thus SHAs indicate an optically transparent property.

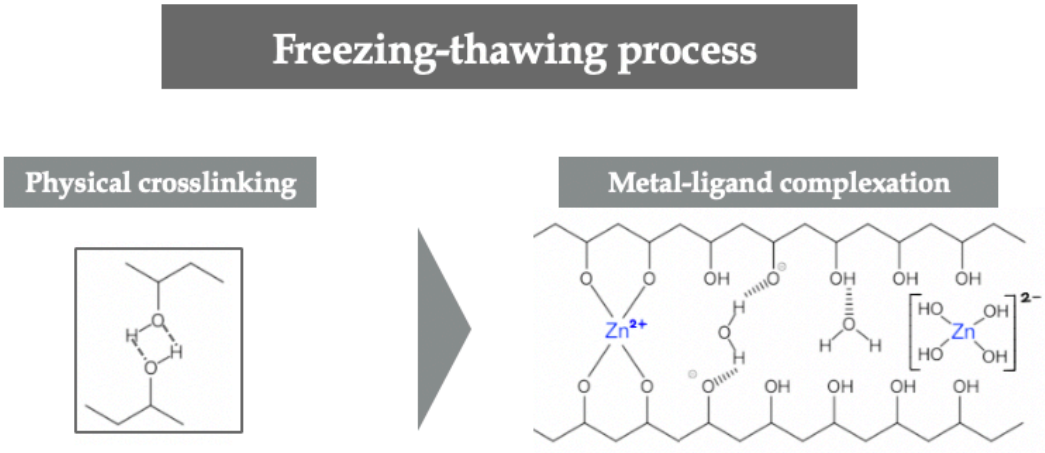

Figure 2.3 Reduction in PVA crystallites formed by physical crosslinking via the freezing-thawing process. The Zn-PVA complexation inhibits the formation of intramolecular hydrogen bonding between PVA chains contributing to the physical crosslinking, thus remaining a large amount of amorphous phases in the SHAs.

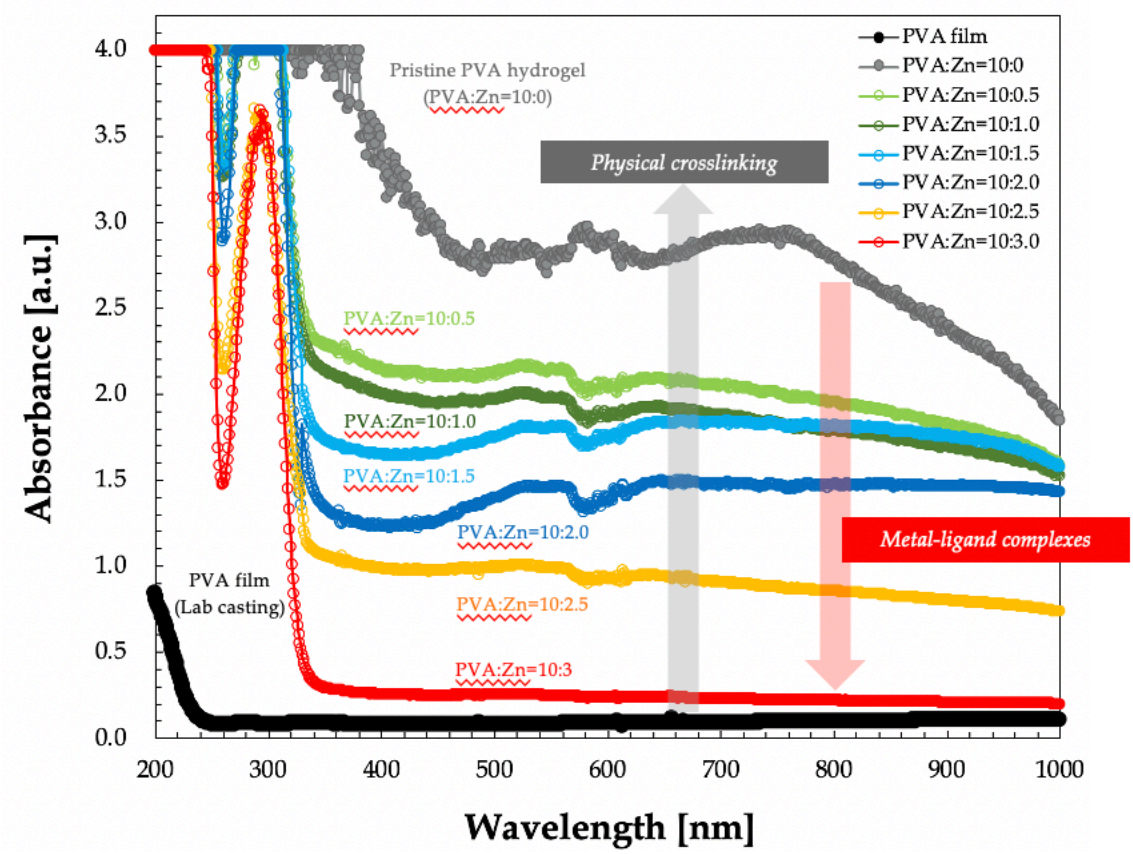

Figure 2.4 UV-Vis spectra of the pristine PVA film, PVA hydrogel and self-healing polymers in terms of the various molar ratios of PVA and zinc ions.

2.3.2 Optical extinction via UV-Vis spectra

Figure 2.4 indicates the UV-Vis spectra of the pristine PVA film, PVA hydrogel and SHAs in terms of the various molar ratios of PVA and zinc ions using an Agilent Cary 6000 UV-Vis spectrophotometer. With an increase of zinc concentration, the transmittance of SHAs increases in the visible wavelengths. Specifically, optical extinction at the wavelength of 550 nm has been extracted as reflected in Figure 2.5 for SHAs having different molar ratios of metal-ligand. The higher extinction indicates the

material is less transparent. Optical extinction of pristine PVA hydrogel physically crosslinked without any metal ions and SHA with a molar ratio of zinc ion and PVA ligand of 10:3 is 2.79 and 0.25, respectively. The extinction of SHA decreases about 91 % compared with that of pristine PVA hydrogel. Therefore, it is indirectly estimated that zinc ions affect the decrease in the density of physical crosslinking in the polymer as previously described. The optical extinction represents a quadratic decrease with respect to a molar ratio of zinc ions and PVA ligands as shown in Figure 2.5.

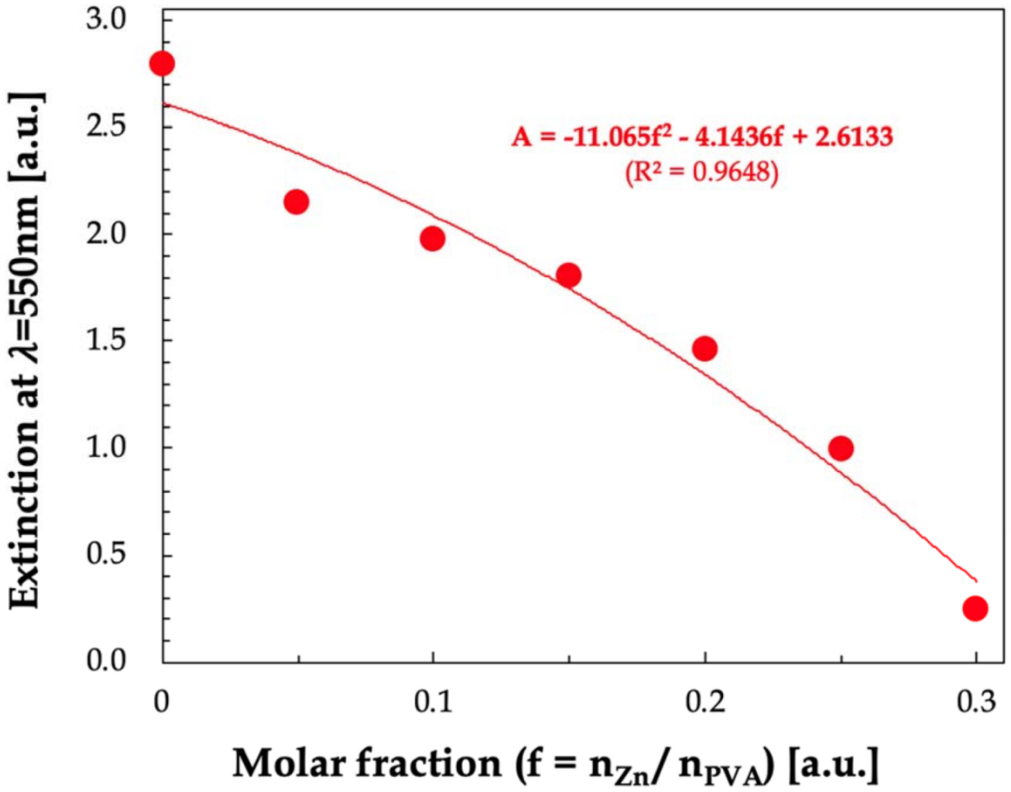

Figure 2.5 Optical extinctions at a wavelength of 550 nm for self-healing polymers having different molar ratios of zinc ion to PVA ligand. The extinction of SHA with a molar ratio of zinc ion and PVA ligand of 10:3 decreases about 91 % compared with that of pristine PVA hydrogel.

2.3.3 Freezing-thawing process for preparation of SHA

To fabricate the self-healing polymer, we have used PVA as a polymer matrix, as previously described. We studied the effect of the degree of hydrolysis (or degree of saponification) in PVA on the gelation. It is common knowledge that the gelation is very sensitive to the degree of saponification, i.e., the bulkiness and lower water-resistance of unsaponificated acetyl groups in the chains prevent the growth and propagation of PVA crystallites in the water environment, and then the gelation is very retarded. A lower saponificated PVA sample (98.7 mol%) than the sample used here (99.8 mol%) needed a considerably larger cycle number of freezing, N > 20 where the porous structure in the xerogel began to be observed [65]. Whereas PVA with the degree of hydrolysis (DOH) > 99 % forms the hydrogel via freezing at -10 ℃ for 12 hours followed by the thawing at room temperature, PVA having the DOH of 88 % could not form the hydrogel under the same conditions, as shown in Figure 2.6.

As a major finding, aqueous PVA solution is highly gelled via the repeated freezing-thawing method and we used this technique to make novel ultra-fast SHAs in the present work. In general, rubber-like elasticity in the resultant PVA hydrogel increases via freezing-thawing cycles. For this reason, PVA has been widely used to fabricate hydrogel-type polymers. As far as we know, PVA is a unique polymer whose hydrogel prepared through the freezing-thawing process exhibits rubber-like elasticity. According to our experiment, other water-soluble polymers such as poly(acrylic acid) (PAA), poly(ethylene glycol) (PEG), and polyacrylamide (PAAm) could not form the hydrogel via freezing-thawing process. The frozen polymers mentioned above were melt into the original solution state under thawing at room temperature, while PVA-water

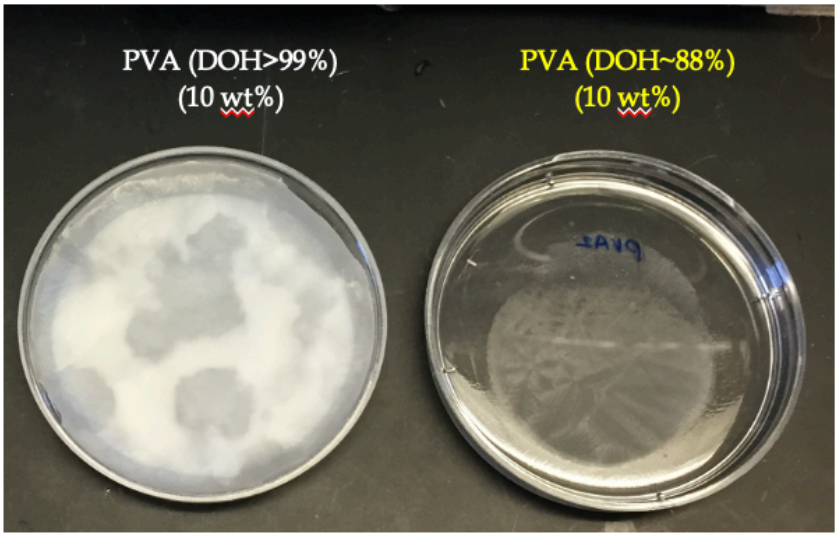

Figure 2.6 Effect of the degree of hydrolysis (or degree of saponification) in PVA on the gelation. The gelation is very sensitive to the degree of saponification, i.e., the bulkiness and lower water-resistance of unsaponificated acetyl groups in the chains prevent the growth and propagation of PVA crystallites in the water environment, and then the gelation is very retarded.

system forms physically crosslinked networks with a porous structure caused by the ice crystals. Instead the aforementioned polymers could form the hydrogel when they mixed with each other [66], otherwise mixed with other polymers involving PVA. A number of investigations have been published about PVA and PAA blend materials, especially as separation membrane materials [67] and PVA/PAA hydrogels as an actuator-sensor [68].

PVA and PAA are both self-associated polymers due to the hydrogen-bonding interactions formed either intermolecularly or intramolecularly among their polar groups, which are hydroxyl groups (-OH···OH) in PVA and carboxyl groups (-COOH···COOH) in PAA. As seen in Figure 2.7, the incorporation of PAA into PVA solution would break some self-associated hydrogen bonds and form a new intermolecular network by the

formation of hydrogen bonds between the hydroxyl group in PVA and the carboxyl group in PAA [69]. It is deduced that PAA could not form the intramolecular hydrogen bonding rather than the intermolecular hydrogen bonding because the strong repulsion between carboxylic anions ($R\text{-}COO^-$) with a high acid dissociation constant (K_a). On the other hand, PVA itself is capable of forming the strong intramolecular hydrogen bonding in a single chain, as shown in the red box of Figure 2.7. Then, the formation of the PVA crystallites which act as the junction points is much facilitated by the chain folding induced by the intramolecular hydrogen bonding and subsequently the gelation is much enhanced. Therefore, it is expected that PVA is an adequate material to make hydrogel-like polymers without any additive polymers for achieving the spontaneous self-healing materials in the present work.

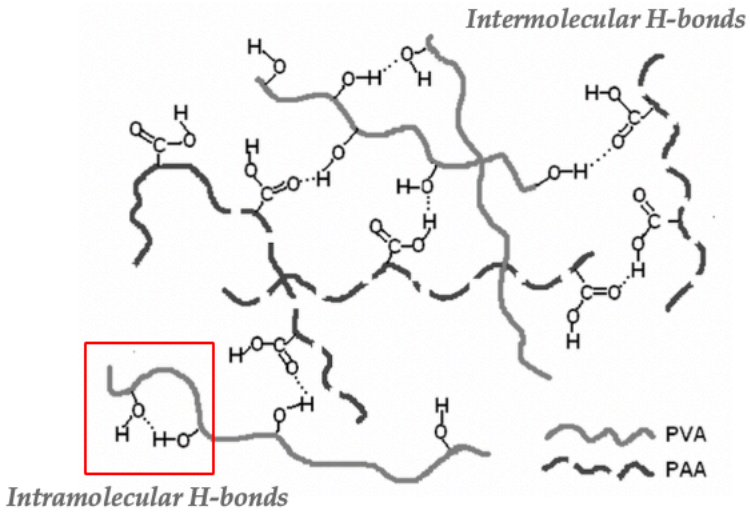

Figure 2.7 Schematic representation of different types of hydrogen bonds formed in PVA and PAA blending system ([69] N. Chen *et al.*, The role of hydrogen-bonding interaction in poly(vinyl alcohol)/poly(acrylic acid) blending solutions and their films, *Chinese Journal of Polymer Science* **28**, 903, 2010).

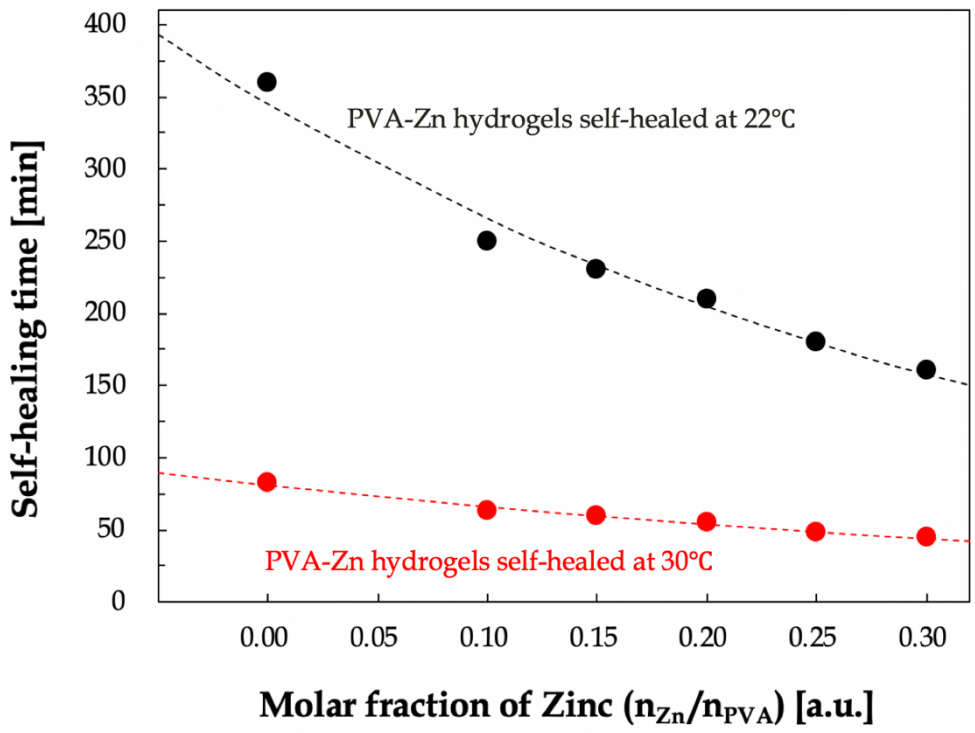

Figure 2.8 Evaluation of self-healing time for self-healing polymers fabricated via a freezing-thawing process. Whereas the self-healing polymers healed at 22°C (designated by black circles) indicates a long self-healing time of about 3 hours through 6 hours to recover to their original state, the self-healing time dramatically deceases when the self-healing polymers are stored at elevated temperature of 30 °C (designated by red circles).

2.3.4 Evaluation of self-healing efficiency in self-healing polymers

We evaluated self-healing time in order to estimate the self-healing efficiency of self-healing polymers. Figure 2.8 shows the self-healing time for self-healing polymers having different molar ratios of zinc to PVA. The self-healing time is defined as a time available to stretch a sample to an elongation of at least 200% without any fractures in healed region. First, a sample is cut into two pieces to replicate potential mechanical damage that may occur. Then, the two pieces are contacted with one another, which may

also be conducted with gently applied pressure. The contact with an optionally applied pressure promotes a dynamic metal-ligand bond, thus adhering and re-bonding the broken parts effectively. After recovery for the prescribed self-healing time, two pieces of specimen cut can self-heal autonomously at 22 ℃ (black circles) and elevated temperatures at 30 ℃ (red circles). Self-healing polymers fabricated via the freezing-thawing method with 3 cycles requires a long self-healing time of about 3 hours through 6 hours to recover to their original state from breaking at room temperature, as represented by black circles and line in Figure 2.8. However, the self-healing time dramatically deceases when the SHAs were stored at elevated temperature of 30 ℃ for 10 minutes, as red circles shown in Figure 2.8.

For further understanding of heating effect on the self-healing time, self-healing tests are conducted at various temperatures (30, 40, 50, and 60 ℃). Figure 2.9 represents the effect of heating temperature on the self-healing time for the self-healing polymers. The self-healing time evidently declines when Zn-PVA complexed polymers are thermally treated at elevated temperatures (30, 40, 50, and 60 ℃) for 10 minutes, as can be seen in Figure 2.9. This effect is believed to result from an increase in the rate of reaction to form the coordination bonds between zinc ions and ligands in the PVA. According to the Arrhenius equation set forth below, the kinetic constant increases with temperature, thereby activating the reaction to form Zn-PVA complexes:

$$k = A \cdot exp\left(-\frac{E_a}{k_B T}\right) \qquad \text{(Eq. 1)}$$

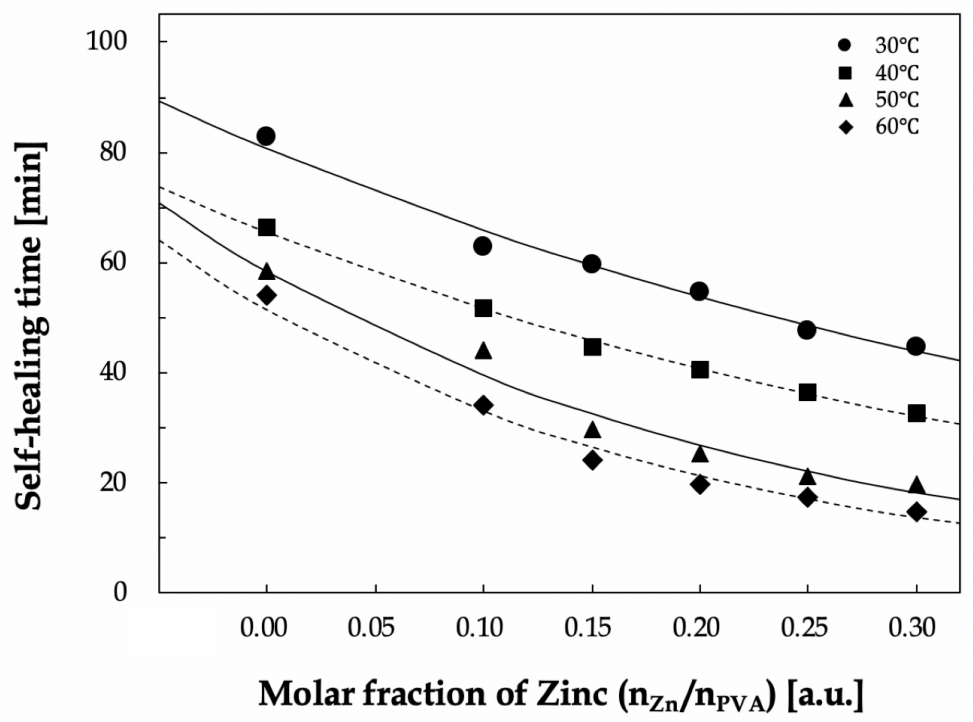

Figure 2.9 Effect of temperature on a self-healing time for self-healing polymers prepared in accordance with certain aspects of the present disclosure based on the coordination bonds formed via the freezing-thawing process followed by additional heating at 30, 40, 50, and 60 ℃.

where k is the kinetic constant related to a self-healing rate, E_a is the activation energy, k_B is the Boltzmann constant, and T is the absolute temperature. According to the Arrhenius equation, a rate of self-healing is dominated by temperature and activation energy. In general, higher temperatures can induce an increase in the reaction constant from the standpoint of kinetics. This feature is corresponding to the tendency of fast self-healing at higher temperatures than room temperature, as shown in Figure 2.9.

Another effective way to increase the kinetic constant is to reduce the activation energy. Figures 2.10A–2.10B illustrate two types of complexes existing within the self-

healing polymeric material. Figure 2.10A shows a Zn-PVA ligand complex that facilitates self-healing bonds in the polymeric material. Figure 2.10B, on the other hand, is a Zn-H_2O complex that appears to inhibit formation of a dynamic bond that promotes self-healing. As a result, the activation energy of certain self-healing polymers could be lowered via a dehumidification process. This result can be attributed to the decrease in the number of Zn-H_2O complexes that inhibit the self-healing efficiency. It is believed that after removing of water molecules, most of the zinc ions can then participate in the formation of coordination bonds with PVA ligands, thus enhancing a reversible ability of breaking and reforming.

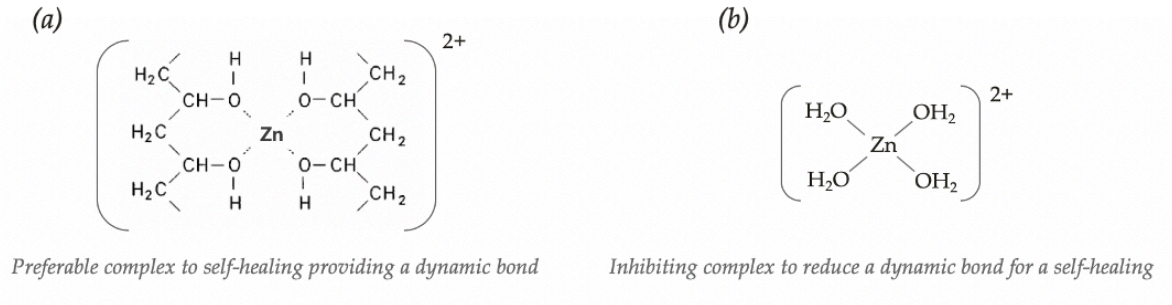

Figure 2.10 Two types of complexes existing within a self-healing polymeric material prepared via freezing-thawing process. Figure 2.10A shows a Zn-PVA complex that facilitates self-healing bonds in the self-healing polymer. Figure 2.10B on the other hand is a Zn-H_2O complex that appears to inhibit self-healing.

Figure 2.11 demonstrates the effect of dehumidification on the self-healing efficiency of self-healing polymers. The self-healing polymers as control samples comprised of PVA and Zn hydrogels that undergo the freezing-thawing process for 3 cycles are shown in Figure 2.11 as black circles. The other set of control samples formed by the same freezing-thawing process with a subsequent heating at 60 °C are shown as

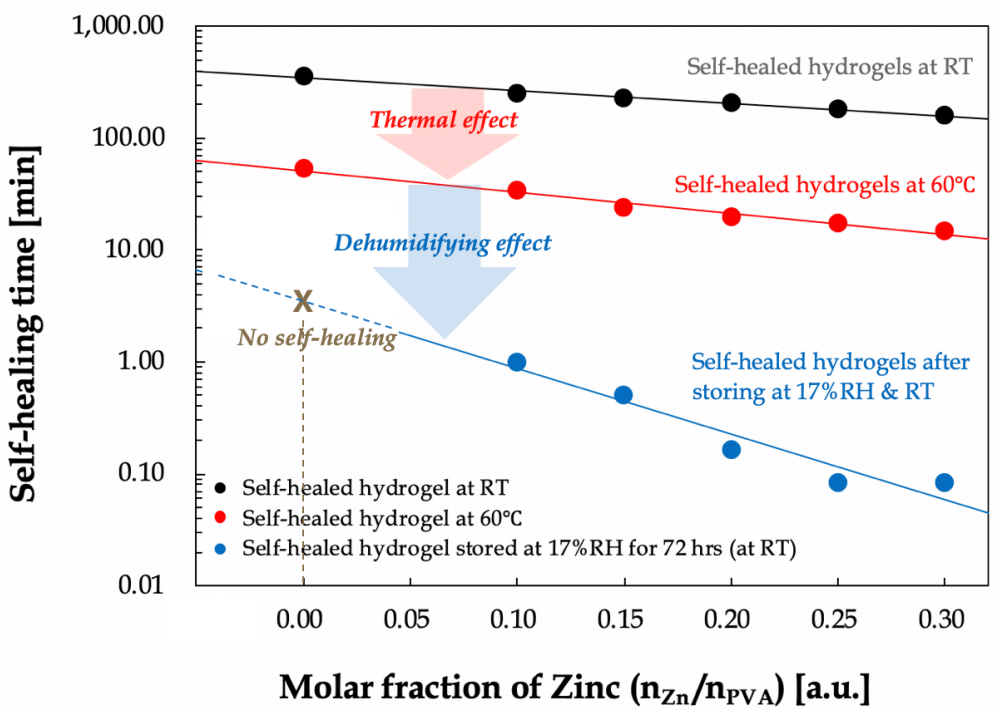

Figure 2.11 Comparative self-healing times for polymers prepared in accordance with certain variations of the present disclosure. Black circles show a self-healing polymer samples comprising PVA and zinc ions formed from 3 cycles of a freezing-thawing process. Red circles indicate Zn-PVA complexed self-healing polymer samples undergoing 3 cycles of a freezing-thawing process followed by subsequent heating at 60°C. Self-healing polymers formed by the same freeze-thaw processes, followed by the dehumidification process in the desiccator set to 22 °C and 17 %RH for 72 hours are shown as blue circles.

red circles. Finally, self-healing polymers formed by the same freezing-thawing processes, followed by the dehumidification process in the desiccator set to 22 °C and 17 %RH for 72 hours are shown as blue circles. Interestingly, the self-healing time is dramatically reduced to about 5 to 10 seconds when a molar ratio of zinc (N_{Zn}) to PVA (N_{PVA}) is 0.3, after dehumidification, as shown in the data (blue circles) of Figure 2.11. This sample can be referred to as the self-healing adhesive (SHA). The ability to undergo ultra-fast self-healing observed in the SHA may be originated from the control of activation energy by

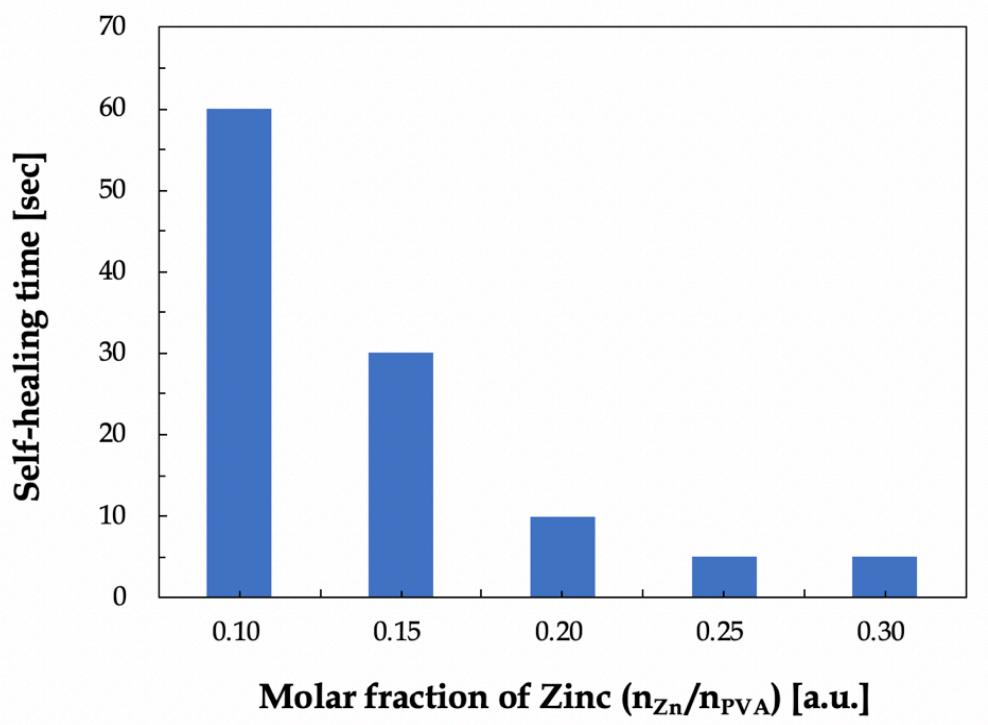

Figure 2.12 Self-healing time of self-healing polymers fabricated by the freezing-thawing process of 3 cycles followed by the dehumidification process in a desiccator set to 22 ℃ and 17 % RH for 72 hours.

removing water from the polymer. Therefore, the dehumidification is an essential process in order to achieve the autonomous elf-healing system.

Figure 2.12 summarizes the self-healing time of the dehumidified self-healing polymers corresponding to blue circles shown in Figure 2.11. This ultra-fast self-healing ability can be attributed to an increase in Zn-PVA complexes, rather than Zn-H_2O complexes as water molecules within hydrogels are removed via the dehumidification process. Water can act as a barrier inhibiting the reaction of zinc ions with hydroxyl groups of PVA to form the coordination bonds. Therefore, the activation energy (E_a) term from the Arrhenius equation increases when the self-healing polymer possesses high

amounts of water within material. From the viewpoint of kinetics, the kinetic constant for the formation of Zn-PVA complexes would increase as a water barrier is removed. Particularly prominent in this study is to control the activation energy of self-healing system via the dehydration process.

2.3.5 Estimation of activation energy in self-healing polymers

Here we demonstrate that the activation energy is affected by the presence of water molecules within the self-healing polymers. Therefore, it is noted that a considerable amount of water should be removed in order to achieve the ultra-fast self-

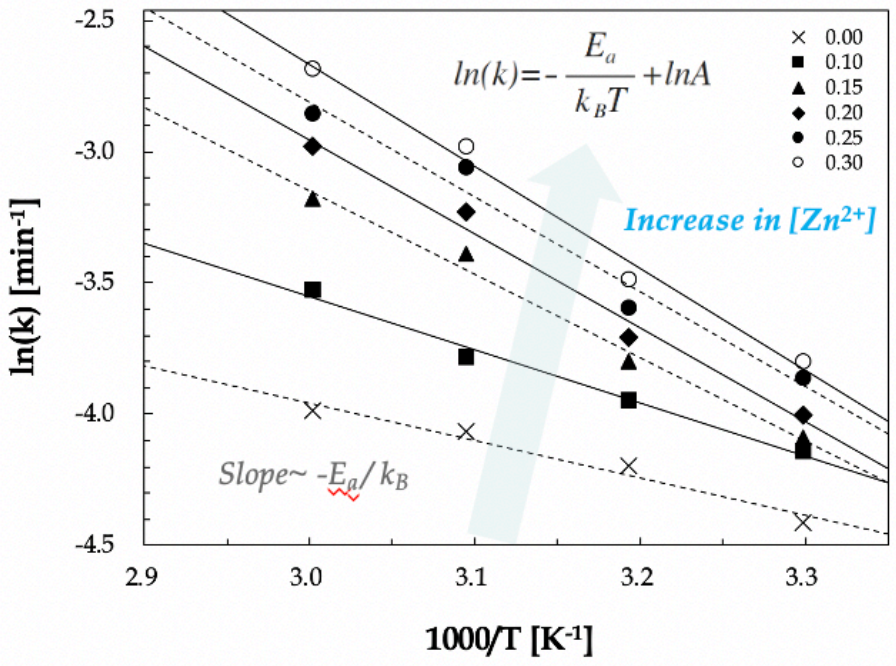

Figure 2.13 Arrhenius plot of ln (k) versus 1000/T to show a self-healing rate constant which is inversely proportional to the absolute temperature for the self-healing polymers fabricated by the freezing-thawing process of 3 cycles without the dehumidification process.

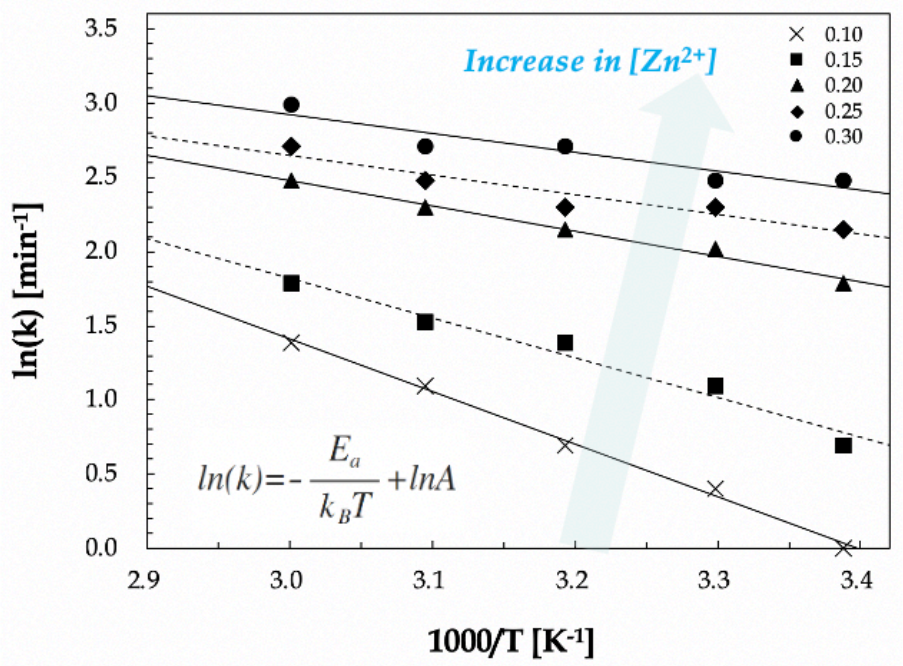

Figure 2.14 Arrhenius plot of ln (k) versus 1000/T to show a self-healing rate constant which is inversely proportional to the absolute temperature for the self-healing polymers fabricated by the freezing-thawing process of 3 cycles followed by the dehumidification process in the desiccator set to 22 ℃ and 17 %RH for 72 hours.

healing. Figures 2.13 and 2.14 represent a relationship of kinetic constant (k) and absolute temperature (T) based on the Arrhenius equation for the self-healing polymers before and after dehumidifying, respectively. Figure 2.13 shows that the logarithmic self-healing rate constant ($ln(k)$) is inversely proportional to the inverse of absolute temperature ($1/T$) for the self-healing polymers fabricated by the freezing-thawing process of 3 cycles without the dehumidification process. The experimental data are in good agreement with the Arrhenius equation, where the activation energy (E_a) corresponds to the slope of linear fitting. Figure 2.14 represents the self-healing rate constant which is inversely proportional to the absolute temperature for the self-healing polymers fabricated by the

freezing-thawing process of 3 cycles followed by the dehumidification process in the desiccator set to 22 ℃ and 17 %RH for 72 hours. The relationship between the activation energy and the molar ratio of zinc ions and PVA represents different aspects. With an increase in the molar ratio of metal-ligand, the slope increases gradually before removing water molecules as seen in Figure 2.13, on the other hand, the activation energy decreases when the self-healing polymers are dehumidified as displayed in Figure 2.14.

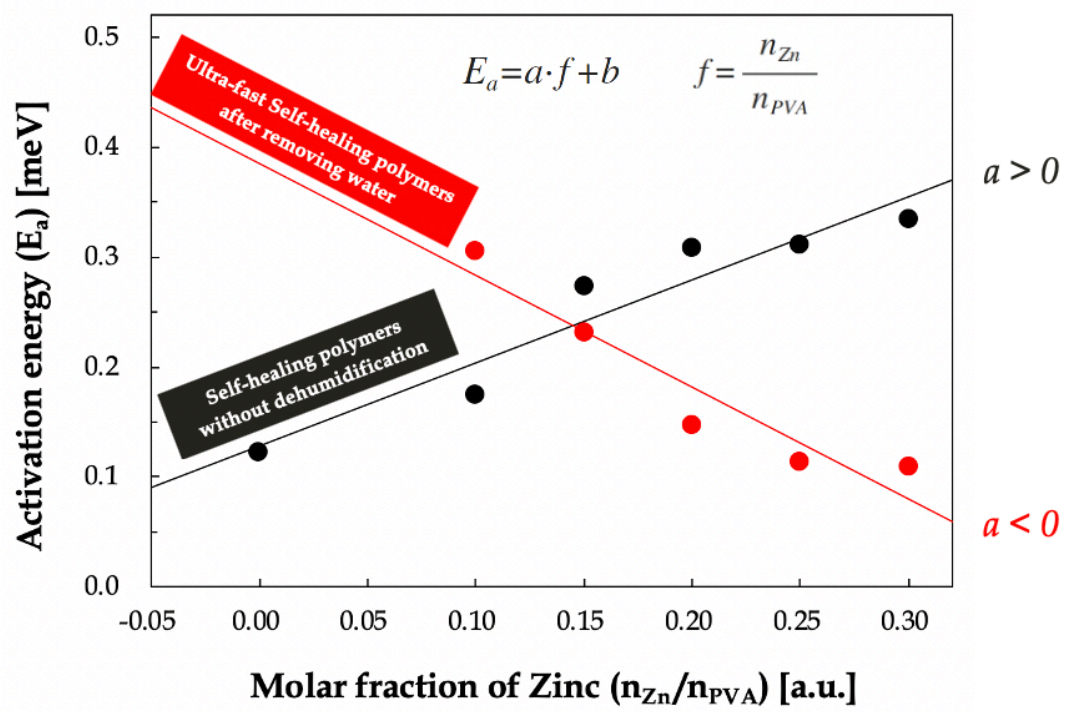

Figure 2.15 Activation energy of the self-healing polymers fabricated by the freezing-thawing process of 3 cycles (black circles) and the same processes followed by the dehumidification process in the desiccator set to 22 ℃ and 17 %RH for 72 hours (red circles).

Figure 2.15 summarizes the activation energies obtained from Figures 2.13 and 2.14 with respect to the molar ratio of metal-ligand. Most of zinc ions are estimated to

participate in forming Zn-PVA complexes contributing to enhancing the self-healing efficiency of the self-healing polymer system by lowering the probability of the formation of Zn-H_2O complexes inhibiting the metal-polymer interactions. Thus, in certain variations, the activation energy of self-healing system is controlled via the dehydration process. Based on the material design strategy, ultra-fast self-healing polymers could be realized by reducing activation energy in order to enhance the interactions between metal ions and polymer ligands. The correlation between the activation energy and the molar ratio of metal-ligand satisfies the following empirical equations

$$E_a = a \cdot f + b \quad \text{(Eq. 2)}$$

$$f = \frac{n_{Zn}}{n_{PVA}} \quad \text{(Eq. 3)}$$

where E_a is an activation energy, f is a molar ratio between number of moles of metal ions and number of moles of ligand (polymer), a is a slope of the linear fitting on a plot of activation energy versus the molar ratio of metal to ligand, b is a y-intercept in the same plot, that is, the activation energy of self-healing polymers without any metal ions.

Figure 2.16 displays the correlation of a and b satisfying (Eq. 2) in terms of the humidity by fitting the experimental data. The activation energy was first estimated when the self-healing polymers were aged at the different humidity (20, 40, and 90 %RH) for 12 hours and then a and b were obtained through the data fitting, as shown in Figure 2.15.

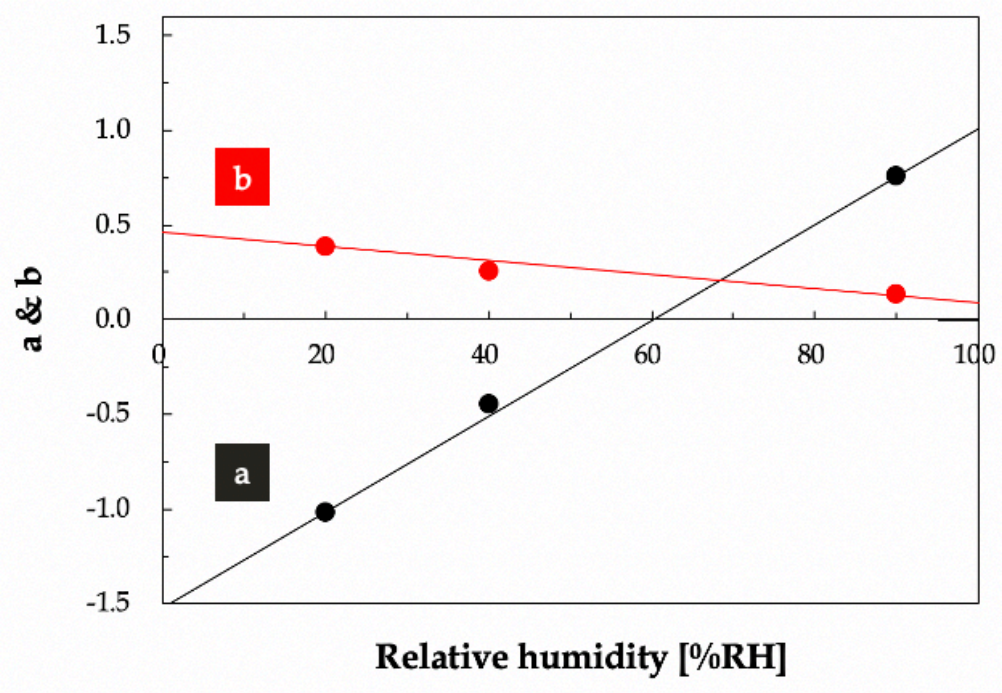

Figure 2.16 Correlation of a and b satisfying $E_a = a \cdot f + b$ in terms of relative humidity based on the data of activation energies obtained experimentally at the various humidity conditions (20, 40, and 90 %RH) for 12 hours in order to control the water amount of self-healing polymers.

Thus, we observe a new correlation of *a* and *b* versus the humidity and estimate those values at unmeasured humidity conditions from the fitting line seen in Figure 2.16.

2.3.6 Kinetic model for self-healing polymers

Here we demonstrate that the analytic equation explaining the correlation of self-healing efficiency and water contents within polymers can be derived by the kinetic model. The Kinetic model indicating the competitive reaction between two complexes, Zn-PVA and Zn-H_2O, for self-healing process can be expressed as:

$$r_A = k[Zn^{2+}][PVA] - k'[Zn^{2+}][H_2O] \quad \text{(Eq. 4)}$$

$$r_A = kf[PVA][PVA] - k'f[PVA][H_2O] \quad \text{(Eq. 5)}$$

$$f = \frac{[Zn^{2+}]}{[PVA]} \quad \text{(Eq. 6)}$$

Let's replace *[PVA]* with *C* as a constant, then (Eq. 5) can be written as the following:

$$r_A = kfC^2 - k'fC[H_2O] \quad \text{(Eq. 7)}$$

$$r_A = kfC^2\left(1 - K\frac{[H_2O]}{C}\right) \quad \text{(Eq. 8)}$$

where

$$K = \frac{k'}{k} \quad \text{(Eq. 9)}$$

This *K* is defined by the inhibition factor showing the ratio of kinetic constants for preferable and inhibitive reaction, respectively. The high value of *K* represents that most of zinc ions are expected to participate in forming Zn-H_2O complexes inhibiting the formation of Zn-PVA complexes contributing to enhancing the self-healing efficiency of the self-healing polymer system. (Eq. 8) can be replaced by substituting the Arrhenius equation to the following equation.

$$r_A = A e^{-\frac{E_a}{k_B T}} f C^2 \left(1 - K \frac{[H_2O]}{C}\right) \quad \text{(Eq. 10)}$$

(Eq. 10) can be rewritten by the Taylor series for the second-order polynomial:

$$r_A = A\left(1 - \frac{E_a}{k_B T} + \frac{1}{2}\left(\frac{E_a}{k_B T}\right)^2\right) f C^2 \left(1 - K \frac{[H_2O]}{C}\right) \quad \text{(Eq. 11)}$$

Here, we can define new parameter R_A as the ratio of rate of self-healing at a certain low water concentration after removing water via the dehumidification process to rate of self-healing of a self-healing polymer with high contents of water without removing water. Therefore, R_A can be expressed as the following:

$$R_A = \frac{r_A|_{[H_2O]}}{r_A|_{[H_2O]_0}} \quad \text{(Eq. 12)}$$

$$R_A = \frac{A\left(1 - \frac{E_a}{k_B T} + \frac{1}{2}\left(\frac{E_a}{k_B T}\right)^2\right)\left(1 - K \frac{[H_2O]}{C}\right)}{A^0\left(1 - \frac{E_a^0}{k_B T} + \frac{1}{2}\left(\frac{E_a^0}{k_B T}\right)^2\right)\left(1 - K^0 \frac{[H_2O]_0}{C}\right)} \quad \text{(Eq. 13)}$$

Assumed that K is equal to K^0 because the kinetic constants do not affected by the concentration of reactants such as chemicals and water molecules. Thus, (Eq. 13) can be expressed as the following:

$$R_A = \frac{A\left(1-\frac{af+b}{k_BT}+\frac{1}{2}\left(\frac{af+b}{k_BT}\right)^2\right)\left(1-K\frac{[H_2O]}{C}\right)}{A^0\left(1-\frac{a^0f+b^0}{k_BT}+\frac{1}{2}\left(\frac{a^0f+b^0}{k_BT}\right)^2\right)\left(1-K\frac{[H_2O]_0}{C}\right)} \quad \text{(Eq. 14)}$$

Finally, (Eq. 14) could explain the reaction rate for self-healing process with respect to the humidity where self-healing polymers are stored for 12 hours. We may estimate the tendency of self-healing efficiency whenever the humidity is changed because (Eq. 14) is expressed as a function of f, K, and $[H_2O]$.

Figure 2.17 represents the relationship between self-healing rate and molar fraction of zinc and PVA estimated analytically through a fitting of (Eq. 14). We have assumed that self-healing polymeric samples are aged under 20 %RH, 40 %RH, 60 %RH, and 80 %RH to observe the humidity effect on the self-healing efficiency. The value of K substituted to (Eq. 14) is 0.1 in Figure 2.17A in order to hypothesize that most of zinc ions participate in forming Zn-PVA complexes by reducing the formation of Zn-H_2O complexes inhibiting the self-healing. On the other hand, Figure 2.17B displays the situation that the inhibition reaction is much preferable to form Zn-H_2O complexes by assuming that K-value is one. The schematic representations of Zn-PVA and Zn-H_2O complexes are depicted in the top right corner of Figure 2.17A and Figure 2.17B, respectively. Since all self-healing polymers are composed of 10 wt% PVA, the value of C is assumed as 0.1 in (Eq. 14). The other parameters, a and b can be used from the data fitted in Figure 12. The input of $[H_2O]$ are 0.2, 0.4, 0.6, and 0.8 to model the humidifying condition at which samples are stored at 20 %RH, 40 %RH, 60 %RH, and 80 %RH. All

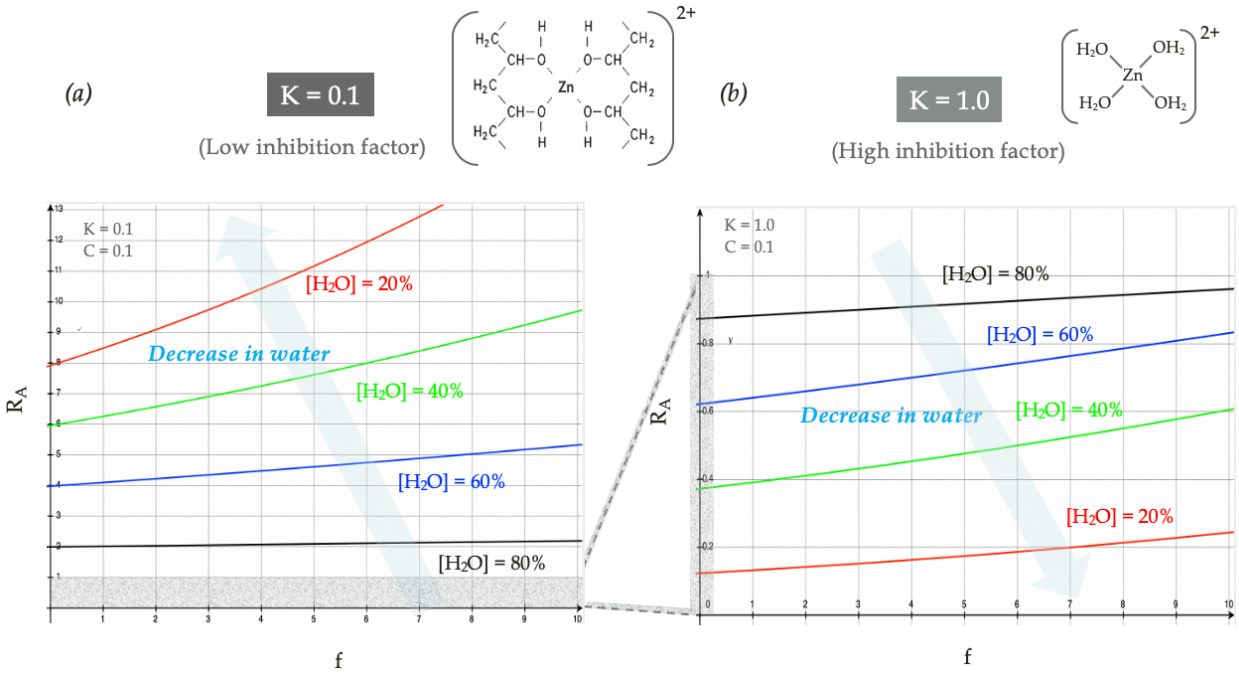

Figure 2.17 Relationship between self-healing rate and molar fraction of zinc and PVA estimated analytically through a fitting of (Eq. 14) describing the self-healing rate in terms of humidity assumed that samples are aged under 20 %RH, 40 %RH, 60 %RH, and 80 %RH.

the control parameters, a^0, b^0, and $[H_2O]_0$, are regarded as the value at a high humidity condition (90 %RH). The analytic model of (Eq. 14) indicating the correlation between the self-healing rate and the molar ratio of metal-ligand explains well the tendency observed in Figures 2.11. First, Figure 2.17A and 2.17B show that the self-healing efficiency increases with an increase in the molar ratio of Zn-PVA. Next, with a decrease in the humidity, the self-healing efficiency increases dramatically, as shown in Figure 2.17A. As previously mentioned, this tendency can be attributed to an increase in the formation of Zn-PVA complexes by reducing in the activation energy of self-healing polymers via the dehumidification. However, the reaction rate shows a very narrow range between zero and one when the inhibitive reaction which forms Zn-H_2O complexes is

preferable. as shown in Figure 2.17B. Within this narrow range, the self-healing efficiency decreases with a decrease in the humidity. Therefore, it is deduced that the self-healing efficiency versus the humidity indicates a different tendency as the preferable complexes presenting within the polymer are changed.

2.3.7 Mechanical self-healing properties

Figure 2.18 is a series of photographs taken while a self-healing polymer system is cut and then reattached and healed. Figure 2.18 demonstrates that the self-healing polymer comprising PVA and Zn shows an autonomous and ultra-fast self-healing property at ambient conditions and absent slight applied manual pressure, the self-healing occurs without any external stimuli such as heat, light, and solvents. The sample has a molar ratio of PVA to Zn^{2+} of 10:3, which is fabricated by undergoing 3 cycles of the freezing-thawing process, followed by a dehumidification process in the desiccator set to 22 ℃ and 17 %RH for 72 hours. The self-healing time is about 10 seconds, after which the healed sample can be stretched out to over 200 % of strain.

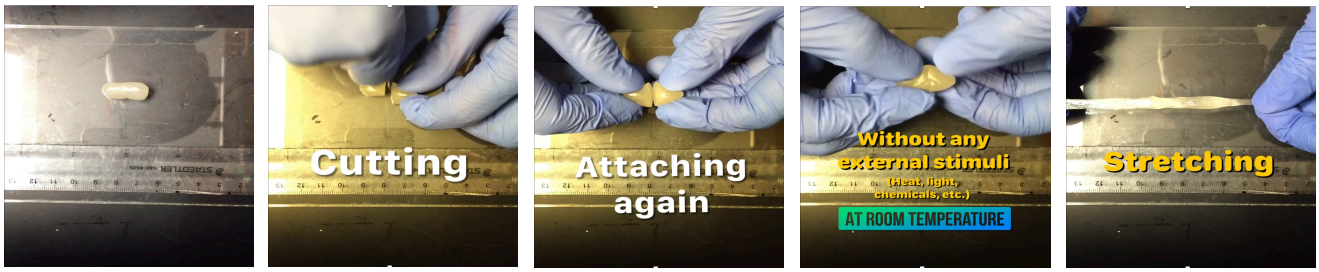

Figure 2.18 A series of photographs where the self-healing polymeric material comprising PVA and Zn is cut, reattached with slight application of pressure at ambient conditions, where a self-healing time is less than 10 seconds, followed by stretching, where the healed polymer remains intact.

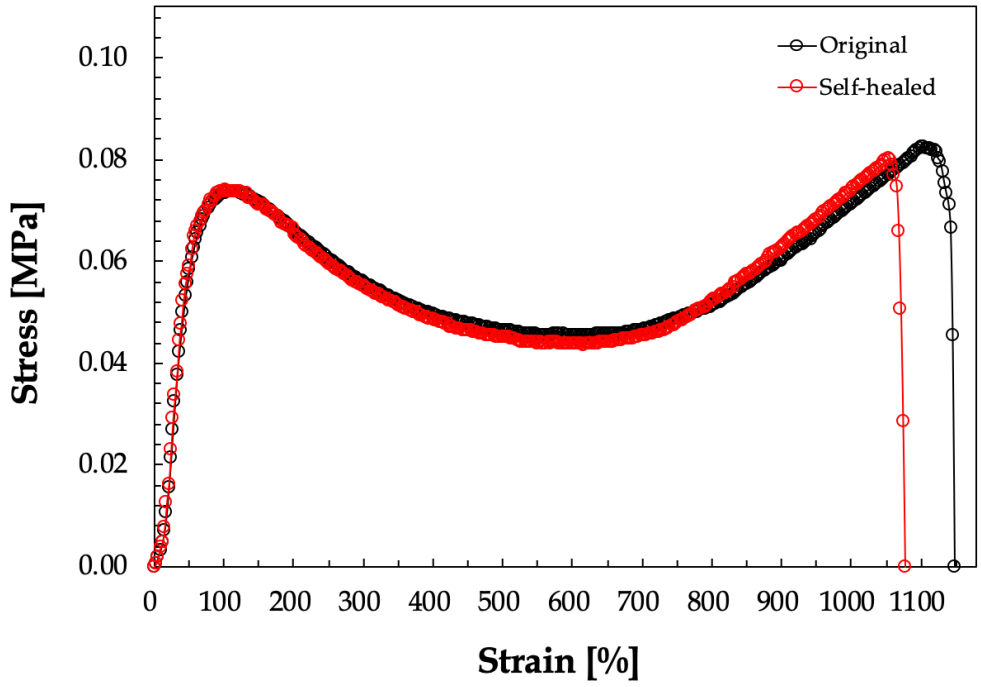

Figure 2.19 Stress-strain curve showing the self-healing behavior of the self-healing adhesive (SHA). The SHA associated with PVA to Zn^{2+} molar ratio of 10:3 was fabricated by the freezing-thawing process of 3 cycles followed by the dehumidification process in the desiccator set to 22 ℃ and 17 %RH for 72 hours. The damage began to be self-healed without any interventions or stimuli at room temperature and the maximum elongation was nearly recovered up to 90 % that of the original state before damaging.

Figure 2.19 shows a stress-strain curve that represents the self-healing behavior of a self-healing adhesive (SHA) with the molar ratio of PVA to Zn^{2+} of 10:3, which is fabricated by undergoing 3 cycles of the freezing-thawing process followed by a dehumidification process in the desiccator set to 22 ℃ and 17 %RH for 72 hours. An originally undamaged film has a maximum elongation of 1107 % in dynamic mechanical analysis (DMA) test. Another film fabricated at the same conditions is cut into two pieces and placed in contact with each other through damaged surfaces. After healing at room

temperature for about 10 minutes without any interventions or stimuli, the joined film sustains about 1056 % of strain with a healing efficiency of about 95 % via stretching test in DMA. The damage began to be self-healed and the maximum elongation is nearly recovered up to at least 90 % of that of the original state before any damage. This behavior is believed to be attributable to metal-ligand coordination bonds in the polymer matrix.

2.3.8 Evaluation for the presence of metal-ligand complexes

To investigate the presence of metal-ligand complexes within self-healing adhesive (SHA), the analysis via FT-IR and UV-Vis spectra were conducted.

2.3.8.1 FT-IR analysis

Figure 2.20 indicates the FT-IR spectra of the pure PVA and the self-healing adhesive (SHA). For pure PVA, the characteristic absorption peaks are at 3249 cm^{-1} (O-H stretching), 2936 cm^{-1} (asymmetric stretching of CH_2), 2906 cm^{-1} (symmetric stretching of CH_2), 1643 cm^{-1} (due to water absorption), 1416 cm^{-1} (CH_2 bending), 1373 cm^{-1} (CH_3 wagging), 1325 cm^{-1} (δ (OH), rocking with CH wagging), 1248 cm^{-1} (C-O-C stretching), 1138 cm^{-1} (shoulder stretching of C-O, crystalline sequence of PVA), 1090 cm^{-1} (stretching of C=O and bending of OH, amorphous sequence of PVA), 916 cm^{-1} (CH_2 rocking), 840 cm^{-1} (C-C stretching) [70-71]. Interestingly, the peak at 1643 cm^{-1} is

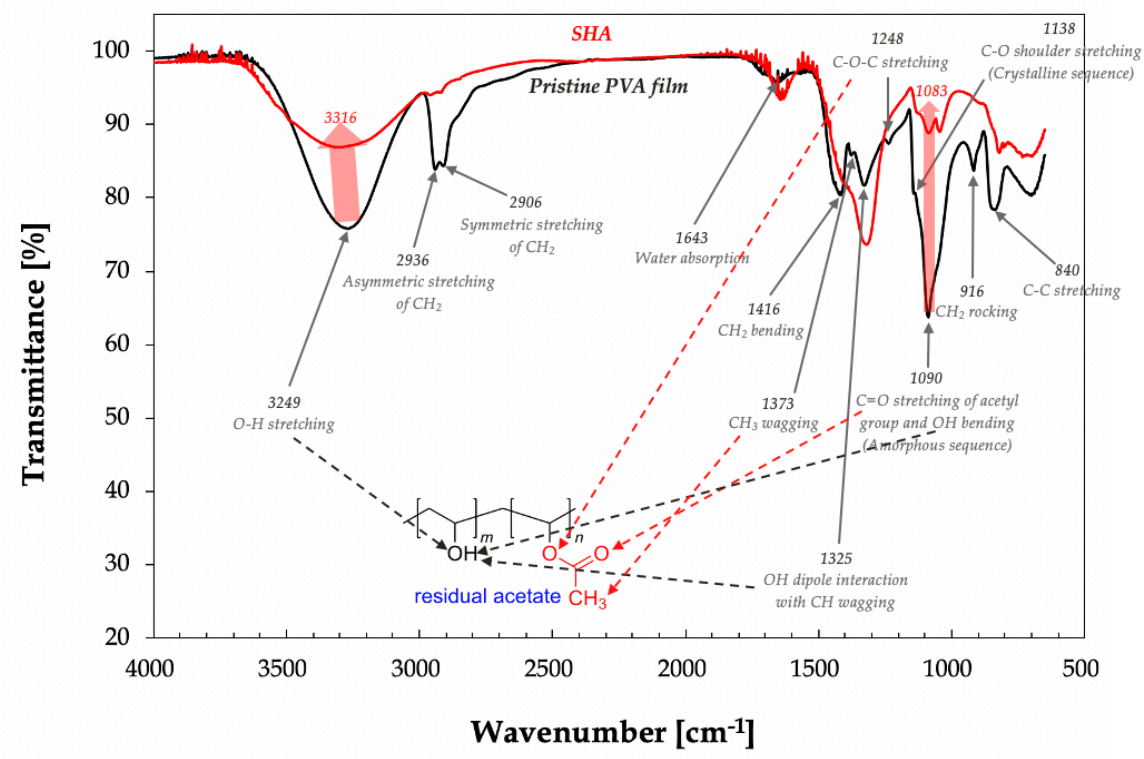

Figure 2.20 FT-IR spectra of the pure PVA and the self-healing polymer. When zinc ions are introduced to PVA, the peak corresponding to the O-H stretching bands shifts from 3249 cm^{-1} to 3316 cm^{-1}. This is because some of the intermolecular and intramolecular hydrogen bonds presenting in PVA might have been broken by the formation of metal-ligand complexes between the oxygen atoms of the hydroxyl group and zinc ions.

attributed to the so-called “bound water”. When zinc ions are introduced to PVA, the peak corresponding to the O-H stretching bands shifts from 3249 cm^{-1} to 3316 cm^{-1}.

According to the theory of IR spectroscopy, the formation of hydrogen bonds (O-H) changes the force constant around the hydroxyl group and results in a decrease in the O-H stretching frequency. In contrast, breaking a hydrogen bond would shift the stretching band of O-H groups to a higher frequency [72]. Based on this fundamental theory, some of the intermolecular and intramolecular hydrogen bonds presenting in PVA

might have been broken by the formation of metal-ligand complexes between the oxygen atoms of the hydroxyl group and zinc ions. Therefore, the O-H stretching peak shows the blue-shift in Figure 2.20. Moreover, the characteristic peak at 1090 cm^{-1} is assigned to the C-OH stretching vibrations of PVA, which shifted to a lower wavenumber of 1083 cm^{-1} when zinc ions are mediated into PVA for the SHA, as seen in Figure 2.20. These results indicate that the introduction of Zn^{2+} ions into PVA facilitates the complexation between Zn^{2+} and the oxygen atoms of O-H groups.

2.3.8.2 UV-Vis spectral analysis

Figure 2.21 illustrates UV-Vis absorption spectra of the pure PVA film, pristine PVA hydrogel, PVA film crosslinked by boric acid, and SHA. The pure PVA film is cast using 10 wt% PVA solution on glass substrate followed by the drying at room temperature. The pure PVA hydrogel is fabricated by a freezing at -10 ℃ for 12 hours and a thawing at room temperature for 3 hours. The SHA with a molar ratio of PVA to Zn^{2+} of 10:3 is prepared by undergoing 3 cycles of the freezing-thawing process, followed by a dehumidification process in the desiccator set to 22 ℃ and 17 %RH for 72 hours. It is noted that pure PVA film, PVA hydrogel, and PVA crosslinked by boric acid have no absorption peak in ultraviolet spectra while the self-healing polymer exhibits a strong absorption peak at 300 nm, which can be attributed to the formation of Zn-PVA complexes. This hypothesis for the formation of metal-ligand complexes is based on the previous report describing that all the films containing silver ions have a shoulder peak at 300 nm and its intensity increase with the $AgNO_3$ dopant content, which is on account of

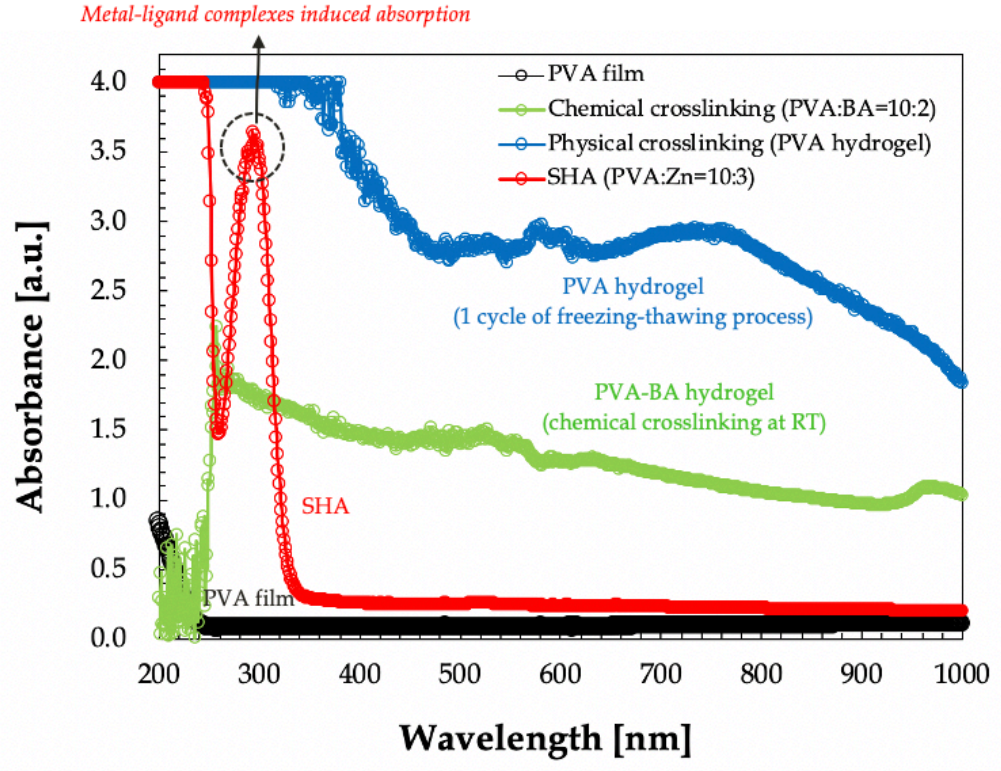

Figure 2.21 UV-Vis absorption spectra of pure PVA film, pristine PVA hydrogel, PVA film crosslinked by boric acid, and SHA. It is noted that pure PVA film, PVA hydrogel, and PVA crosslinked by boric acid have no absorption peak in ultraviolet spectra while the SHA exhibits a strong absorption peak at 300 nm, which can be attributed to the formation of Zn-PVA complexes.

the substitution of Ag-PVA complex for Ag-H_2O complex and the increase of Ag-PVA complex amount [73].

2.3.9 Amorphous structure of SHA

We describe herein a concept of material design that enables to tune the ultra-fast and spontaneous self-healing as well as the high stretchability and good adhesive

property. To combine autonomous and reversible self-healing at room temperature, a self-healing polymeric material comprising a polymer network comprising PVA that defines one or more ligands having a transition metal ion coordination site has been investigated. This self-healing polymeric material has a transition metal ion such as zinc distributed in the polymer network. The transition metal ion is capable of interacting with the transition metal ion coordination site via a reversible coordination bond. Thus, the polymer network is capable of self-healing a mechanical crack or cut in less than or equal to about 10 minutes at ambient conditions. Although the reversible bond based on the metal-ligand interactions is a significant factor to achieve a spontaneous self-healing, polymers as a ligand need to fulfill additional material requirements. An amorphous structure of polymer with a low glass transition temperature (T_g) enables polymer chains on mechanically damaged interfaces to be activated, interact and recombine, thus allowing self-healing under ambient conditions without any interventions [43]. The metal-ligand chelation formed in the amorphous ligand with a low T_g could readily break and re-bond because the metal ions being on the damaged interfaces still remain near the ligands, which is favorable for self-healing by providing the dynamic bonding sites.

2.3.9.1 Differential scanning calorimetry (DSC) analysis

To estimate the chain mobility of SHA, we evaluated the T_g via DSC measurement. The T_g of SHA is around -4 °C, much lower than that of pristine PVA film (72 °C), as seen in Figure 2.22. This T_g which is even lower than room temperature allows polymer chains at the mechanically fractured interfaces to be rearranged and inter-

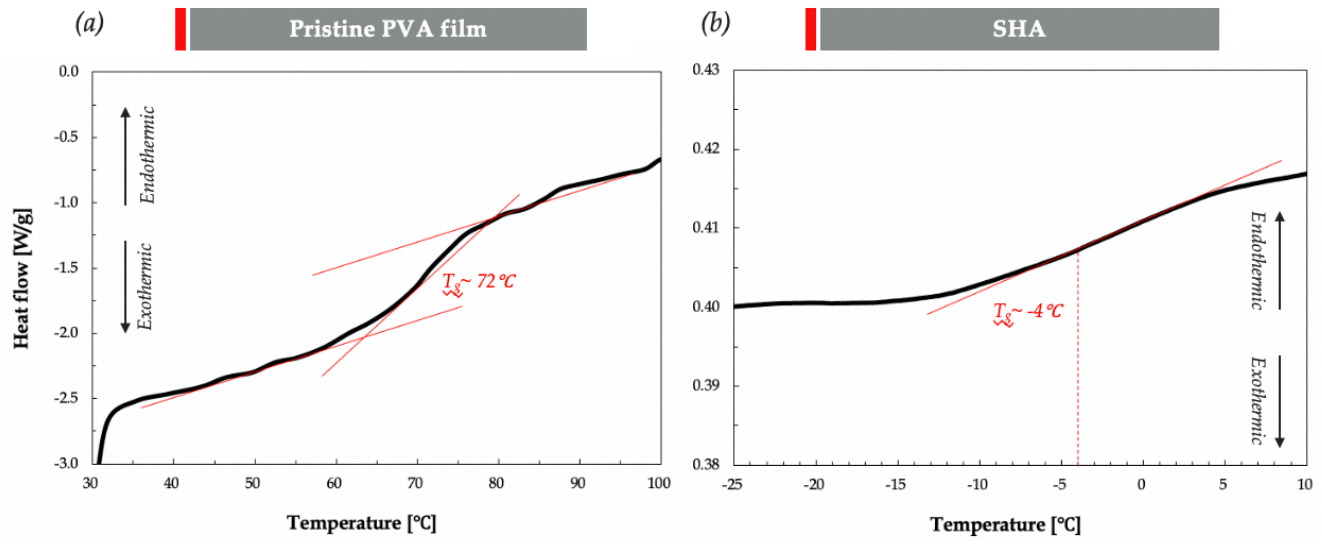

Figure 2.22 Measured glass transition temperature (T_g) for the pure PVA film and the SHA. The T_g of SHA is around -4 ℃, much lower than that of pristine PVA film (72 ℃), as seen in Figure 2.22. This extremely low T_g is caused by the innate amorphous nature of SHA based on the material design for ultra-fast self-healing.

diffused. The thermal transition observed in the SHA results from the enhanced PVA chain relaxation and mobility due to its weakened hydrogen-bonded supramolecular networks and the plasticizing effect of water molecules [74]. Therefore, an increase in PVA chain mobility could enhance the dynamic bonding ability of SHA caused by the transient coordination of Zn-PVA complexes.

Figure 2.23 confirms that the extremely low T_g is indeed caused by the intrinsically amorphous nature of SHA we designed. The thermal behavior measured by differential scanning calorimetry (DSC) indicates the amorphous structure of our self-healing polymer, as evidenced by the lack of a recrystallization peak during the cooling process over the entire temperature range. Whereas the recrystallization peak of pristine PVA film is observed around 200 ℃ (Figure 2.23A), any exothermic peaks in the SHA

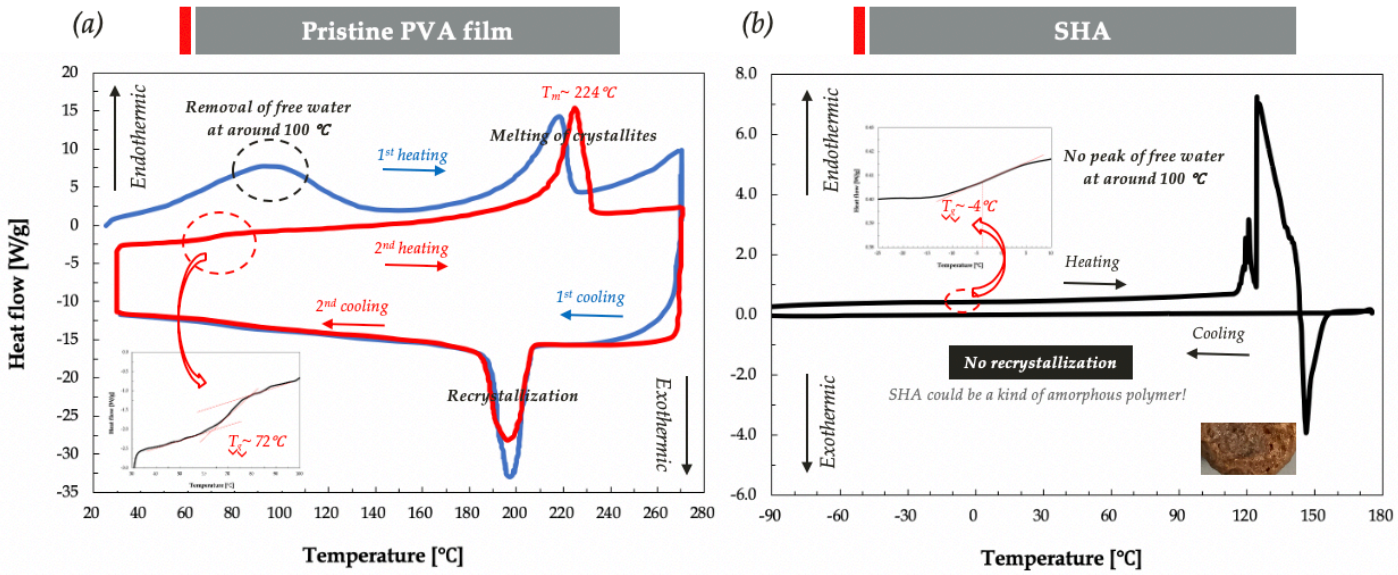

Figure 2.23 Differential scanning calorimetry (DSC) measurement to evaluate the amorphous nature of self-healing polymer, as evidenced by the lack of a recrystallization peak during the cooling process over the entire temperature range.

have not been scanned during the cooling except for one peak appeared around 150 ℃ during the heating process.

This unexpected exothermic peak appeared in the range of 140-170 ℃ may be caused by the redox reaction that take place between PVA and zinc nitrate. This redox reaction results in the oxidation of PVA to carboxylate anions that coordinate to the metal cations forming carboxylate coordination compounds, used as precursor for the desired zinc oxides [75]. M. Stoia et al. also studied that a redox reaction takes place between the metal nitrates and PVA, at temperatures around 140-170 ℃, resulting in its oxidation to carboxylate anions that coordinate to the metal cations forming different carboxylate coordination compounds [76]. The reddish-brown oxide material shown in the inset of Figure 2.23B is an affirmation of the redox reaction that forms carboxylate coordination

compounds. A. Pathak et al. suggested the tentative reaction mechanism for the decomposition of PVA as well as the chelation of PVA with metal ions at high temperature, as shown in Figure 2.24 [77]. Nitric oxide formed during the reaction is the reason for a reddish-brown color of a byproduct. We directly observed this reddish-brown specimen which has been collected as the residual after finishing the DSC evaluation.

This reddish-brown oxide material is an affirmation of the redox reaction that forms carboxylate coordination compounds around 140-170 °C.

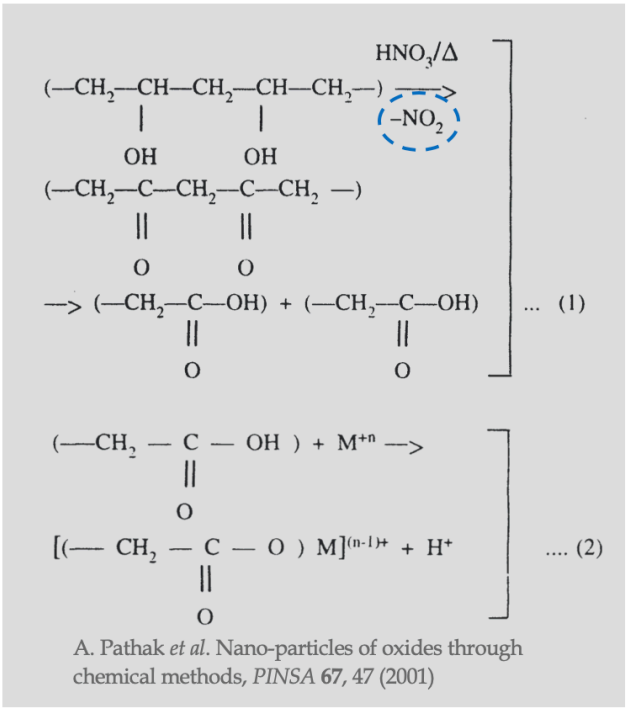

A. Pathak *et al*. Nano-particles of oxides through chemical methods, *PINSA* **67**, 47 (2001)

Figure 2.24 Tentative reaction mechanism for the decomposition of PVA as well as the chelation of PVA with metal ions at high temperature ([77] A. Pathak *et al*. Nano-particles of oxides through chemical methods, *PINSA* **67**, 47, 2001).

Y. Gan et al. proposed that this decomposition peak observed in DSC measurement of PVA-metal complexed materials is related to the reduction in crystallinity of PVA [72]. Compared with the degradation temperature of pure PVA (220-275 ℃), the degradation of PVA/metallic nitrate composite film takes place at early stage before 275 ℃. This phenomenon suggests the presence of complexes formed by the hydroxyl groups of PVA and metallic ions, which destroy the hydrogen bonds of the preexisting PVA molecules and weaken the interactions between the molecular chains, and thus decrease the crystalline phase of PVA.

More importantly, double endothermic peaks were observed around 121 ℃ and 125 ℃, as seen in Figure 2.23B. These two consecutive peaks may be assigned to the disruption of bound water which can be coordinated with metal ions and the collapse of Zn-PVA complexes, respectively. Y. Zhang et al. studied that the similar double endothermic peaks were observed in the complexed polymers [78]. Specifically, it is known that four water molecules from the Zn-ligand complexes can be released in one stage in the narrow temperature range 110–140 ℃ [79]. This process is accompanied by a very strong endothermic effect with the molar dehydration enthalpy 174.8 kJ mol^{-1}. B. Liu et al. also published that the first stage of weight loss below 150 ℃ observed in their TGA analysis of Zn-PVA complexed materials is due to the removal of physisorbed and bound water [75]. L. V. Ababei et al. investigated the presence of coordinated water or bound water for various metal-ligand complexed materials via thermoanalytical methods as well [80]. As a result, the amorphous characteristics of the SHA have been studied by the DSC analysis, as evidenced by the lack of a recrystallization peak during the cooling process.

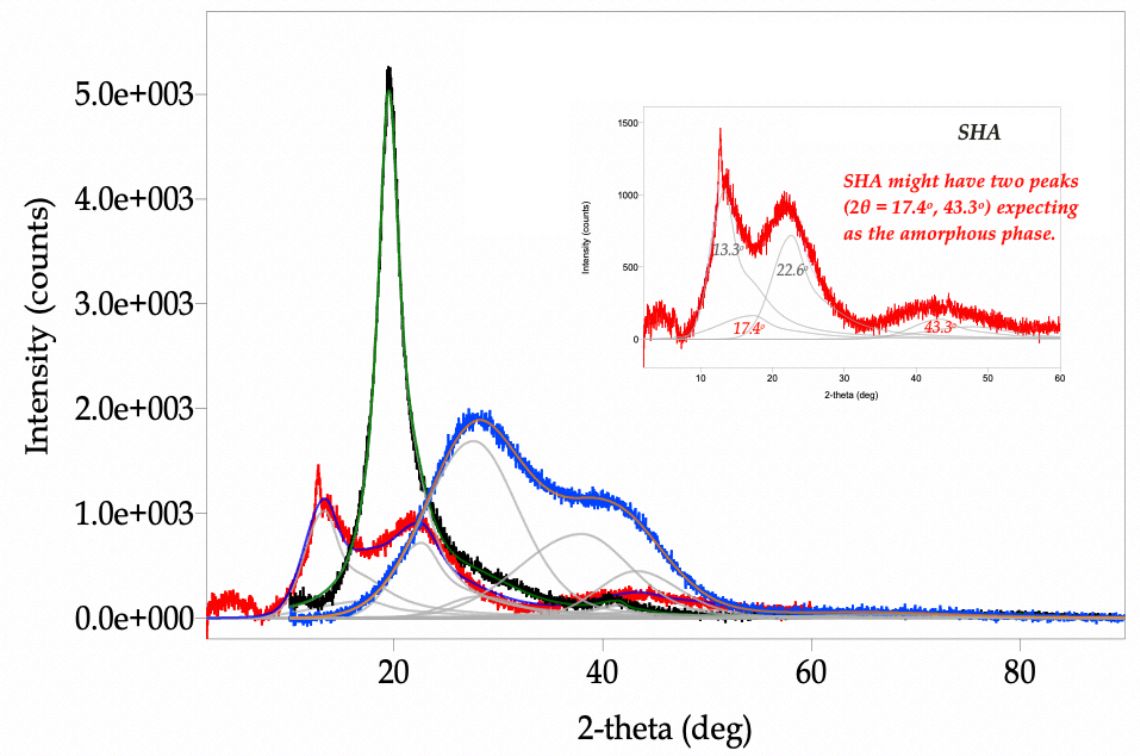

Figure 2.25 XRD peaks for the pristine PVA film, PVA hydrogel and self-healing polymer. The intensity of the peak at 2θ = 19.8° for the crystal form of the pure PVA film decreases significantly and only a much broader, less intense peak at 2θ = 28° is detected for the PVA hydrogel. the self-healing polymer shows an apparently broad amorphous peak at 2θ = 43.3°. This change in the XRD patterns is due to the complexation between zinc ions and the oxygen atoms of the hydroxyl group in PVA.

2.3.9.2 X-ray diffraction (XRD) analysis

The X-ray diffraction (XRD) pattern also provide an evidence for the amorphous nature of our self-healing polymer. Figure 2.25 indicates the XRD peaks for the pristine PVA film, PVA hydrogel and SHA. As seen in Figure 2.25, both the PVA hydrogel and the SHA shows a decrease in the intensity of the peak at 2θ = 19.8° exhibiting the

crystalline form of the pure PVA film. Specifically, the PVA hydrogel displays only a much broader and less intense peak at $2\theta = 28^{o}$ as observed in the published report [81]. More importantly, the SHA also exhibits the similar shape of broad and less intense peaks at different peak positions. Intriguingly, the SHA shows an apparently broad amorphous peak at $2\theta = 43.3^{o}$. The other amorphous peak at $2\theta = 17.4^{o}$ could be estimated by the decomposition of measured peak into three independent Gaussian peaks, as shown in the inset of Figure 2.25. This change in the XRD patterns is due to the complexation between zinc ions and the oxygen atoms of the hydroxyl group in PVA, thus efficiently reducing the intermolecular and intramolecular hydrogen bonding and destroying the crystal structures mediated by the PVA chain folding. Consequently, the metal-ligand complexation forms the amorphous structure within the polymer through a disruption of crystalline phases and thus the dynamic reassociation ability of metal-ligand complexes leads to autonomous self-healing.

2.3.9.3 FT-IR analysis

To prove the presence of amorphous structure in the self-healing polymer, we have implemented the FT-IR analysis. Figure 2.26 shows the FT-IR spectra of the pure PVA and the SHA. It is noted that the peak at 1138 cm^{-1} which was assigned to the skeletal motion of C-O and C-C stretching in the pure PVA is correlated with the degree of crystallinity of PVA. Once this peak is practically disappeared in the spectrum of SHA, that may indicate a disruption of crystalline phases in PVA [70]. This peak change in the FT-IR spectra is caused by the complexation between the Zn^{2+} and the hydroxyl groups

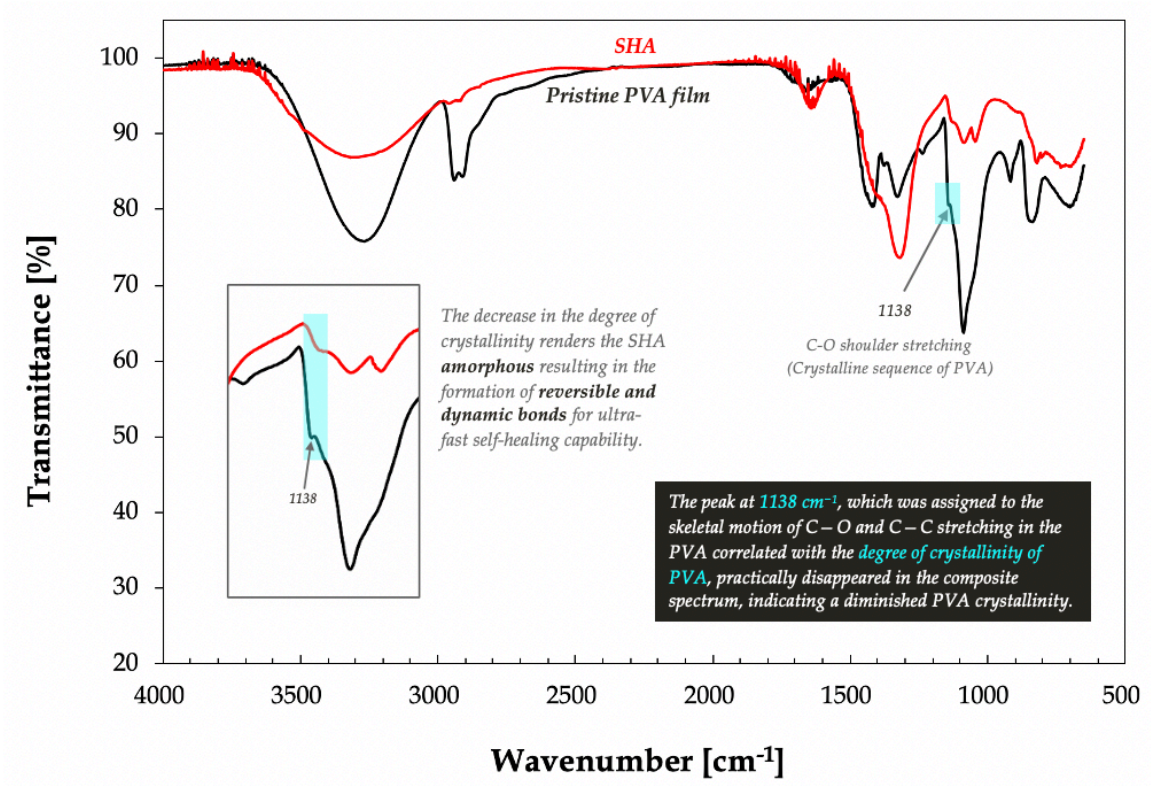

Figure 2.26 FT-IR spectra of the pure PVA and the SHA. The peak at 1138 cm^{-1} which was assigned to the skeletal motion of C-O and C-C stretching in the PVA correlated with the degree of crystallinity of PVA, practically disappeared in the spectrum of SHA, indicating a diminished PVA crystallinity.

of PVA chains, thus efficiently reducing the crystalline structure resulting from the chain folding of PVA.

2.3.9.4 Structural evolution in SHA

So far, we have demonstrated our self-healing polymer exhibits the amorphous structure via characterization using DSC, XRD, and FT-IR. Figure 2.27 shows an evolution of structure from a semi-crystalline PVA to an amorphous self-healing polymer.

Kubo et al. reported that the crystallites of PVA could be destroyed by the addition of $Mg(NO_3)_2 \cdot 6H_2O$ and PVA/$Mg(NO_3)_2 \cdot 6H_2O$ blend films with low crystallinity were very soft and rubber-like [82]. Jiang et al. has also proved that $MgCl_2 \cdot 6H_2O$ could effectively destroy the crystallites of PVA and reduce the degree of crystallinity of PVA [83]. This phenomenon has been observed in our self-healing polymer as well. As shown in Figure 2.20, it can be seen that the -OH stretching peak at 3249 cm^{-1} in the FT-IR was shifted to a higher wave number with the addition $Zn(NO_3)_2 \cdot 6H_2O$ to PVA. This indicates that the addition of metal salts would reduce the intensity of the intermolecular and intramolecular hydrogen bonding between PVA molecules. This is most probably caused by the interaction between the negatively charged hydroxyl groups and positive zinc ions, as shown in Figure 2.10A. With the addition of metal salts, the diffraction peak of PVA in the XRD decreased in intensity and became broader. Moreover, an apparent amorphous peak at $2\theta = 43.3^{o}$ was observed, as seen in Figure 2.25. This also means that the addition of metal salts into PVA destroys the crystallites of PVA and the degree of crystallinity decreased sharply due to the plasticization effect [84].

The obtained data from the DSC analysis indicated that the self-healing polymer has no recrystallization peak in an entire temperature range. This observation is also consistent with the systematic evolution from crystalline phase to amorphous structure as revealed in the XRD and FT-IR study. With comparison, we conclude that the metal salt could effectively destroy the hydrogen bonding of PVA and form newly strong metal-ligand interactions with hydroxyl group of PVA, thus yielding an amorphous phase within the polymer, as depicted in Figure 2.27. We designed the polymer to have an amorphous structure with a low T_g in order to develop the ultra-fast self-healing polymer

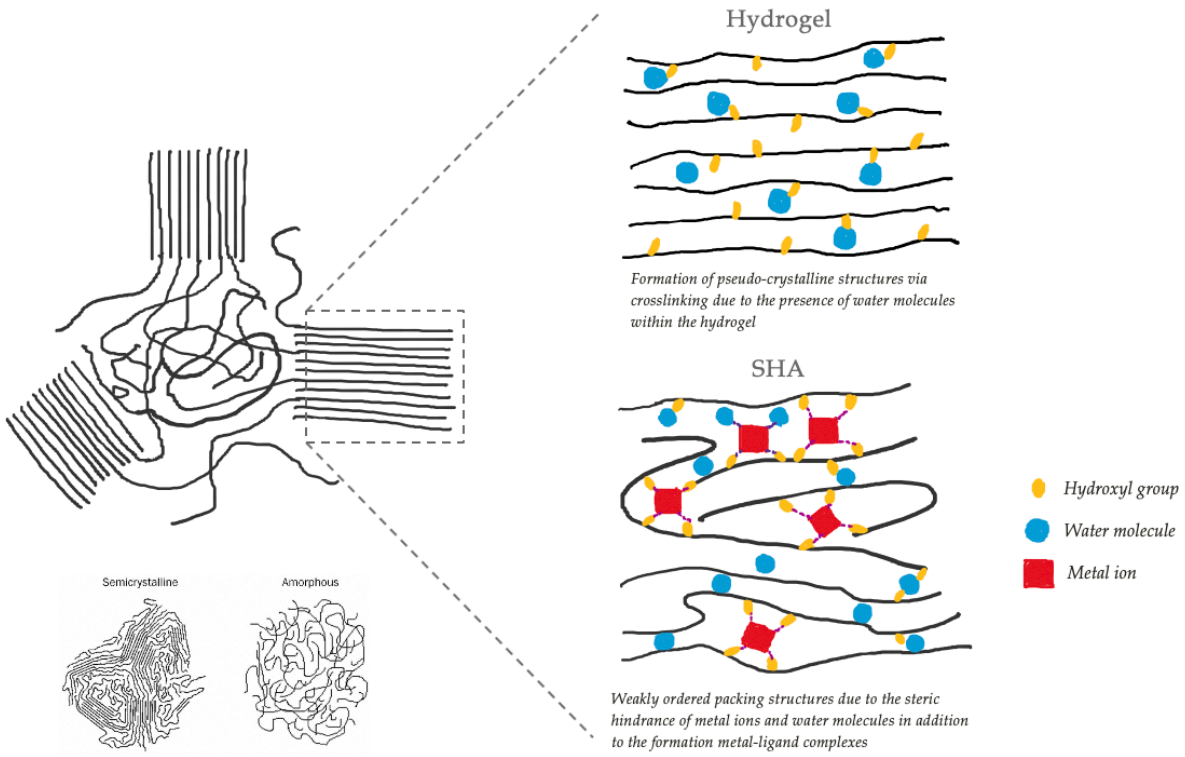

Figure 2.27 Schematic illustration describing a disruption of the crystallites of PVA via metal-ligand interactions.

and recognized that we implemented it successfully. Our polymer shows the dynamic reassociation ability during the healing process and leads to spontaneous self-healing at room temperature without any interventions.

As discussed, the SHA is prepared by the complexation of PVA with zinc ions, exhibiting the amorphous structures. Figure 2.28 shows the structural comparison of the SHA (Zn-PVA complex) and the PVA crosslinked with boric acid (BA-PVA complex). The former complex is formed by the complexation of metal-ligand, whereas the latter one results from a chemical crosslinking. Figure 2.28 shows the difference of structure between two complexes by comparing the extinction at the wavelength of 550 nm in

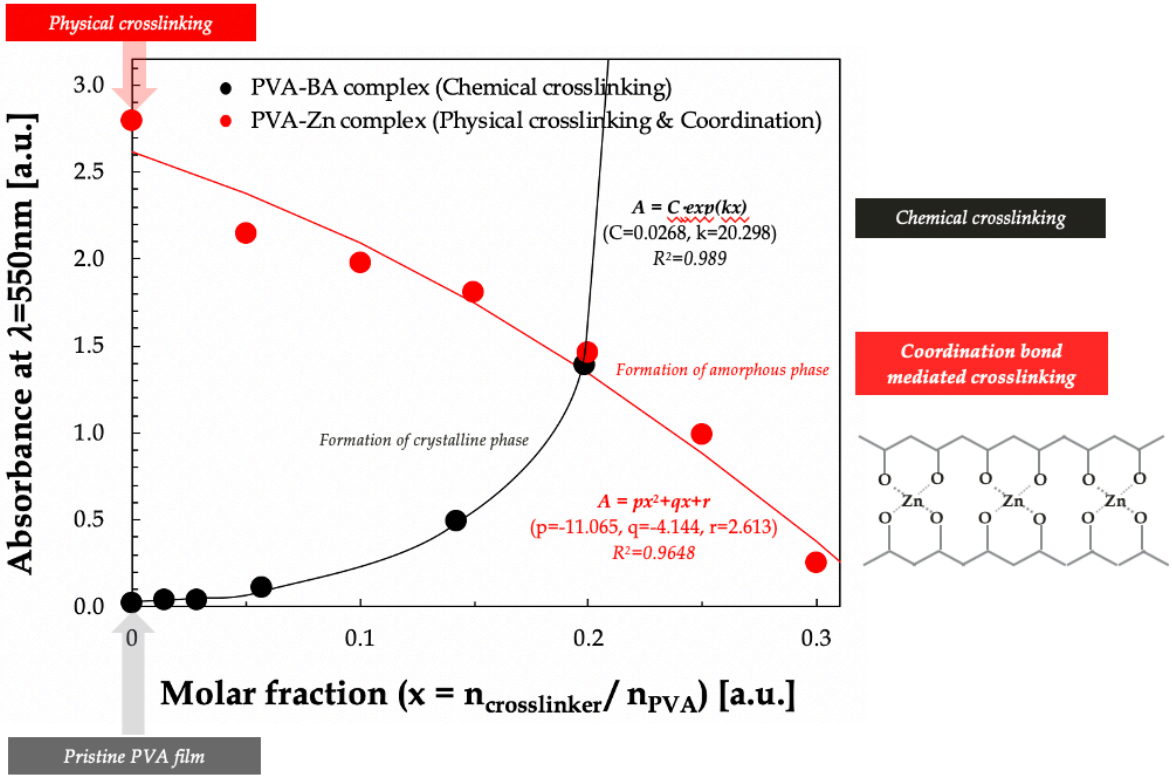

Figure 2.28 Optical extinctions at a wavelength of 550 nm for the SHA and the PVA-boric acid (BA) complex in terms of a molar ratio of crosslinker (zinc ions and/or boric acid) to PVA ligand.

terms of the molar fraction of crosslinker (zinc ions and/or boric acid) and PVA. The SHA represents an exponential increase in the extinction with an increase in the molar fraction. Conversely, the extinction of BA-PVA complex quadratically decreases as the molar fraction increases. It is deduced that the zinc ions could effectively destroy the intermolecular and intramolecular hydrogen bonding between PVA chains and form the dynamic metal-ligand interactions with the hydroxyl groups of PVA. Therefore, the SHA could generate the amorphous phases within the polymer, resulting in the decrease in extinction as seen in Figure 2.28. On the other hand, the boric acid could additionally

form the intermolecular hydrogen bonding with the hydroxyl groups of PVA chain, thus yielding more crystalline phases within the polymer.

2.3.10 Mechanical properties of SHA

We demonstrate herein the mechanical properties of self-healing polymers through the static tensile tests performed by the dynamic mechanical analysis (DMA). Figures 2.29 and 2.30 show the stress-strain curves of self-healing polymers before and

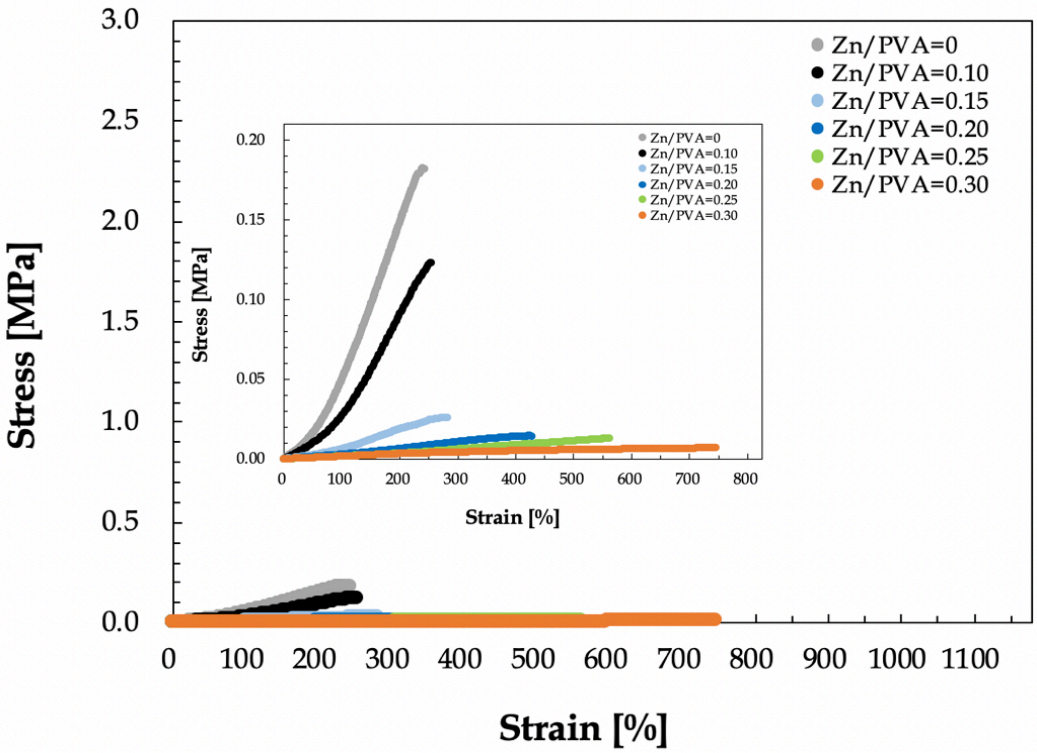

Figure 2.29 Stress-strain curves of the self-healing polymers based on the coordination bond of Zn-PVA via the freezing-thawing process of 3 cycles without the dehumidification process. The inset indicates the enlarged view over y-axis for the same result.

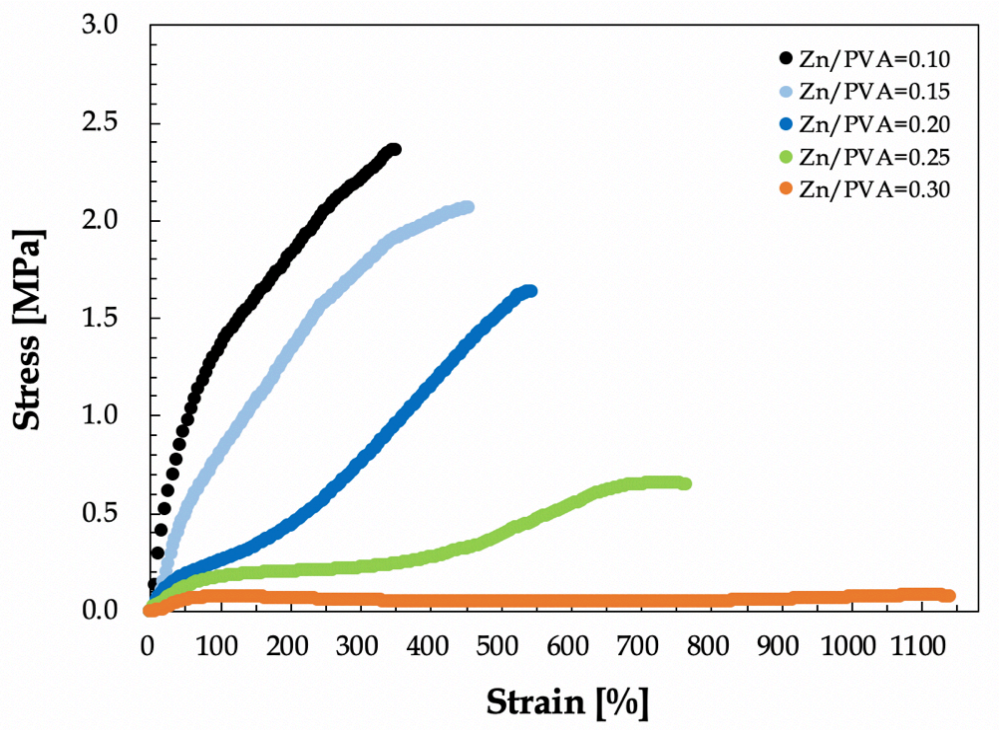

Figure 2.30 Stress-strain curves of the self-healing polymers based on the coordination bond of Zn-PVA via the freezing-thawing process of 3 cycles followed by the dehumidification process.

after removing water molecules within the samples, respectively. In the case of Figure 2.30, the samples are stored in the desiccator set to 22℃ and 17 % RH for 72 hours. As shown in Figure 2.30, maximum tensile strain at breaking point is improved from 350% (black curve) to 1,150% (orange curve) with increasing of N_{Zn}/N_{PVA} from 0.1 to 0.3. The lower the molar ratio (N_{Zn}/N_{PVA}), the higher Young's modulus and tensile strength that results from greater amounts of physical crosslinking formed within the material during freezing-thawing process. On the other hand, the self-healing polymers with the higher molar ratio of 2.5 or 3.0 tend to show much lower Young's moduli as well as even higher elongations. The higher concentration of zinc ions may interfere with the formation of

physical crosslinking between PVA backbone chains during the freezing-thawing process, thereby rendering hydrogels to be soft and lowering Young's modulus. These aspects of mechanical properties are nearly consistent with the results of transparency in terms of the molar ratio between Zn^{2+} and PVA observed in Figure 2.1. With an increase in the amount of zinc ion, the density of the coordination bonds resulting from the chelation of Zn^{2+} to PVA ligands increases, while the physical crosslinking via hydrogen bonds between PVA backbones decreases. These enhanced coordination bonds would contribute to destroying the crystalline phases of PVA and then forming the amorphous structures. Therefore, self-healing polymers with a number of the coordination bonds represent the superior stretchability [60] and transparency to conventional PVA hydrogels comprised of the physical crosslinking.

Figure 2.31 indicates the Young's modulus (E) obtained from Figures 2.29 and 2.30 for the self-healing polymers in terms of a molar ratio of zinc and PVA. The Young's modulus is a mechanical property referring to a ratio of stress to strain for a given material as the following expression:

$$E = \frac{Stress}{Strain} = \frac{\sigma}{\varepsilon} = \frac{L_0}{\Delta L} \times \frac{F}{A} \qquad \text{(Eq. 15)}$$

where σ is the engineering stress, ε is the tensile strain, E is the Young's modulus, L_0 is an equilibrium length, ΔL is a length change under the applied stress, F is the force applied and A is the area over which the force is applied. In Figure 2.31, the blue and red circles represent the modulus of the self-healing polymers before and after dehumidifying

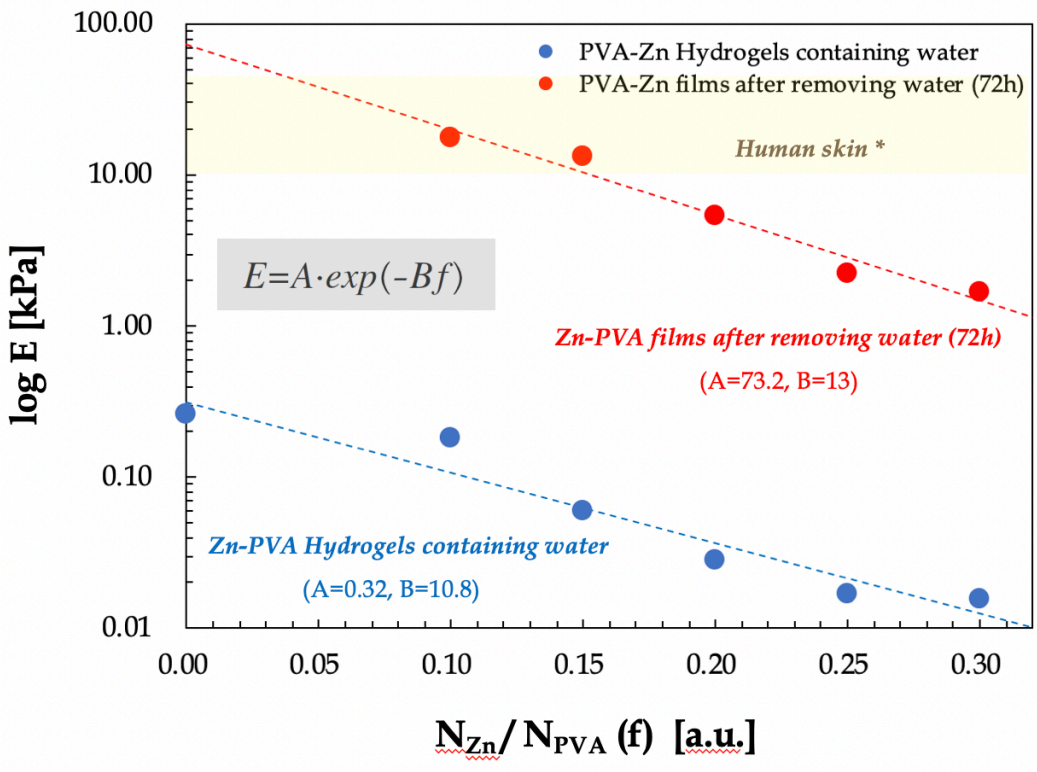

Figure 2.31 Young's modulus (E) of self-healing polymers based on Zn-PVA complexes subjected to a freezing-thawing process of 3 cycles. The blue and red circles indicate a measured moduli of self-healing polymers in terms of molar fractions between zinc ions (Zn^{2+}) and PVA before and after dehumidifying in the desiccator (22 ℃ and 17 %RH) for 72 hours, respectively. All data are fitted by blue and red dot lines by the equation inset in the Figure 25. The yellow box shows the modulus range of human skin surveyed from references [85-86].

in the desiccator (22 ℃ / 17 %RH) for 72 hours, respectively. Two groups of samples similarly show that the moduli exponentially diminish with increasing molar ratio. As can be seen in Figure 2.31, the moduli of water-containing samples are two orders of magnitude lower than those of dehumidified samples due to the plasticization effect of water molecules on the softening. The general hydrogels become mechanically harder

and stronger as water is removed. Besides, the Young's modulus gradually decreases with an increase in the molar ratio of metal ions-ligand.

As previously mentioned, the steric hindrance of zinc ions interferes with formation the physical crosslinking during the freezing-thawing process. In addition, most of the zinc ions begin to participate in the formation of Zn-PVA complexes by bonding with hydroxyl groups of PVA so that the crystallites of PVA distributed within polymer matrix decreases. For these reasons, the self-healing polymers represent a decrease in the Young's modulus with an increase of the molar ratio of metal-ligand resulting from the formation of amorphous structure which is capable of having a highly mobile polymer chain. Particularly, the Young's modulus in the self-healing polymers shows the following correlation with respect to the molar ratio of metal-ligand:

$$E=A\cdot exp(-Bf) \qquad \text{(Eq. 16)}$$

where E is the Young's modulus, f is the molar ratio between mole number of metal ions and mole number of ligand (polymer), A and B are the fitting parameters. As a result, the self-healing polymers have a wide range of Young's modulus by controlling the moisture content and the molar ratio of metal-ligand. This tunability of modulus is based on the formation of polymer networks induced by the coordination bonds between zinc ions and PVA backbones, instead of physical crosslinking, thus yielding a potential application of artificial skin or flexible electronics. Furthermore, the Young's modulus of dehumidified self-healing polymers shows a similar range with that of human skin. A

yellow box seen in Figure 2.31 indicates the modulus range of human skin, as published earlier [85-86].

Figure 2.32 displays the measured elongation and tensile strength of self-healing polymers with respect to the molar fractions of Zn^{2+} and PVA. Whereas the tensile strength at a breaking point decreases with an increase in the molar ratio of zinc ions to PVA, the maximum elongation dramatically increases. Most conventional hydrogels,

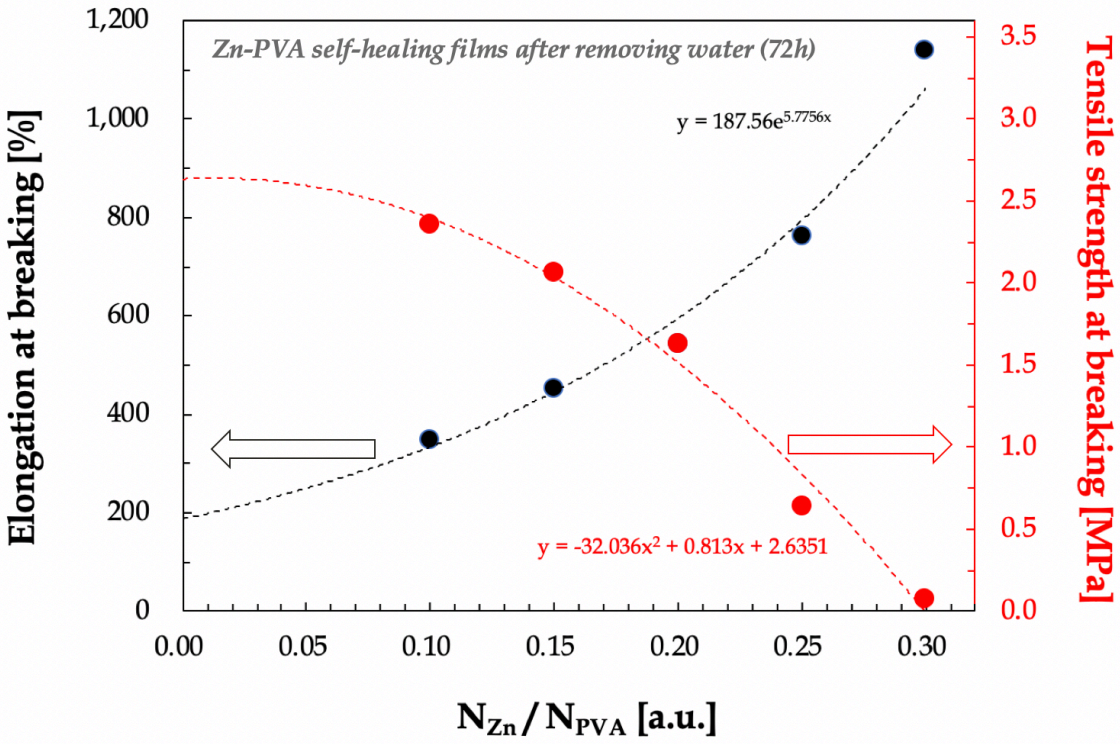

Figure 2.32 Measured elongation and tensile strength of self-healing polymers with respect to the molar fractions of Zn^{2+} and PVA. All samples based on Zn-PVA complexes are fabricated by the freezing-thawing process of 3 cycles followed by the dehumidification under 22 ℃ and 17 %RH for 72 hours. Red shows tensile strength at breaking, while black shows elongation at breaking.

such as pristine PVA hydrogel with no metal ions, formed by the freezing-thawing process demonstrate strong physical crosslinking in conjunction with hydrogen bonds. These supramolecular physical networks within hydrogels tend to give rise to strengthening modulus and tensile strength of materials. For this reason, the hydrogels based on physical crosslinking formed via freezing-thawing process show a good tensile strength other than a high elongation. As discussed above, zinc ions inhibit the formation of physical crosslinking between PVA backbones during the freeze-thaw process by chelating to the hydroxyl groups of PVA. This polymer network based on metal-polymer ligand interactions could contribute to replacing crystallites of PVA with amorphous structures by preventing polymer chains from folding, thereby significantly improving the elongational properties of self-healing polymers.

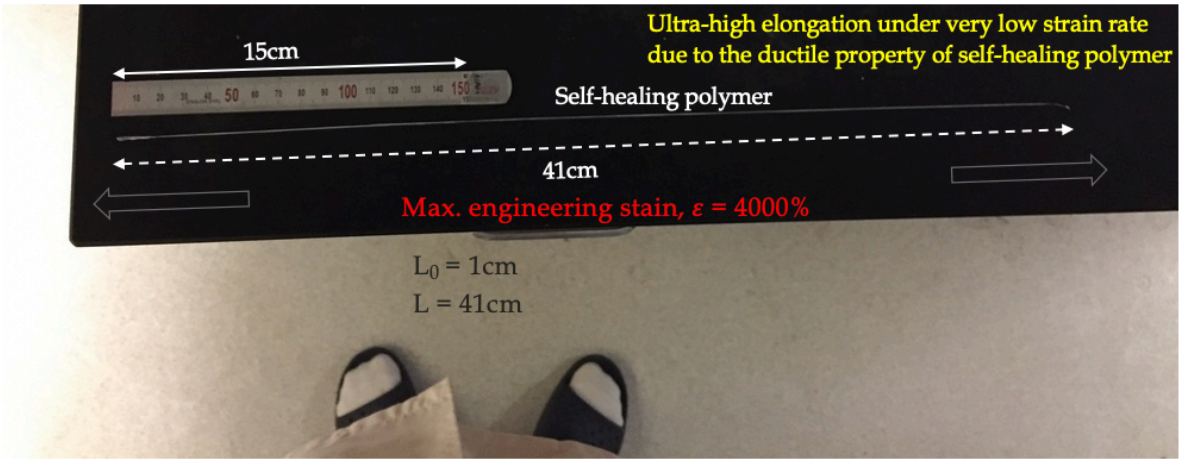

Figure 2.33 A photograph of a self-healing polymeric system comprising PVA and Zn that demonstrates ultra-high elongation (approximately 4000 %) under a low strain rate of 10 mm/min.

The self-healing polymer demonstrates ultra-high elongation of over 4000 % under very low strain rate (about 10 mm/min), as shown in Figure 2.33. The SHA sample with a molar ratio of PVA to Zn^{2+} of 10:3 is prepared by undergoing 3 cycles of the freezing-thawing process, followed by a dehumidification process in the desiccator set to 22 ℃ and 17 %RH for 72 hours. This result suggests that the SHA is a promising material for the stretchable electronics with remarkable practical potential for re-bondable and adjustable adhesives.

2.3.11 Applications of SHA

Here, we introduce some promising applications of SHA including a transparent anti-scratching coating, pressure sensitive adhesive (PSA), and interlayer for laminated safety glass, etc.

2.3.11.1 Transparent anti-scratching coating

Figure 2.34 shows a scratching and recovery test of SHA having a thickness of 300 μm. The SHA film is fabricated by undergoing 3 cycles of a freezing-thawing process followed by a dehumidification process in the desiccator set to 22 ℃ and 17 %RH for 72 hours. Then the film formed is laminated on the 1.1 mm thick glass substrate. A scratch is induced by hand scribing using a razor blade through the 300 μm thick film. The damage begins to be self-healed autonomously without any interventions or stimuli and then the scratch nearly disappears within 5 minutes at room temperature.

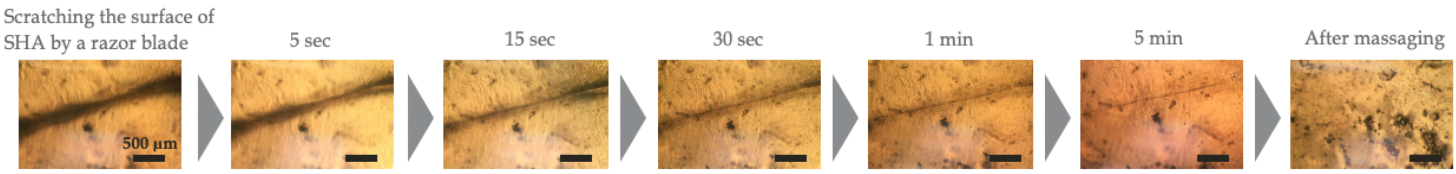

Figure 2.34 Photographs of an anti-scratching test of a self-healing polymer system at 0 second and after 5 seconds, 15 seconds, 30 seconds, and 1 minute after scratching. The self-healing polymer has a thickness of 300 µm laminated on a 1.1 mm thick glass substrate. The self-healing polymer is formed by undergoing the freezing-thawing process of 3 cycles followed by the dehumidification process in the desiccator set to 22 ℃ and 17 %RH for 72 hours. A scratch is induced by hand scribing using a razor blade through the 300 µm thick film. The damage began to be self-healed without any interventions or stimuli and the scratch nearly disappeared within 5 minutes at room temperature.

When the damaged surface is smoothly massaged by a finger, the trace of scratch completely disappears. Therefore, the self-healing polymer associated with the dynamic coordination bonds based on zinc-PVA interactions exhibits an excellent anti-scratching function applicable to anti-scratch coating for automobiles, constructions, displays, and electronics

2.3.11.2 Energy dissipating materials

The excellent performance of anti-scratching observed in the self-healing polymers can be attributed to the energy dissipating behaviors. Thus, rheological analysis can provide the insight into the structure-property relation of materials. Storage modulus (G') reflects the strength of hydrogels and the larger G' represents the stronger of strength. In general, pure viscous liquids are differently categorized from strong elastic

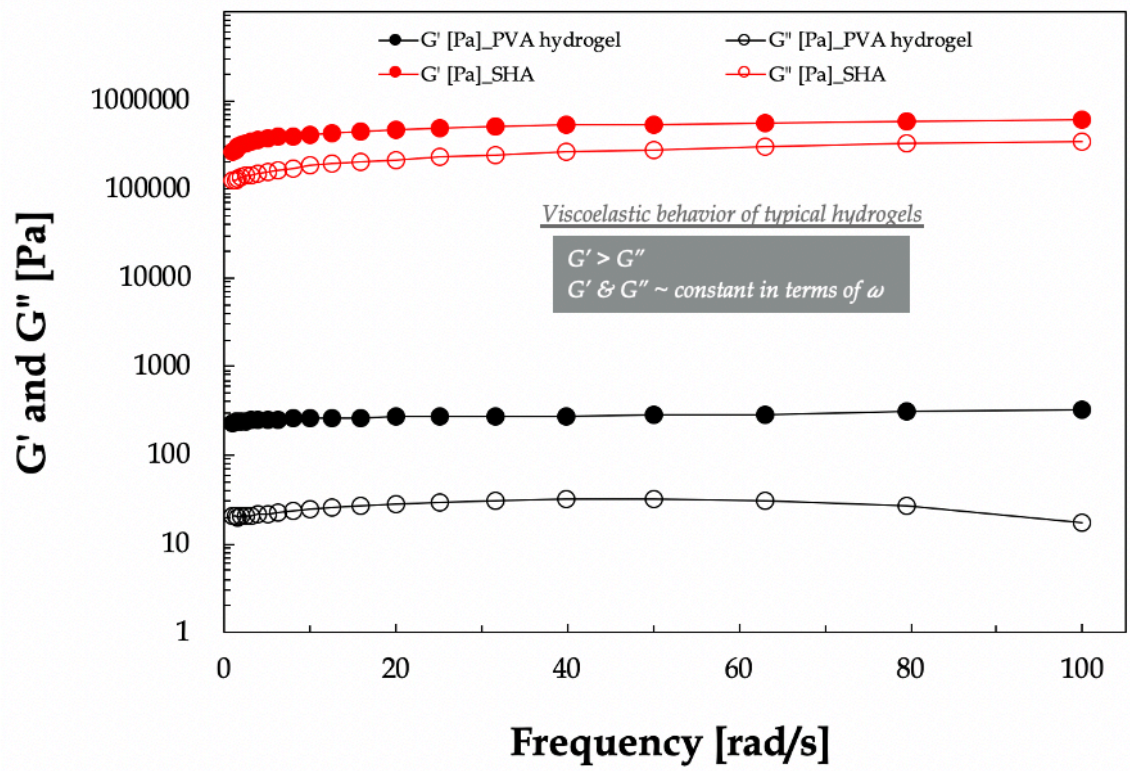

Figure 2.35 Rheological properties (G' and G") of the pure PVA hydrogel and the self-healing polymer as the functions of angular frequency ω from 1 to 100 rad/s at a fixed strain of 1 % at room temperature. The G′ values of all samples exhibit an intrinsically elastic response and are larger than the G″ values over the entire range of frequencies, representing that all samples are crosslinked polymers (G′ > G″). Specifically, the self-healing polymer shows three orders of magnitude greater storage modulus (2.7×10^5 Pa) than that of PVA hydrogel (2.3×10^2 Pa).

gels by evaluating their mechanical behavior, specifically undergoing the system to strain under oscillatory conditions for a large range of frequencies using a rheometry. For limiting angular frequency, ω, namely $\omega \rightarrow 0$, viscous liquids will demonstrate the storage modulus, G', lower than the loss modulus, G"; they typically scale with the following laws: $G' \approx \omega^2$ and $G'' \approx \omega$. Conversely, strong gels typically show $G' \gg G''$

with almost constant values over a wide range of frequencies, thus behaving as elastic solids [87].

Figure 2.35 shows G′ and G″ of the pure PVA hydrogel and the SHA as the functions of angular frequency (ω) from 1 to 100 rad/s at a fixed strain of 1 % at room temperature. The G′ values of all samples exhibit an intrinsically elastic response and are larger than the G″ values over the entire range of frequencies, representing that all samples are crosslinked polymers (G′ > G″). More specifically, the SHA shows three orders of magnitude greater storage modulus (2.7×10^5 Pa) than that of PVA hydrogel (2.3×10^2 Pa). It is noted that the self-healing polymer might have much higher density of crosslinking than that of the pristine PVA hydrogel, indicating the rheological behavior of general hydrogels.

Figure 2.36 indicates the damping factor (tan δ) of pure PVA hydrogel and SHA. The tan δ is determined by the ratio of storage modulus and loss modulus like the following:

$$tan\ \delta = \frac{G''}{G'} \qquad \text{(Eq. 17)}$$

Unlike the storage modulus, the tan δ of SHA shows the dynamic behavior in the entire range of angular frequencies. The tan δ reduces at the initial state of shear test because the increased crosslinking density limits the movement of partial polymer chains. As shown in Figure 2.36, the tan δ value exhibits a clear critical frequency at approximately 5.5 rad/s and increases rapidly with an increase in frequency. This increase in tan δ may be caused by the intermolecular frictions due to the rupture of ionic

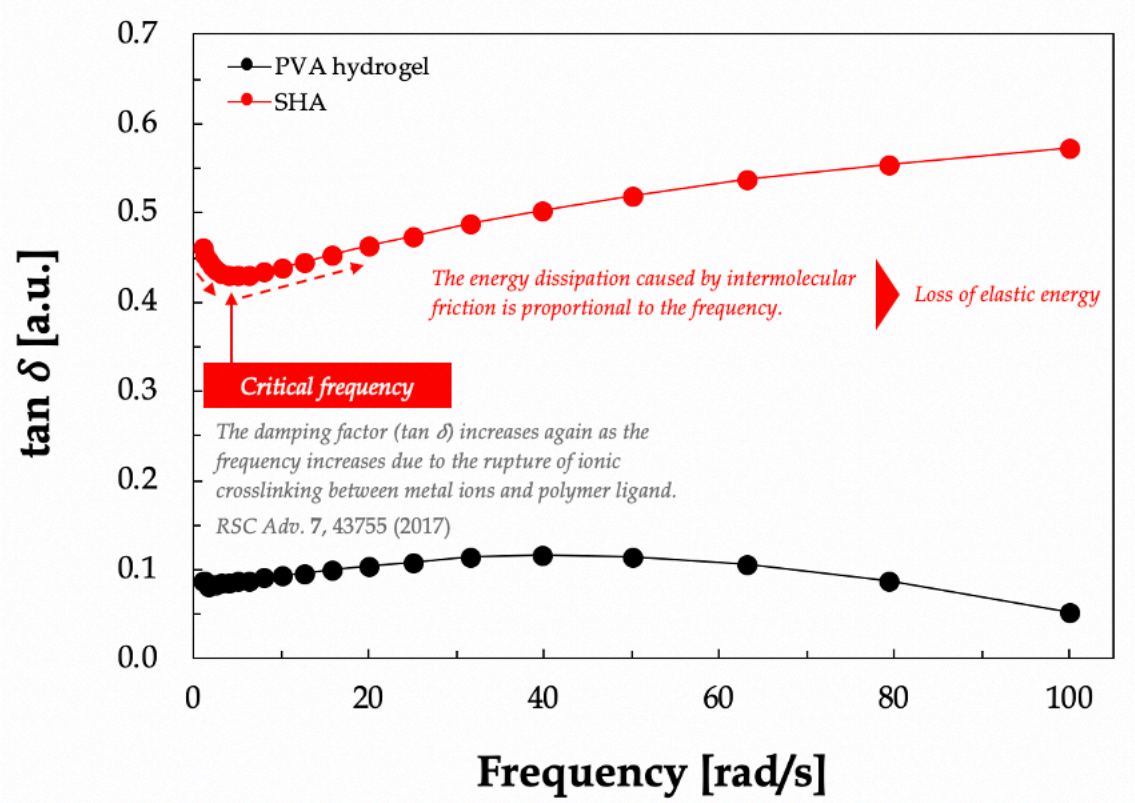

Figure 2.36 Damping factor (tan δ) of the pure PVA hydrogel and SHA. The tan δ is determined by the ratio of storage modulus and loss modulus. The tan δ value exhibits a clear critical frequency at approximately 5.5 rad/s and increases rapidly with an increase in angular frequency. This increase in tan δ may be caused by the intermolecular frictions due to the rupture of ionic crosslinkings within the SHA based on Zn-PVA complexes.

crosslinkings within the SHA based on Zn-PVA complexes. On the other hand, the tan δ of pristine PVA hydrogel diminishes at the high frequency range after around 50 rad/s. The PVA hydrogel is mainly crosslinked by the physical crosslinking by the formation of crystalline microdomains via freezing-thawing process. This physical crosslinking might have much higher fracture energy than the dynamic bond based on metal-ligand complexes formed in the self-healing polymer when the polymer is deformed. Under deformation, the metal-ligand complexed dynamic bond will more readily decrosslink in

order to dissipate mechanical energy. Therefore, the tan δ of PVA hydrogel decreases at the high angular frequency, while that of self-healing polymer increases at the same regime. The damping characteristics of self-healing polymer contributes to its potential application in the field of anti-scratching materials, as shown in Figure 2.34.

2.3.11.3 Pressure sensitive adhesive (PSA)

As a derivative of self-healing materials, the SHA have received great interest in recent years. Similar to traditional self-healing materials, the SHA should have the potential ability to heal and repair the adhesive joints after being damaged. Therefore, the appropriate strategy for material design may serve as a versatile method to prepare self-healing and efficient adhesives. The self-healing polymers comprised of the dynamic networks could be a promising candidate for SHA due to its innate characteristics of pressure sensitive adhesive (PSA). However, a high self-healing efficiency as well as an adjustable adhesion are indispensable for self-healing PSAs, and until now no single PSA has been reported to meet both of the two criteria simultaneously. Therefore, it is a great challenge to develop the self-healing PSAs. Here we demonstrate novel PSA based on the SHA with a transient coordination bond indicating ultra-fast self-healing ability at room temperature.

Figure 2.37 represents a measurement of the normal adhesive strength of SHA. All SHA samples are prepared by undergoing 3 cycles of a freezing-thawing process followed by the dehumidification process in the desiccator set to 22 ℃ and 17 % RH for

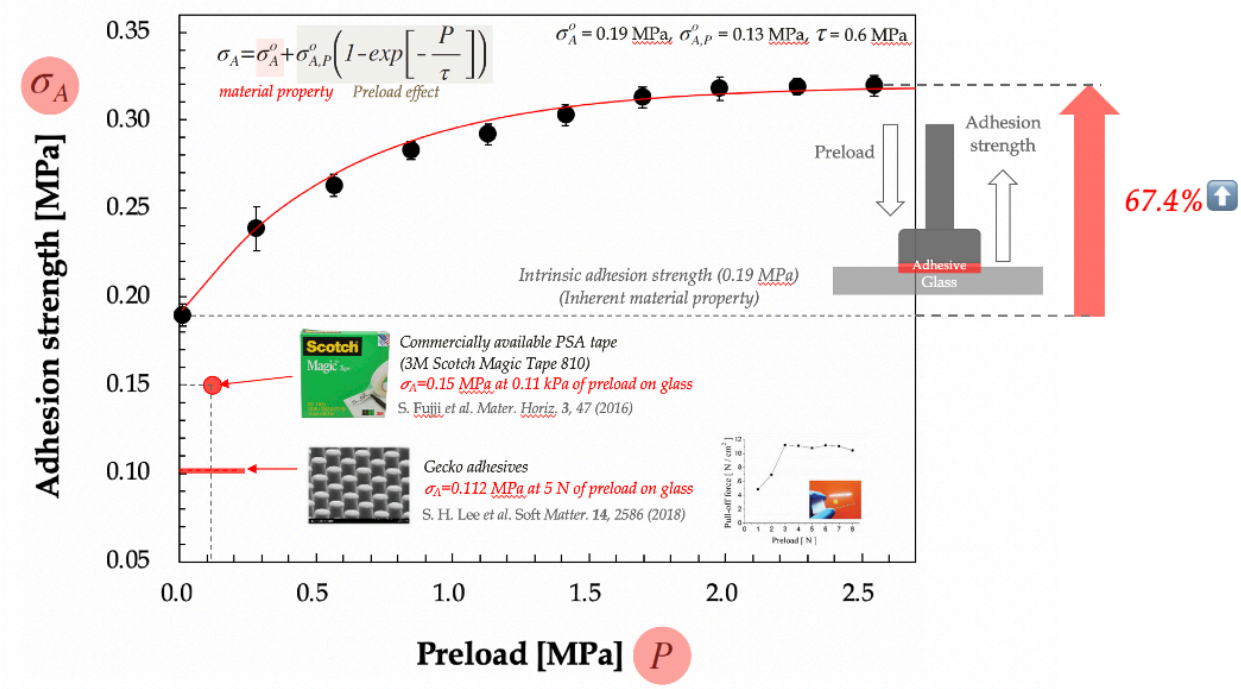

Figure 2.37 A normal adhesive strength of a self-healing adhesive (SHA) laminated on a 1.1 mm thick glass substrate having a preload to estimate the property of pressure sensitive adhesive (PSA). All samples are fabricated by freezing-thawing process of 3 cycles followed by the dehumidification process in the desiccator set to 22 ℃ and 17 %RH for 72 hours. A comparison is provided for results for a commercially available product (3M Scotch Magic® Tape 810) [88] and bio-inspired Gecko-patterned physical adhesive [89].

72 hours. The prepared SHA films have a thickness of 200 μm and are laminated on the 1.1 mm glass with a preload to estimate the property of pressure sensitive adhesive (PSA).

The normal stress of self-healing adhesives is measured as an adhesive strength by FDHT (Larson System Inc) to evaluate the characteristics of pressure sensitive adhesive (PSA) with or without the preload. The self-healing adhesive is laminated onto the metal press with a diameter of 1.5 cm. The metal press is translated vertically downward and then adheres to the substrates with or without the preload in accordance

with experimental conditions. The force or stress is then measured while the metal press moves upward and the maximum normal stress is recorded before the press is completely detached from the substrate.

The adhesive strength monotonically increases with the preload at first and then shows the saturated value from the preload of about 2 MPa. The adhesive strength of SHA with the preload of 2.55 MPa is about 67.4 % higher than that of intrinsic adhesive strength, which indicates the adhesive strength of SHA without any preload. The measured adhesive strength (black circles) are in agreement with the fitting model as the following:

$$\sigma_A = \sigma_A^o + \sigma_{A,P}^o \left(1 - exp\left[- \frac{P}{\tau} \right] \right) \quad \text{(Eq. 18)}$$

where σ_A is a total adhesive strength, σ^0_A is a normal adhesive strength without any preload as an intrinsic material property, $\sigma^0_{A,P}$ is a saturation value of normal adhesive strength with the preload, P is the preload applied to SHA, and τ is a relaxation preload. The intrinsic adhesive strength (σ^0_A) of SHA is extracted as 0.19 MPa from the measured data and then $\sigma^0_{A,P}$ and τ are calculated as 0.13 MPa and 0.6 MPa by the fitting of the equation, respectively. Consequently, ultra-fast self-healing adhesives shows a unique characteristic of a pressure sensitive adhesive (PSA) satisfying (Eq.18). In addition, the SHAs indicate a stronger adhesive strength than that of a commercially available product (3M Scotch Magic® Tape 810) [88] and bio-inspired Gecko-patterned physical adhesive [89], as shown in Figure 2.37. The adhesive strength of 3M Scotch Magic Tape and Gecko patterned dry adhesive is 0.15 MPa and 0.112 MPa, respectively.

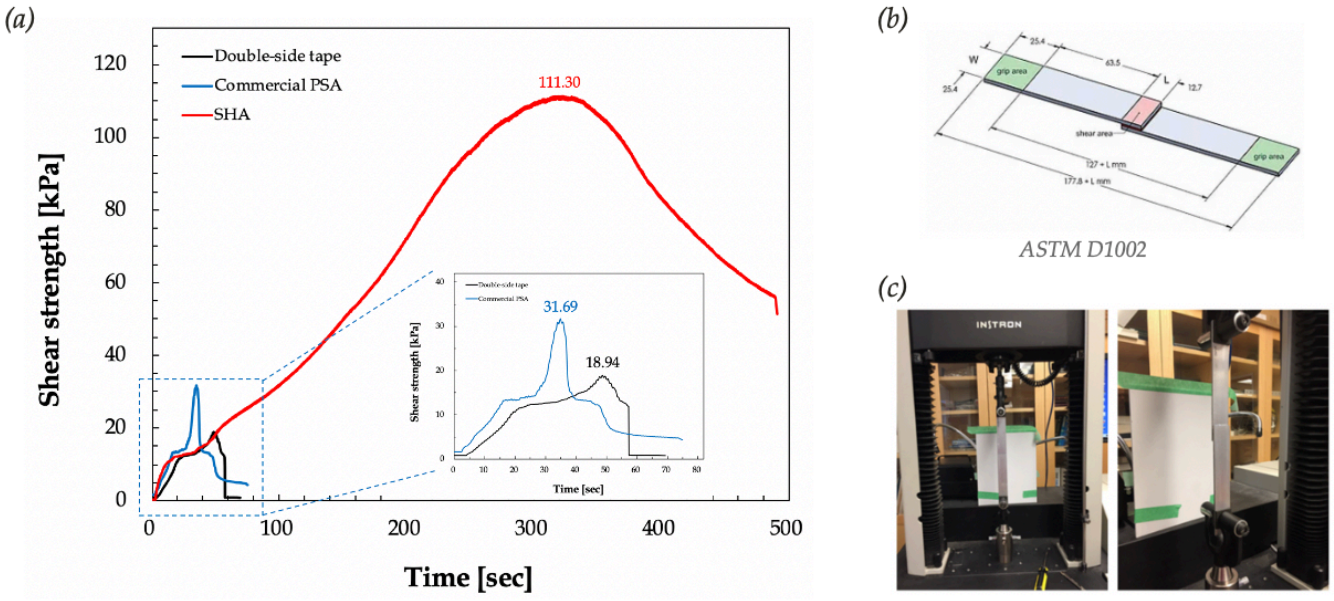

Figure 2.38 Measurement of shear strength for the SHA based on ASTM D1002. Figure 2.38A shows a comparison of shear strength in terms of time for double-sided tape, a commercial pressure sensitive adhesive, and a SHA prepared via the freezing-thawing process of 3 cycles followed by the dehumidification process in the desiccator set to 22 ℃ and 17 %RH for 72 hours. Figure 2.38B shows a schematic of the setup for shear strength testing based on ASTM D1002. Figure 2.38C indicates two photographs of the testing instrument for conducting the shear strength measurement.

Figure 2.38 displays a lap-shear test of SHA as different measures of adhesive strength based on ASTM D1002. Figure 2.38A shows a comparison of shear strength in terms of time for double-sided tape, a commercial pressure sensitive adhesive, and a SHA. Figures 2.38B and 2.38C illustrate how shear strength is measured during testing and the INSTRON^{TM} ultimate tensile machine used. The SHA with a molar ratio of PVA to Zn^{2+} of 10:3 is fabricated by undergoing 3 cycles of the freezing-thawing process followed by a dehumidification process in the desiccator set to 22 ℃ and 17 %RH for 72 hours. Each

of the adhesive sample was directly sandwiched between two aluminum alloy adherends, as shown in Figure 2.38B. The shear strength is then measured on the INSTRON™ ultimate tensile machine, with measurements following ASTM D1002. The maximum shear strength of SHA is about 111.30 kPa compared to those of a commercially available product (3M Scotch Magic® Tape 810) that has a shear strength of 18.94 kPa and a commercial PSA (3M OCA) having a shear strength of 31.69 kPa. As a consequence, the present SHA film could provide a new opportunity to develop a mechanically durable and commercially viable pressure sensitive adhesive for stretchable electronics due its excellent shear strength.

Figure 2.39 shows photographs observing adhesion properties of the SHA with different substrates. The SHA samples are based on Zn-PVA complexes formed via the

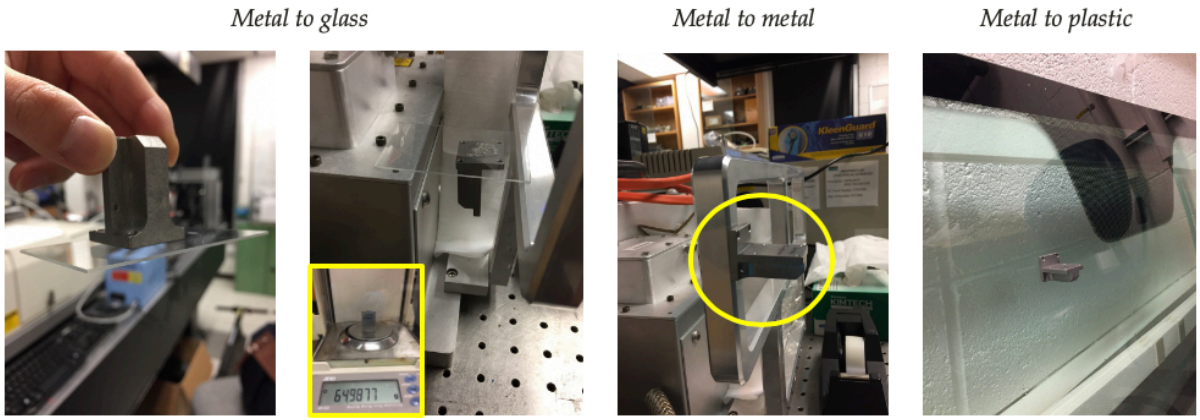

Figure 2.39 Photographs of observation of adhesive properties of the SHA based on Zn-PVA complexes via the freezing-thawing process of 3 cycles followed by the dehumidification process in the desiccator set to 22 ℃ and 17 %RH for 72 hours. The adhesive characteristics of the SHA are evaluated by adhering it to various different substrates, including glass, metal, and plastic.

freezing-thawing process of 3 cycles followed by the dehumidification process in the desiccator set to 22 ℃ and 17 % RH for 72 hours. As seen in Figure 2.39, the SHA provides outstanding adhesion to various interfaces involving metal to glass, metal to metal, metal to plastic, and so on. As previously discussed, the SHA has the amorphous structure with a low T_g of around -4 ℃. Moreover, the SHA also has a flowing property as expected from its rheological properties including a high tan δ. For these reasons, the SHA gradually spread along the adherend, permeating into small unevenness on the rough surface, and then joined the two adherends without any voids. Therefore, the high adhesive strength of SHA for various adherends can be attributed to the intrinsic material properties of SHA. However, the most significant factor resulting in the high adhesive strength may be the presence of coordination bonds within polymer. Specifically, the SHA strengthens its adhesion on the glass.

Figure 2.40 represents the schematic illustrations of chemical structures for SHA when adhered to a glass substrate comprising silicon oxides. M Tupy et al. studied the presence of optimum amount of water molecules in polymer matrix with a side chain of hydroxyl group such as poly(vinyl butyral) could enhance the adhesive strength between polymer and glass [90]. Water molecules play a role to not only activate the -OH groups of polymer chains to form hydrogen bonds with the glass rapidly and efficiently but also accelerate the diffusion rate of macromolecules toward the interface between polymer and glass. For this reason, keeping of water content in polymer at a range 0.3-0.5 % is necessary for maintaining the required adhesion grade. The hydroxyl groups in the SHA would be activated with the hydration, thus increasing in bonding site for both hydrogen

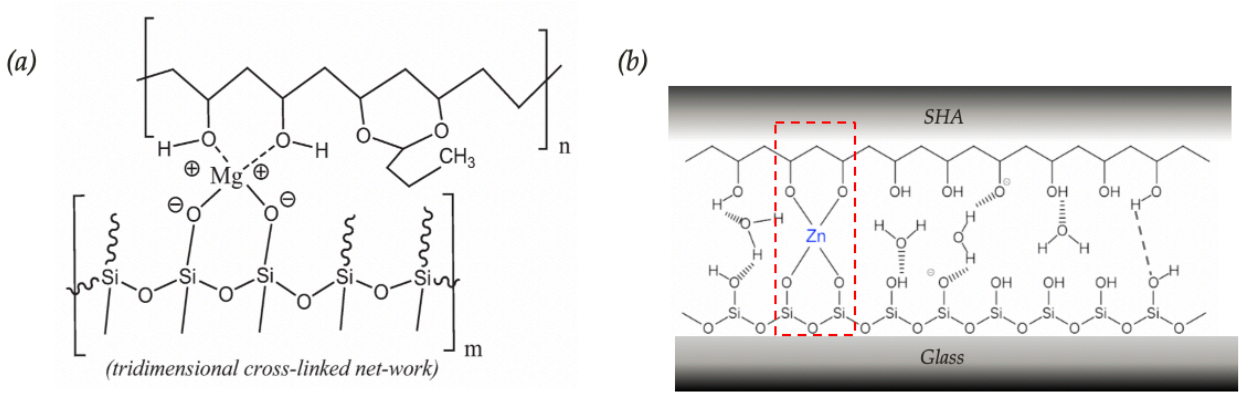

M. Tupy *et al.* Effect of water and acid-base reactants on adhesive properties of various plasticized poly(vinyl butyral) sheet, *J. Appl. Polym. Sci.* **127**, 3474 (2013)

Figure 2.40 Influence of coordination bonding on adhesion between self-healing adhesive (SHA) and a glass substrate. As shown in Figure 2.40A, a transition metal ion could form the coordination between glass and polymer including the hydroxyl group ([90] M. Tupy *et al*., Effect of water and acid-base reactants on adhesive properties of various plasticized poly(vinyl butyral) sheet, *J. Appl. Polym. Sci.* **127**, 3474, 2013). A hypothesized schematic illustration indicating the adhesion mechanism between SHA and glass is represented, as shown in Figure 2.40B. The SHA exhibits an excellent adhesion on glass due to additional coordination bonds between metal ions and ligand sites presenting on the glass surface, as can be seen in Figure 2.40B.

bonds and coordination bonds. With the presence of water molecules within the polymer, metal-ligand complexes can form the coordination bonds with the ligand sites (Si-O-) provided by the glass, as shown in Figure 2.40A. Therefore, the adhesion between the SHA and glass could be enhanced due to the coordination bonds between metal ions within the SHA and ligand sites presenting on the glass surface, as can be seen in Figure 2.40B.

Figure 2.41 displays a self-healing property of SHA as a pressure sensitive adhesive (PSA). As shown in Figure 2.41A, a SHA is cut into two pieces and then self-

healed for 10 minutes at room temperature without any stimuli. It is then adhered to a glass substrate with preloading to test adhesion strength. This self-healed SHA is then evaluated for adhesive strength with the same method as PSA evaluation, as represented in Figure 2.37. Figure 2.41B shows adhesion strength versus preload, both before self-healing and after self-healing. As can be seen in Figure 2.41B, the adhesion strength is very similar for samples tested before and after self-healing. Furthermore, the SHA after self-healing shows the same behavior as the SHA before being damaged following (Eq. 18) inset in Figure 2.41B. The relaxation preload (τ) of the original SHA before damage

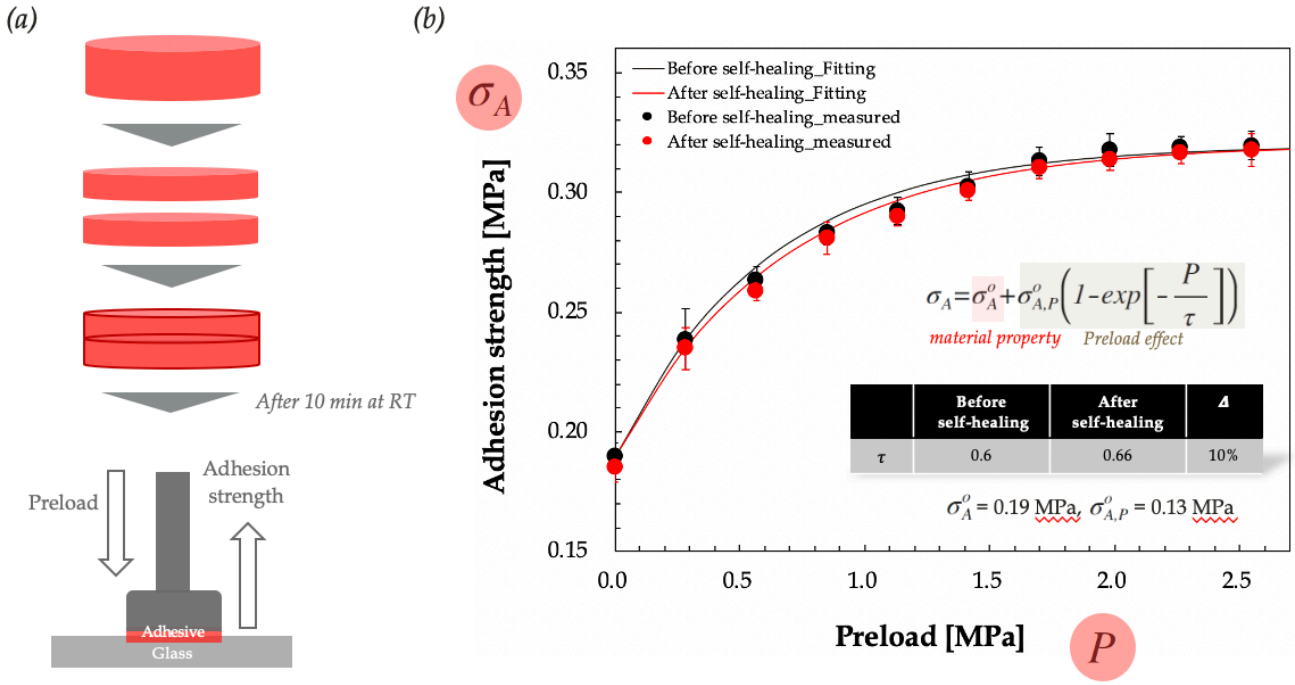

Figure 2.41 Self-healing properties of the SHA as a pressure sensitive adhesive (PSA). Figure 2.41A shows a schematic illustration of a self-healing process for the SHA followed by adhesion to a glass substrate. Figure 2.41B represents comparative adhesion strength versus preload for the SHA samples before and after self-healing.

and self-healed SHA is 0.60 MPa and 0.66 MPa, respectively. This difference of about 10 % in the relaxation preload between original SHA and self-healed SHA means that an additional preload of about 10 % might be required to reach out to 1/e the saturated adhesive strength in case of the self-healed SHA. However, the adhesive strength of SHA before and after the self-healing process has been nearly consistent in the range of preload over 2.0 MPa, therefore no additional preload is needed for SHA even after self-healing.

At the molecular level, the self-healing ability of SHA likely arises from the dynamic coordination bond and polymer chain movement. As previously observed, the SHA has the amorphous structure with a very low T_g of around -4 ℃. Therefore, a considerable amount of flexible chains are retained within the SHA, which can be alternatively arranged in polymer backbone chains at room temperature. The previously reported SHA requires a high temperature over 180 ℃ to induce the dynamic state of polymer chains [91]. Provided enough time for the self-healing process before cooling to room temperature, the adhesive resin in a damaged interface would repair completely. However, our SHA indicates that the re-association of dynamic bonds is perfectly occurred at room temperature, which made the self-healed interface almost identical to undamaged regions.

The self-healing test was repeated with 30 cycles, as shown in Figure 2.42. After 30 cycles of damage and repair process at room temperature without any stimuli, the self-healed SHA regains its adhesive strength (0.275 MPa), which is about 85 % of the pristine strength (0.325 MPa). The reported SHAs shows approximately 51.1 % of self-healing efficiency after 20 cycles of damage-repair process when self-healed at 180 ℃

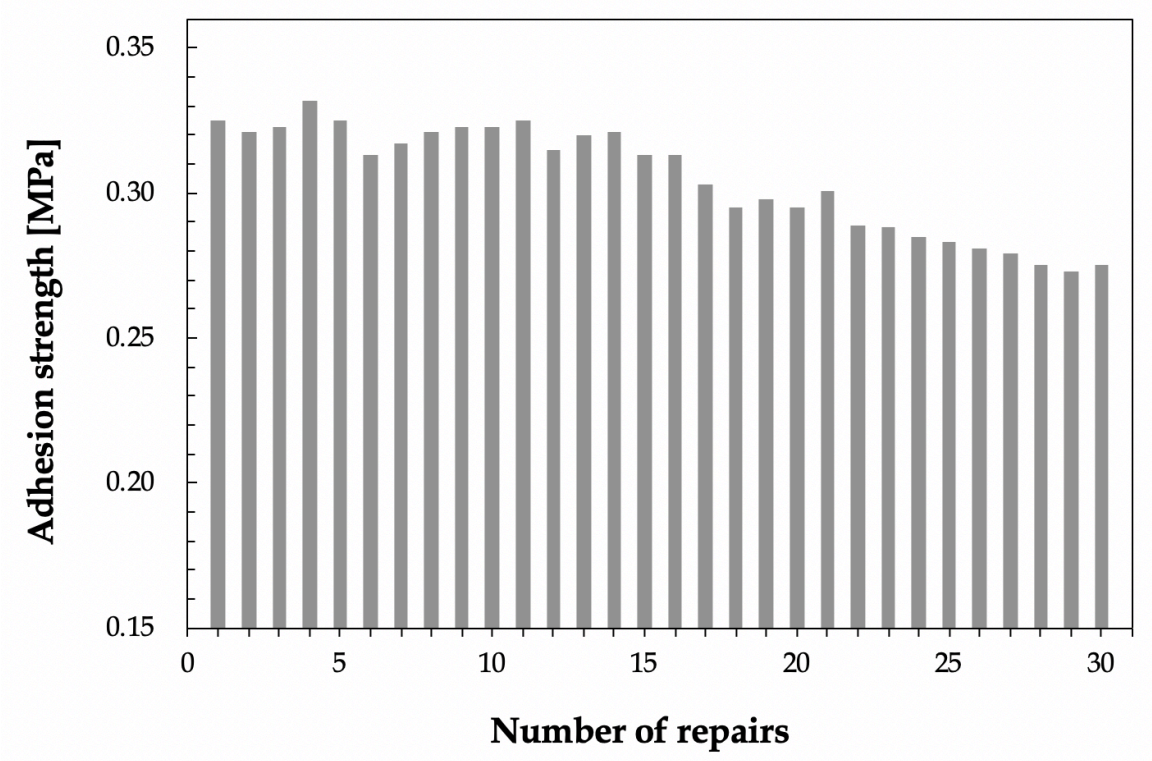

Figure 2.42 Cycling test of the SHA with 30 cycles of damage and repair process. After 30 cycles of self-healing test at room temperature without any stimuli, the self-healed SHA regains its adhesive strength (0.275 MPa), which is about 85 % of the pristine strength (0.325 MPa).

for 1 hour [91]. Most of SHAs reported previously indicate a limited cycle number of self-healing, which was approximately 10 times. As a result, the efficient self-healing properties would endow the SHA with reusable ability along with adjustable adhesion property. If a joint is broken, it can be directly repaired many times simply without any interventions at room temperature. Conversely, for a conventional PSA or thermo-setting adhesive, the residual resin needs to be removed by the cleaning before the damaged joint is repaired with a new adhesive. In some cases, the whole part including the adherends and adhesives should be replaced or discarded for repair. In this aspect, the reusability of

SHA with a high self-healing efficiency shown in Figure 2.42 could reduce the waste of materials and environmental pollution.

2.3.11.4 Sealing agent with chemical stability

Figure 2.43 illustrates sealing performance and chemical stability of adhesive joints formed by the SHA. A 500 µm thick glass slide and the glass vials are filled with deionized water, isopropyl alcohol (IPA), acetone, dimethylformamide (DMF), and benzene, which are sealed by a SHA film. The setup of test specimen is shown in Figure 2.43A. After sealing for 5 minutes, the glass slide side is placed on the bottom and then

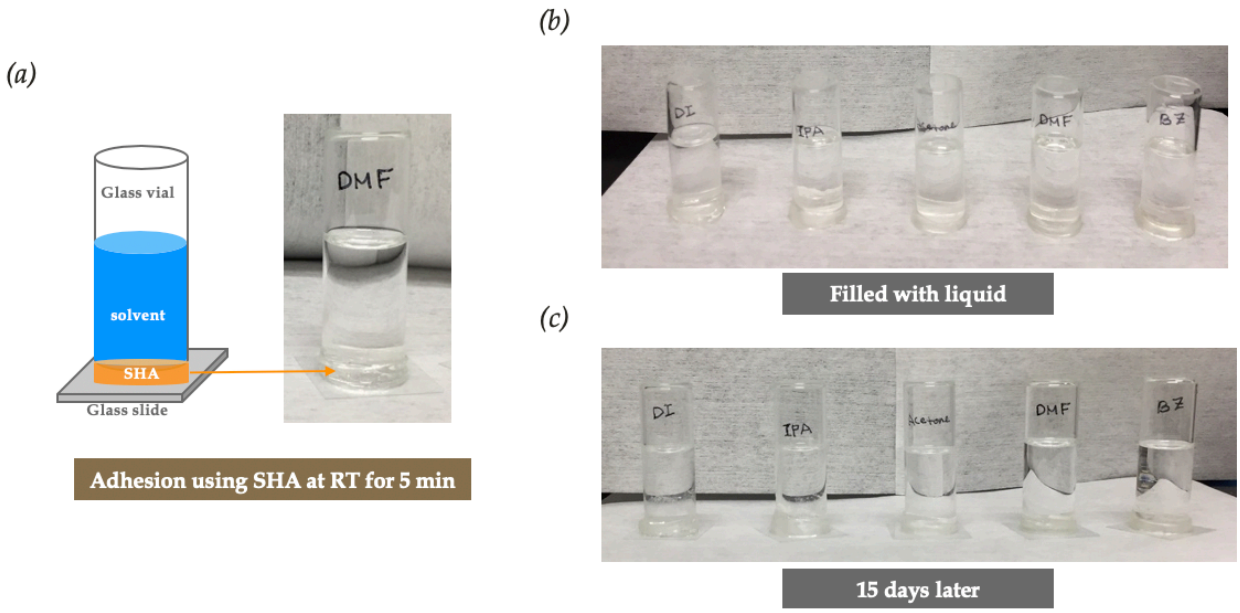

Figure 2.43 Chemical stability and sealability of the SHA in deionized water, isopropyl alcohol (IPA), acetone, dimethylformamide (DMF), and benzene when a glass vial and a glass slide are sealed with SHA for 15 days at ambient conditions. Figure 2.43A shows adhesion in the presence of DMF, Figure 2.43B is a photograph of samples filled with the various solvents listed above and Figure 2.43C is a photograph of the same samples taken 15 days later.

stored for 15 days. As shown in comparing Figures 2.43B and 2.43C, the sealed SHA has excellent solvent resistance: bonded bottles are filled with water, IPA, acetone, DMF, and benzene and left to stand for 15 days without any leakage. This indicates that the SHA has a good solvent resistance and is particularly suitable for use as a leak-free sealant. In certain aspects, the SHA could be contemplated as a self-healing pressure sensitive adhesive that is stable in the presence of solvent attack, namely solvent resistant. This strong chemical resistance of SHA can be attributed to the crosslinked networks based on metal-ligand interactions and renders SHA to be applied to a vulnerable region where the joint is readily exposed to organic solvents.

In addition to chemical stability, we also observed the thermal stability of the SHA. Figure 2.44 represents the effect of temperature on the adhesive strength of SHA. All samples are fabricated by undergoing 3 cycles of a freezing-thawing process followed by the dehumidification process in the desiccator set to 22 ℃ and 17 % RH for 72 hours. The prepared SHA films have a thickness of 200 μm and are laminated on the 1.1 mm glass with a preload to estimate the property of pressure sensitive adhesive (PSA) with respect to temperature. The normal stress of SHA is measured as an adhesive strength by FDHT (Larson System Inc) to evaluate the characteristics of pressure sensitive adhesive (PSA). The SHA is laminated onto the metal press with a diameter of 1.5 cm. The metal press installed in the apparatus at which is attached by the temperature/humidity sensor shown in Figure 2.44 is translated vertically downward and then adheres to the substrates. The air near the metal press laminated by the SHA is heated by the heat-gun and the temperature measured by the sensor is displayed on thermometer. The temperatures set

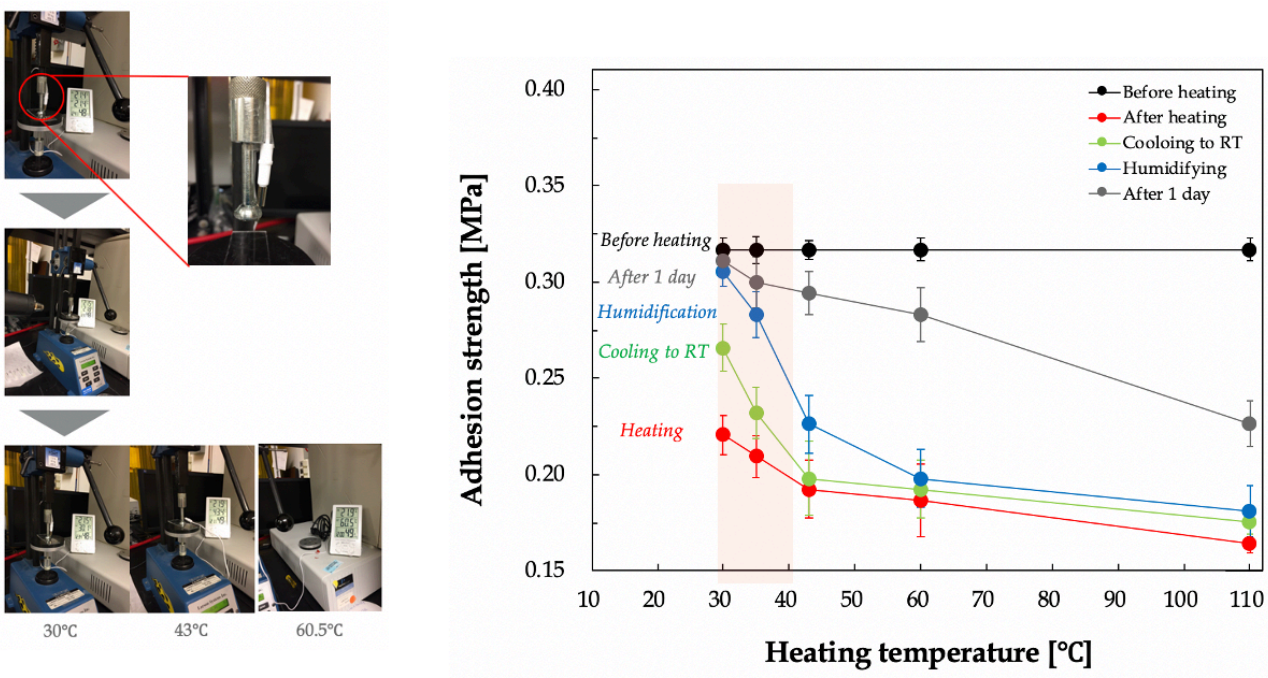

Figure 2.44 Temperature effect on the adhesive strength of the SHA fabricated via the freezing-thawing process of 3 cycles followed by the dehumidification process in the desiccator set to 22 ℃ and 17 %RH for 72 hours.

forth are 30 ℃, 43 ℃, 60 ℃, and 110 ℃. The force or stress is then measured while the metal press moves upward and the maximum normal stress is recorded before the press is completely detached from the substrate.

The adhesive strength of SHA diminishes after heating for all temperatures as displayed to red circles in Figure 2.44. The adhesive strength monotonically decreases with an increase in heating temperature and then shows the recovered value when cooled to room temperature. Whereas the adhesive strength at low heating temperature becomes recovered to the initial state via humidification followed by aging for 1 day at room temperature, those at high temperature represent an irreversible behavior, that is, the

SHAs heated at over 60 ℃ have lost its intrinsic property of PSA. For instance, the adhesive strength of SHA with the initial strength of 0.317 MPa is recovered to about 98.2 % the initial strength under heating at 30 ℃, on the other hand, the adhesive strength when heated at 110 ℃ is retrieved to 71.4 % the initial strength after humidifying and aging at room temperature for 1 day.

This decrease in adhesive strength of SHA when heated at high temperature could be resulted from the following three reasons: First, heating effect on the adhesive strength is due to the loss of water from SHA during heating. As previously mentioned, the presence of optimum amount (0.3 – 0.5 %) of water molecules in polymer is required to enhance the adhesion between adhesives and substrates such as glass. This is because water molecules could activate the hydroxy groups of PVA chains to form hydrogen bonds with the bonding sites (Si-O-) provided by the glass efficiently.

Second, the weakening of hydrogen bonds gives rise to decreasing the adhesive strength at high temperature. A. Khan demonstrated that the weakening of hydrogen bonds, from about 23 kJ/mol to about 17 kJ/mol, is observed when many bonds are broken at temperatures (> 100 °C) in his paper [92]. The hydrogen bonds existing at the interface between SHA and glass substrates would be dramatically weakened with the increase in heating temperature, thus reducing the adhesive strength of SHA. In addition, water molecule itself located at the interface between SHA and glass substrates could lose its physical properties due to the disruption of strong tetrahedrally-placed hydrogen bonds at high temperature [93]. Therefore, water molecules could not play a role as a linker bonding with SHA and glass via hydrogen bonds.

Third, high temperature might result in the weakening of ionic crosslinking based on zinc-PVA and/or zinc-glass interactions. In an ionomer such as the SHA, the polar ionic groups are attracted to each other from being apart from the nonpolar chain groups. This polar ionic groups tend to form very small clusters surrounded by a sea of non-ionic segments. This clustering acts like a physically crosslinked junction and allows SHA to act as thermoplastic ionomers in ways similar to chemically crosslinked polymers or sometimes like block copolymers. However, most ionomers are not chemically crosslinked polymers, and in fact, are a type of thermoplastic with reversible crosslinked networks. When heated, the ionic groups will lose their attractions for each other because they have insufficient energy to sustain the ionically crosslinked networks and the chains would move around freely. If the temperature increases enough, the chains move around faster and faster and the groups cannot stay in their clusters. This disruption of ionic clusters gives rise to weakening the cohesion of SHA, thus decreasing the adhesive strength of material at elevated temperature.

Figure 2.45 represents the optical transmittance for a SHA measured by Agilent Cary 6000 UV/Vis Spectrophotometer. The single SHA film shows the transmittance of about 78 % due to the diffuse reflection induced by its rough surface. However, a SHA film sandwiched between two 1.1 mm thick glass substrates has a transmittance of about 92%, which is nearly similar with that of bare glass, as seen in Figure 2.45. The haze evaluated by Ocean Optics Spectrophotometer is about 0.6 %, thus yielding an optically transparent self-healing polymer. This optically transparent property of the SHA film is due to the presence of amorphous phases induced by metal-ligand coordination bonds in

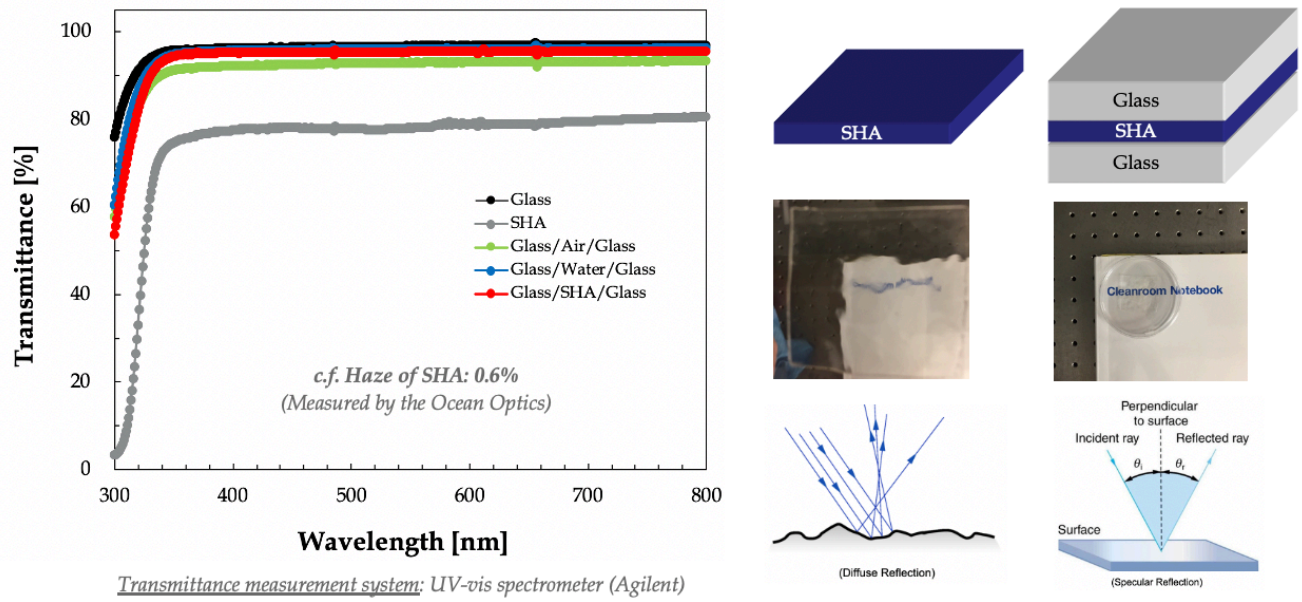

Figure 2.45 Optical transmittance and haze of the SHA. The single SHA film shows the transmittance of about 78 % due to the diffuse reflection induced by its rough surface. However, a SHA film sandwiched between two 1.1 mm thick glass substrates has a transmittance of about 92%, which is nearly similar with that of bare glass.

the polymer matrix. The steric hindrance of zinc ions chelating to the hydroxyl groups of PVA inhibits the formation of physical crosslinking during the freezing-thawing process. The pristine PVA hydrogels with localized crystalline phases associated with physically crosslinked networks without any metal ions indicate an optically opaque property. Therefore, an addition of zinc ions to PVA ligand followed by freezing-thawing process can result in an increase in the density of amorphous phases, which in turn, improves optical transparency. This optically transparent characteristics of SHA enable to develop a transparent anti-scratching coating in conjunction with the features observed in Figure 2.34 as well as a transparent PSA for an application of displays or packages.

In summary, the SHA in the present work has many advantages for practical applications as a novel adhesive. In contrast to conventional fluid-type adhesives (bond, glue, cement, or paste), the SHA can be supplied with a solid film that can be easily handled in the adhesion process with no solvent. It can also serve as a membrane-type PSA with precise size and controllable thickness. In addition, there is no requirement for a complicated curing procedure as with conventional thermo-setting adhesives.

2.3.11.5 Laminated safety glass

A laminated safety glass is a composite material that consists of the unique properties of glass with the benefits of a tough but highly elastic organic material [94]. The laminated safety glass is resistant towards impact and penetration. Even upon impact, it will hold the glass fragments together, thus lowering the risk of injuries due to glass shatters. The plasticized poly(vinyl butyral) (PVB) sheets are extensively used for laminated safety glasses for an automotive and a building industry. PVB is a polyacetal produced by the condensation of poly(vinyl alcohol) with n-butyraldehyde in the presence of an acid catalyst. The main function of PVB sheet is gluing two or more glass surfaces together, providing an excellent mechanical resistance to the break of the laminated glass [95]. Adhesive force is mainly provided by hydrogen bonds between -OH groups of PVB chain and the -OH groups in the glass [90]. PVB interlayer is able to hold glass fragments on its surface without any shatters and simultaneously adsorb shock energy in car accidents.

The metal-ligand complexed SHA, which has a good adhesive strength to glass as shown in Figure 2.38 as well as a high toughness, could be exploited as a novel interlayer for laminated safety glass. The SHA with a molar ratio of PVA to Zn^{2+} of 10:3 is fabricated by undergoing 3 cycles of the freezing-thawing process followed by a dehumidification process in the desiccator set to 22 ℃ and 17 %RH for 72 hours. Next, the SHA film is laminated on the surface of a 1.1 mm thick glass and then the other side of SHA film is attached to another glass with the same thickness. The adhesion test of laminated glass associated with the SHA is implemented based on Pummel test [90]. A laminate of non-specific size is frozen to -18° and held at about 5° angles to plane of the Pummel plate. And then, the sample is pummeled using a hammer with weight 450 grams (1 pound) on a steel plate in such a way, that the glass on both sides pulverizes. Subsequently, the sample is visually rated according to a scale from 0 to 10, where 0 corresponds to complete exposure of the PVB interlayer and 10 to 100% coverage of the PVB by glass fragments. The test can be carried out by hand or by custom made apparatus.

Figure 2.46 shows pummeling test of a laminated safety glass sandwiched by a SHA film between two glass slides each of which has a thickness of 1.1 mm. Figure 2.46A indicates the structure of broken laminated glass glued by the SHA film as an interlayer after pummeling test. The SHA film keeps the layers of glass bonded even when broken, and its high toughness prevents the glass from breaking up into large sharp pieces. This induces a typical characteristic "spider web" cracking pattern observed in conventional laminated glasses when the impact is not enough to completely pierce the glass. With the presence of hydrogen bonds between the polymer and glasses, metal-

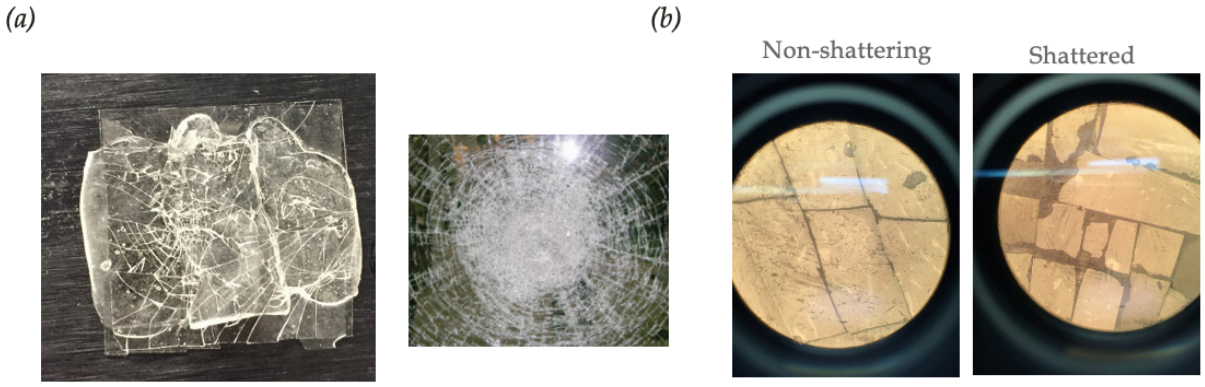

Figure 2.46 Pummeling test of laminated safety glass associated with SHA film with a molar ratio of PVA to Zn^{2+} of 10:3 is fabricated by undergoing 3 cycles of the freezing-thawing process followed by a dehumidification process in the desiccator set to 22 ℃ and 17 %RH for 72 hours. The SHA film as an interlayer keeps the layers of glass bonded even when broken, and its high toughness prevents the glass from breaking up into large sharp pieces seen in Figure 2.46A. Figure 2.46B represents two microscope images of broken laminated glass, one of which is associated with SHA involving a tiny amount of water (left) and another is laminated by a fully dried SHA film (right). A laminated glass using the SHA including a little water shows better adhesion to glass without any shatters, on the other hand, the sample laminated by a fully dried SHA film is exposed to the interlayer after shattering.

ligand interactions mediated by zinc ions within SHA film might form the coordination bonds with the ligand sites (Si-O-) provided by the glass, as shown in Figure 2.46A. Therefore, novel laminated safety glass associated with SHA could represent better performances due to the supplementary coordination bonds formed between zinc ions within the SHA and ligand sites presenting on the glass surface, as seen in Figure 2.39B.

In addition, self-healing ability of SHA could prevent the interlayer from being mechanically damaged and/or fractured without any loss of interaction with glasses. Figure 2.46B represents two microscopic images of broken laminated glass, one of which is sandwiched with the SHA film involving a tiny amount of water (left) and the other is

laminated by a fully dried SHA film (right). A laminated glass using the SHA including a little water shows better adhesion to glass without any shatters, on the other hand, the sample laminated by a fully dried SHA film is exposed to the interlayer after shattering. As previously mentioned, the presence of optimum amount of water molecules in polymer matrix could enhance the adhesive strength between polymer and glass [90]. Water molecules could activate the -OH groups of polymer chains to form hydrogen bonds with the glass effectively and accelerate the diffusion rate of macromolecules toward the interface between polymer and glass. For this reason, the hydroxyl groups in the SHA would be activated with the hydration, thus increasing bonding sites in order to facilitate both hydrogen bonds and coordination bonds. Consequently, novel SHA laminated safety glass could be promising to protect the head and face from serious injury via shattering of the windshield in car accidents. The strong adhesive property as well as energy absorbing ability of SHA resulting from its high toughness and stretchability is resistant towards impact and penetration, that is, it will hold the glass fragments together, thus lowering the risk of injuries due to glass shatters.

2.4 Conclusions

In summary, we have demonstrated a novel self-healing polymer by strategically programming a dynamic network comprised of metal-ligand complexes. The mechanical and adhesive properties of the materials can be conveniently tuned by varying several material parameters such as the molar ratio of metal and ligand as well as the moisture contents. The simple material design based on the dynamic coordination bond enables

remarkable self-healing properties under ambient conditions without any interventions. Compared to the conventional self-healing polymers based on the hydrogen bond, the transient coordination bond may serve as a versatile method to develop ultra-fast self-healing and autonomous self-healing polymers. However, the main purpose of this present work may differ from that of other research groups because we need to make the self-healing polymer to have a practical potential as a self-healing adhesive (SHA) with re-bondable and adjustable adhesion. For this reason, we have investigated to develop novel ultra-fast SHA and intensively explicated the principle of self-healing based on the kinetics for complex formation. As a major finding, we have contemplated the effect of activation energy on the self-healing efficiency and revealed the role of water molecules in the formation of dynamic and reversible bonds in this work. When mechanical damaged, the SHA indicates excellent self-healing ability that can be attributed to the high chain mobility resulting from the amorphous structure of SHA with a very low T_g of around -4 ℃. In addition to the prominent property of pressure sensitive adhesives (PSAs), the SHA is optically transparent with a low haze of less than 1 %, which enables it to be exploited as a platform of flexible and foldable displays. Overall, the SHA would open up a new opportunity for the application of stretchable electronics, biomedical sensors, shock absorbing materials, and special adhesives that is applicable to a safety laminated glass in automobile industry.

Chapter 3

Stretchable and Self-healable Sensors based on Ultra-fast Self-healing Adhesives (SHAs) via Dynamic Coordination bonds

3.1 Introduction

In recent years there has been intense research into self-healing materials, which exhibit repeatable mechanical and electrical healing ability at the same damage location, much like human skin. Electronic skins are mimicking the innate nature of human skin that is soft, compliant, and self-repaired when damaged so that these great efforts enable to develop wearable devices. For practical use, wearable strain sensors for applications in medical diagnosis [96], healthcare [97-98], prosthetics [99], smart bandage [100], and robotics [101-102] have been widely studied. A human skin-like biomimetic sensor should demonstrate electromechanical sensing and repeatable self-healing capabilities with the fulfillment of natural bending and stretching motions. Furthermore, this stretchable sensor should be directly mounted onto human skin in order to monitor physiological signals and body motions without any delamination even from wet skins while continuously sensing the external stimuli. However, it is still challenging to develop repeatable skin attachable/detachable strain sensors with a good compatibility to

the skin as well as a high accuracy even after repeated self-mending. It is known that a variety of stretchable and flexible sensors that are soft and conformable has relied heavily (over 90 %) on a PDMS as the elastomeric substrate [61]. However, the intrinsic shortcomings of PDMS - a low stretchability (< 200 % strain), poor adhesion to human skins without self-healing ability after mechanically damaged – limit its potential use in wearable sensors. Furthermore, other materials involving polyurethane, ecoflex, and synthetic rubbers other than PDMS are likely to exploit organic solvent such as toluene that restricts to eco-friendly and safely skin attachable applications. Although the sensor was fabricated by biocompatible hydrogels comprised of biopolymers or non-toxic materials, additional elastomers such as PDMS and/or commercial tapes involving 3M-VHB has been required for wearable sensors [103, 156-158].

In this present work, skin-inspired strain sensors based on self-healing adhesive (SHA) that can accurately sense the deformation variations and repeatedly self-repair at the same damaged location are demonstrated. We have studied the effect of activation energy via dehumidifying process on ultra-fast (< 10 sec) and spontaneous self-healing ability of SHA, thus enabling the preparation of stretchable and skin attachable material for potential use in electronic skin. These features of SHA result from diminishing the density of metal-water complexes inhibiting the formation of metal-polymer ligand complexes that are directly contributing to self-healing efficiency. The zinc-PVA complexes impart an electrically conductive property to SHA which is mechanically flexible and is capable of sensing the strain variations even after repeated self-healing. Moreover, we demonstrate the pressure sensitive adhesive (PSA) property of SHA to

undergo skin-attachable sensors with no use of any additional adhesives and commercial tapes.

3.2 Experimental Methods

In the present work, stretchable strain sensors were fabricated by the self-healing adhesive (SHA) based on Zn-PVA complexes, which were basically obtained by a freezing-thawing method. First, 10 g of PVA (Sigma-Aldrich, M_w ~ 89,000 g/mol, >99% hydrolysis) was dissolved in the deionized water of 100 ml while vigorously stirring it with a magnetic bar at 90 ℃ for 1 hour and then the mixed solution was cooled to room temperature. For metal-ligand complexation, zinc nitrate hexahydrate, $Zn(NO_3)_2 \cdot 6H_2O$, was chosen as the Zn^{2+} source due to its good solubility with water as well as thermal stability in the solid state. Zinc nitrate hexahydrate (Sigma-Aldrich, purum p.a., crystallized >99% grade, M_w ~ 297.49 g/mol) was added into 10 wt% PVA solution prepared with molar ratios (N_{PVA}:N_{Zn}) of 10:1, 10:1.5, 10:2, 10:2.5, and 10:3 followed by additional mixing using a magnetic bar at 25 ℃ for 1 hour. Then each of these as-prepared homogeneous aqueous solutions were poured into a polycarbonate petri-dish of desired dimension and then frozen in a refrigerator at −15 °C for 24 hours. Next, the fully frozen samples were thawed out at room temperature for 3 hours. This freezing-thawing process was repeated to three cycles, resulting in the formation of Zn-PVA complexed hydrogels. Likewise, we have put the prepared samples into a desiccator to remove residual water existing within Zn-PVA complexes. The observed humidity and temperature inside the desiccator were 17 ± 2 %RH and 22 ± 1 ℃, respectively. These

dehumidified samples were prepared to analyze the electrically conducting properties based on the percolation model. Finally, the sensing performance of the prepared SHA film as a stretchable strain sensor was evaluated in response to tensile strain. We also fabricated the composite-type strain sensors based on SHA associated with silver nanowires (AgNWs) as a conducting material in order to enhance the sensitivity as well as gauge factor of sensors as prepared.

3.3 Results and discussion

3.3.1 Electrically conductive properties of SHA

Figure 3.1 demonstrates both electrically conductive property and adhesive strength of a SHA in terms of a molar fraction of Zn^{2+} to PVA as a ligand. All SHA samples were fabricated by undergoing 3 cycles of the freezing-thawing process followed by a dehumidification process in the desiccator set to 22 ℃ and 17 %RH for 72 hours. The SHA is a kind of ionomer indicating the electrical conductivity that can be attributed to an ionic crosslinking network mediated by metal-ligand interactions. It is deduced that the electrically conductive property and the adhesive property in the SHA may be originated from the same reason. This hypothesis could be confirmed by the comparison of two properties by fitting the corresponding data with the same theory. As seen in Figure 3.1, both the adhesive strength (black circles) and the inverse of electrical resistance (red circles) are in good agreement with the fitting model (black and red solid lines) based on the percolation theory which can be expressed as the following:

$$P = P_0(f - f_c)^r \qquad \text{(Eq. 19)}$$

where P is an arbitrary property such as an adhesive strength (σ_A) and an inverse of electrical resistance ($1/R$) of SHA, P_0 is the maximum value of an aforementioned arbitrary properties of SHA, f is the molar fraction of zinc to PVA, f_c is the percolation threshold, and r is a critical exponent. Six samples for each of the molar fraction (total 36

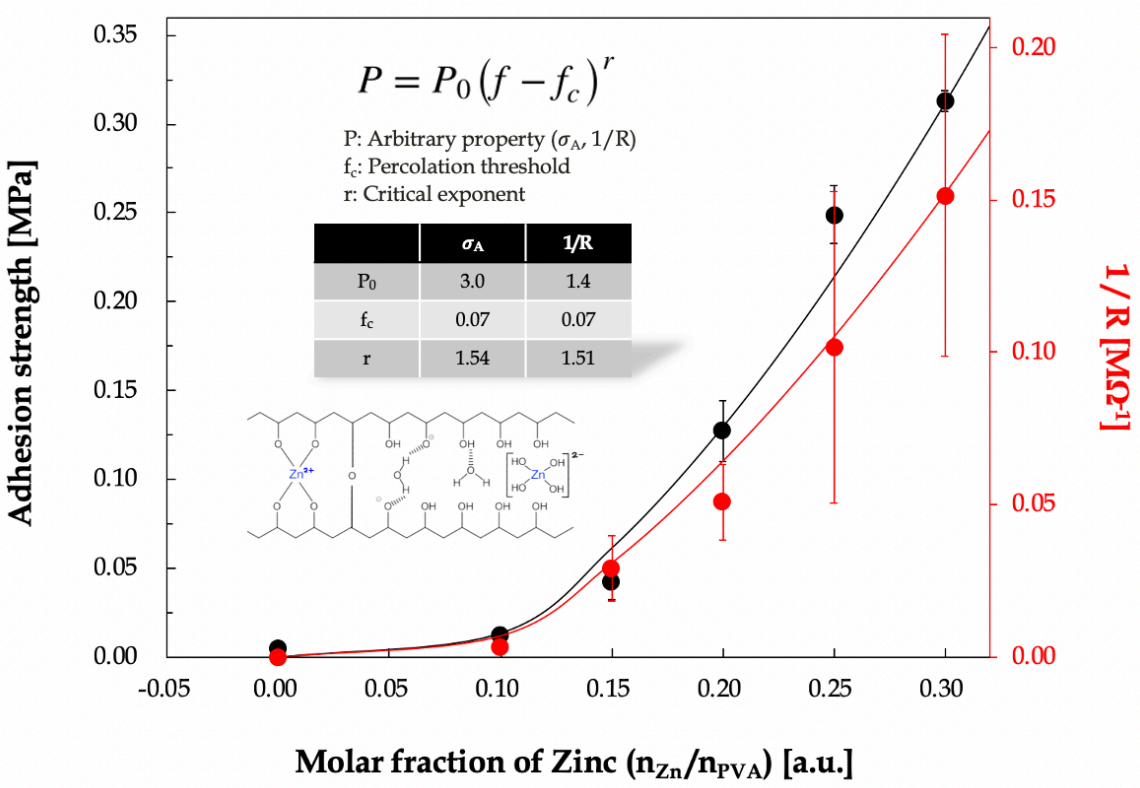

Figure 3.1 Electrically conductive property and adhesive strength of the self-healing adhesive (SHA) as an ionomer based on the metal-ligand coordination bond and the percolation model shown inset and the solid lines which are in good agreement with the measure data (circles).

samples) were measured, and the average inverse resistance are plotted with error bars (standard deviation), as shown in Figure 3.1. When f equals 0.3, the inverse resistance reached 0.15 Ω^{-1}, making the SHA suitable for use in piezoresistive sensors. The trend of an increase in inverse resistance with an increase in molar fraction agrees well with the percolation theory [104], which describes an exponential increase in conducting property above the percolation threshold, as displayed in Figure 3.1.

The percolation threshold is found to be 0.07, the same value for both properties, as shown in the inset table of Figure 3.1. Below the percolation threshold, the conducting property is considerably lower, which also agrees with the percolation theory. This electrically conductive property of SHA without any conductive additives such as CNT and metallic nanowires can be attributed to cation transport due to the presence of zinc ions. In the field of solid polymer electrolytes, the high cationic conductivity requires polymer networks via the crosslinking of mobile chains, which are easily dissociated by metallic ions, as shown in Figure 3.2 [105]. Composite materials comprised of metallic ions and polymers which has amorphous structures and high chain mobility with a low T_g could form transient complexations, which facilitates a reversible association and dissociation of metal ions between ligands.

The cation transport within the SHA can be described as the motion of zinc ions between complexation sites assisted by the segmental motion of the amorphous polymer matrix which is liquid-like. As previously discussed, some experimental data based on XRD, FT-IR, and DSC provide an evidence that the SHA has the amorphous structure with a low T_g. Therefore, the origin of electrically conductive property observed in the SHA which has a high chain mobility can be explained by the cation jumping that easily

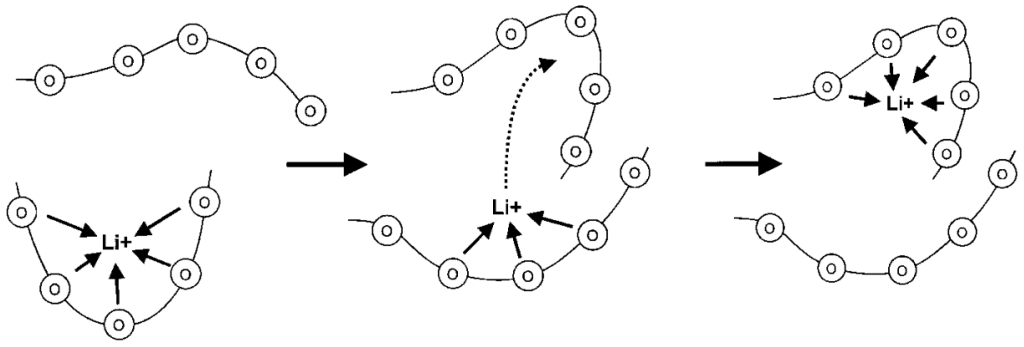

Figure 3.2 Schematic illustration of the cation transport based on segmental motions of Li^+-PEO complexes. The cation transport is described as the motion of the Li^+ species between complexation sites assisted by the segmental motion of the PEO matrix [105].

occurs in the amorphous polymers. In the composition of SHA, zinc nitrate hexahydrate is being used as a source of metallic ions for the coordination bonds. At this point, the anion such as nitrate ion (NO_3^-) could be taken account into a major carrier for ionic conduction. However, it is known that most anions are not strongly solvated by the polymer host due to the repulsion of negative charges [106].

On the other hand, cations could participate in the formation of transient coordination bond which evolves freely, as a single linkage such as $M^+\cdots B$ (M^+ = metal ion, B = Lewis base site on polymer) is changed at a time. As a consequence, the cation jumping corresponds to a transient ligand exchange process from one ligand to the other by forming a new metal-ligand complex. T. Grotthuss described that the charge is not transported by the movement of particles but by breaking and reformation of bonds in his publication [107]. S. Neyertz et al. carried out a molecular dynamic simulation on the cationic jumping between neighboring sites on the amorphous PEO chain, as seen in Figure 3.3 [108]. Based on their modeling, anions and oxygen atoms on the polymer

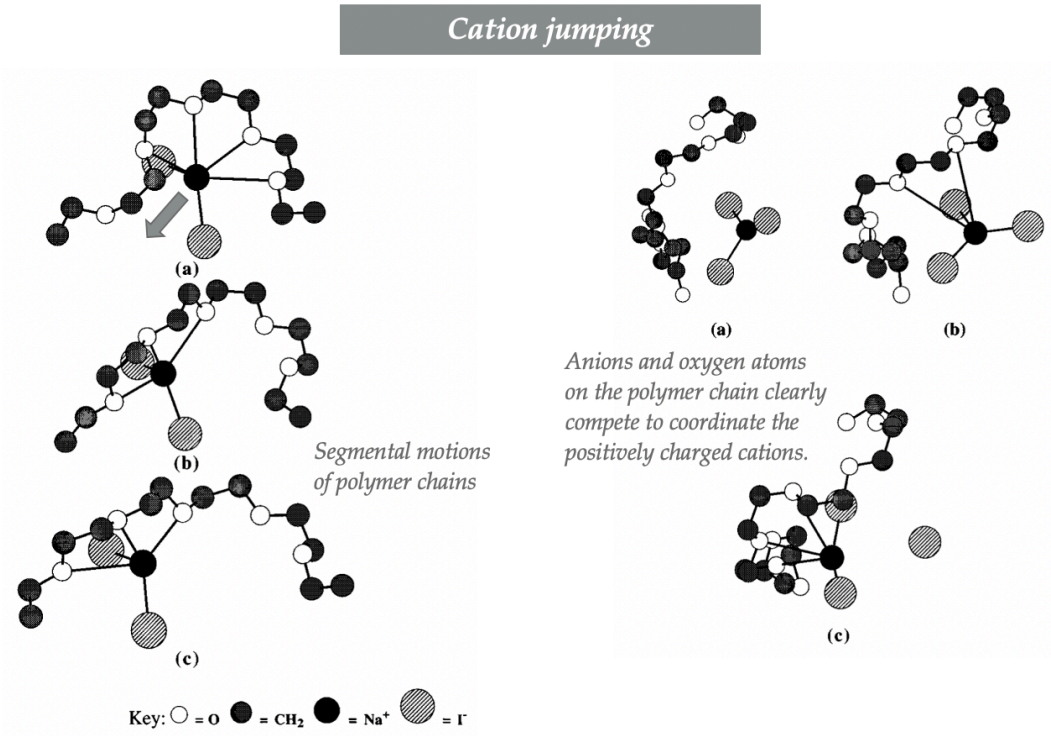

Figure 3.3 Schematic representations of the cation jumping model based on molecular dynamic simulation of PEO-Na^+I^- complexes. The cation (Na^+) transfers via the ligand exchange process that is described as the motion of the Na^+ species between neighboring complexation sites on the amorphous PEO chain with a high mobility [108].

chain clearly compete to coordinate the positively charged cations. The segmental motion of amorphous polymer chains assists the cation transfer via forming new bonding between metal ion and polymer ligand as a transient coordination.

More interestingly, the tendency of an increase in adhesive strength versus a molar fraction of zinc ions to PVA is consistent with the percolation theory as well. Furthermore, the parameters such as percolation threshold and critical exponent indicate the similar values for both adhesive strength and inverse resistance, as shown in the inset table of Figure 3.1. The percolation threshold for both properties has a value of 0.07, and

the critical exponent of adhesive strength and inverse resistance are 1.54 and 1.51, respectively. Therefore, it is noted that the basic mechanism of both adhesive strength and electrically conducting property have been originated from the transient coordination bond that can be attributed to the high chain mobility and the cation jumping.

3.3.2 Stretchable and self-healable strain sensors based on SHA

On the basis of the merits of the SHA, it has great potential in flexible and stretchable electronics. We demonstrate herein a wearable strain sensor based on the SHA acting as a sensing material and stretchable substrate simultaneously. Figure 3.4 shows that the resistance change as a response for tensile strain applied to strain sensor made of SHA in terms of time. The high sensitivity and fast response of SHA-based sensor without any conducting additives were demonstrated by a tensile loading and unloading cycle. The resistance response of the sensor installed on the stretchable actuator being connected with real-time measuring equipment by electrical wires has been evaluated, as shown in the inset of Figure 3.4. The resistance gradually increases with an increase in tensile strain from 0 to 500 %, indicating that the electrical conducting property of SHA as a sensing material is strongly affected by the mechanical deformation, as presented in Figure 3.4. More importantly, the resistance signals tend to immediately rise up and fall back when the strain sensor is loaded and unloaded to certain elongation, thus yielding the ultra-fast response capability.

The sensing responses observed in Figure 3.4 are calculated into a relative resistance change that is defined as the sensitivity as the following:

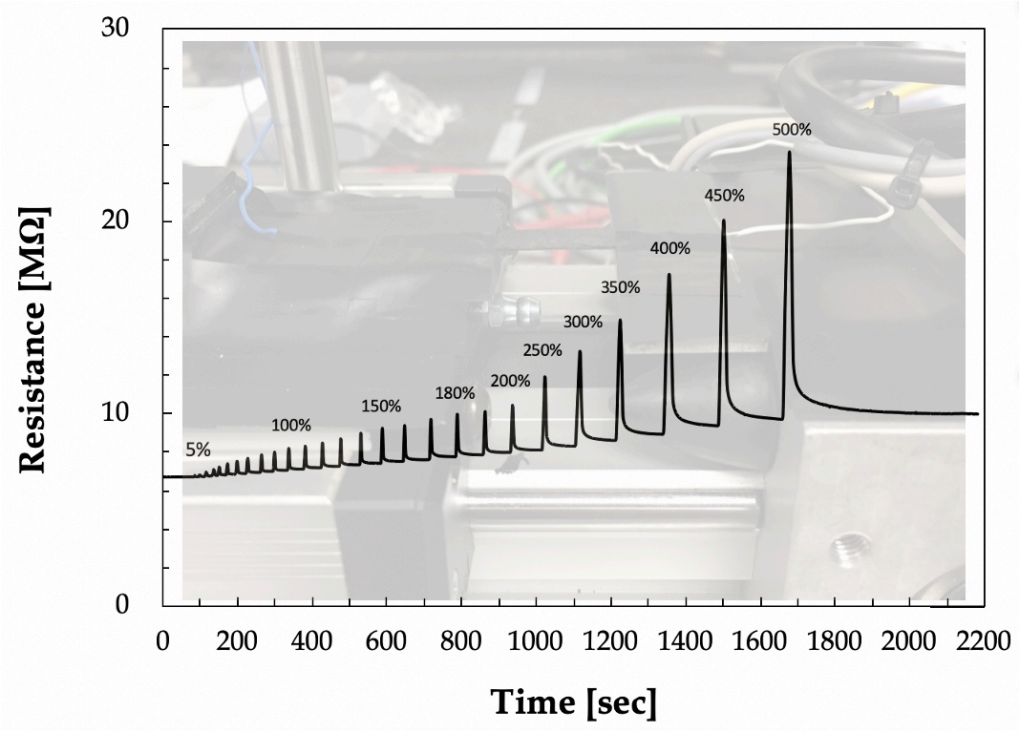

Figure 3.4 Real-time resistance change in response to tensile strains imposed to strain sensor made of SHA without any conducting additives. The resistance gradually increases with an increase in tensile strain from 0 to 500 %. The SHA-based strain sensor is installed on the stretchable actuator being connected with real-time measuring equipment through electrical wires, as shown in the inset of Figure 3.4.

$$\frac{\Delta R}{R_0} = \frac{(R - R_0)}{R_0} \times 100\ [\%] \qquad \text{(Eq. 20)}$$

where R and R_0 are the resistance of stretched SHA-sensor and original one, respectively. Figure 3.5 represents the sensitivity of SHA-based strain sensor without any conductive fillers with respect to tensile strain from 0 to 500 %. As shown in Figure 3.5, the sensitivity of SHA sensor significantly increases with an increase in strain. The increasing tendency for sensitivity of SHA sensor could be interpreted with the following two hypotheses: First, SHA as a novel sensing material has been fabricated by

undergoing 3 cycles of the freezing-thawing process followed by a dehumidification process in the desiccator set to 22 ℃ and 17 %RH for 72 hours. The microscopic image inset with Figure 3.5 exhibits a micro-porous structure with 3D interconnected networks. The hierarchically porous network inside the SHA is beneficial to the ionic transport contributing to the electrically conducting property of hydrogel-like films [109]. The hierarchically porous network within SHA is likely to act as the pathway of ionic transport, exhibiting a prompt elongation and fast recovery toward strain changes. Therefore, this porous microstructure for ion transport could be elongated with the stretching of SHA, thus resulting in the growth of resistance [110, 163].

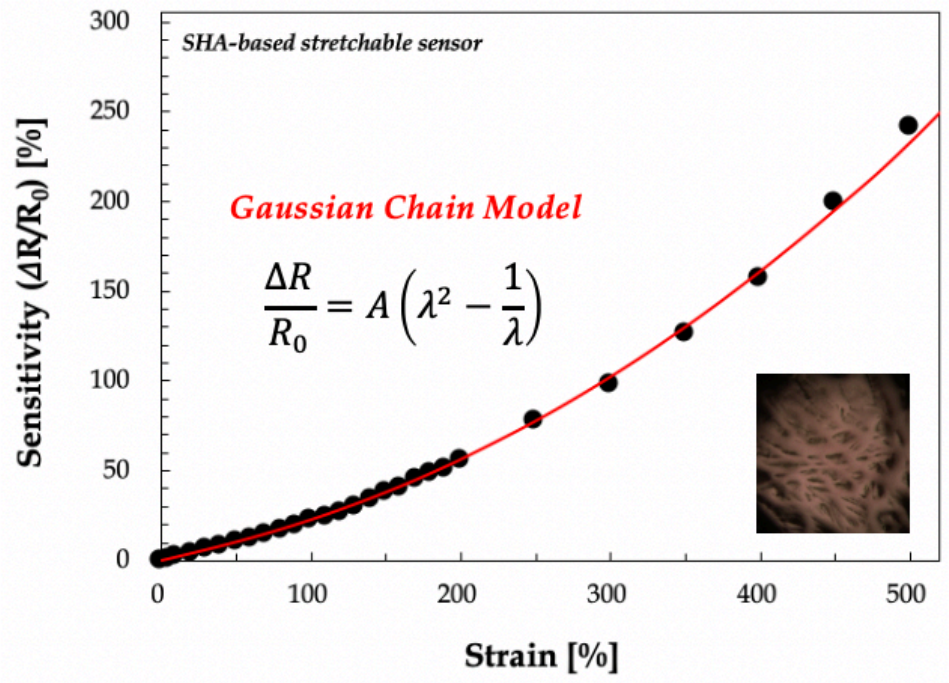

Figure 3.5 Measured sensitivity (black circles) which is in accordance with the true stress corresponding to the right side of the equation which describes the Gaussian chain configuration (red solid line) shown in the inset of Figure 3.5. The segmental motion of the Gaussian chain resulting from the intrinsically amorphous structure of SHA affects the sensing performances involving high sensitivity and prompt response.

Second, the sensitivity of SHA-based sensor could be affected by the Gaussian chain behavior that can be attributed to the intrinsically amorphous structure of SHA. A true stress (σ_t) to elongate the Gaussian chain as crosslinked networks can be expressed by the following:

$$\sigma_t = \frac{\eta}{V} kT \left(\lambda^2 - \frac{1}{\lambda}\right) \quad \text{(Eq. 21)}$$

where σ_t is the true stress applied to extend the Gaussian chain, k is the Boltzmann's constant, T is the absolute temperature, η is the total number of elastically effective strands, V is the total volume of sample, and λ is the draw ratio. (More specific details for the derivation of (Eq. 21) are introduced in the *Appendix A*.) As shown in Figure 3.5, the measured sensitivity in terms of tensile strain is in agreement with the true stress (σ_t) to stretch the Gaussian chain by satisfying the following relation:

$$\frac{\Delta R}{R_0} = A\left(\lambda^2 - \frac{1}{\lambda}\right) \quad \text{(Eq. 22)}$$

where A is a fitting constant. As exhibited in Figure 3.5, the measured sensitivity data (black circles) are in accordance with the true stress derived from the Gaussian chain model (red solid line). As early discussed, SHA is composed of amorphous structure that is attested by some of the previous data including XRD, FT-IR, and DSC. It is known that cation jumping could readily take place within amorphous polymer ligands, as illustrated in Figure 3.2 and Figure 3.3. The cation such as zinc ion in the SHA participate in the local coordination bonds which evolve steadily so that they would jump

via ligand exchanging process by repeating to break and reform the coordination bonds. For this reason, SHA represents electrically conductive property induced by the facile ionic transport, thereby enabling SHA to be exploited as a sensing material. The Gaussian chain shows that the probability of end-to-end vector is the most probable at the peak which end-to-end distance is zero, that is, the random walk returns to the origin. As shown in Figure 3.5, the measured sensitivity in terms of strain is in consistent with the true stress (σ_t) to stretch the Gaussian chain, thus resulting in the amorphous chain configurations of SHA even after stretching a chain with true stress. As a result, the segmental motion of SHA caused by its intrinsic amorphous structure not only enhances the cation transport but also enables to develop strain sensors exhibiting high strain sensitivity as well as the fast response.

Figure 3.6 demonstrates that the real-time resistance change of SHA-based strain sensor during stretching-recovering-cutting-healing cycles in order to investigate the self-healing ability of sensor. The same location of sensor is cut and brought two separated parts for self-mending at room temperature without any interventions. The sensor is healed for about 0.5-2 minutes and then stretched out under 200 % strain followed by getting back to the original state of 0 % strain. As exhibited in Figure 3.6A, the resistance is not measured due to the infinite range when the strain sensor is cut in half, forming open circuit, and then gets recovered quickly through the reformation of dynamic bonds once the two parts get in contact. The healed sensor still shows a stable sensing performance during stretching at 200 % strain. After eight stretching-recovering-cutting-healing cycles, the average sensitivity is 55.6 % at 200 % strain and the variation of

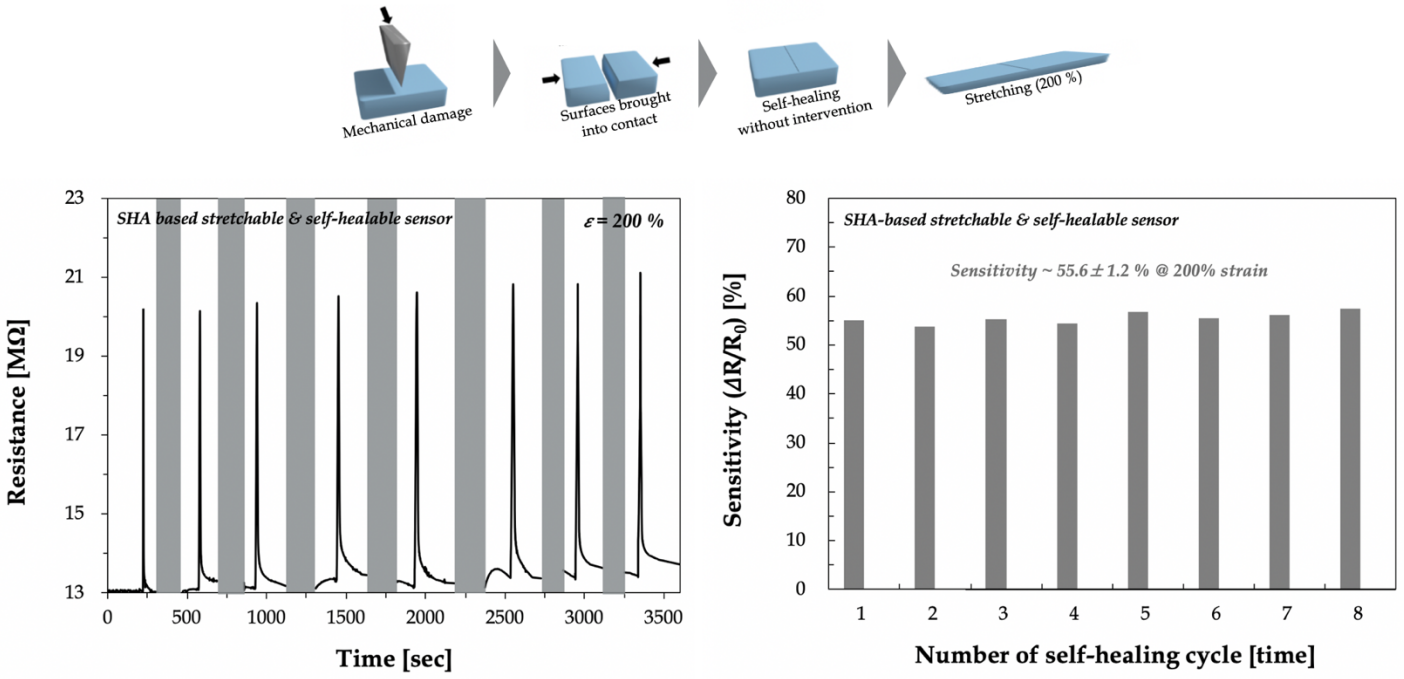

Figure 3.6 Real-time resistance change of SHA-based strain sensor during multiple stretching-releasing-cutting-healing cycles in order to investigate the self-healing ability of sensor. Figure 3.6A indicates that the resistance is recovered quickly through the reformation of dynamic bonds after healing and healed sensor shows a stable and repeatable sensing performance during stretching at 200 % strain. After eight stretching-releasing-cutting-healing cycles, the sensitivity is 55.6 ±1.2 % at 200 % strain that maintains at a stable state, as seen in Figure 3.6B.

sensitivity is less than 2 % which maintains at a stable state, as seen in Figure 3.6B. This excellent self-healing of sensing ability is determined by the presence of dynamic bonds within the polymer which enables the re-association of the coordination bonds at room temperature by allowing zinc ions to be closely packed at the healing interface under gentle contact pressures. Therefore, SHA-based strain sensor shows a repeatable and excellent self-healing property.

Figure 3.7 shows an application of wearable strain sensor which is fixed on the joint of index finger in order to monitor joint motions. Due to a good adhesion of SHA to skin, any commercially available conductive tapes or adhesives were not used excepting for both ends of sensor to fix the electrical wires connected with real-time measurement system. When the bending degree of index finger changed from 0° to 120° and vice versa during consecutive bending-holding cycles, the resistance of SHA sensor has been promptly changed in response to the movements of the finger. As shown in Figure 3.7, the variations of resistance in the sensor exhibit practically similar peaks and shapes against the bending angles in real time, thereby resulting in the reliable sensors displaying a stable sensing signal.

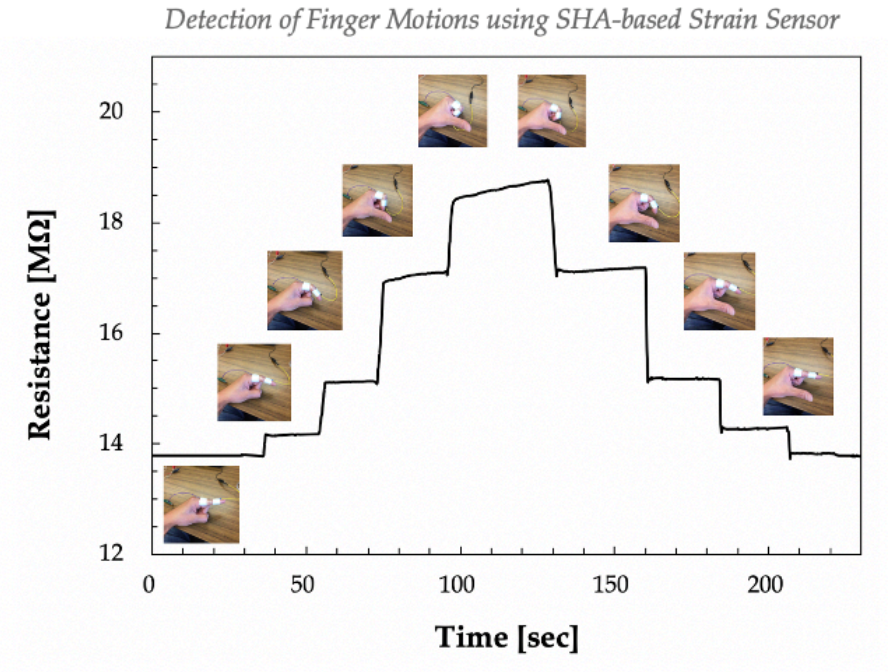

Figure 3.7 Application of SHA-based wearable strain sensor which is fixed on the joint of index finger in order to monitor joint motions. When the bending degree of index finger changed from 0° to 120° and vice versa during consecutive bending-holding cycles, the resistance of SHA-based sensor has been promptly changed in response to the movements of the finger.

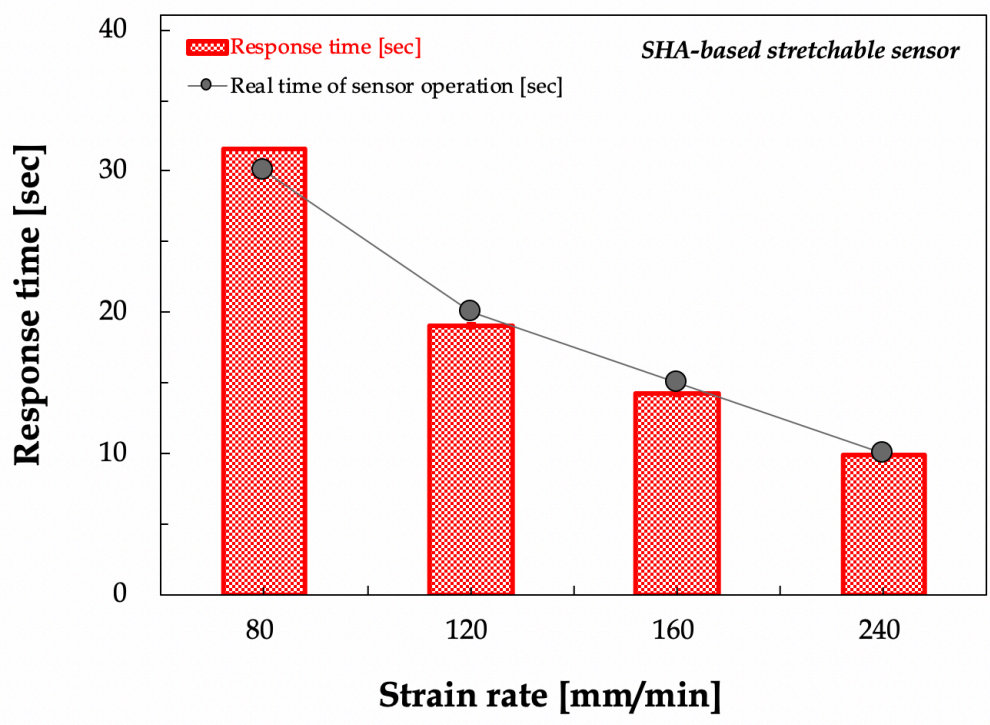

Figure 3.8 Comparison of the response time extracted from the experimental data of resistance change with the measured real operation time by a stopwatch during the test. The SHA-based strain sensor is elongated at 200 % strain followed by the recovery to the original state, and then both response time and real operation time in terms of strain rate (80, 120, 160, and 240 mm/min) have been evaluated. The response times (red boxes) obtained from the data are in consistent with the actually counted time (black circles) during a stretching-releasing process for all strain rates, as seen in Figure 3.8.

We have also studied the actual response time of SHA-based sensor for a real application of strain sensor. In order to evaluate the accuracy of data on the sensing performance of sensor, the response time displayed by data shown in Figure 3.4 should be in accordance with the actual time measured during the sensing experiment. The response time at a resistance peak in response to strain change is defined by a time taken from start point to end point of a peak during stretching-recovering process. The actual time has been counted during the test with a cycle of elongation and restoration as well.

Figure 3.8 displays the comparison of the response time extracted from data of the resistance peak as a sensing signal with the actually measured time during the test. The SHA sensor is elongated at 200 % strain followed by the recovery to the original state, and then both response time and real time in terms of strain rate (80, 120, 160, and 240 mm/min) have been evaluated. The response times (red boxes) obtained from the data are in consistent with the actually counted time (black circles) during a stretching-recovering process for all strain rates, as seen in Figure 3.8. Therefore, the sensing performance of SHA-based strain sensor has been accurately evaluated by our experimental setup. As a consequence, the reliability and stability of SHA sensor could be originated to a promptly responsive ability against strain changes.

Figure 3.9 demonstrates the real-time resistance change of SHA-based strain sensor when elongated at 200 % strain with various strain rates of 80, 120, 160, and 240 mm/min. As displayed in Figure 3.9A, the resistance peak becomes much sharper as the strain rate increases, i.e., the SHA strain sensor exhibits a fast response at a high strain rate. Furthermore, the sensitivity linearly increases with an increase in strain rate representing the following relation:

$$\frac{\Delta R}{R_0} = m\dot{\varepsilon} + n \qquad \text{(Eq. 23)}$$

where $\dot{\varepsilon}$ is the strain rate, a and b are the slope and y-intercept in the plot of sensitivity versus strain rate. This tendency might be related to the viscoelastic property of SHA. As displayed in Figure 3.4, a slight increase in resistance after stretching-

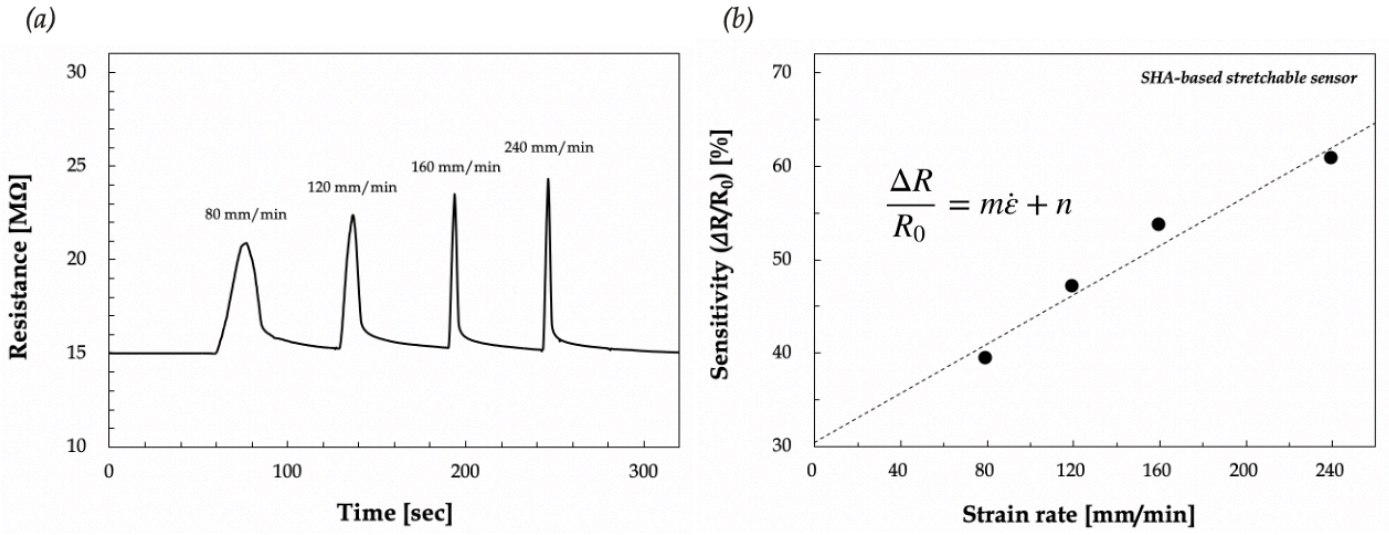

Figure 3.9 Real-time resistance change of SHA-based strain sensor when elongated at 200 % strain and released to the original state with respect to different strain rates of 80, 120, 160, and 240 mm/min. As shown in Figure 3.9A, the resistance peak becomes sharper as the strain rate increases, that is, the SHA-based strain sensor exhibits a fast response at a high strain rate. The sensitivity linearly increases with a strain rate due to a fast recovery with a little time delay at a high strain rate.

releasing cycles was observed. This increase can be explained by the viscoelastic characteristics of SHA, which slightly increases the conduction path distance due to the loss of elastic energy. Such a hysteresis induces a time delay which the deformation is not immediately recovered during releasing process. The sensor working at low strain rate region might be affected by the hysteresis due to the innate viscoelastic property, on the other hand, the recovery at high strain rate regime is rapid with no time-lag. The SHA has shown the behavior of Gaussian chain configurations that act as Hooke's spring, as seen in Figure 3.5. Therefore, the elastic behavior of SHA could be more dominant than the viscoelastic property at high strain rate regime.

3.3.3 Stretchable and self-healable composite (SHA/AgNW) sensors

The most significant function of strain sensors is to generate repeatable electrical changes upon mechanical deformations. In this aspect, the sensitivity can be a good measure of evaluating performances of strain sensors. The gauge factor (GF) that means the ratio of sensitivity to mechanical strain has been used at times as the following expression:

$$GF = \frac{\Delta R/R_0}{\varepsilon} \quad \text{(Eq. 24)}$$

where $\Delta R/R_0$ is relative resistance change, R_0 is the resistance at 0% strain, R is the resistance under stretching, and ε is the applied strain. Usually, the metallic materials have a higher gauge factor. However, these materials indicate small stretchability less than 5 % [111]. To date, some representative strain sensors using carbon nanotubes, semiconducting materials, metallic nanowires, graphene, and conducting polymers as conductive materials associated with elastomeric substrates have been investigated. Although these nanoscale material-embedded strain sensors exhibit higher gauge factors [112-114], shortcomings including low stretchability and lack of self-healing ability still limit their applications in robotics, health monitors, and medical diagnosis, etc.

Although the gauge factor of SHA-based strain sensor is lower than of conventional metal-based strain sensors, it is still higher than 0.35 at 700 % strain for Ionic conductive ink (NaCl+glycerol+PEG)/Silicone-based capacitive strain sensor [154] and 0.06 at 200 % strain for SWCNT/PDMS-based piezoresistive strain sensor [133],

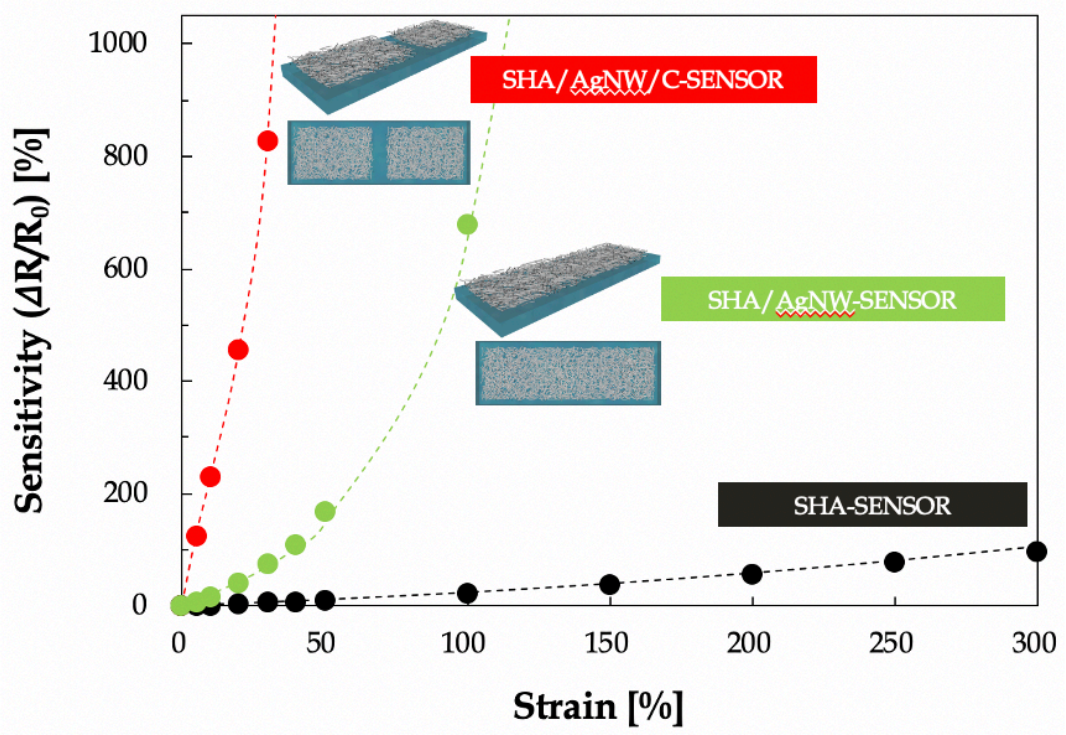

Figure 3.10 Measured sensitivity versus tensile strain for three types of strain sensors: SHA-SENSOR which is made of SHA without any electronic conducting component; SHA/AgNW-SENSOR using AgNWs deposited on the top surface of SHA; and SHA/AgNW/C-SENSOR having the same structure as SHA/AgNW-SENSOR excepting for the formation of crack in AgNW layer deposited on the SHA surface. The sensitivity of SHA/AgNW-SENSOR at 5 % strain is 6.2 % that is nearly six times higher than that of SHA-SENSOR. Likewise, SHA/AgNW/C-SENSOR shows two orders of magnitude higher sensitivity (125.3 %) than that of SHA-SENSOR at 5 % strain. With the addition of metallic nanowires and the formation of crack, the sensitivity could be dramatically enhanced, as seen in Figure 3.10.

otherwise it is comparative to 0.23 at 100 % strain for κ-carrageenan/PAAm hydrogel-based piezoresistive strain sensor [158].

We herein demonstrate the self-healing piezoresistive strain sensor with a high gauge factor using SHA associated with AgNWs as an additional conducting substance, as shown in Figure 3.10. Furthermore, we have simultaneously designed and fabricated

the ultrahigh sensitive strain sensor by forming a 200 μm wide crack located in the center of AgNW-layer on the SHA, as seen in the inset of Figure 3.10. These approaches may serve as a versatile method to increase the gauge factor dramatically without any complicated processes. The sensitivity versus tensile strain for three types of strain sensors: SHA-SENSOR which is made of SHA without any electronic conducting component (AgNWs); SHA/AgNW-SENSOR by using AgNWs deposited on the top surface of SHA; and SHA/AgNW/C-SENSOR having the same structure as SHA/AgNW-SENSOR excepting for the formation of crack in AgNW layer deposited on the SHA surface have been evaluated, as shown in Figure 3.10. The sensitivity for all sensors increases with increasing tensile strain. The sensitivity of 6.2 % for SHA/AgNW-SENSOR (green circles) measured under 5 % strain is nearly six times higher than that of SHA-SENSOR (black circles). More interestingly, SHA/AgNW/C-SENSOR (red circles) shows two orders of magnitude higher sensitivity (125.3 %) than that of SHA-SENSOR at 5 % strain. These gaps of sensitivity among sensors become larger with an increase in the tensile strain. These results reflect that the SHA/AgNW-SENSOR and/or SHA/AgNW/C-SENSOR could work well from small strain to extreme strain.

The electrical conductivity of SHA-SENSOR comes from ion conductivity as early discussed. However, in case of the SHA/AgNW-SENSOR, the AgNW-layer formed on the SHA enables generation of percolative pathways, exhibiting much larger piezoresistive variations than that of pristine SHA itself under stretching-releasing cycles. The rearrangement of AgNWs as well as the loss of contact between AgNWs could be readily occurred during the elongation of sensors including the AgNW-layer. More specifically, SHA/AgNW/C-SENSOR generates additional resistance changes due to the

presence of crack making the AgNW layer two independently discrete AgNW-clusters being apart from each other, thus yielding an extremely high resistance change upon stretching. Therefore, the total resistance change in SHA/AgNW/C-SENSOR arises from the summation of resistance changes in intrinsic SHA, alignment of individual AgNWs, and crack effect resulting in the spatial variations between the separated AgNW-clusters. It is known that nano- or micro-cracks formed in metallic layer such as platinum deposited on the elastic polyurethane substrate can enhance the sensitivity of strain sensors [115]. Therefore, the sensitivity of SHA/AgNW/C-SENSOR is higher than those of SHA-SENSOR and SHA/AgNW-SENSOR, which is consistent with the experimental data shown in Figure 3.10.

Figure 3.11 shows that the real-time resistance change as a response for tensile strain applied to SHA/AgNW/C-SENSOR. The sensor displays an ultra-high sensitivity and rapid response were during the tensile loading and unloading cycles. The resistance signals tend to immediately rise up and fall back when the strain sensor is loaded and unloaded to certain elongation, thus yielding the super-fast response. More importantly, the hysteresis observed in SHA-SENSOR during the stretching-releasing test decreases dramatically. Although such a SHA typically suffer from a viscoelastic effect as shown in Figure 3.9, which affects the time response to mechanical forces, the addition of AgNWs significantly reduces the viscous modulus. Therefore, the composite type piezoresistive sensors (SHA/AgNW/C-SENSOR) can track mechanical loads without showing significant relaxation times, by responding promptly to various ramped loads exhibited in Figure 3.11.

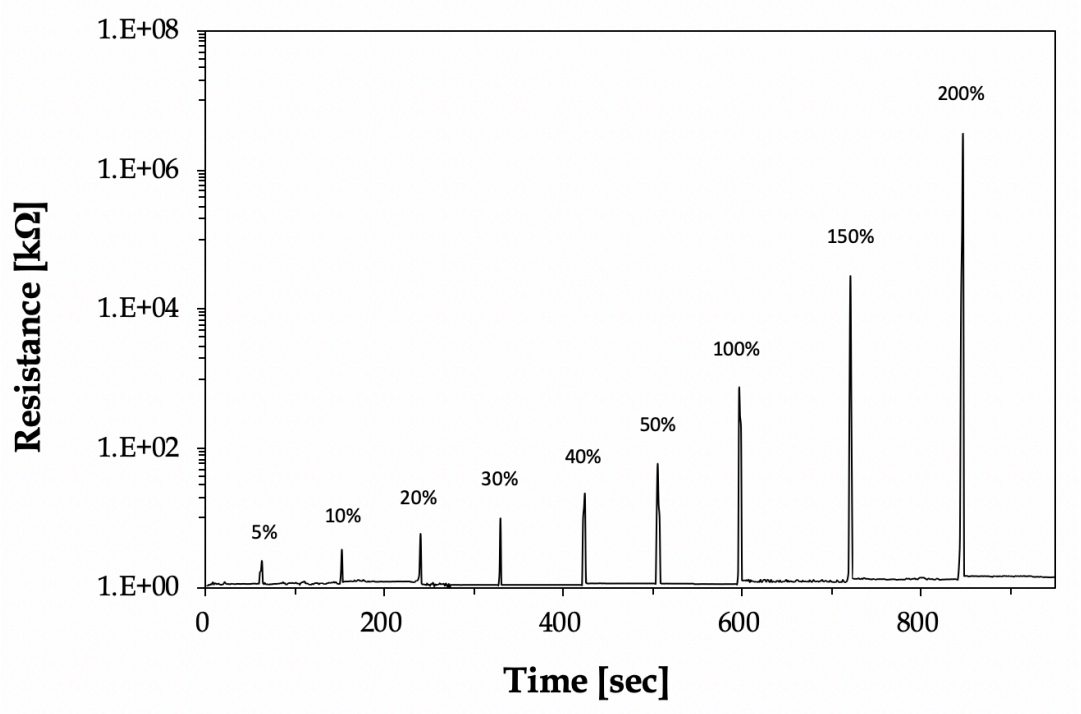

Figure 3.11 Real-time resistance change in response to tensile strains applied to SHA/AgNW/C-SENSOR which shows a very sharp peak indicating high sensitivity and fast response. This composite type piezoresistive sensors can track mechanical loads without any obvious relaxation during stretching-releasing cycles. This is because the addition of AgNWs may reduce the viscous modulus of SHA.

Figure 3.12 demonstrates that the sensitivities of SHA-SENSOR and SHA/AgNW/C-SENSOR could fit into the Gaussian chain model and the modified Gaussian chain model, respectively. As discussed in Figure 3.5, the sensitivity of SHA-SENSOR is affected by the Gaussian chain configurations under stretching due to its intrinsic amorphous structure of SHA. Although the original Gaussian chain model contains a quadratic term for draw ratio (λ^2), we have expressed it into as a generalized form including λ^N as the following:

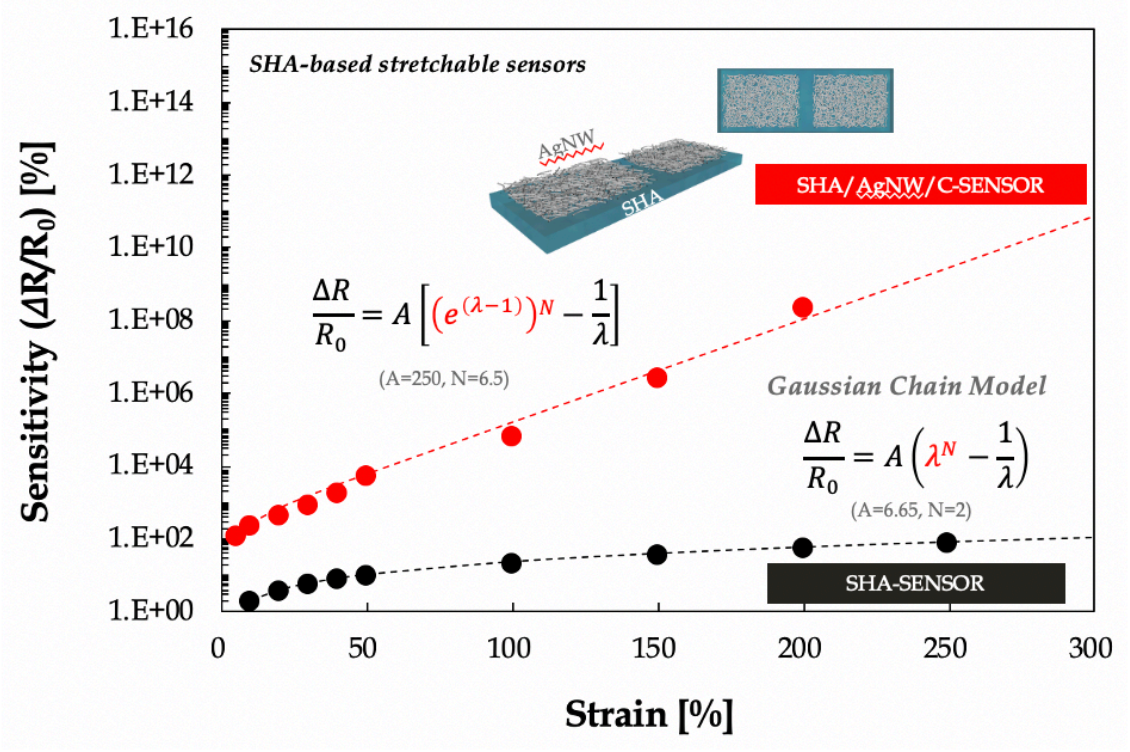

Figure 3.12 Measured sensitivities of SHA-SENSOR and SHA/AgNW/C-SENSOR fitted by the Gaussian chain model and the modified Gaussian chain model, respectively. The plot of sensitivity of SHA/AgNW/C-SENSOR versus tensile strain well fits the modified Gaussian chain model (A=250, N=6.5), as seen in Figure 3.12. An exponential term of draw ratio, $(e^{\lambda-1})^N$, could explain a drastic increase in the sensitivity of SHA/AgNW/C-SENSOR.

$$\frac{\Delta R}{R_0} = A\left(\lambda^N - \frac{1}{\lambda}\right) \qquad \text{(Eq. 25)}$$

where $\Delta R/R_0$ is relative resistance change, R_0 is the resistance at 0% strain, R is the resistance under stretching, λ is the draw ratio, A and N are the fitting parameters. In general, (Eq. 25) represents the typically known Gaussian chain model having the entropy induced chain configurations when N has a value of two. On the other hand, the sensing performance of SHA/AgNW/C-SENSOR is in good accordance with the modified Gaussian chain model that can be expressed by:

$$\frac{\Delta R}{R_0} = A\left[(e^{\lambda-1})^N - \frac{1}{\lambda}\right] \quad \text{(Eq. 26)}$$

The plot of sensitivity of SHA/AgNW/C-SENSOR versus tensile strain well fits the modified Gaussian chain model of (Eq. 26) (A=250, N=6.5), as seen in Figure 3.12. Interestingly, an exponential term of draw ratio, $(e^{\lambda-1})^N$ could explain a drastic increase in the sensitivity of SHA/AgNW/C-SENSOR.

Figure 3.13 and Table 3 represent the comparison of gauge factors for SHA-SENSOR and SHA/AgNW/C-SENSOR with the previously reported strain sensors in terms of stretchability and self-healing ability [116-163]. The blue circles and red circles in Figure 3.13 represent the gauge factors calculated from the measured sensitivity of SHA-SENSOR and SHA/AgNW/C-SENSOR, respectively. References symbolized from S1 to S8 represent the self-healable strain sensors, whereas those from 1 to 40 show strain sensors without self-healing ability. The gauge factor has dramatically improved with an addition of AgNWs to SHA even when compared with the previous reports, as seen in Figure 3.13. We have observed that the SHA sensor without the electronic conducting media can be used to accurately detect large-scale human motions displayed in Figure 3.7. However, we realize a composite type strain sensor, SHA/AgNW/C-SENSOR, which surpasses SHA-SENSOR over an entire range of strain. The large resistance change is prerequisite for strain sensors with a high sensitivity. Therefore, the enhanced piezoresistivity induced by the addition of AgNWs to SHA in conjunction the crack effect results in improving a sensing performance of strain sensors.

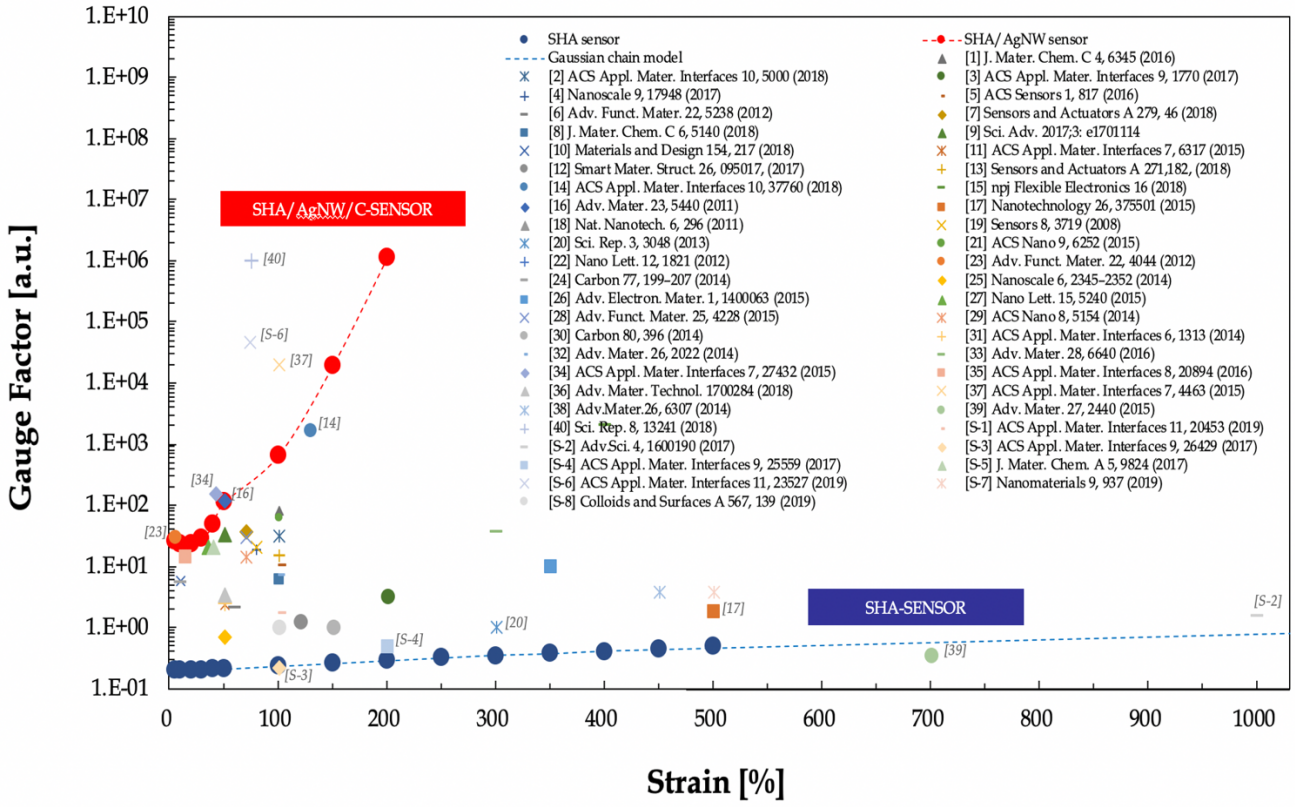

Figure 3.13 Comparison of gauge factors for SHA-SENSOR and SHA/AgNW/C-SENSOR with the previously reported strain sensors in terms of stretchability and self-healing ability. References symbolized from S1 to S8 represent the self-healable strain sensors, whereas those from 1 to 40 show strain sensors without self-healing ability. The enhanced piezoresistivity induced by the addition of AgNWs to SHA in conjunction the crack effect results in improving a sensing performance of strain sensors.

Ref No.	Materials	Strain	Gauge Factor	Bibliography in the thesis
[1]	Graphene/Styrene-butadiene rubber/Natural rubber	***100.0***	***82.50***	[116] *J. Mater. Chem. C* **4**, 6345, 2016
[2]	poly(3-hexylthiophene-2,5-diyl) (P3HT)/AgNW/PDMS	***100.0***	***32.00***	[117] *ACS Appl. Mater. Interfaces* **10**, 5000, 2018
[3]	Ionic liquid (Ethylene glycol+NaCl)/Epoxy	***200.0***	***3.20***	[118] *ACS Appl. Mater. Interfaces* **9**, 1770, 2017
[4]	Fragmented Carbon/Melamine	***80.0***	***18.70***	[119] *Nanoscale* **9**, 17948, 2017
[5]	Long MWCNT/Polycarbonate-urethane	***100.0***	***10.50***	[120] *ACS Sensors* **1**, 817, 2016
[6]	SWCNT/PDMS	***60.0***	***2.08***	[121] *Adv. Funct. Mater.* **22**, 5238, 2012
[7]	Graphite/PDMS	***70.0***	***37.00***	[122] *Sensors and Actuators A* **279**, 46, 2018
[8]	MWCNT/PDMS	***100.0***	***6.00***	[123] *J. Mater. Chem. C* **6**, 5140, 2018
[9]	P3HT-NFs (nanofibrils)/PDMS	***50.0***	***33.00***	[124] *Sci. Adv.* **3**, 701114, 2017
[10]	MWCNT/Ecoflex	***10.0***	***5.62***	[125] *Materials and Design* **154**, 217, 2018
[11]	Graphene nanoplatelets/Nylon	***50.0***	***2.30***	[126] *ACS Appl. Mater. Interfaces* **7**, 6317, 2015
[12]	SWCNT+CB/PDMS	***120.0***	***1.25***	[127] *Smart Mater. Struct.* **26**, 095017, 2017
[13]	Graphene nanoflakes/Adhesive pads	***100.0***	***15.20***	[128] *Sensors and Actuators A.* **271**,182, 2018
[14]	CNT/Ecoflex	***130.0***	***1666.00***	[129] *ACS Appl. Mater. Interfaces* **10**, 37760, 2018
[15]	AgNW+PEDOT:PSS/Ecoflex	***400.0***	***2000.00***	[130] *npj Flexible Electronics* **16**, 2018
[16]	ZnONW/PS	***50.0***	***116.00***	[131] *Adv. Mater.* **23**, 5440, 2011
[17]	CNT/Ecoflex	***500.0***	***1.75***	[132] *Nanotechnology* **26**, 375501, 2015
[18]	SWCNT/PDMS	***200.0***	***0.06***	[133] *Nat. Nanotechnol.* **6**, 296, 2011
[19]	CB/Thermoplastic elastomer	***80.0***	***20.00***	[134] *Sensors* **8**, 3719, 2008
[20]	CNT/PDMS	***300.0***	***1.00***	[135] *Sci. Rep.* **3**, 3048, 2013
[21]	SWCNT+PEDOT:PSS/PU	***100.0***	***62.30***	[136] *ACS Nano* **9**, 6252, 2015
[22]	CNT/Silicone	***100.0***	***0.99***	[137] *Nano Lett.* **12**, 1821, 2012
[23]	CB/PDMS	***5.0***	***29.00***	[138] *Adv. Funct. Mater.* **22**, 4044, 2012
[24]	CB/PDMS	***10.0***	***5.50***	[139] *Carbon* **77**, 199, 2014
[25]	AgNW/PDMS+Ecoflex	***50.0***	***0.70***	[140] *Nanoscale* **6**, 2345, 2014
[26]	AuNW/PDMS	***350.0***	***9.90***	[141] *Adv. Electron. Mater.* **1**, 1400063, 2015
[27]	AgNW/PDMS	***35.0***	***20.00***	[142] *Nano Lett.* **15**, 5240, 2015
[28]	Graphene/PDMS	***70.0***	***29.00***	[143] *Adv. Funct. Mater.* **25**, 4228, 2015
[29]	AgNW/PDMS	***70.0***	***14.00***	[144] *ACS Nano* **8**, 5154, 2014
[30]	CNT/Ecoflex	***150.0***	***1.00***	[145] *Carbon* **80**, 396, 2014
[31]	Polypyrrole/PU	***50.0***	***2.50***	[146] *ACS Appl. Mater. Interfaces* **6**, 1313, 2014
[32]	Graphene/PDMS	***100.0***	***7.10***	[147] *Adv. Mater.* **26**, 2022, 2014
[33]	CB/Silk fabric	***300.0***	***37.50***	[148] *Adv. Mater.* **28,** 6640, 2016
[34]	Graphene oxide/PDMS	***42.7***	***150.00***	[149] *ACS Appl. Mater. Interfaces* **7**, 27432, 2015
[35]	Graphite/Silk fiber	***15.0***	***14.50***	[150] *ACS Appl. Mater. Interfaces* **8**, 20894, 2016
[36]	CB/Ecoflex	***50.0***	***3.37***	[151] *Adv. Mater. Technol.* **3**, 1700284, 2018
[37]	Carbon/PDMS	***100.0***	***20000.00***	[152] *ACS Appl. Mater. Interfaces* **7**, 4463, 2015
[38]	Carbon grease/Ecoflex	***450.0***	***3.80***	[153] *Adv.Mater.* **26**, 6307, 2014
[39]	Ionic conductive ink (NaCl+glycerol+PEG)/Silicone	***700.0***	***0.35***	[154] *Adv. Mater.* **27,** 2440, 2015
[40]	(silver ink patterned silicone elastomer)-(silver plated nylon structure)	***75.0***	***1000000.00***	[155] *Sci. Rep.* **8**, 13241, 2018
[S-1]	poly(2-acrylamido-2-methyl-1-propanesulfonic acid), polyaniline, phytic acid	***100.0***	***1.70***	[156] *ACS Appl. Mater. Interfaces* **11**, 20453, 2019
[S-2]	SWCNT/PVA-Boric acid hydrogel	***1000.0***	***1.51***	[157] *Adv.Sci.* **4**, 1600190, 2017
[S-3]	κ-carrageenan/PAAm DN hydrogel	***100.0***	***0.22***	[158] *ACS Appl. Mater. Interfaces* **9**, 26429, 2017
[S-4]	PVA/PVP/CNC/Fe^{3+} hydrogel	***200.0***	***0.48***	[159] *ACS Appl. Mater. Interfaces* **9**, 25559, 2017
[S-5]	CNT/CNC/Polyethyleneimine/Carboxylated nitrile rubber	***40.0***	***20.00***	[160] *J. Mater. Chem. A.* 5, 9824, 2017
[S-6]	Graphene nanosheets/Gelatin/Fe^{3+}/Epoxidized natural rubber nanocomposite	***73.7***	***45573.10***	[161] *ACS Appl. Mater. Interfaces* **11**, 23527, 2019
[S-7]	Graphene/Cellulose nanofibers/PVA/Boric acid hydrogel	***500.0***	***3.80***	[162] *Nanomaterials* **9**, 937, 2019
[S-8]	Graphene oxide/Polydopamine/PVA/Boric acid hydrogel	***100.0***	***1.00***	[163] *Colloids and Surfaces A.* **567**, 139, 2019

Table 3 Summary of the previously reported stretchable strain sensors in terms of gauge factor [116-163].

Figure 3.14 shows the self-healing property of SHA/AgNW/C-SENSOR implemented by the repetitive cutting-healing processes with eight cycles at the same location on a crack region. The resistance change of the sample is relatively stable during the cycling. The high self-healing efficiency is observed in each cutting-healing process. The sensitivity measured is for the eight self-healing cycles within about 1-2 minutes. The SHA/AgNW/C-SENSOR exhibits an excellent stretchability and a high sensitivity without the loss of self-healing ability as an intrinsic nature of SHA. Therefore, the presence of crack in sensor structure plays a role to enhance the piezoresistivity as well as the self-healing ability of wearable electronic skin.

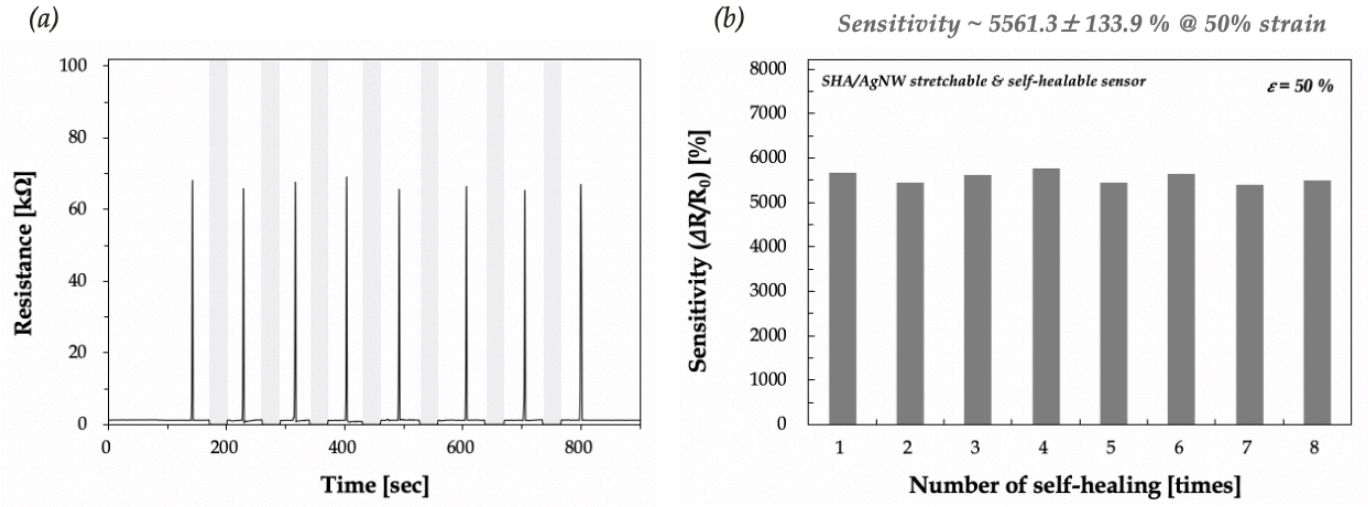

Figure 3.14 Self-healing property of SHA/AgNW/C-SENSOR implemented by the repetitive stretching-releasing-cutting-healing processes with eight cycles at the same location on a crack region. The variation of sensitivity of this composite strain sensor is about 2.4 % after mechanically damaged and healed at room temperature.

3.4 Conclusions

In summary, we demonstrate herein an ultra-stretchable and self-healable strain sensor based on the autonomous self-healing polymer with a dynamic coordination bond. The presented sensor surpasses the performance of previously reported state-of-the-art stretchable strain sensors in terms of stretchability, skin attachability, and self-healing capability. The self-healable and ultra-stretchable sensor can easily be fabricated via the metal-ligand complexed self-healing polymer having an electrically conductive property that endows it with consistent and reliable sensing performance. Furthermore, the self-healing adhesive (SHA) exhibits a repeatable autonomous self-healing ability at room temperature with high self-healing efficiencies and re-bondable adhesion to skin. Because of its intrinsically amorphous structure, the observed sensitivity ($\Delta R/R_0$) is in consistency with the configuration of Gaussian chain in responses to strain. Furthermore, the SHA-based wearable sensor can be attached directly on the skin in order to accurately detect complex human motions. Compared with the previously reported sensors, the composite-type strain sensor comprised of the SHA associated with AgNWs indicates a dramatic improvement of the gauge factor, rendering it to be worked from small strain to extreme strain. Overall, with high stretchability, predictable responses, autonomous self-healing ability, and ease of processing, the applications of SHA-based sensor can be extended to pressure sensing, health monitoring, medical diagnosis, soft robotics, and artificial skin.

Chapter 4

Stretchable Ammonia Vapor Sensors with High Sensitivity and Fast Recovery Based on Plasticized Polymer Electrolytes

4.1 Introduction

4.1.1 Introduction to conventional ammonia sensors and materials

Over the past few decades, the detection of gaseous air pollutants has been extensively studied because of their toxicity and fatality. Ammonia (NH_3) is a colorless flammable gas with a very pungent smell that is commonly used as a compressed gas and in aqueous solutions. It is also used in household cleaning products, in fertilizers, and as a refrigerant [164-165]. The Occupational Safety and Health Administration (OSHA) in the US Department of Labor regulates the level of ammonia in the air and lists a 50 ppm limit in the air, or a 35 ppm limit for an 8-hour work day based on a time weighted average [166]. The inhalation of large quantities of ammonia can cause harmful effects on human health such as eye irritation, pulmonary edema, and respiratory arrest [167]. Exposure to ammonia occurs as a result of accidents during highway and railway transportation, accidental releases at manufacturing facilities in industry, and farming

accidents. However, it is known that the odor detection level just ranges from 5 to 53 ppm due to the limitation of olfactory sense of humans [166]. Therefore, reliable and even inexpensive sensors which can monitor lower concentrations of NH_3 and be operated at room temperature have been required in industry. Recently, robots are being taken into account as an alternative which can replace humans to implement tasks related to a rescue in disaster region. Therefore, a wearable chemical sensor which can be directly attached to robots and human skins is indispensable for next-generation flexible electronics. Recently in Chicago in the US, the accident of NH_3 leaking from a gas tank at a food processing plant occurred. With this accident, five employees were taken to the hospital due to the complaint of breathing problems and even two firefighters who were exposed to vapors during their task for a rescue were transported as well [168]. In another accident that occurred in India in 2015, five people who inhaled large amounts of NH_3 gas that leaked from an NH_3 gas tank were killed [169]. These precedents related to the seriousness of NH_3 exposure inspire to develop flexible NH_3 sensors attachable to robots that could be available to the catastrophe by a gas leak.

To date, a variety of flexible electronic devices with a reliable stretchability and robust durability have been demonstrated. Unprecedented applications in rollable displays, stretchable batteries, and wearable health sensors have allowed technological advances in the field of flexible and wearable electronics. However, the development of stretchable chemical sensors showing a fast response and high sensitivity under deformation has been still challenging.

The traditional sensors for detecting chemical vapor are mostly based on semiconducting materials such as carbon nanotubes (CNTs) and metal oxides. These

materials are based on a transport of carriers involving electrons and holes as a main sensing mechanism. In recent years, CNTs which are among the most interesting classes of nanomaterials have been exploited as a sensing material for chemical sensors due to their good electrical conductivity as well as high surface to volume ratios. In particular, single-walled carbon nanotubes (SWCNTs) as a p-type semiconducting material have been shown to exbibit significant changes in conductance in response to some of the chemical gases [170]. It was also reported that the sensitivity of SWCNT-based chemical sensors can be enhanced by assembling with metals [171], metallic nanoparticles [172], and metallic oxides [173]. This attempt is based on the fundamentals that the π-electrons of SWCNTs tend to have a strong interaction with a different electron configuration of additives. For this reason, the electrical conductivity of SWCNTs could be readily tuned through combining with other chemical species. As another promising material for chemical sensors, graphene, a carbon nanostructure with a densely packed honeycomb two-dimensional lattice, has also emerged due to its inherently high mechanical strength and electrical conductivity as well as excellent electron transfer rate [174]. However, in the case of these carbon-based nanomaterials involving SWCNTs and graphenes, high cost of the material and complicated processes for device fabrication would be a restriction to develop the reliable and inexpensive chemical sensors.

As a different category of sensing material, conducting polymers have been widely used to design chemical vapor sensors as well. In particular, poly(3,4-ethylenedioxythiophene) polystyrene sulfonate (PEDOT:PSS) which has a high conductivity and a thermal stability compared with the other conducting polymers has been exploited in order to fabricate the chemical sensors that can detect various gases

involving nitrogen dioxide gas [175], ammonia gas [176], acetone gas [177], and even ions such as K^+ and Ca^{2+} [178]. Recently, some of the hybrid-type sensors comprised of the conducting polymer in combination with other complementary materials: PEDOT:PSS/graphene [179], poly(methyl methacrylate)/polypyrrole (PMMA/PPy) [180], and polyaniline/MoS_2 (PANI/MoS_2) [181] have been extensively studied to improve the sensing performance. However, shortcomings of the conducting polymers involving high cost and low stability of material as well as even relatively lower sensitivity compared to that of SWCNTs limit to develop mass-productive chemical sensors.

Likewise, many of the existing NH_3 sensors are based on metal oxides having a high sensitivity and selectivity [182-183]. However, these metal oxide-based gas sensors need to be operated at extremely high temperature more than 200 ℃ with high power consumption rendering their practical application difficult at room temperature [184-185]. Therefore, it is imperative to develop NH_3 sensor using a novel material surpassing the conventional materials in terms of sensitivity, selectivity, and stretchability. Tables 4 and 5 summarize the previously reported NH_3 sensor based on CNTs and non-CNT materials, respectively.

4.1.2 Research goal: Novel polymer electrolyte-based ammonia sensors

In the present work, we demonstrate an unprecedented NH_3 sensor based on the polymer electrolyte composed of poly(vinyl alcohol) (PVA) and glycerol as a polymer matrix and plasticizer, respectively. The PVA is a widely used water-soluble polymer which has many excellent characteristics such as good mechanical properties and film

Ref.	Sensor type	Sensing material	Concentration	Sensitivity	Response time	Recovery time
Sensors and Actuators B **113**, 341 (2006)	Resistor	SWCNT	5 ppm	5%	10 min	20 min (80℃)
Science. **287**, 622 (2000)	FET	SWCNT	0.1 wt%	10-100%	< 10 min	1 h (200℃)
Sensors **14**, 5502 (2014)	FET	SWCNT	100 ppm	95%		-
Sensors and Actuators B **117**, 426 (2006)	Resistor	SWCNT	5 ppm	8%	10 min	10 min (70℃)
Sensors and Actuators B **188**, 571 (2013)	Resistor	SWCNT/AuNP	300 ppb 6 ppm	0.03% 0.16%	3 min	5 min
Nanotechnology **28**, 035502 (2017)	Resistor	SWCNT/ITO NP	9 ppm	3%	110 min	300 min
Nano Lett., **9**, 4, 1626 (2009)	FET	SWCNTs	50 ppm	800%	500 sec	700 sec
Nanotechnology **18**, 165504 (2007)	Resistor	SWCNT/PABS[1)]	100 ppb	2%	20 min	20 min
Sensors and Actuators B **178**, 279 (2013)	Resistor	SWCNT/PEDOT	20 ppm	4.8%	12 sec	18 sec
Sensors and Actuators B **134**, 1022 (2008)	Resistor	SWCNT/Au	120 ppb	1.5%	150 sec	200 sec
Sensors and Actuators B **134**, 1022 (2008)	Resistor	SWCNT/Pt	5 ppm	70% (150℃)	10 min	40 min
Physical Status Solidi A **204**, 1820 (2007)	Resistor	SWCNT/SnO_2	10 ppm	17%	100 sec	3.2 min
Sensors and Actuators B **81**, 32 (2001)	Resistor	MWCNT	10 ppm	2%	3 min	Several days
Physica E **37**, 54 (2007)	Resistor	MWCNT	2500 ppm	75%	10 sec	100 sec
Sensors and Actuators B **129**, 888 (2008)	Resistor	MWCNT/SnO_2	60 ppm	100-500%	5 min	5 min
J. Mater. Sci. **18**, 1131 (2007)	Resistor	MWCNT/TiO_2	0.5 wt%	120%	1 min	5 min

[1)] PABS: Poly(aminobenzene sulfonic acid)

Table 4 Summary of the reported CNT-based NH_3 sensors in terms of sensitivity, response time, recovery time.

Ref.	Sensor type	Sensing material	Concentration	Sensitivity	Response time	Recovery time
MRS Bull. **24**, 18 (1999)	Resistor	Metal oxide (SnO_2)	200 ppm	1% (300℃)	1 min	1 h (300℃)
J. Chem. Soc. **82**, 1117 (1986)	Resistor	CP (Polypyrrole)	0.1 wt%	5%	15 min	15 min
Adv. Mater. **17**, 1616 (2005)	Resistor	PEDOT[1)] nanorods	10 ppm	6%	10 sec	70 sec
Talanta **82**, 1338 (2010)	Resistor	PEDOT nanotubes	5 ppm	2.5%	1 sec	30 sec
Sensors. **9**, 6752 (2009)	Resistor	PEDOT/TiO_2	5 ppm	0.15%	15 min	30 min
Mater. Sci. Eng. B, **157**, 87 (2009)	Resistor	PEDOT nanowires	10 ppm	2%	10 sec	10 sec
Sensors and Actuators B **156**, 849 (2011)	Resistor	PEDOT nanofibers	20 ppm	7.8%	13 sec	3 min
IEEE Sensors Journal **16**, 6149 (2016)	Resistor	PEDOT/Graphene	30 ppm	37.5%	7.7 min	10 min
Organic Electronics **15**, 2971 (2014)	Resistor	PEDOT/Graphene	50 ppm 500 ppm	5.5% 9.6%	3 min	5 min
IEEE Elec. Device. Lett. **38**, 975 (2017)	Resistor	PEDOT/AgNW	500 ppb 15 ppm	3% 28%	5 min	5 min
Mater. Manuf. Process **21**, 263 (2007)	Resistor	PANI[2)]	750 ppm	2.3%	8 min	7 min
Optics Express **23**, 2837 (2015)		PANI	0.1-1.0 wt%	4-6%	2.3 min	10 min
Optical Materials Express **7**, 1858 (2017)	Resistor	PANI/Graphene	0.1 wt%	133%	112 sec	185 sec

[1)] PEDOT: Poly(3,4-ethylenedioxythiophene)
[2)] PANI: Polyaniline

Table 5 Summary of the reported NH_3 sensors based on non-CNT materials (conducting polymers, metal oxides, etc.).

forming ability as well as non-toxic, anti-static and biodegradable properties [83-84]. It can be used as a raw material for applications in the field of coating, adhesive, surfactant, emulsifier, dispersants, and films [57]. On the basis of the merits of PVA, it was also exploited to make the polymer electrolyte as a polymer matrix [186-187]. However, it is known that the PVA is a brittle polymer due to its semi-crystalline nature. Therefore, the plasticizer is needed to make the PVA soft and flexible for stretchable sensors. The plasticizer penetrates into between polymer backbone chains, thus increasing the interchain distances and free volume, which in turn decreases the glass transition temperature of polymer. For this reason, the plasticizer would turn the texture of polymer to become softer and more flexible.

In the present work, glycerol is used as the plasticizer to modify the properties of PVA. The glycerol as a major by-product of biodiesel production is a very reactive molecule having three hydroxyl groups [188]. These rich amounts of hydroxyl groups enable the glycerol to form intermolecular hydrogen bonds with other polymer's backbones including polar groups [189]. Therefore, the glycerol has been used as the plasticizer in this work to prevent the PVA backbone chains from being folded, thereby increasing the flexibility of PVA. In addition to the plasticizing effect, the glycerol induces an electrically conductive property that can be attributed to an increase in ionic mobility. This characteristic allows the glycerol to be exploited for fabrication of the proton conducting polymer electrolytes. According to the previous reports, carboxymethyl cellulose and PVA were plasticized with the glycerol in order to develop ionic conducting polymer electrolytes [190-191].

The solid polymer electrolyte has been attracted to their potential applications in rechargeable batteries, fuel cells, and displays [192]. As a specific area, proton conducting polymer electrolytes have received considerable attention due to their high ionic conductivity [193]. However, many of the investigation on the conventional polymer electrolyte have been mainly focused on enhancing the ionic conductivity in order to develop the ionic conductors for an application in batteries and fuel cells. Therefore, we demonstrate herein a new application of polymer electrolytes based on the plasticized PVA with the glycerol indicating good flexibility and remarkable ability interacting with ammonia molecules.

By integrating all concepts described above, a novel stretchable NH_3 vapor sensor based on the polymer electrolyte has been extensively investigated. The presented sensor exceeds the performance of SWCNT-based NH_3 sensors in terms of sensitivity, recovery time, and stretchability. This stretchable chemical sensor has the advantage of easy fabrication, low cost, convenient scale-up and reliable sensing performances. In addition to the high sensitivity and stretchability, a remarkable selectivity discriminating NH_3 with different chemicals including water has been also observed in novel polymeric sensor. Moreover, we have suggested a proton jumping as well as Freundlich isotherm adsorption model to explain the sensing mechanism of novel sensor surpassing the conventional SWCNT-based NH_3 sensors in sensing performance. From our knowledge so far, this report would be the first attempt to develop NH_3 vapor sensor using new materials with a superior sensing ability and stretchability to conventional ones. The findings in the present work could offer a new possibility to realize the cost effective and highly stretchable NH_3 sensor showing an outstanding sensing performance.

4.2 Experimental Methods

4.2.1 Synthesis of silver nanowires (AgNWs)

The conventional polyol method was exploited in order to synthesize relatively long (50-100 μm) AgNWs with a diameter of 100 nm. 0.2 g of PVP (Sigma-Aldrich, M_w ~ 360,000 g/mol) was first dissolved in 50 mL of ethylene glycol (EG) used as a polyol to synthesize long AgNWs for 1 hour at room temperature. Next, 0.25 g of silver nitrate ($AgNO_3$) was added to prepared PVP solution and then continuously stirred by a magnetic bar for 1 hour at the same temperature. After mixing, 400 μL of $CuCl_2$ (3.3 mM) dissolved in EG was rapidly injected into the admixture and mixed mildly by hand for 1 minute. The mixed solution was then suspended in a preheated silicone oil bath at 130 °C and stirred using a magnetic bar for 3 hours. Color change from transparent solution into milky-colored suspension that can be attributed to the longitudinal growth of AgNWs was observed during this polyol-mediated synthesis. After synthesis, the purification process was required to remove the chemical residues remaining within the solution. Consequently, the resultant solution was cleaned by using acetone and then the aggregated AgNWs were re-dispersed in ethanol. This purification was repeated by three or four times. Last, the purified AgNWs were kept being dispersed in ethanol for use.

4.2.2 Fabrication of PVA-glycerol solution

As a polymer matrix, 10 g of PVA (Sigma-Aldrich, M_w ~ 89,000 g/mol) was dissolved in the DI water of 100 ml by vigorously stirring it with a magnetic bar at 90 °C

for 1 hour. At this point, a plasticizer, glycerol of 10 ml, was added to the PVA solution and then continuously stirred for additional 30 minutes at the same temperature. After stirring, the PVA-glycerol solution was cooled to room temperature.

4.2.3 Fabrication of chemical sensor based on polymer electrolyte

The synthesized AgNWs were used to fabricate electrodes of chemical sensor in this thesis work. The network of AgNWs could be formed through the vacuum assisted filtration (VAF) method which has been widely used to make a thin film using nanomaterials such as nanowires, as shown in Figure 4.1 [194].

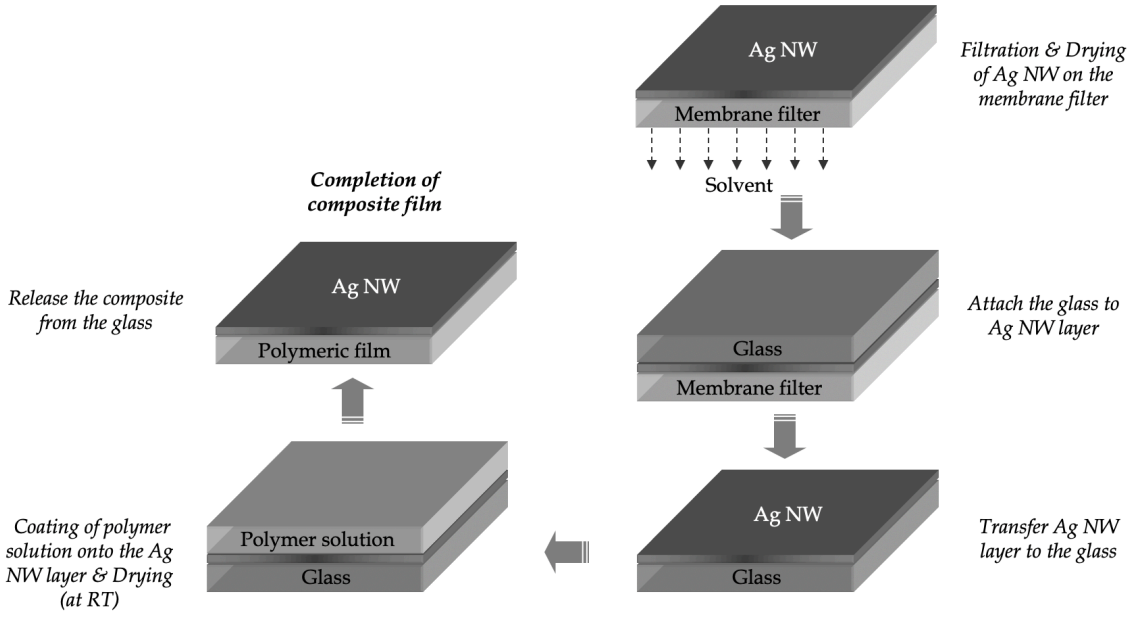

Figure 4.1 Schematic illustrations of the vacuum assisted filtration (VAF) method which has been widely used to fabricate a thin film using nanomaterials such as nanowires.

A percolative network comprised of AgNWs was first formed on a polytetrafluoroethylene (PTFE) membrane filter with a diameter of 47 mm. This percolative layer of AgNWs was then transferred onto a 1.1 mm thick glass slide ultra-sonificated within acetone, followed by rinsing with methanol and DI water. After evaporation of a residual solvent in the layer of AgNWs at room temperature, the measured electrical resistance of AgNWs network was 1-5 Ω/sq^2 so that it could be applied to the electrodes of resistive sensors. (More specific details for the percolation model describing the correlation between the resistance and the AgNW concentrations are introduced in the *Appendix B*.) After fabricating of electrodes on the glass substrate, the center line, which has a width of 100 um, was generated by using a sharp razor blade, as shown in Figure 4.2. The purpose of this center line is to form a space, which will be later filled with a sensing material. Next, the PVA-glycerol solution was poured onto the layer of silver nanowires and the centerline. When the layer of AgNWs was coated by the PVA-glycerol solution, the center line that had been created earlier was also filled with the solution at the same time. This solution was then dried at room temperature for 12 hours to obtain a uniform coating layer by avoiding a drastic volume contraction of

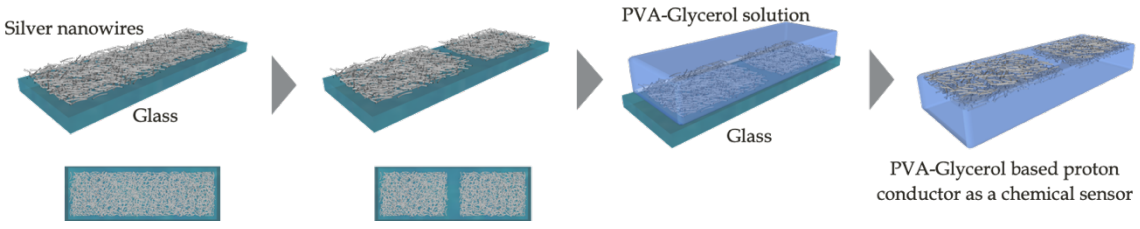

Figure 4.2 Fabrication procedures of novel polymer electrolyte-based NH_3 vapor sensor comprised of the plasticized PVA with glycerol. The layer of silver nanowires (AgNWs) formed by the vacuum assisted filtration technique were transferred onto the PVA-glycerol electrolyte to fabricate electrodes.

polymer that could result from an overly rapid drying process. This alleviated drying condition could give rise to reduction in the Marangoni diffusion that can be attributed to the difference of surface tension between the layer of AgNWs and the center line having a glass surface exposed to air. After completion of drying, the formed PVA-glycerol film was easily detached from the glass substrate along with the layer of AgNWs as electrodes, as seen in Figure 4.2.

4.2.4 Fabrication of SWCNT-based chemical sensor (control sample)

SWCNTs (diameter: 1.2 – 1.7 nm, length: 100 nm – 4 μm, purity: >99%) were purchased from the Sigma-Aldrich. In order to prepare 0.04 mg/mL of SWCNT colloid, 0.02 mg of SWCNTs were uniformly dispersed in 50 mL of 1,2-dichlorobenzene ($C_6H_4Cl_2$, Sigma-Aldrich) during 4 hours of ultrasonication at room temperature. Next, with the same procedures of polymer-based sensor mentioned in the previous section, the glass substrate being coated with the AgNW percolative layer as electrodes was prepared. A center line with the width of 100 um was then generated by scraping the AgNW layer off with a sharp razor so that the bare glass was exposed to air, thereby enabling it to be filled with SWCNTs. Subsequently, the glass substrate comprising the layer of AgNWs along with the center line was dipped in the SWCNT dispersed solution for 3 minutes and then rinsed in pure dichlorobenzene for 1 minute. These processes were repeated three times to deposit suitable amount of SWCNTs on the center line of the glass substrate, followed by blowing with N_2 gas for a drying of residual solvent. For this process, the layer of AgNWs was covered by a chemically crosslinked PVA film as a protecting layer

to prevent as-coated AgNWs from being destroyed by chemicals. This chemically crosslinked PVA film was fabricated using 10 wt% PVA solution mixed with 4 wt% boric acid to induce a crosslinked network which could provide an excellent stability for most of the chemical invasion. Consequently, the crosslinked PVA film laminated onto the layer of AgNWs enabled to protect the as-coated electrodes from a chemical attack when the glass substrate was dipped into 1,2-dichlorobenzene. Different types of polymer film such as polyimide, PDMS, epoxy, acrylate, and even non-crosslinked PVA film were also tested to investigate their protective function as well as the adhesion property showing a good attachability with the as-coated AgNW layer during a solution process. Exception for the crosslinked PVA film, other polymeric films have failed to protect the AgNW-electrodes when dipped into 1,2-dichlorobenzene. It was observed that the as-coated AgNW layers were delaminated from the glass substrate or cracked on the surface of electrodes. After completion of the formation of SWCNT layer on the sensing area, the protection film was removed, followed by blowing with N_2 gas for an additional drying of residual solvent.

4.2.5 Measurement of sensing performances for NH_3 detection

The experimental setup of gas sensing is shown in Figure 4.3. It consists of the conical flask interconnected with gas sensing chamber and computer interfaced high resistance electrometer (Keithley 2400 SourceMeter, USA). Definite ppb and ppm level of liquor ammonia was injected into the conical flask and NH_3 vapor was collected from the upper side of the conical flask. This collected NH_3 vapor was allowed to pass through

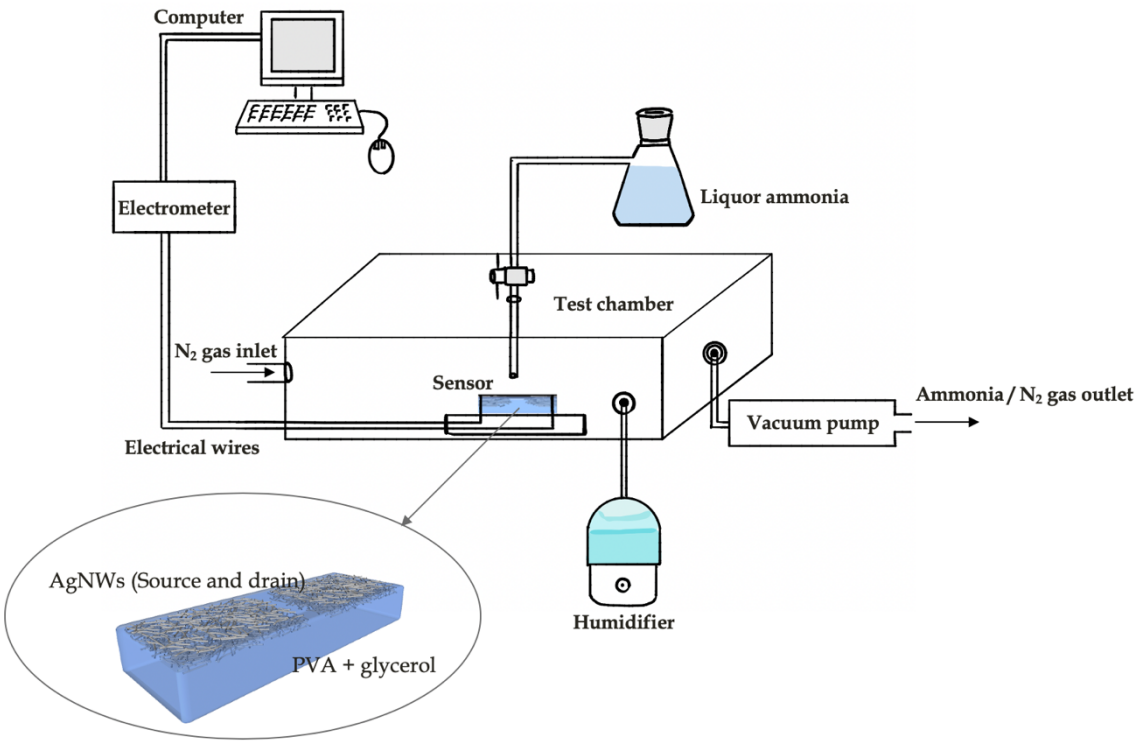

Figure 4.3 Schematic diagram of the NH_3 vapor sensing set-up. It consists of the conical flask interconnected with gas sensing chamber and computer interfaced high resistance electrometer (Keithley 2400 SourceMeter, USA).

the gas sensing chamber adjusting the needle valve without any carrier gas. For gas sensing measurements, sensors were exposed to NH_3 with a concentration from 10 ppb to 500 ppm at room temperature. Once the steady state was achieved during the measurement, the chamber was evacuated by vacuum pump. All of the sensing performances were evaluated under dry air as well as humidity conditions at room temperature. The relative humidity was controlled from 10 %RH to 90 %RH to investigate the effect of moisture around sensors on the sensing performances. In order to examine the changes in the electrical properties of the thin films in specific gas

atmosphere, two probes technique for high resistance measurements was exploited. The two-probes were well contacted to the as-coated AgNW electrodes showing the ohmic contact at the driving voltage of 1 V. The resistance was continuously monitored while specific ppm level of test gas was injected into the gas testing chamber. Once the steady state response was achieved, the change in resistance with reference to the baseline was noted. The stretchable sample holder was placed inside the in-house designed gas sensing chamber in order to evaluate the characteristics of stretchable chemical sensors. The stretchable sensors were exposed to NH_3 vapor under stretched states with 0-50 % strain and then the sensing performances such as sensitivity and recovery time were evaluated. The recovery times of the sensing element were calculated from time vs. resistance plot, which are defined as the time taken to attain 10% of the change in resistance from its baseline resistance.

4.3 Results and discussion

4.3.1 Sensing performances of novel NH_3 vapor sensor

The real-time resistance change in polymer electrolyte-based sensor and SWCNT-based sensor was measured to evaluate the sensing performance for each sensor, as seen in Figure 4.4. By mounting the sensor on the board inside the gas testing chamber, the resistance, temperature, and relative humidity were recorded simultaneously. During all measurements, the temperature and the relative humidity were 25 ± 2 °C and 40 ± 5 %RH, respectively. Figure 4.4A shows the response and recovery curves of the

(a)

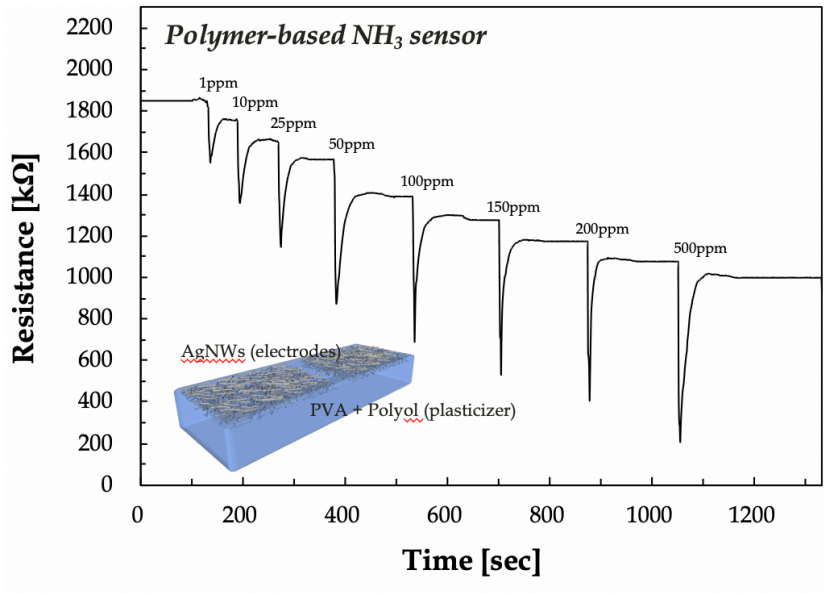

(b)

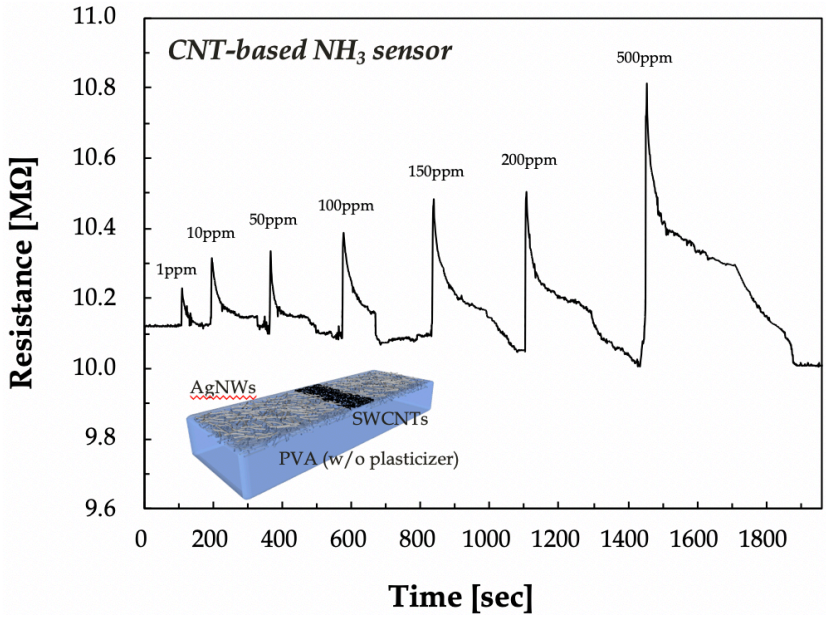

Figure 4.4 (a) Response curve of the polymer electrolyte-based sensor to 1 – 500 ppm NH_3 at room temperature. (b) Response curve taken from the SWCNT-based sensor to the same concentration range of NH_3 at room temperature. Inset figures show the schematics of sensor structure.

polymer electrolyte-based sensor exposed to 1 - 500 ppm NH_3 at 25 ℃. As seen in Figure 4.4A, the sensor displays a dramatically sharp response to NH_3 exposure even at 1 ppm of concentration. NH_3 molecules adsorbed on the sensor surface are likely to form the hydrogen bond with neighboring water clusters, thereby enabling the proton to transfer along the hydrogen bonding bridges. An increase in the number of proton transfer hopping through the hydrogen bonds could result in an increase in the electrical conductivity, thus leading to high sensitivity and fast response of novel polymer sensor. The details in this mechanism will be further discussed in the next section. Figure 4.4B indicates the real-time resistance change of SWCNT-based sensor upon exposure to NH_3 at different concentration (1 - 500 ppm). As described earlier, NH_3 is an electron donating molecule so that the transferred electrons from NH_3 to SWCNT would recombine with holes of SWCNTs behaving as a p-type semiconductor, as shown in Figure 4.5 [195]. For this reason, the hole concentration in the SWCNT decreases and a consequent increasing in the electrical resistance can be observed, as seen in Figure 4.4B. As a result, novel polymer electrolyte-based sensor representing much sharper and narrower peaks in the resistance change could surpass SWCNT-based NH_3 sensor in terms of sensing performances.

4.3.2 Analysis of sensitivity for novel NH_3 vapor sensor

The Figure 4.6 shows that the sensitivity for novel polymer electrolyte-based NH_3 sensor and SWCNT-based sensor. In general, the sensitivity which is referred to as an ability of gas sensor in response to gas exposure. It is mathematically defined in terms of

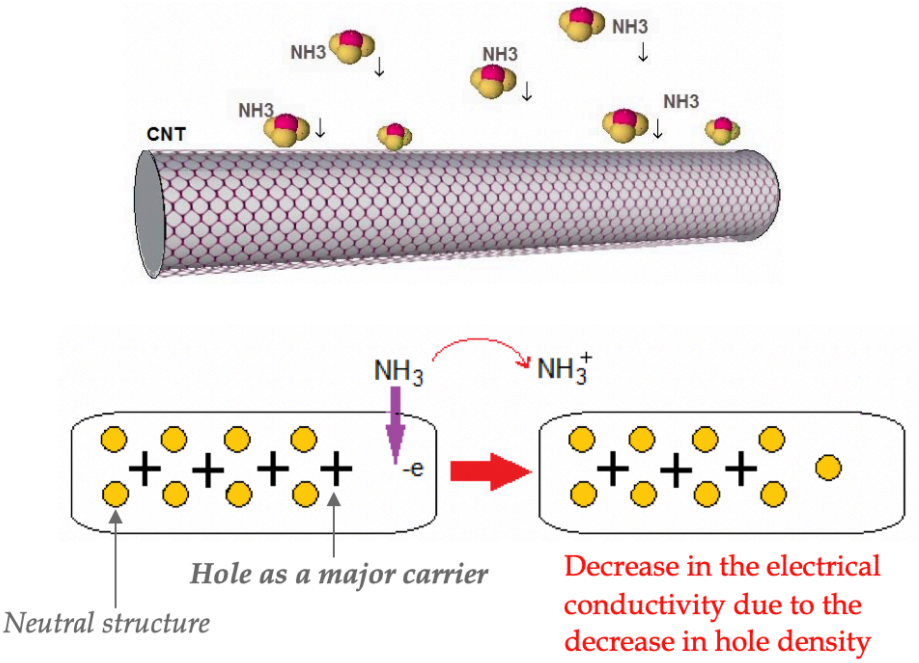

Figure 4.5 Schematic illustrations of the NH_3 sensing mechanism for conventional SWCNT-based NH_3 sensors. NH3 donates electrons to the underlying nanotube structure. As SWCNTs behave as a p-type semiconductor, the transferred electrons will recombine with hole carriers, thereby decreasing the charge carrier (hole) concentration in the support and a consequent increasing the electrical resistance [195].

resistance variation, $\Delta R/R_0\ [\%] = (R_g - R_0)/R_0 \times 100$, where R_g is the resistance upon gas exposure and R_0 the baseline resistance before exposure to gas. The sensitivity data shown in Figure 4.6 were calculated by using R_0 and R_g evaluated in Figure 4.4. The sensitivity of the polymer electrolyte-based sensor when exposed to 1 – 500 ppm NH_3 at 25°C represents an order of magnitude higher than that of SWCNT-based sensor. As shown in Figure 4.6A, the sensitivity of polymeric sensor increases with the concentration of NH_3, following by a power law:

$$\frac{\Delta R}{R_0} = K_A C_A{}^r \qquad \text{(Eq. 27)}$$

where C_A is the concentration of NH_3, both K_A and r are the fitting parameters. The fitting model of (Eq. 27), which corresponds to the Freundlich isotherm adsorption, describes the inherent sensing mechanism of novel polymeric sensor. The original Freundlich adsorption model is displayed in the inset of Figure 4.6A. Here, θ_A means the surface area adsorbed by the adsorbate and has been replaced with $\Delta R/R_0$ in (Eq. 27). As seen in Figure 4.6A, the measured sensitivities of polymer electrolyte-based NH_3 sensor are well fitted with the Freundlich adsorption model. From this analysis based on the Freundlich adsorption model, we could interpret the resistance change of our polymeric sensor results from the adsorption of NH_3 molecules on the sensor surface.

In general, the Langmuir isotherm adsorption model is most adequate to model a homogeneously adsorbed surface, which represents a dashed line in Figure 4.6A. On the contrary, the Freundlich adsorption model is preferred over microporous structures or non-homogeneous layers. PVA and glycerol, raw materials of novel polymer sensors studied in the present work, show a dehydration reaction when they are miscible each other without any phase separation [196]. This condensation reaction of water molecules could result in the formation of water clusters, which covers the whole surface of sensing area forming a heterogeneous surface rather than a monolayer which is close to homogeneous surface. Adsorbed NH_3 molecules on the sensor surface instantaneously interact with water clusters, thereby forming the strong intermolecular hydrogen bonds as a bridge for proton jumping. As a result, the enhanced sensitivity of polymer electrolyte-

(a)

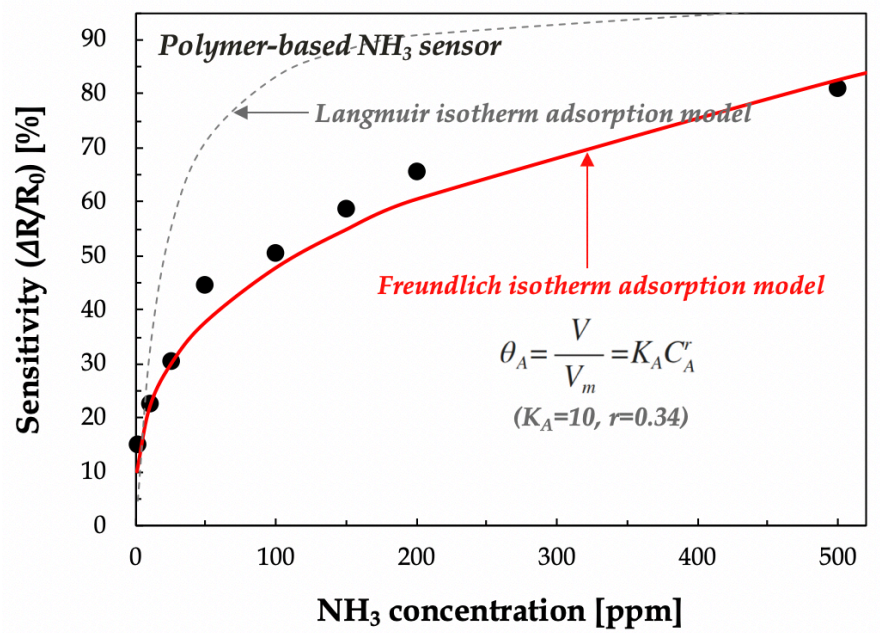

(b)

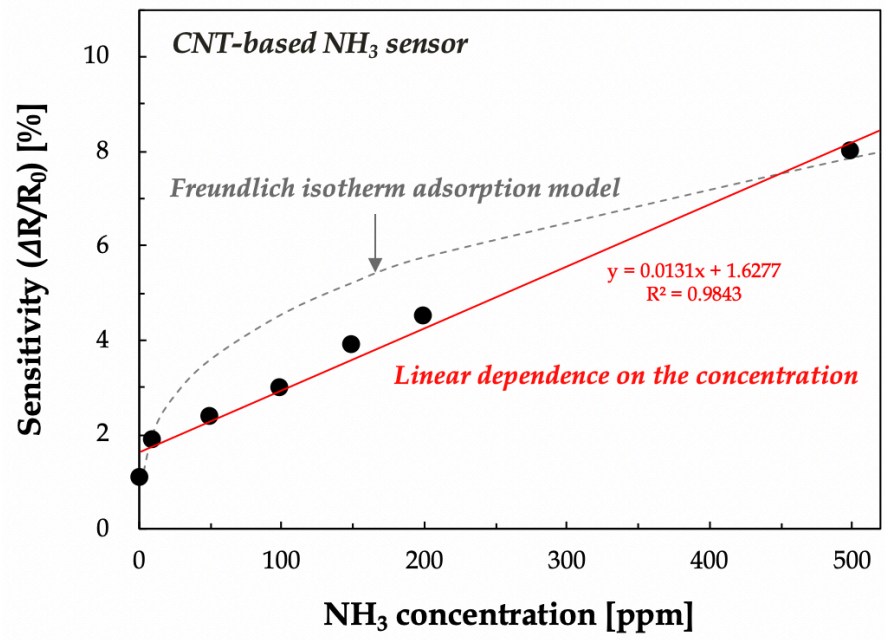

Figure 4.6 (a) Sensitivity of the polymer electrolyte-based sensor as a function of NH_3 concentration (1 – 500 ppm) at room temperature. (b) Sensitivity of the SWCNT-based sensor in terms of NH_3 concentration (1 – 500 ppm) at the same temperature.

based sensor can be attributed to the Freundlich adsorption of NH_3 molecules on water clusters.

On the other hand, the sensitivity of SWCNT-based sensor shows a linear regression with NH_3 concentration, as seen in Figure 4.6B. Although the sensitivity of the SWCNT-based sensor increases with the NH_3 concentration, the collected data set is not fitted with the Freundlich adsorption model shown as a dashed line in Figure 4.6B. Unlikely the case of polymer sensor, the sensitivity of SWCNT-based NH_3 sensor is based on the interaction between holes of SWCNT and electrons donated by the adsorbed NH_3 molecules. This tendency observed in SWCNT-based sensor is nearly similar with the previously reported results [171-172].

4.3.3 Recovery time of novel NH_3 vapor sensor

Figure 4.7 shows the recovery time, which is another critical factor to evaluate the sensor performance, for polymer electrolyte-based sensor and SWCNT-based sensor. The recovery time is referred to as the time required to be returned to the original state before exposure to gas. In this thesis work, the recovery times of the sensing element were calculated from time vs. resistance plot, which are defined as the time taken to attain 10% of the change in resistance from its baseline resistance. As shown in Figure 4.7, the recovery time of novel polymeric sensor is approximately an order of magnitude faster than that of the SWCNT-based sensor. Whereas the recovery time of SWCNT-based sensor increases gradually with an increase in NH_3 concentration, polymeric sensor shows the fast recovery within 1 minute for all concentrations. This fast recovery of

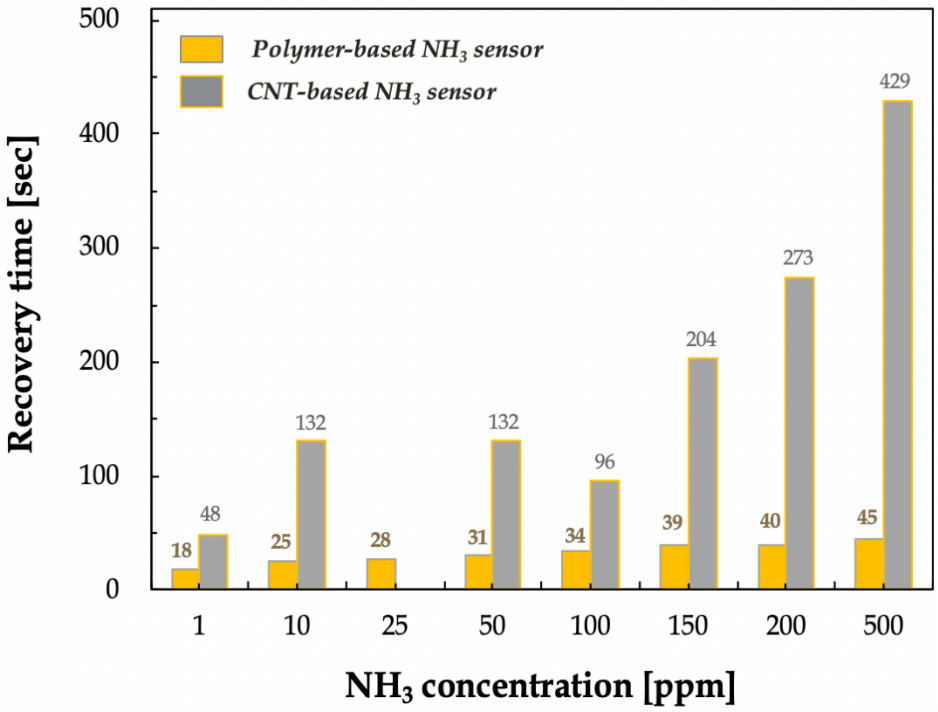

Figure 4.7 Recovery time of the polymer electrolyte-based sensor and the SWCNT-based sensor as a function of NH_3 concentration (1 – 500 ppm) at room temperature.

novel polymeric sensor can be attributed to the rapid desorption rate of NH_3 molecules from water clusters presenting on the sensor surface. It is noted that NH_3 has a low enthalpy of vaporization, thus rendering NH_3 molecules to be readily evaporated from water clusters by breaking the hydrogen bond formed between NH_3 and water molecules. The hydrogen bond is known as a physically intermolecular interaction showing a dynamic reversibility able to break and re-bond repeatedly. Therefore, our novel polymeric sensor which is a physisorption-type sensor based on the dynamic hydrogen bond exhibits a fast response and recovery compared to a chemisorption-type sensor based on strongly chemical bonds [179]. The long recovery time of SWCNT-based

sensor results from the strong interaction of NH_3 with SWCNTs via the combination of electrons and holes [197].

4.3.4 Selectivity of novel NH_3 vapor sensor

As previously described, novel polymer electrolyte-based sensor is comprised of PVA and glycerol. These two materials show the dehydration reaction that makes the surface of electrolyte to be covered by water clusters. We demonstrate herein the effect of water clustering layer formed by sensing material on the selectivity of polymeric sensor for external water vapors. Figure 4.8 represents the real-time resistance changes of NH_3 vapor sensors when exposed two types of water; one is urban water-supply (Ann Arbor, Michigan, United States), which has a resistance of 300-400 kΩ, and the other is deionized water having a resistance of about 10 MΩ. As seen in Figure 4.8A, the polymer electrolyte-based sensor has not shown any responses to water exposures. In contrast, the SWCNT-based sensor indicates the resistance change when exposed to urban water-supply as well as deionized water, as shown in Figure 4.8B. This means that the electrons donated by water molecules could interact with the holes of SWCNTs. Therefore, the SWCNT-based sensor generally shows the poor selectivity between NH_3 and water, on the other hand, the polymeric sensor is capable of discriminating NH_3 vapor against water. This is because the additional adsorption of water molecules on the sensor surface which has been already covered with plenty of water could not affect the electrical signal change anymore.

(a)

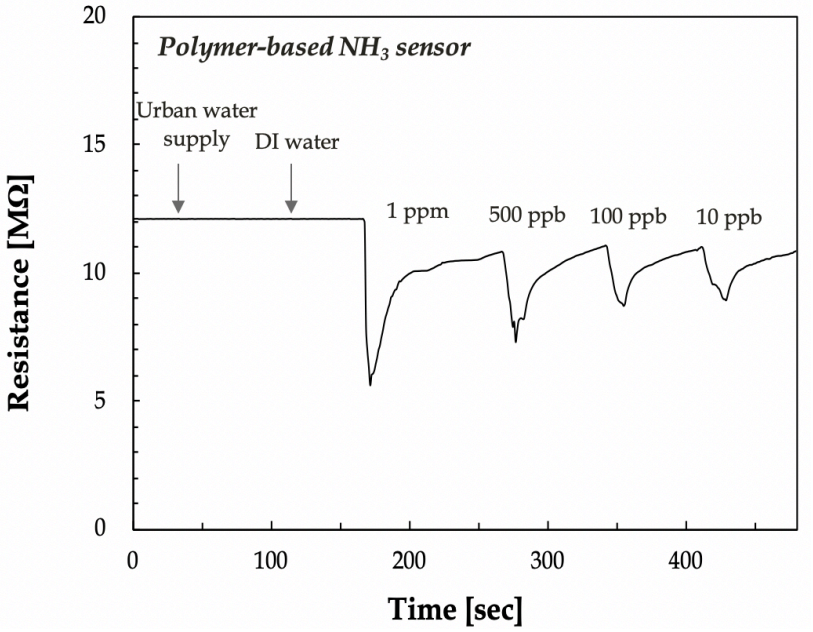

(b)

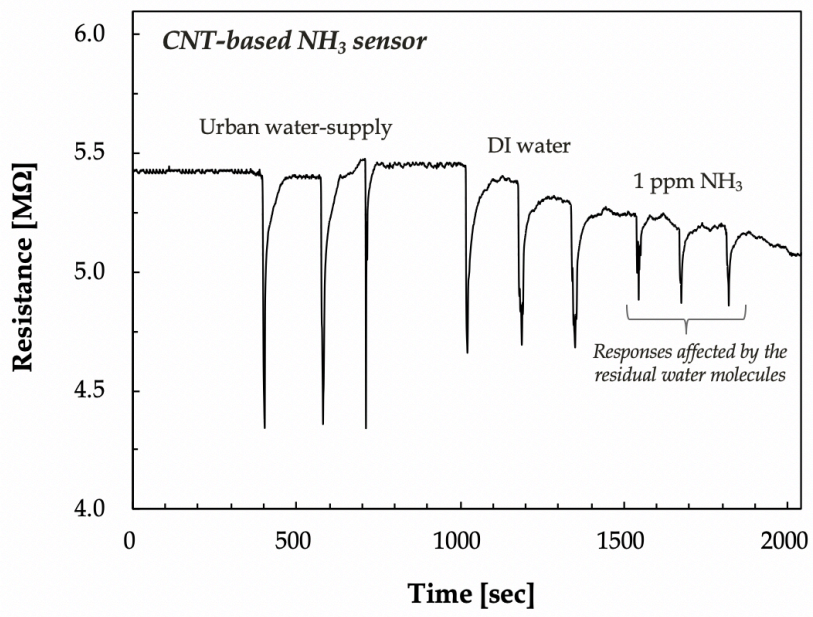

Figure 4.8 (a) Response curve of the polymer electrolyte-based sensor exposed to water (Michigan urban water-supply and deionized water) and extremely lower NH_3 concentration (10 – 1000 ppb) at room temperature. (b) Sensitivity of the SWCNT-based sensor. (b) Response curve of the SWCNT-based sensor exposed to water (Michigan urban water-supply and deionized water), followed by the subsequent exposure to NH_3 with a concentration of 1 ppm at room temperature.

In addition, the sensors were subsequently exposed to NH_3 vapors when recovered from water exposures. The polymer electrolyte-based sensor shows the delicate resistance change when exposed to even 10 ppb of NH_3, as shown in Figure 4.8A. Interestingly, it is noted that the SWCNT-based sensor shows a decrease in electrical resistance when exposed to 1 ppm of NH_3, as displayed in Figure 4.8B. This is an opposite response compared with the previous result observed in Figure 4.4B, increasing the resistance in response to NH_3 exposures. Based on this observation, we could assure that the performance of SWCNT-based sensor is affected by the residual water once the water is adsorbed on the sensor surface. Therefore, the SWCNT-based sensor may require additional heating system or thermal annealing process due to its long recovery time. As a result, novel polymer electrolyte-based sensor in the present work opens up the possibility of commercially available NH_3 sensor indicating high sensitivity, fast recovery time, and outstanding selectivity without any heating facilities.

Figure 4.9 shows the selectivity of novel NH_3 vapor sensor based on polymer electrolyte when exposed to various organic solvents: acetone, hexane, methanol, isopropyl alcohol, benzene, nitrobenzene, 1-nitrobenzene, ethanol, dimethyl sulfoxide, and dimethyl formamide. In the meantime, NH_3 with the concentration of 1 ppm and 10 ppm was periodically exposed to the same sensor to confirm the NH_3 sensing ability at room temperature. As shown in Figure 4.9, no response for all chemicals and water excepting for NH_3 has been observed, exhibiting a remarkable selectivity of novel chemical sensor.

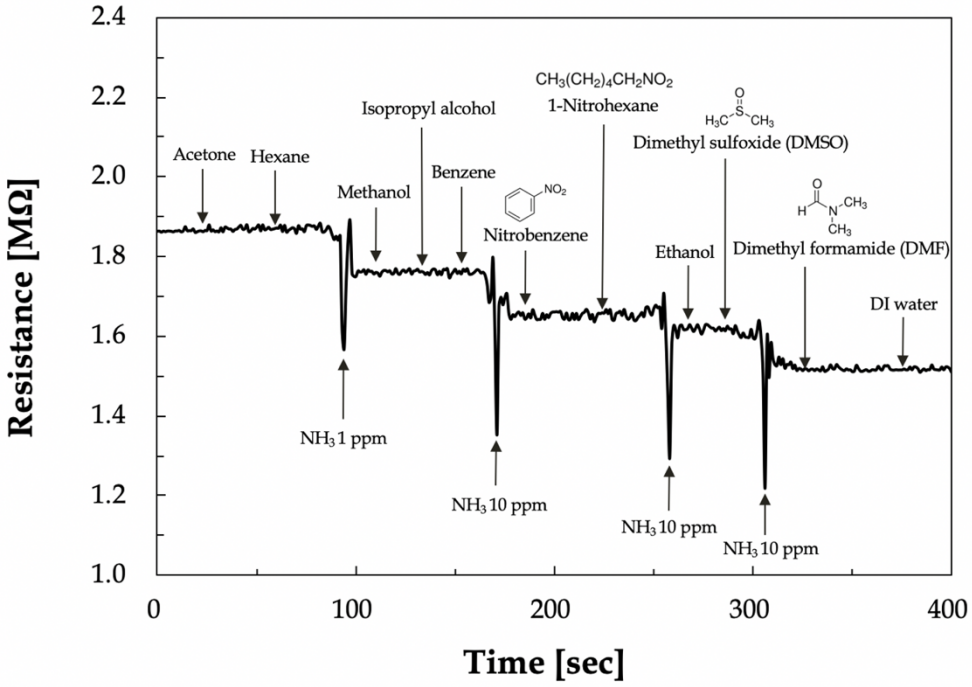

Figure 4.9 Selectivity of the polymer electrolyte-based NH_3 vapor sensor when exposed to various organic solvents: acetone, hexane, methanol, isopropyl alcohol, benzene, nitrobenzene, 1-nitrobenzene, ethanol, dimethyl sulfoxide, dimethyl formamide. During the test, NH_3 with the concentration of 1 ppm and 10 ppm was periodically exposed to the same sensor to confirm the NH_3 sensing ability at room temperature. As shown in Figure 4.9, no response for all chemicals and water excepting for NH_3 has been observed, exhibiting a remarkable selectivity of novel chemical sensor.

4.3.5 Effect of water clusters on conductivity of polymeric electrolyte

Here we demonstrate that novel polymer electrolyte-based NH_3 vapor sensor indicates outstanding sensing performances in terms of sensitivity, recovery, and selectivity. On account of the dehydration reaction of PVA-glycerol, water clusters formed on the sensor surface facilitate the adsorption of NH_3 molecules onto them. As a consequence, a sharp decrease in electrical resistance has been observed when exposed to

NH_3. Furthermore, novel polymeric sensor shows the distinct selectivity between NH_3 and water compared with the SWCNT-based sensor that responses instantaneously to water. Therefore, water clustering layer formed on the sensor surface via the dehydration reaction of PVA-glycerol could affect directly to the performances of polymeric sensor. For this reason, we describe herein the correlation of water layer formed on the sensor surface and the sensing performance.

Figure 4.10 shows the electrical conductivity of polymeric electrolytes based on the plasticized PVA with glycerol. With an increase in volume fraction of glycerol as a plasticizer, the conductivity of polymeric electrolyte containing sufficient water molecules dramatically increases, as shown in Figure 4.10. However, the electrolyte stored in desiccator at 10 %RH and room temperature for 12 hours to remove water existing on the surface of polymer electrolyte represents a slow increase in the conductivity in terms of volume fraction of glycerol. The measured conductivity data are fitted well with the percolation model as follows:

$$\sigma = \sigma_0 (v_{pcz} - v_c)^s \qquad \text{(Eq. 28)}$$

where σ is the electrical conductivity of polymer electrolyte, σ_0 is the electrical conductivity of bulk plasticizer at room temperature, v_{pcz} is the volume fraction of plasticizer, v_c is the percolation threshold which means the volume fraction indicating the conductive property, s is the critical exponent as a fitting parameter. According to the percolation model, the conducting elements dispersed in the insulative materials can effectively form the conductive pathways, thereby enhancing the conductivity of

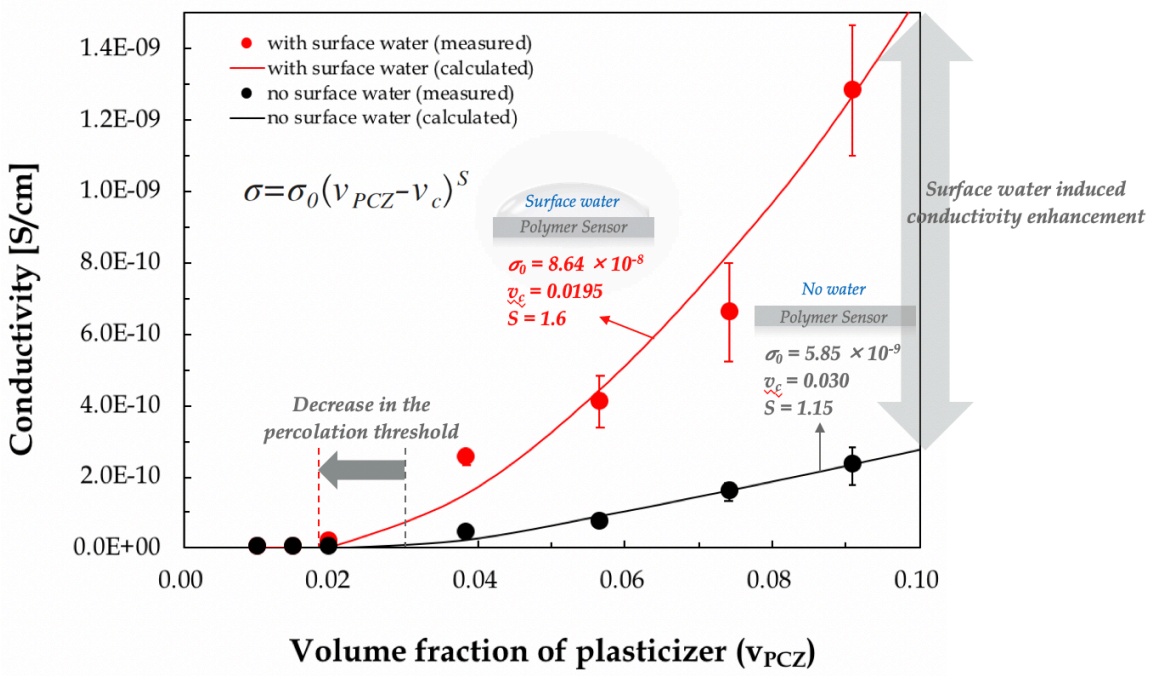

Figure 4.10 Correlation of electrical conductivity and volume fraction of plasticizer of polymer electrolytes based on the plasticized PVA with glycerol. The polymer electrolytes comprised of PVA-glycerol with sufficient water on the surface (red circles) and those with relatively low amount of water after storing them in desiccator at 10 %RH and room temperature (black circles) have resulted in the increase in conductivity with the volume fraction of plasticizer. The measured data were fitted by the percolation model inset in Figure 4.10.

composite materials. As a conducting plasticizer, glycerol contributes to enhance the conductivity of polymer electrolytes as well as the flexibility due to the plasticization effect. As shown in Figure 4.10, the measured electrical conductivity data in the polymer electrolytes are in consistent with the percolation model.

Importantly, a difference of the conductivity between two polymer electrolytes is caused by the difference of water amount presenting on the surface of electrolyte. As seen in Figure 4.10, the percolation threshold (v_c) diminishes from 0.03 (black line) to 0.02 (red line) with an increase in water amount on the electrolyte surface, thereby

rendering polymer electrolyte to be electrically conductive even at low concentrations of glycerol. In addition, the critical exponents are 1.6 and 1.15 for polymer electrolytes before and after dehumidifying, respectively. This result means that the presence of water clusters on the electrolyte surface increases the conductivity more rapidly in terms of plasticizer concentration. As a result, the polymer electrolyte comprised of PVA-glycerol generally forms water clustering layer contributing to an increase in the electrical conductivity.

4.3.6 Correlation of conductivity and sensing performance

In this present work, we hypothesize that the water clusters formed through the dehydration reaction of PVA-glycerol leads to an increase in sensitivity of NH_3 sensors. Figure 4.11 represents the correlation between conducting property and sensitivity of sensor in terms of the volume fraction of glycerol as a plasticizer. As seen in Figure 4.11, the sensitivity at 10 ppm of NH_3 increases with the concentration of plasticizer. The sensitivity exhibits a similar correlation with the conductivity of polymeric electrolyte in terms of glycerol concentration. It is expected that the sensing performance of polymeric sensor is caused by the conductive property of the polymer electrolyte due to the plasticization effect that could be described by the percolation model inset in Figure 4.11. As a consequence, the superior sensitivity of novel polymer electrolyte-based NH_3 sensor to that of conventional SWCNT-based sensor results from the presence of water clusters formed via the dehydration reaction of PVA-glycerol.

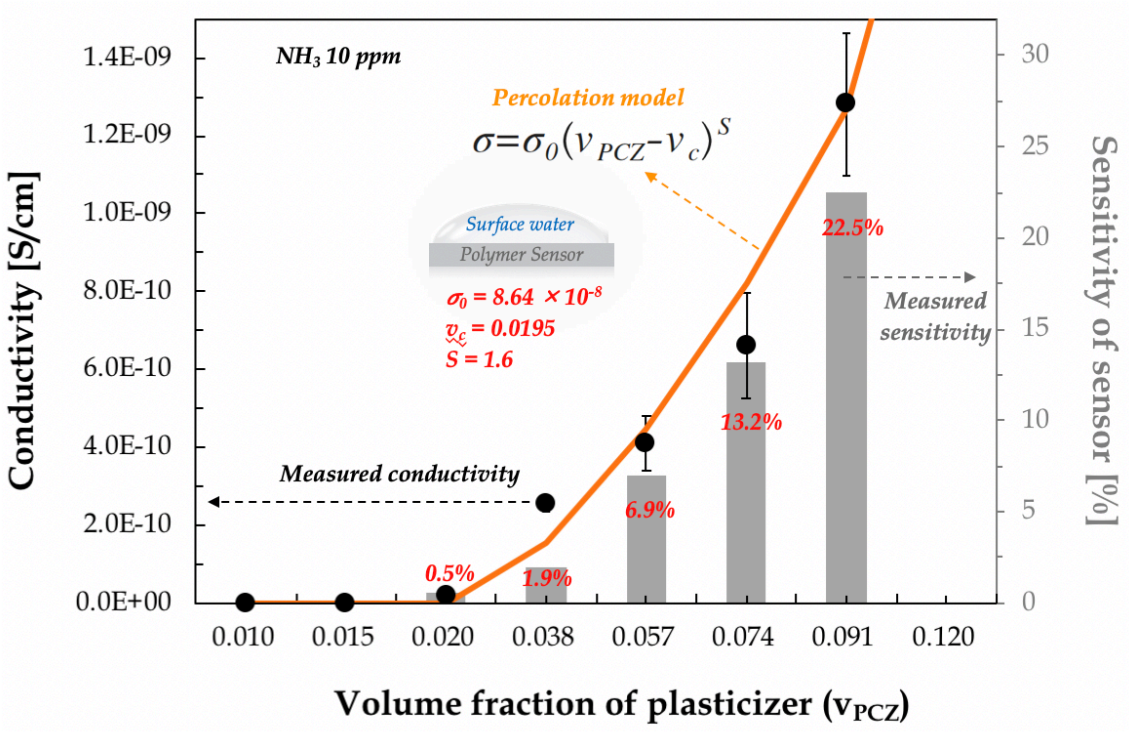

Figure 4.11 Correlation of electrical conductivity and sensitivity of sensor in terms of the volume fraction of plasticizer in polymer electrolyte-based NH_3 sensor fabricated by the plasticized PVA with glycerol. The sensitivity measured at 10 ppm of NH_3 increases with the concentration of plasticizer, which this behavior is totally similar with the conductivity followed by the percolation model (fitted by orange line using the equation inset within the figure). The superior sensitivity of novel polymer electrolyte-based NH_3 sensor to that of conventional SWCNT-based sensor is can be attributed to the water molecules as a product of PVA-glycerol dehydration reaction.

4.3.7 Sensing mechanism of novel polymeric NH_3 vapor sensors

Here, we describe that the sensing mechanism of novel polymeric sensor is closely correlated with the interaction of NH_3 vapors adsorbed on water clusters formed by the dehydration reaction of PVA-glycerol. It is generally known that a water molecule

can generate hydronium ion (H_3O^+) by reacting with the other water molecule through the autoionization as follows:

$$H_2O + H_2O \rightleftarrows H_3O^+ + OH^- \quad (1)$$

From the chemical reaction (1) above, the hydronium ion plays a role as an Arrhenius acid, thereby donating a proton (H^+) to the surrounding water molecules when dissolved in water. This proton can be transferred through the hydrogen bonds formed strongly between water molecules. This phenomenon is referred to as the Grotthuss mechanism, which protons tunnel across a series of hydrogen bonds between hydronium ions and water molecules [107]. According to the Grotthuss mechanism, the charge is not transported by the movement of particles but by breaking and reformation of hydrogen bonds. This principle is frequently used to explain the proton jumping as a mechanism of ionic conductivity.

The interaction of NH_3 molecules with water clusters could be explained by the same mechanism as described above. When an NH_3 molecule meet with water, the following reaction could be instantaneously occurred:

$$NH_3 + H_2O \rightleftarrows NH_4^+ + OH^- \quad (2)$$

From the reaction (2) above, water and ammonia could act as a Brønsted-Lowry acid and a Brønsted-Lowry base to form ammonium ion (NH_4^+), respectively. When the ammonia molecule is adsorbed on the water clustering layer, it can accept a proton (H^+) from the surrounding water molecules, thereby forming the ammonium ion. Through the reaction (2), a NH_3 molecule can generate ammonium ion (NH_4^+) by reacting with water molecules through acid-base reaction. With the similarity in the molecular structure, we can note that two species, H_3O^+ and NH_3, could have very similar material properties.

These molecules are referred to as the isoelectronic chemical species, indicating similar chemical properties because N and O^+ have the same electronic configurations ($1s^2 2s^2 2p^3$). Therefore, chemical species having the same isoelectronicity shows an identical process for electron donating and electron withdrawing during the chemical reaction.

Figure 4.12 shows the schematic illustration representing the sensing mechanism of polymer electrolyte-based NH_3 sensor. The fundamental sensing mechanism can be explained not by only the Grotthuss mechanism as previously described but by also the solvation model that describes the arrangement of hydronium ions along with surrounding water molecules. As seen in Figure 4.12A, a unit water cluster forms the Eigen cation that the centered hydronium ion is strongly connected with three neighboring water molecules via the hydrogen bond [198]. This is very stable solvation state of water clusters and known as the static cation. When an NH_3 molecule meets with this water cluster, it could be positioned in a series of water clusters comprised of water molecules, hydronium ion, and NH_3 molecule, as shown in Figure 4.12B. At this moment, the proton is shared not only equally by two water molecules in a symmetric hydrogen bond but also between water and NH_3 molecule by an asymmetric hydrogen bond. This rearranged cluster is referred to as the Zundel cation representing the dynamic cation [198]. In the present work, we suggest the modified Eigen and Zundel cation by replacing hydronium ion with NH_3 molecule. The isoelectronicity between hydronium ion and NH_3 molecule enables them to play a role of an intermediate bridge for proton jumping based on the Grotthuss mechanism.

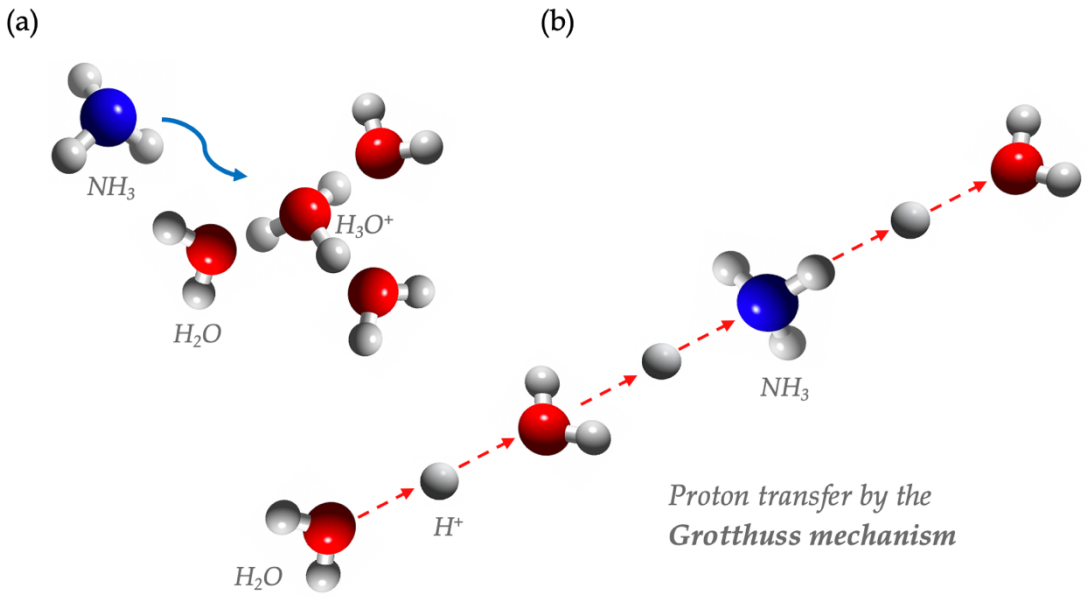

Figure 4.12 Sensing mechanism of novel polymer electrolyte-based NH_3 sensor comprised of the plasticized PVA with glycerol. (a) Schematic illustration of the adsorption of NH_3 molecule on the water cluster solvated into the Eigen cation state. (b) Schematic representation of the modified Zundel cation model exhibiting the substitution of NH_3 molecules for the hydronium ion (H_3O^+). Due to the isoelectronicity of NH_3 molecules with hydronium ion, protons are still able to tunnel across a series of hydrogen bonds between NH_3 molecules and water molecules base on the Grotthuss mechanism.

The presented polymeric NH_3 vapor sensor exceeds the performance of SWCNT-based sensor. This result can be attributed to new sensing mechanism based on the proton jumping through a series of hydrogen bonds. Therefore, the ability to form the hydrogen bond with NH_3 molecules is a requisite for sensing material. In the present work, we exploit glycerol as a conducting plasticizer that makes PVA flexible and electrically conductive. In addition to the plasticizing effect, the glycerol has a strong capability to form the hydrogen bond. To estimate the contribution of hydrogen bond to the solubility of polar materials, the Hansen solubility parameters can be used and expressed as the following:

$$\delta_t = \sqrt{\delta_d{}^2 + \delta_p{}^2 + \delta_h{}^2} \quad \text{(Eq. 29)}$$

where δ_t is the total solubility parameter ($[cal/cm^3]^{1/2}$ or $[MPa]^{1/2}$), δ_d is the solubility parameter due to the dispersion force, δ_p is the solubility parameter caused by the polar interactions, and δ_h is the solubility parameter that can be attributed to the hydrogen bond in polar systems.

The glycerol is known as a reactive chemical having the largest value of hydrogen bonding component (δ_h = 29.3 $MPa^{1/2}$) among polyhydric alcohols at room temperature, as seen in Table 6 [199]. Therefore, the glycerol can generate the uniform solvation resulting from the formation of water clusters due to its high δ_h.

	δ_t	δ_d	δ_p	δ_h
Ethylene glycol	32.9	17.0	11.0	26.0
Glycerol	36.1	17.4	12.1	29.3
Propylene glycol	30.2	16.8	9.4	23.3
Diethylene glycol	29.9	16.2	14.7	20.5
Triethylene glycol	27.5	16.0	12.5	18.6
Dipropylene glycol	31.7	16.0	20.3	18.4
Water	47.8	15.6	16.0	42.3

Table 6 Hansen parameters of the polyhydric alcohols along with water [199].

When NH_3 vapor is absorbed on water clusters formed on the sensing material, it generates the strong hydrogen bonds with the neighboring water molecules. This is because the hydrogen bonding energy between NH_3 and water (29 kJ/mol) is much

stronger than that between hydronium ion and water (18 kJ/mol) [200]. As seen in Figure 4.12B, the proton can transfer through not only the tentative hydrogen bonds formed by NH_3 and water molecules but also the conventional hydrogen bonds between water molecules. A considerable number of hydrogen bond provide a bridge for proton hopping based on the Grotthuss mechanism. Consequently, the adsorption of NH_3 molecules on the sensor surface induces a dramatic increase in the electrical conductivity, thus yielding outstanding sensing performances in novel chemical sensor.

4.3.8 Stretchable NH_3 vapor sensors

We demonstrate herein the stretchable chemical vapor sensor based on the plasticized PVA electrolyte with glycerol. Figure 4.13 shows that the sensitivity for novel stretchable polymer electrolyte-based NH_3 sensor and SWCNT-based sensor. As described earlier, the sensitivity is defined in terms of resistance variation, $\Delta R/R_0\ [\%] = (R_g - R_0)/R_0 \times 100$, where R_g is the resistance upon gas exposure and R_0 the baseline resistance before exposure to gas. As shown in Figure 4.13, the novel polymeric sensor represents a consistent sensitivity (20-23 %) when exposed to 10 ppm NH_3 at 25°C under stretching compared with the SWCNT-based sensor having no stretchability. This remarkable sensing capability of novel polymeric sensor in the stretched state results from the stable conducting property of PVA-glycerol electrolyte as a sensing material along with an excellent stretchability due to the plasticization with glycerol. Therefore, the presented polymeric chemical sensor could be applicable to robots, artificial skin, and wearable sensors attachable to the clothes for tasking a rescue in the disaster area.

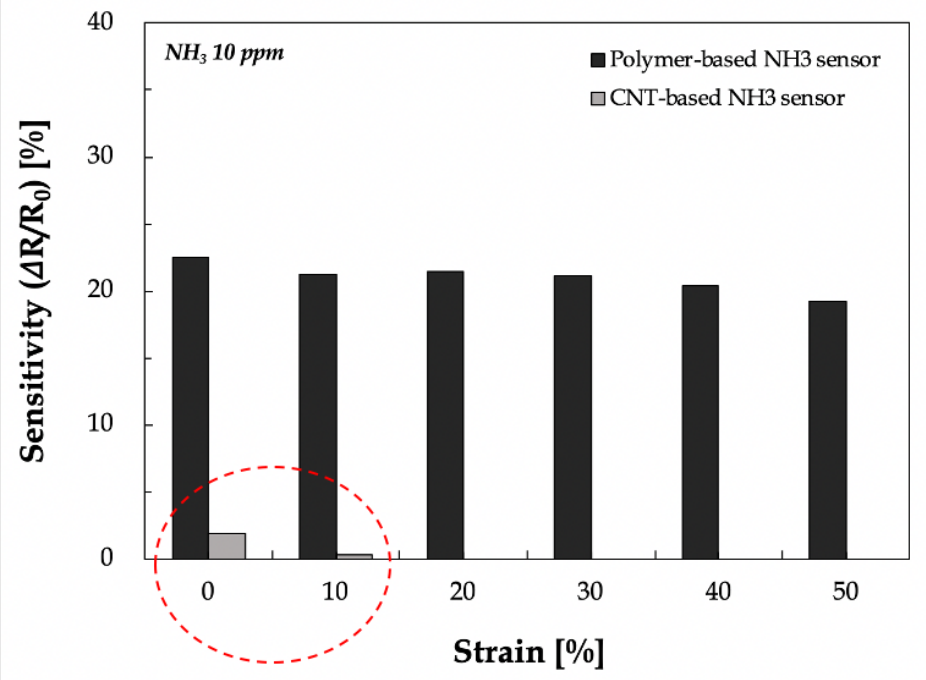

Figure 4.13 Sensitivity for novel stretchable polymer electrolyte-based NH_3 sensor and SWCNT-based sensor. The novel polymeric sensor represents a consistent sensitivity (20-23 %) when exposed to 10 ppm NH_3 at 25°C under stretching compared with the SWCNT-based sensor having no stretchability.

4.4 Conclusions

In summary, we have been investigating the development of a novel stretchable NH_3 sensors based on the polymer electrolyte comprised of the plasticized PVA with glycerol. This conductive plasticizer, glycerol endows PVA with a flexibility and remarkable sensing capability in response to NH_3 exposures. The presented polymeric sensor exceeds the performance of SWCNT-based sensors in terms of sensitivity,

selectivity, and stretchability. The novel polymeric sensor shows an order of magnitude higher sensitivity and faster recovery than those of the SWCNT-based sensors when exposed to NH_3 vapor at room temperature. The water clusters formed by the dehydration reaction between PVA and glycerol leads to the facile adsorption of NH_3 molecules on the sensor surface. This water clustering layer would form the nonhomogeneous surface rather than a monolayer. For this reason, the sensitivity of novel polymeric sensors is in good agreement with the Freundlich isotherm adsorption model. The electrically conducting characteristic of PVA-glycerol electrolytes is a major motif of chemical sensing. An increase in the electrical conductivity with the concentration of glycerol results from the formation of percolative pathways via hydrogen bonding networks for proton jumping. Based on the solvation of NH_3 molecules in water, the modified Eigen and Zundel cation model has been suggested for further understanding of sensing mechanism. Due to the much stronger hydrogen bond of NH_3-water than water-water, NH_3 molecule would be readily adsorbed to the water clusters formed on the sensor surface. The proton tunnels across a series of hydrogen bonds via breaking and reformation process, thus enhancing the sensing signal of chemical sensors by reducing the electrical resistance. This behavior of the proton hopping based on the Grotthuss mechanism is an indispensable requisite to develop novel polymeric NH_3 sensor with a higher sensitivity and faster recovery. In addition to remarkable sensing ability, the novel polymeric sensor represents a superior stretchability to SWCNT-based sensors due to the plasticization of glycerol. Therefore, the flexible polymer electrolyte-based NH_3 sensor studied in this present work will provide new opening insights to create commercially available and cost-effective chemical sensors.

Chapter 5

Conclusion and Future Work

5.1 Summary of thesis

Self-healing polymers have received a burgeoning amount of interest and have been demonstrated by the use of physical entanglement, chemical reaction, and non-covalent bonds. In this thesis work, an ultra-fast self-healing adhesive (SHA) has been developed by strategically programming a dynamic network comprised of metal-ligand complexes. The mechanical and adhesive properties of the materials can be conveniently tuned by varying several material parameters such as the molar ratio of metal and ligand as well as the moisture contents. The simple material design based on the dynamic coordination bond enables remarkable self-healing properties under ambient conditions without any interventions. Compared to the conventional self-healing polymers based on the hydrogen bond, the transient coordination bond may serve as a versatile method to develop ultra-fast and autonomous self-healing polymers. Novel self-healing polymer allows us to have a practical potential as a self-healing adhesive (SHA) with re-bondable and adjustable adhesion. For this reason, novel ultra-fast SHA comprised of zinc ions and

PVA as a ligand is intensively investigated to explicate the principle of self-healing based on the kinetics for complex formation. As a major finding, water molecules within the polymer could form the undesirable complexes with zinc ions inhibiting the self-healing reaction. This observation is the first direct evidence that zinc ions under dehumidification process which lowers an activation energy generate the preferable zinc-PVA complexes, which can subsequently undergo the formation of dynamic and reversible bonds. On account of this mechanism, the SHA having the high chain mobility resulting from the amorphous structure of SHA with a very low T_g of around -4 ℃ represents ultra-fast self-healing ability when damaged. In addition to the prominent property of pressure sensitive adhesives (PSAs), the SHA is optically transparent with a low haze of less than 1 %, which enables it to be exploited as a platform of flexible and foldable displays. Overall, the SHA would open up a new opportunity for the application of stretchable electronics, biomedical sensors, shock absorbing materials, and special adhesives that is applicable to a safety laminated glass in automobile industry.

It is also demonstrated that an ultra-stretchable and self-healable strain sensor based on the SHA with a dynamic coordination bond. The presented sensor surpasses the performance of previously reported state-of-the-art stretchable strain sensors in terms of stretchability, skin attachability, and self-healing capability. The self-healable and ultra-stretchable sensor can easily be fabricated via the metal-ligand complexed self-healing polymer having an electrically conductive property that endows it with consistent and reliable sensing performance. Furthermore, the SHA-based strain sensor exhibits a repeatable self-healing ability at room temperature with a stable sensing performance and

re-bondable adhesion to skin when self-repaired. Because of its intrinsically amorphous structure, the observed sensitivity ($\Delta R/R_0$) is consistent with the configuration of Gaussian chain model in responses to strain. Likewise, the SHA-based wearable sensor can be directly attached on the skin in order to accurately detect complex human motions. Compared with the previously reported sensors, the gauge factor of the composite-type strain sensor comprised of the SHA with AgNWs has been dramatically improved, thus rendering it to be worked from small strain to extreme strain. Overall, with high stretchability, predictable responses, autonomous self-healing ability, and ease of processing, the applications of SHA-based sensor can be extended to pressure sensing, health monitoring, medical diagnosis, soft robotics, and artificial skin.

In this dissertation work, the development of a novel stretchable NH_3 sensors based on the polymer electrolyte comprised of the plasticized PVA with glycerol is extensively investigated. Glycerol as a conductive plasticizer endows PVA with a flexibility and remarkable sensing capability in response to NH_3 exposures. The presented polymeric sensor exceeds the performance of SWCNT-based sensors in terms of sensitivity, selectivity, and stretchability. The novel polymeric sensor shows an order of magnitude higher sensitivity and faster recovery than those of the SWCNT-based sensors when exposed to NH_3 vapor at room temperature. The water clusters formed via the dehydration reaction between PVA and glycerol leads to the facile adsorption of NH_3 molecules on the sensor surface. This water clustering layer would form the nonhomogeneous surface rather than a monolayer. For this reason, the sensitivity of novel polymeric sensors is in good agreement with the Freundlich isotherm adsorption

model which describes the molecular adsorption on the heterogeneous surfaces. The electrically conducting characteristic of PVA-glycerol electrolytes is a major motif of chemical sensing. An increase in the electrical conductivity with the concentration of glycerol results from the formation of percolative pathways via hydrogen bonding networks for proton jumping. Based on the solvation of NH_3 molecules in water, the modified Eigen and Zundel cation model has been suggested for further understanding of sensing mechanism in this work. Due to the much stronger hydrogen bond of NH_3-water than water-water, NH_3 molecule would be readily adsorbed to the water clusters formed on the sensor surface. The proton tunnels across a series of hydrogen bonds via breaking and reformation process, thus enhancing the sensing signal of chemical sensors by reducing the electrical resistance. This behavior of the proton hopping based on the Grotthuss mechanism is an indispensable requisite to develop novel polymeric NH_3 sensor with a higher sensitivity and faster recovery. In addition to remarkable sensing ability, the novel polymeric sensor represents a superior stretchability to SWCNT-based sensors due to the plasticization effect of glycerol. Therefore, the flexible polymer electrolyte-based NH_3 sensor studied in this present work will provide new opening insights to create commercially viable and cost-effective chemical sensors.

5.2 Future works

5.2.1 Medical sensors and wound patches

The presence of the dynamic bond has quite efficiently evolved the self-healing ability of elastomers. However, to find wider application of self-healing polymers in reality, a variety of measurable properties need to be extensively studied. Despite significant characteristics of the SHA involving ultra-fast self-healing and electrical conductivity, the realization of commercially viable electronics is limited due to little information on material properties. In this respect, an impedance sensing device based on the SHA is envisioned to be attractive candidates when provided with impedance spectroscopy as an essential property.

It is known that impedance is robustly correlated with tissue health across multiple animals and wound types [96]. From an electrical perspective, a cell can be represented as an ion-rich conductive center (cytoplasm) embedded in an ion-rich conductive medium (extracellular fluid), separated by a relatively non-conductive barrier (cell membrane). These ion-rich media can be described in terms of their ability to conduct charge by modelling them as resistances. Likewise, barriers to charge flow (for example, the cell membrane) can be modelled as electrical capacitances. The combination of the loss terms (that is, resistance) and energy storing terms (that is, capacitance and inductance) is known as electrical impedance. Because the impedance of a material is a function of the electrical signal being passed through it, impedances are measured across many frequencies to form a spectrum plot, which is known as impedance spectroscopy.

Certain disturbances of the biological structures result in detectable changes in the impedance spectrum. For example, in vitro impedance measurements have been shown to detect cell proliferation and cell–drug interaction, quantify biomass in suspensions and create two-dimensional images of cell migration. Much of this work utilizes the electrical 'signature' of the cell membrane: a well-functioning cell membrane is relatively impermeable and thus behaves like a capacitor in the presence of electric current. Cell damage or death results in a loss of membrane structure and integrity, allowing ions and current to pass through the membrane. Thus, damaged cells will exhibit higher electrical conductance through the membrane and less capacity to store charge; in other words, the cell behaves less like a capacitor and more like a resistor. We could demonstrate the possibility of a flexible and electronic device that non-invasively maps pressure-induced tissue damage, even when such damage cannot be visually observed by using impedance spectroscopy of the SHA. The feasibility of an automated, non-invasive 'smart bandage' for early detection of pressure ulcers might be provided with our prospective study.

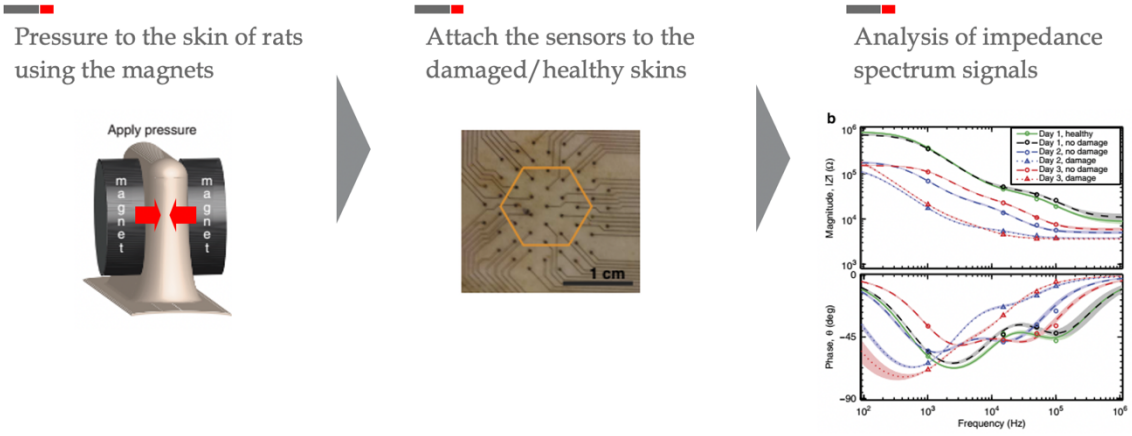

Figure 5.1 Expected experimental procedures for detection and diagnosis of pressure ulcers using the SHA-based impedance sensor. Impedance spectral data are referred to [96].

5.2.2 Self-healable electroluminescent devices

Electroluminescent (EL) devices have been developed as indispensable elements in various commercially viable electronic systems in daily life. A variety of EL devices have been applied in different fields, such as bioinspired soft robotics for visual disguise and epidermal electronics, flexible and stretchable electronics, wearable electronics, displays, and sensors. Most of the EL-integrated systems is vulnerable to the mechanical deformations and the concomitant damage. The degradation of EL device performance is always concerned if the strain exceeds the withstanding limit. Maintaining and replacing a faulty component in a multifunctional integrated electronic system would be either intractable or costly. Therefore, developing an effective strategy to avoid or minimize the failure or decay of device performances under mechanical deformations is essential to realize the stretchable EL devices in the aspect of extending the lifetime of a device. The strategy of self-healing is an emerging solution to renovate and revive the EL device performances in situ. However, the majority of self-healing performances achieved for multilayered electronic devices such as light-emitting elements were based on the self-healing properties of one constituent layer, whereas other functional layers were not treated in terms of self-healing. Designing and developing omni-layer-healable electronic devices are more challenging than realizing single-layer-healable devices because each functionalized constituent layer needs to be self-healable in a complex configuration. In order to achieve self-healing EL devices, all constituent layers such as electrodes, light-emitting layers, and other functionalized layers should be self-healable.

The ultra-fast self-healing ability of the SHA could endow light-emitting devices with the capability to store their structure, physicochemical, and mechanical properties

from damage. With the innate characteristics of our SHA, the design of electrodes for self-healing light-emitting devices requiring several criteria such as visible-light transmittance and conductivity, as well as self-healing ability can be easily available. For further investigation, the modified SHA including electroluminescent materials or phosphors such as ZnS could be used as a light-emission layer in the self-healable light-emitting devices. G. Liang et al. studied the highly self-healable EL devices with excellent self-healing capability by adopting modified self-healable polyacrylic acid (PAA) hydrogel that contains NaCl as an ionic electrode and self-healable polyurethane (PU) that contains ZnS particles as a phosphor composite layer, as shown in Figure 5.2 [208].

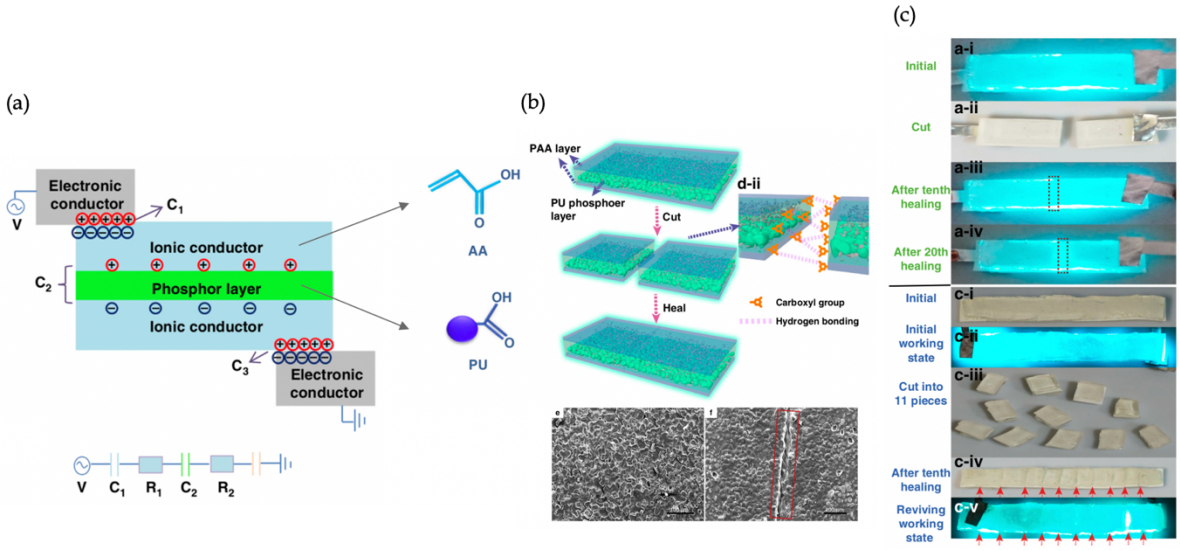

Figure 5.2 Schematic illustrations of self-healable electroluminescent devices. (a) Schematic principle and structure of the self-healable EL device and equivalent circuit of an EL device, where C represents the corresponding capacitor and R represents the resistance of the ionic conductor. (b) Cutting–healing process of the as-fabricated self-healable EL device and SEM images of healed PU phosphor layer before and after self-healing; the healed wound was represented by the red rectangle. (c) Photographs of the EL device subjected to multiple cutting–healing times [208].

5.2.3 Self-healable batteries

The self-healing feature is also desirable for energy storage devices because the lifetimes of many rechargeable batteries are limited by the similar dilemma of mechanical fractures over the cycling process. It is known that electrochemical reactions in battery materials normally result in structural changes, which may give rise to degradation as well as damage, and ultimately render the battery to be non-functional with cycling. Silicon anodes for lithium-ion batteries are vulnerable to mechanical failures because they react with greater amounts of lithium and thus undergo more drastic structural changes. Despite silicon anodes have a theoretical specific capacity ten times higher than that of conventional graphite anodes, usually suffers from fast capacity decay and short cycle-life. This limitation is mainly caused by the volume expansion by up to three times on full lithium insertion (lithiation) and significant contraction on lithium extraction (delithiation). These extreme volumetric changes could cause cracking and pulverization in the electrode, which lead to loss of electrical contact and excessive solid–electrolyte interphase (SEI) growth. Even when incorporating the silicon materials with metal alloys or high-modulus polymer binders, mechanical fractures and damages still occur. C. Wang et al. investigated novel silicon anodes comprised of silicon microparticles coated with a thin layer of hydrogen bond mediated self-healing polymer to improve the cycling lifetime of lithium batteries [209]. The ultra-fast self-healing ability of the SHA may render lithium batteries to be healed autonomously without any interventions from the mechanical damage in the electrode, thus increasing the lifetime of anodes.

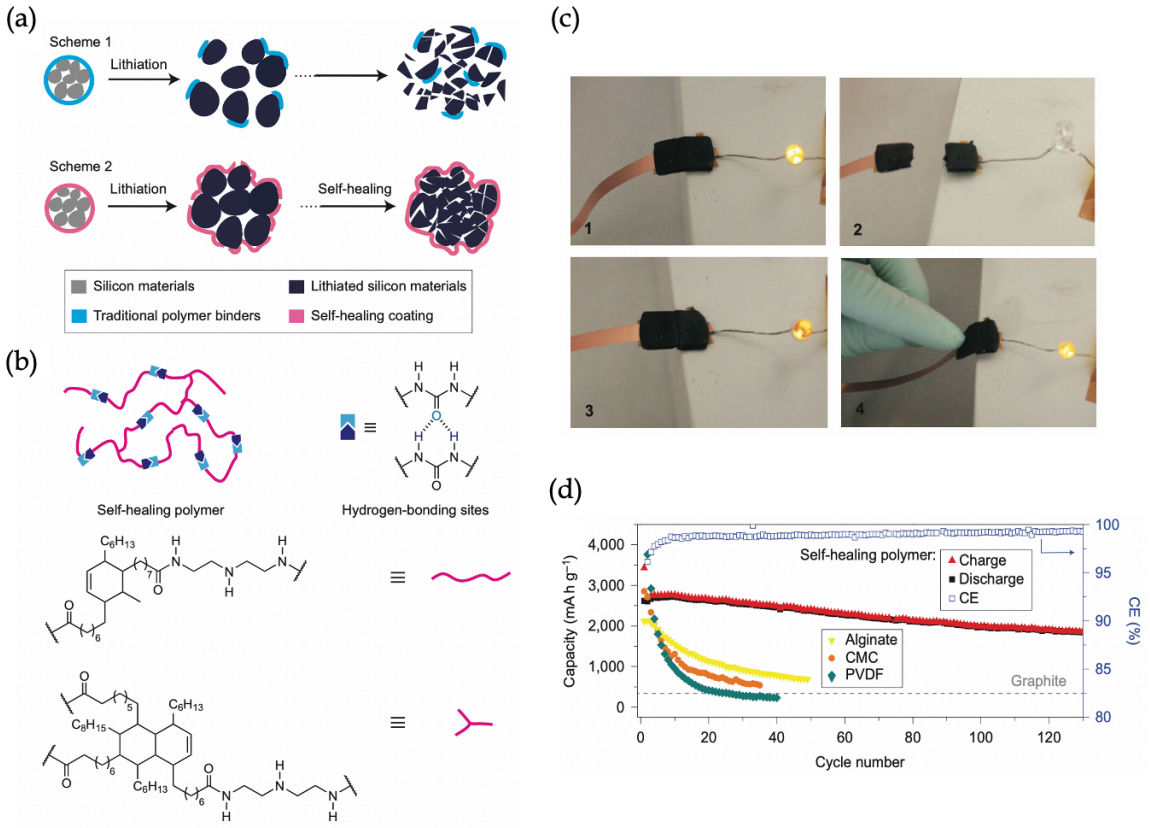

Figure 5.3 Schematic representations of the self-healing electrode. (a) Scheme 1: schematic illustration of the design and behavior of a conventional silicon electrode that shows failure of the electrode because of cracking in particles and polymer binder, which results in loss of electrical contact. Scheme 2: schematic illustration of the design and behavior of our stretchable self-healing electrode that shows the maintaining of electrical contact between the broken particles and no cracks in the polymer binder because of the stretchability and incorporation of self-healing chemistry. (b) Chemical structure of the self-healing polymer. Magenta lines, polymer backbones; light-blue and dark-blue boxes, hydrogen-bonding sites. (c) Demonstration of the electrical and mechanical self-healing capability of the conductive composite using a battery-powered circuit with the composite self-healing polymer as the conductive pathway that connects the LED to the battery. (d) Capacity retention of silicon microparticle electrodes with different polymer additives, including the SHP/CB composite and conventional polymer binders (PVDF, CMC and alginate). All samples were cycled at the same charge/discharge rate of C/10 with a potential window of 0.01–1 V versus Li/Li^+. The grey dashed line indicates the theoretical capacity of a graphite electrode [209].

5.2.4 Self-healable cementitious materials

In a similar work, self-healing of cementitious materials can be investigated. Concrete is arguably the most important construction material. Whereas concrete shows a strong material property in compression, it tends to be brittle in tension. Engineered cementitious composites (ECC, also known as Bendable Concrete) has been designed to overcome the brittleness of concrete. ECC is a family of ductile concrete with a compressive strength ranging from 50 MPa to 200 MPa. Unlike high strength concrete, ECC has a design basis that does not aim at eliminating flaws, but rather controlling the size distribution of flaws so that controlled microcracking is allowed. With a tensile ductility of 2-5% and a self-controlled tight crack width less than 100 μm, ECC enables high damage tolerance of structural members even under fully reversed shear loading and impact loading. These microcracks with tight crack width contribute to the tensile ductility when overloaded, then subsequently undergo self-healing. The self-healing mechanism is an accelerated form of continued hydration and pozzolanic reaction. This damage management paradigm (as opposed to damage prevention) is similar with that of nature's nacre - the iridescent material on the inside of abalone shells. Similar to cement, nacre is made of brittle calcium carbonate platelets that slip over one another under load. The ductile deformation then undergoes self-healing to protect the soft body of the abalone. In many ways, ECC is designed for a self-healing function by emulating the amazing features of nature's nacre. ECC undergoes self-healing of crack damage requiring only the presence of air and water, as shown in Figure 5.4 [210]. It is estimated that in practical conditions cracks can be effectively healed by autonomous process if their width is less than 0.1 mm (and even up to 0.3 mm if material contains fiber,

specifically PVA fibers). PVA fiber having high polarity is able to restore water tightness and precipitate large quantities of self-healing substances to a greater extent than the polyethylene and polypropylene fibers [211]. Novel cementitious materials associated with our SHA with ductile and self-healable property my lead to a variety of improvements in concrete infrastructure and the construction industry.

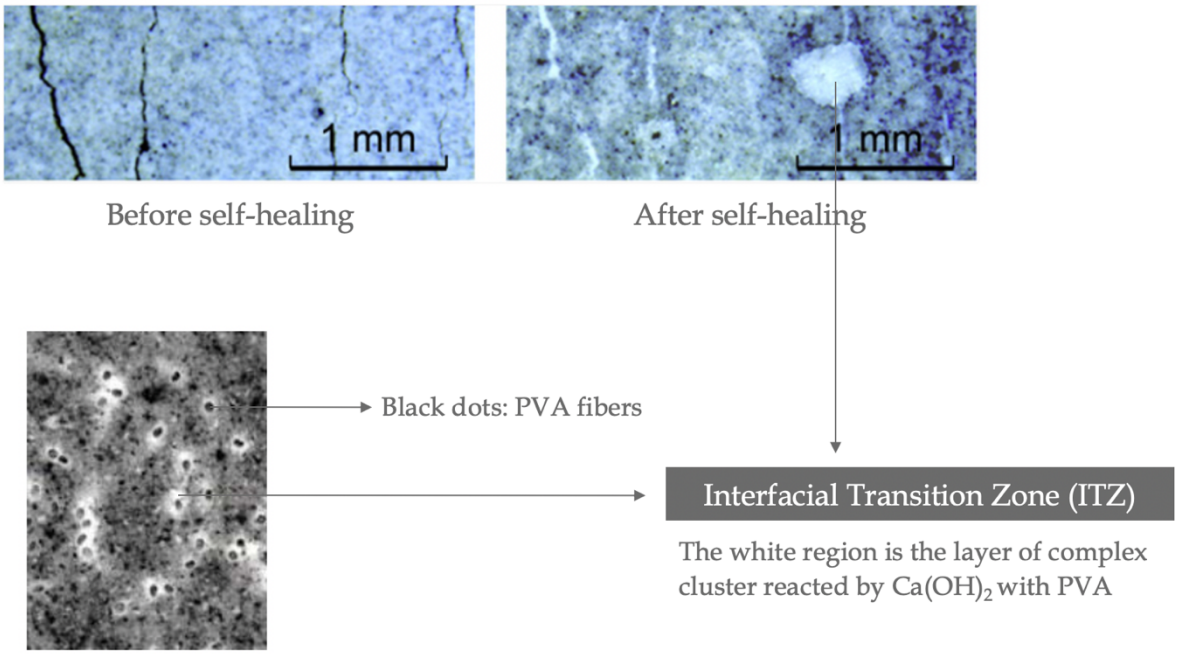

Figure 5.4 Self-healable engineering cementitious composite (ECC) which is also known as bendable concrete. Unlike high strength concrete, ECC has a design basis that does not aim at eliminating flaws, but rather controlling the size distribution of flaws so that controlled microcracking is allowed. With a tensile ductility of 2-5% and a self-controlled tight crack width less than 100 μm, ECC enables high damage tolerance of structural members even under fully reversed shear loading and impact loading. ECC self-heals crack damage when exposed to water and air. The white region shown in Figure 5.4 represents the layer of complex cluster reacted by $Ca(OH)_2$ with PVA fibers [210].

5.2.5 Self-healable coating for automotive

The automotive industry is the largest market for self-healing products (59%) with estimated expenditures of $27.69 billion by 2022 [212]. According to a new study by Grand View Research Inc., increasing demand for coatings owing to its ability to protect vehicles against UV radiation, acid rain and harsh weather is expected to drive market growth. Ramezanzadeh et al. studied the self-healing ability of automotive coatings that improve significantly the scratch resistance of the clearcoat using the addition of polysiloxane additive or nano-SiO_2 to polymer matrix [213]. As discussed in chapter 2 in this thesis, the SHA represents a substantial healing ability against the severe scratch formed on the coating surface. Therefore, a synergistic multilayer corrosion-resistant coating for a metal surface of automotive might be achieved by our SHA to improve the resistance to acids and saline water as well as adhesion properties.

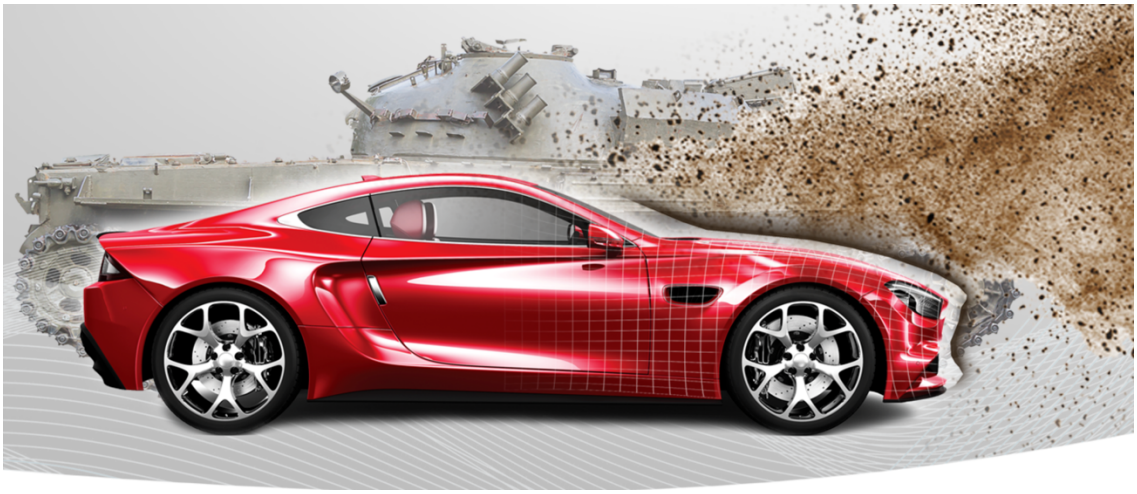

Figure 5.5 Schematic illustration of self-healing protection coating for automotive (https://www.crystgard.com).

5.2.6 Self-healing thermally conductive adhesives

U. Lapont et al. investigated thermally conductive composites with a temperature-triggered self-healing response by dispersing boron nitride (BN) or graphite particles into two types of polysulphide-based thermoset matrices [214]. The composites produced exhibit recovery of both cohesion and adhesion properties upon thermally activated

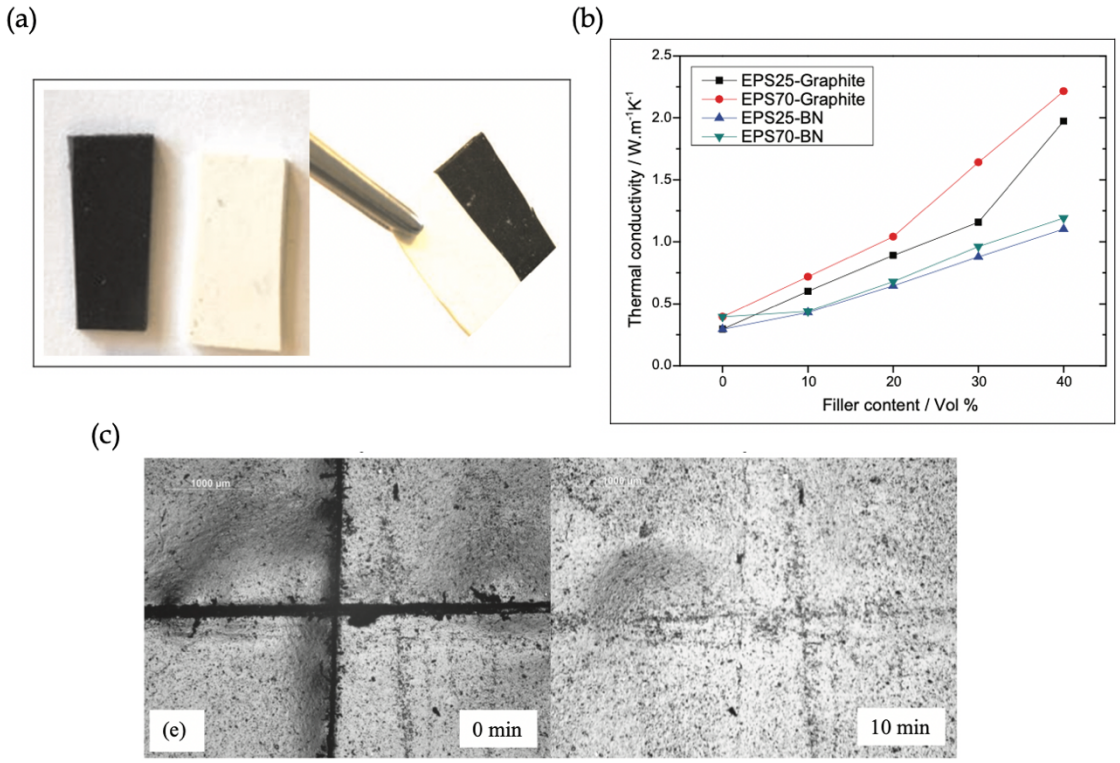

Figure 5.6 Self-healing thermally conductive adhesives. (a) A graphite- and BN-based thermally conductive composite before (left) and after (right) thermal mending at 65 °C. (b) Thermal conductivity as function of the filler content for BN- and graphite-based composites using epoxidized polysulphide (EPS) matrix (EPS25: aliphatic, EPS70: aromatic). (c) Micrograph showing the cohesive healing recovery of EPS25–20 vol% graphite composite before and after 10 min healing time at 65°C [214].

healing. The materials show full recovery of their initial adhesive strength during multiple healing cycles at a healing temperature (65°C). The composites behave differently regarding the cohesion recovery: 20%–100% recovery is achieved depending on the filler type, filler loading and the type of matrix. The thermal conductivities of the composites are 1 and 2 W/m K for the boron nitride and graphite-based composite, respectively. The thermal conductivity increases with the amount of filler, as seen in Figure 5.6.

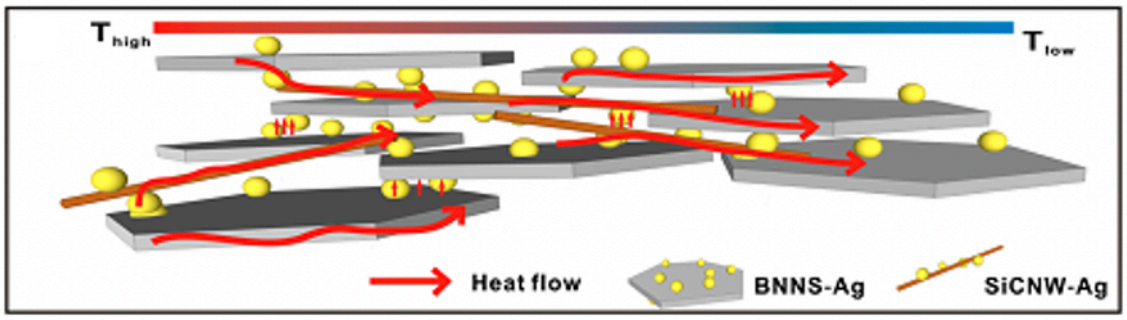

Figure 5.7 Proposed model of silver nanoparticles (AgNPs) and silicon carbide nanowires (SiCNWs) for thermal conduction [215].

Y. Yao et al. studied the thermally conductive composite paper comprised of two-dimensional (2D) boron nitride nanosheets (BNNSs) and one-dimensional (1D) silicon carbide nanowires (SiCNWs) decorated with AgNPs, and PVA as a polymer matrix [215]. Specifically, AgNPs are expected to pierce the PVA layer and link the BNNSs together, which would result in the formation of more thermally conductive pathways inside the composite film, as shown in Figure 5.7.

In the future work, we could design a novel kind of composite material with delicate interface and well-organized orientation. Novel composites based on the SHA associated with nano-fillers such as AgNW, BN, graphite, and graphene may also enable multifunctional materials such as thermally conductive adhesives. It is known that most of failure in electronic devices involving displays and LEDs is caused by the heat generated within the devices and/or the external conditions. Therefore, the SHA-based self-healing composite with thermal conduction properties could open up new opportunity to create smart materials and heat dissipation components for the industry of microelectronics, displays, construction, aerospace, and automotive.

APPENDICES

Appendix A

Correlation of Sensitivity of SHA-based Stretchable Sensors and True Stress induced by Chain Configurations based on the Gaussian Chain Model

We introduce herein the Gaussian chain model to fit with the sensitivity data obtained experimentally, as seen in Figure 3.5. We may understand that the sensing performance of SHA-based strain sensor could be related to the fundamental behavior of the Gaussian chain that has an entropy dependent elasticity. We will cover both macroscopic thermodynamics and statistical thermodynamics in pursuit of a molecular model to demonstrate the elastic response of SHA as crosslinked networks via metal-ligand complexes.

The first law of thermodynamics defines the change dU in the internal energy of a system (SHA) as the sum of the heat absorbed by the system, dq, plus the work done on the system, *dw*:

$$dU = dq + dw \qquad \text{(Eq. S1)}$$

The element of work is generally written -*PdV*, where *P* is the external pressure, but in conjunction with the increment of elastic work associated with an increment in elongation *dL*, it is:

$$dw = -PdV + fdL \qquad \text{(Eq. S2)}$$

When a tensile force is applied to strain sensors that exhibit a distortion like a stretching, *f*, *dL* and *dw* are all defined to be positive quantities. Thus, *dw* is positive when the sensor is stretched, on the other hand, *dw* is defined as a negative quantity when the elastomer snaps back to its original size. A positive *dV* and *dL* correspond to an expanded system during the elongation of elastomer. The second law of thermodynamics gives the change in entropy associated with the isothermal, reversible absorption of an element of heat *dq* as

$$dS = \frac{dq}{T} \qquad \text{(Eq. S3)}$$

With the substitution of *dw* from (Eq. S2) and the replacement of *dq* with *TdS*, (Eq. S1) becomes

$$dU = TdS - PdV + fdL \qquad \text{(Eq. S4)}$$

We now turn to the Gibbs free energy *G* defined as

$$G = H - TS \quad \text{(Eq. S5)}$$

The Gibbs free energy, which is generally the most appropriate for processes of importance in chemistry: P, T, and number of moles are the natural independent variables could be beneficial to derive the relationship between the force to stretch the SHA and the entropy.

Taking the derivative gives

$$dG = dH - TdS - SdT \quad \text{(Eq. S6)}$$

The enthalpy is defined by

$$H = U + PV \quad \text{(Eq. S7)}$$

The enthalpy can be also differentiated into

$$dH = dU + PdV + VdP \quad \text{(Eq. S8)}$$

With the substitution of (Eq. S8) into (Eq. S6)

$$dG = dU + PdV + VdP - TdS - SdT \quad \text{(Eq. S9)}$$

Combining (Eq. S9) with (Eq. S4) gives

$$dG = VdP - SdT + fdL \qquad \text{(Eq. S10)}$$

Thus establishing the desired connection between the stretching experiment and thermodynamics by replacing several terms by fdL.

Since G is a state variable and forms exact differentials, an alternative expression for dG is

$$dG = \left(\frac{\partial G}{\partial P}\right)_{T,L} dP + \left(\frac{\partial G}{\partial T}\right)_{P,L} dT + \left(\frac{\partial G}{\partial L}\right)_{P,T} dL \qquad \text{(Eq. S11)}$$

Comparing (Eq. S11) and (Eq. S10) enables us to write

$$f = \left(\frac{\partial G}{\partial L}\right)_{P,T} \qquad \text{(Eq. S12)}$$

We differentiate (Eq. S5) with respect to L, keeping P and T constant:

$$\left(\frac{\partial G}{\partial L}\right)_{P,T} = \left(\frac{\partial H}{\partial L}\right)_{P,T} - T\left(\frac{\partial S}{\partial L}\right)_{P,T} \qquad \text{(Eq. S13)}$$

The left-hand side of this equation gives f according to (Eq. S12):

$$f = \left(\frac{\partial H}{\partial L}\right)_{P,T} - T\left(\frac{\partial S}{\partial L}\right)_{P,T} \qquad \text{(Eq. S14)}$$

This expression could be called the equation of state for an elastomer, which is beneficial to demonstrate the elastic property of SHA. (Eq. S14) shows that the force required to stretch SHA as an elastomer can be divided into two contributions: one that measures how the enthalpy of the elastomer changes with elongation and another that measures the same effect on entropy. It can be assumed that the SHA is an ideal elastomer for which $(\partial H/\partial L)_{P,T} = 0$; in this case, (Eq. S14) reduces to

$$f = -T\left(\frac{\partial S}{\partial L}\right)_{P,T} \quad \text{(Eq. S15)}$$

The ideal elastomer can be taken account into an ideal gas in which molecules are noninteracting and so it makes no difference how far apart they are. Therefore, we can hypothesize that there is no change in the enthalpy of the SHA during the stretching process based on the following assumptions.

(1) No density change occurs during the extension due to the lack of intermolecular interactions within the SHA. This indicates that the average energy of interaction between different molecules is not changed. The fundamental concept of material design for the SHA is rooted to induce the dynamic bonding by lowering the interaction energy, thus enabling ultra-fast self-healing. The average interaction energy based on the dynamic coordination bonds is even distributed to the whole networks and then no change in the intermolecular energy takes place during the stretching. Moreover, zinc ions contribute to suppress the formation of other types of intermolecular interaction

such as hydrogen bonds. They could activate the weak and reversible ionic interactions with polymer ligands instead, thereby no enthalpy change can be assumed.

(2) No intramolecular contribution that arises from the conformational energy of each chain occurs in the SHA during the stretching process. The conformational energy could be determined by the relative population of *trans* and *gauche* conformers. Therefore, we can estimate that there is no change in the enthalpy resulting from the lack of conformers within the SHA.

(3) No crystallization takes place in the SHA during the stretching. There is certainly an enthalpy change associated with crystallization, so $(\partial H/\partial L)_{P,T}$ would not vanish if there is a stretching induced crystal formation which could be sometimes occurred in natural rubber.

As a result, (Eq. S15) demonstrates that the force to extend a polymer chain of ideal elastomer is a differential derivative of entropy in terms of the deformation. This stretching force could be estimated if the entropy change versus the deformation is clarified. We now proceed to use a molecular model to derive predictions for the stress-strain behavior of an ideal elastomer. We will begin by considering the force required to extend a single Gaussian chain, and then apply this result to an entire ensemble of crosslinked chains. The Boltzmann relation to define the entropy effect on the elasticity is:

$$S = kln\Omega \qquad \text{(Eq. S16)}$$

where S is the entropy, k is the Boltzmann's constant, and Ω is the number of possible states which demonstrate the chain configurations at a time. As then, the difference in entropy between two states of different thermodynamic probability is:

$$\Delta S = S_2 - S_1 = kln\frac{\Omega_2}{\Omega_1} \quad \text{(Eq. S17)}$$

Next we need to consider extending a single Gaussian chain of N units, with statistical segment length b. The single chain has one end fixed at the origin *(0, 0, 0)* and the other is held at (x_0, y_0, z_0) before stretching. The imposed end-to-end distance of this single chain is:

$$h_0 = ({x_0}^2 + {y_0}^2 + {z_0}^2)^{1/2} \quad \text{(Eq. S18)}$$

In a stretched state, the single Gaussian chain fixed at both ends, *(0 ,0, 0)* and *(x, y, z)*, may have the end-to-end distance, h:

$$h = (x^2 + y^2 + z^2)^{1/2} \quad \text{(Eq. S19)}$$

These end-to-end distances may be compared to the equilibrium mean square end-to-end distance:

$$\langle h^2 \rangle = Nb^2 \quad \text{(Eq. S20)}$$

The number of ways that this chain can satisfy the imposed constraint before stretching is given by the Gaussian distribution:

$$P_i(N, \vec{h_0}) = \left(\frac{3}{2\pi < h^2 >} \right)^2 exp \left[-\frac{3{h_0}^2}{2 < h^2 >} \right] \quad \text{(Eq. S21)}$$

$$P_i(N, \vec{h_0}) = \beta^{3/2} exp[-\pi\beta {h_0}^2] \quad \text{(Eq. S22)}$$

where we define the normalization factor, β as

$$\beta = \frac{3}{2\pi < h^2 >} = \frac{3}{2\pi N b^2} \quad \text{(Eq. S23)}$$

And the subscript "i" on P denotes the "initial" state. We then extend this description to the end-to-end distance after stretching, thus the corresponding "final" state distribution function P_f is

$$P_f(N, \vec{h}) = \beta^{3/2} exp[-\pi\beta h^2] \quad \text{(Eq. S24)}$$

We now associate the number of possible conformations with the entropy defined by (Eq. S16), that is, we can define Ω

$$\Omega = AP \quad \text{(Eq. S25)}$$

where A is some unspecified proportionality constant. Then we can demonstrate the change in entropy

$$\Delta S_{single} = kln\Omega_f - kln\Omega_i = kln(AP_f) - kln(AP_i) = kln\left(\frac{P_f}{P_i}\right) \quad \text{(Eq. S26)}$$

$$\Delta S_{single} = -k\pi\beta(h^2 - {h_0}^2) \quad \text{(Eq. S27)}$$

where we use the subscript "single" to emphasize that this is a single chain calculation. The unknown constant A cancels out when we calculate the change in entropy. So far, we have proceeded to correlate the change in entropy with the end-to-end distances by using the concept of P, which indicates a statistical state of end-to-end distance of a single polymer chain. If P follows the Gaussian distribution, this polymer chain could be the Gaussian chain.

We now consider displaying the change in entropy of a single Gaussian chain by using more practical parameter such as draw ratio. Then we will develop the model to demonstrate the force to extend an ideal network made up of Gaussian strands, not a single chain. We now impose a macroscopic deformation on the bulk polymer, namely, the polymer might be stretched out into x direction. The deformation of bulk elastomer is restricted by three draw ratios λ_x, λ_y, and λ_z, given by L_x/L_0, L_y/L_0, and L_z/L_0, respectively. If we begin with a cube of material of length L_0 on each side, that cube will be deformed to a three-dimensional volume element with sides L_x, L_y, and L_z. This deformational behavior of bulk elastomer could be utilized to demonstrate the microscopic deformation

of end-to-end vector of each single chain. The end-to-end vector of a single Gaussian chain is deformed so that the coordinates of one end transform from *(x_0, y_0, z_0)* to *(x, y, z)* during stretching, when the other end is fixed at the origin. This concept is sometimes called *affine junction assumption*: each junction point corresponding to one end point is deformed in proportion to the macroscopic deformation. At this point, (Eq. S27) could be re-written by

$$\Delta S_{single} = -k\pi\beta[(\lambda_x{}^2 x_0{}^2 + \lambda_y{}^2 y_0{}^2 + \lambda_z{}^2 z_0{}^2) - (x_0{}^2 + y_0{}^2 + z_0{}^2)] \quad \text{(Eq. S28)}$$

$$\Delta S_{single} = -k\pi\beta[(\lambda_x{}^2 - 1)x_0{}^2 + (\lambda_y{}^2 - 1)y_0{}^2 + (\lambda_z{}^2 - 1)z_0{}^2] \quad \text{(Eq. S29)}$$

It is assumed that there is no volume change during the deformation,

$$V = V_0,\ xyz = x_0 y_0 z_0 \quad \text{(Eq. S30)}$$

Thus, we can derive the following relation:

$$\lambda_x \lambda_y \lambda_z = 1 \quad \text{(Eq. S31)}$$

Above all, if this deformation is based on the uniaxial extension to x direction with $\lambda_x = \lambda$, and thus

$$\lambda_y = \lambda_z = \frac{1}{\sqrt{\lambda}} \quad \text{(Eq. S32)}$$

We now note that the Gaussian chain shows a random chain configuration without any directional dependence, thus x_0, y_0, and z_0 may have the same value which is on average the equilibrium mean square end-to-end distance:

$$x_0{}^2 = y_0{}^2 = z_0{}^2 = \frac{Nb^2}{3} \qquad \text{(Eq. S33)}$$

With the substitution of (Eq. S23), (Eq. S32) and (Eq. S33) into (Eq. 29), the change in entropy of a single Gaussian chain can be expressed by

$$\Delta S_{single} = -\frac{k}{2}\left(\lambda^2 + \frac{2}{\lambda} - 3\right) \qquad \text{(Eq. S34)}$$

Assumed that the SHA is comprised of η the Gaussian chains, the change in entropy of bulk SHA can be expressed:

$$\Delta S = -\frac{\eta k}{2}\left(\lambda^2 + \frac{2}{\lambda} - 3\right) \qquad \text{(Eq. S35)}$$

where η is the total number of elastically effective Gaussian chains and ΔS is the change of entropy for an entire ensemble of crosslinked chains.

The force required to extend the SHA is given by

$$f = -T\left(\frac{\partial \Delta S}{\partial L}\right) = -\frac{T}{L_0}\left(\frac{\partial \Delta S}{\partial \lambda}\right) = \frac{\eta k T}{L_0}\left(\lambda - \frac{1}{\lambda^2}\right) \qquad \text{(Eq. S36)}$$

If we now divide both sides of (Eq. S36) by the cross-section area normal to the stretching direction, we can obtain the true stress applied to the SHA which works as the strain sensor:

$$\sigma_t = \frac{f}{Area} = \frac{f}{L_y L_z} = \frac{f}{\lambda_y L_0 \cdot \lambda_z L_0} = \frac{f}{\frac{1}{\sqrt{\lambda}} L_0 \cdot \frac{1}{\sqrt{\lambda}} L_0} = \frac{\lambda f}{{L_0}^2} \qquad \text{(Eq. S37)}$$

$$\sigma_t = \frac{\lambda}{{L_0}^2} \frac{\eta k T}{L_0} \left(\lambda - \frac{1}{\lambda^2} \right) = \frac{\eta k T}{{L_0}^3} \left(\lambda^2 - \frac{1}{\lambda} \right) \qquad \text{(Eq. S38)}$$

$$\sigma_t = \frac{\eta k T}{V} \left(\lambda^2 - \frac{1}{\lambda} \right) \qquad \text{(Eq. S39)}$$

where V is the total volume of SHA, $V=L_0^3$. This (Eq. S39) represents the principal result of this molecular network theory. So far, we have proceeded to derive the prediction model for the stress-strain behavior of SHA. As seen in Figure 42, the sensitivity of SHA-based strain sensor is in good agreement with (Eq. S39), thereby enabling to estimate the following relation.

$$\frac{\Delta R}{R_0} = \frac{\eta k T}{V} \left(\lambda^2 - \frac{1}{\lambda} \right) \qquad \text{(Eq. S40)}$$

The above relation represents that the sensitivity of SHA-based strain sensor might be directly relevant to the true stress applied to the sensor. In addition, it can be seen that (Eq. S40) may be further reasonable when the material comprising of strain

sensors indicates the elastic response of crosslinked networks based on the Gaussian chains. We have herein established the connection between the sensing performance and the material property via exploring from macroscopic thermodynamics to statistical thermodynamics, thus enabling to develop the stretchable sensor with the justification for its working mechanism.

Appendix B

Percolation Model describing the Correlation between Electrical Conductivity of AgNWs Network and AgNW Concentrations

The synthesized AgNWs were used to fabricate electrodes of chemical sensor in this thesis work. A percolative network of AgNWs was formed through the vacuum assisted filtration (VAF) method, as shown in Figure 4.1. The measured electrical resistance of this AgNWs network was 1-5 Ω/sq^2 so that it was applied to the electrodes of NH_3 sensors, as seen in Figure 4.2. We demonstrate herein the percolation model describing the correlation between the conductivity and the AgNW concentrations.

When the AgNWs network is formed on a substrate as shown in Figure S.1, the number density of AgNWs can be calculated as the following:

$$N = \frac{CV}{\rho_{Ag}\pi\left(\frac{D}{2}\right)^2 L} \Big/ \pi\left(\frac{D_m}{2}\right)^2 \qquad \text{(Eq. S41)}$$

where, N [#/m^2] is the number density of AgNWs, C [g/mL] is the concentration of AgNWs, V [mL] is the volume of AgNW solution used in the VAF process, ρ_{Ag} is the

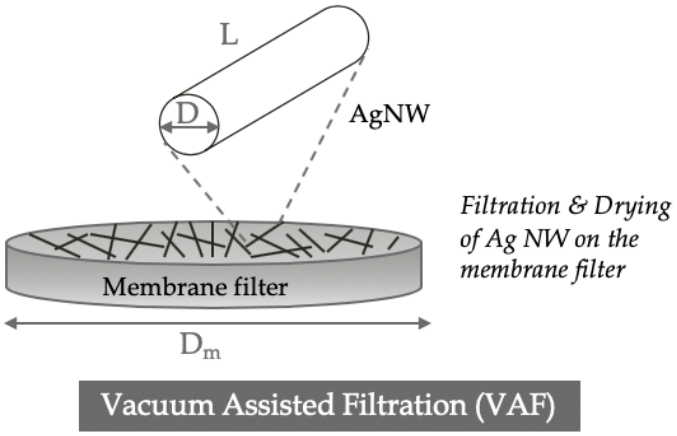

Figure S.1 Schematic illustrations of AgNWs network formed on a membrane filter via vacuum assisted filtration (VAF) method and a single AgNW with a diameter of D and length of L.

density of bulk silver (10.5 g/mL), D [m] is the diameter of AgNW, L [m] is the length of AgNW, and D_m [m] is the diameter of the membrane filter.

The percolation model for AgNWs network can be expressed as below:

$$\sigma = \sigma_o (N - N_c)^s \qquad \text{(Eq. S42)}$$

where σ is the electrical conductivity of AgNWs network, σ_0 is the electrical conductivity of bulk silver, N is the number density of AgNWs which can be obtained by (Eq. S41), N_c is the percolation threshold, and s is the critical exponent.

To obtain the critical exponent (s), (Eq. S42) can be expressed into the following logarithmic form:

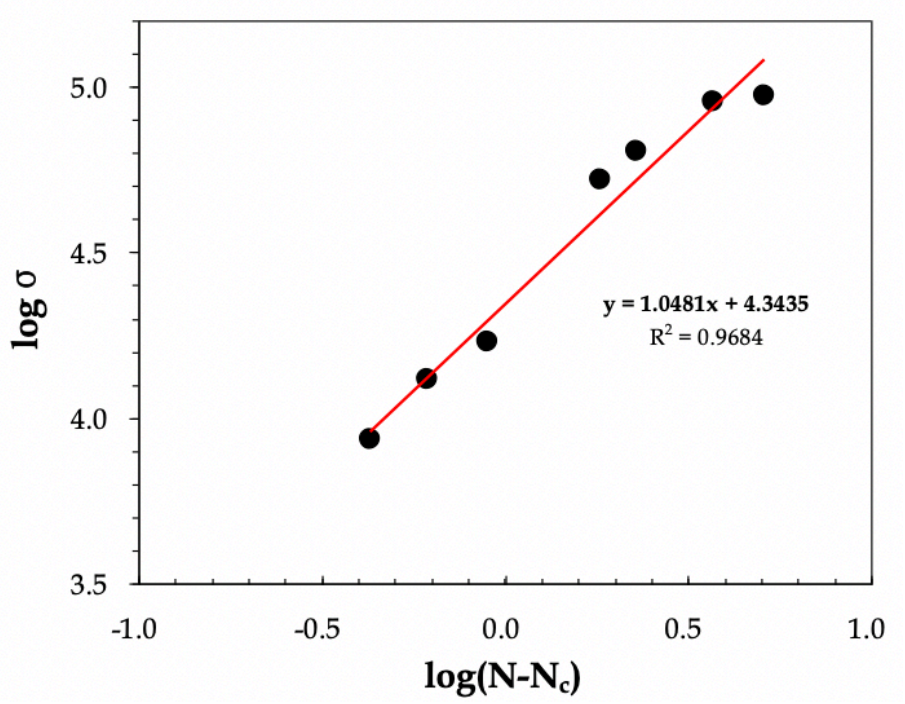

Figure S.2 Log plot of σ with respect to log(N–N_c) showing a linear fit based on (Eq. S43). The critical exponent (s) is determined to be 1.05 from the slope in the log-log plot.

$$\ln \sigma = \ln \sigma_o + s \ln(N - N_c) \qquad \text{(Eq. S43)}$$

In order to describe the behavior of AgNWs network in terms of the power-law of percolation theory of (Eq. S42), the critical exponent (s) is determined to be 1.05 from the slope in the log-log plot, as shown in Figure S.2. Therefore, we can complete the percolation model describing the relationship between the conductivity of AgNWs network and the AgNW concentration, as seen in Figure S.3. All of the measured conductivities are in agreement with the percolation model of (Eq. S42). The obtained percolation threshold is to be 0.503×10^{12} from the fitting. The inset microscopic image

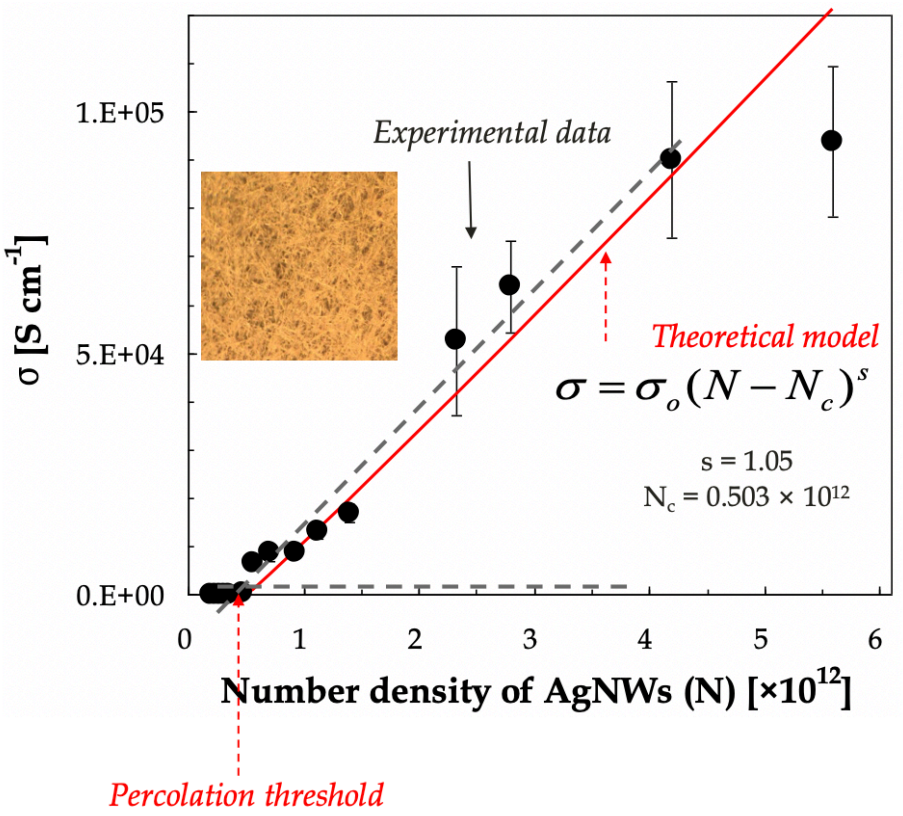

Figure S.3 Percolation model describing the relationship between the conductivity of AgNWs network and the AgNW concentration. The obtained percolation threshold is to be 0.503×10^{12} from the fitting.

represents the AgNWs network having the electrical resistance of 1-5 Ω/sq^2 so that it can be applied to the electrodes of NH_3 sensors, as displayed in Figure 4.2.

Bibliography

[1] X. Duan *et al*. High-performance thin-film transistors using semiconductor nanowires and nanoribbons, *Nature*, **425**, 274, 2003.

[2] K. Takei *et al*., Nanowire active-matrix circuitry for low-voltage macroscale artificial skin, *Nat. Mater*. **9**, 821, 2010.

[3] S. Xu *et al*., Self-powered nanowire devices, *Nat. Nanotechnol*, **5**, 366, 2010.

[4] M. C. McAlpine *et al*., Highly ordered nanowire arrays on plastic substrates for ultrasensitive flexible chemical sensors, *Nat. Mater.* **6**, 366, 2007.

[5] S. Ju *et al*., Fabrication of fully transparent nanowire transistors for transparent and flexible electronics, *Nat. Nanotechnol.* **2**, 378, 2007.

[6] M. L. Hammock *et al*., 25th Anniversary article: The evolution of electronic skin (E-Skin): A brief history, design considerations, and recent progress, *Adv. Mater.* **25**, 5997, 2013.

[7] K. Jain *et al.*, Flexible electronics and displays: high-resolution, roll-to-roll projection lithography and photoablation processing technologies for high-throughput production. *Proceedings of IEEE,* **93**, 1500, 2005.

[8] L. Polavarapu *et al.*, Preparation of conductive silver films at mild temperatures for printable organic electronics. *Chem. Mater.*, **23**, 3273, 2011.

[9] J. Jeon *et al.*, Micro-imprinted prism substrate for self-aligned short channel organic transistors on a flexible substrate, *Appl. Phys. Lett.* **100**, 043301, 2012.

[10] M. Neophytou *et al.*, Inkjet-printed polymer–fullerene blends for organic electronic applications, *Microelectronic Engineering* **95**, 102, 2012.

[11] S. K. Lee et al., Stretchable graphene transistors with printed dielectrics and gate electrodes, *Nano Lett.* **11**, 4642, 2011.

[12] J. A. Rogers *et al*., Materials and mechanics for stretchable electronics, *Science*, **327**, 1603, 2010.

[13] S. Lai *et al.*, Ultra-low voltage OTFT-based sensor for label-free DNA detection, *Adv. Mater.* **25**, 103, 2012.

[14] M. L. Hammock *et al.*, Organic transistors with ordered nanoparticle arrays as a tailorable plat- form for selective. In situ detection, *ACS. Nano* **6**, 3100, 2012.

[15] P. Lin *et al.*, Organic thin-film transistors for chemical and biological sensing, *Adv. Mater.* **24**, 34, 2012.

[16] H. U. Khan *et al.*, Pentacene based organic thin film transistors as the transducer for biochemical sensing in aqueous media, *Chem. Mater.* **23**, 1946, 2011.

[17] B. Y. Lee *et al.*, Scalable assembly method of vertically-suspended and stretched carbon nanotube network devices for nanoscale electro-mechanical sensing components, *Nano. Lett.* **8**, 4483, 2008.
[18] M. Ying *et al.*, Silicon nanomembranes for fingertip electronics, *Nanotechnology* **23**, 344004, 2012.
[19] D. H. Kim *et al.*, Electronic sensor and actuator webs for large- area complex geometry cardiac mapping and therapy, *PNAS* **109**, 19910, 2012.
[20] C. Pang *et al.*, A flexible and highly sensitive strain-gauge sensor using reversible interlocking of nanofibres, *Nat. Mater.* **11**, 795, 2012.
[21] C. Yu *et al.*, A stretchable temperature sensor based on elastically buckled thin film devices on elastomeric substrates, *Appl. Phys. Lett.* **95**, 141912, 2009.
[22] H. Stoyanov *et al.*, Soft conductive elastomer materials for stretchable electronics and voltage controlled artificial muscles, *Adv. Mater.* **25**, 578, 2012.
[23] K. Liu *et al.*, Cross-stacked superaligned carbon nanotube films for transparent and stretchable conductors, *Adv. Funct. Mater.* **21**, 2721, 2011.
[24] D. J. Lipomi *et al.*, Electronic properties of transparent conductive films of PEDOT:PSS on stretchable substrates, *Chem. Mater.* **24**, 373, 2012.
[25] S. C. B. Mannsfeld SCB, *et al.*, Highly sensitive flexible pressure sensors with microstructured rubber dielectric layers. *Nat. Mater.* **9**, 859, 2010.
[26] M. Ramuz *et al.*, Transparent, optical, pressure-sensitive artificial skin for large-area stretchable electronics. *Adv. Mater.* **24**, 3223, 2012.
[27] D. J. Lipomi *et al*., Skin-like pressure and strain sensors based on trans- parent elastic films of carbon nanotubes, *Nat. Nanotechnol.* **6**, 1, 2011.
[28] M. A. Meitl *et al*., Transfer printing by kinetic control of adhesion to an elastomeric stamp, *Nat. Mater.* **5**, 33, 2005.
[29] D. J. Lipomi *et al*., Toward mechanically robust and intrinsically stretchable organic solar cells: evolution of photovoltaic properties with tensile strain, *Solar Energy Materials and Solar Cells.* **107**, 355, 2012.
[30] J. Lee *et al*., Stretchable semiconductor technologies with high areal coverages and strain-limiting behavior: demonstration in high- efficiency dual-junction GaInP/GaAs photovoltaics, *Small.* **8**, 1851, 2012.
[31] D. H. Kim *et al*., Complementary metal oxide silicon integrated circuits incorporating monolithically integrated stretchable wavy interconnects, *Appl. Phys. Lett.* **93**, 044102, 2008.
[32] G. S. Jeong *et al*., Solderable and electroplatable flexible electronic circuit on a porous stretchable elastomer, *Nat. Commun.* **3**, 977, 2012.
[33] P. Lee *et al*., Highly stretchable and highly conductive metal electrode by very long metal nanowire percolation network, *Adv. Mater.* **24**, 3326, 2012.
[34] [34] X. Hu *et al*., Stretchable inorganic-semiconductor electronic systems, *Adv. Mater.* **23**, 2933, 2011.
[35] V. Vijai *et al*., In situ studies of strain dependent transport properties of conducting polymers on elastomeric substrates, *J. Appl. Phys.* **109**, 084525, 2011.
[36] K. A. Williams *et al*., Towards electrically conductive, self-healing materials, *J. Royal Soc. Interface* **4**, 359, 2007.
[37] Y. Li. *et al*., Polyelectrolyte multilayers impart healability to highly electrically conductive films, *Adv. Mater.* **24**, 4578, 2012.

[38] Y. Li *et al*., Bioinspired self-healing superhydrophobic coatings, *Angew. Chem. Int. Ed.* **49**, 6129, 2010.
[39] Y. Chen *et al*., Multiphase design of autonomic self-healing thermoplastic elastomers, *Nature Chem.* **4**, 467, 2012.
[40] E. Palleau *et al*., Self-healing stretchable wires for reconfigurable circuit wiring and 3D microfluidics, *Adv. Mater.* **25**, 1589, 2013.
[41] T.-P. Huynh *et al*., Self-healing, fully functional, and multiparametric flexible sensing platform, *Adv. Mater.* **28**, 138, 2016.
[42] J. Hur *et al*., Polypyrrole/Agarose-Based Electronically Conductive and Reversibly Restorable Hydrogel, *ACS Nano* **8**, 10066, 2014.
[43] B. C-K. Tee *et al*., An electrically and mechanically self-healing composite with pressure- and flexion-sensitive properties for electronic skin applications, *Nat. Nanotechnol.* **7**, 825, 2012.
[44] J. X. Wang *et al*., Extremely stretchable electroluminescent devices with ionic conductors, *Adv. Mater.* **28**, 4490, 2016.
[45] J.-Y. Sun *et al*., Ionic skin, *Adv. Mater.* **26**, 7608, 2014.
[46] D. S. Wie *et al.*, Wafer-recyclable, environment-friendly transfer printing for large-scale thin-film nanoelectronics. *PNAS* **115**, 7236, 2018.
[47] S. H. Cho *et al*., Self-healing polymer coatings. *Adv. Mater*. **21**, 645, 2009.
[48] B. J. Blaiszik *et al*., Autonomic restoration of electrical conductivity, *Adv. Mater*. **24**, 398, 2012.
[49] S. Ji *et al*., Visible-light-induced self-healing diselenide-containing polyurethane elastomer, *Adv. Mater*. **27**, 7740, 2015.
[50] Y. Cao *et al*., A transparent, self-healing, highly stretchable ionic conductor, *Adv. Mater*. **29**, 1605099, 2017.
[51] G. Deng *et al.*, Dynamic hydrogels with an environmental adaptive self-healing ability and dual responsive sol–gel transitions, *ACS. Macro. Lett.* **1**, 275, 2012.
[52] E. J. Markvicka *et al.*, An autonomously electrically self-healing liquid metal-elastomer composite for robust soft-matter robotics and electronics, *Nat. Mater.* **17,** 618, 2018.
[53] B. Ghosh *et al.*, Self-repairing oxetane-substituted chitosan polyurethane networks, *Science* **323**, 1458, 2009.
[54] M. Burnworth *et al*., Optically healable supramolecular polymers, *Nature* **472**, 334, 2011.
[55] S. Bode *et al.,* Self-healing polymer coatings based on crosslinked metallo supramolecular copolymers, *Adv. Mater.* **25**, 1634, 2013.
[56] C.-H. Li *et al.,* A highly stretchable autonomous self-healing elastomer, *Nature Chem.* **8**, 618, 2016.
[57] H. S. Mansur *et al*., Characterization of poly(vinyl alcohol)/poly(ethylene glycol) hydrogels and PVA-derived hybrids by small-angle X-ray scattering and FTIR spectroscopy, *Polymer* **45**, 7193, 2004.
[58] H. Zhang *et al*., Poly(vinyl alcohol) hydrogel can autonomously self-Heal, *ACS Macro Lett.* **1**, 1233, 2012.
[59] W. Maret *et al.*, Coordination dynamics of zinc in proteins, *Chem. Rev.* **109**, 4682, 2009.

[60] D. Mozhdehi *et al*., Self-Healing multiphase polymers via dynamic metal−ligand Interactions, *J. Am. Chem. Soc*. **136**, 16128, 2014.
[61] A. Vohra *et al*., Reinventing Butyl Rubber for Stretchable Electronics, *Adv. Funct. Mater*. **26**, 5222, 2016.
[62] Y. Rao *et al*. Stretchable self-healing polymeric dielectrics cross-linked through metal−ligand coordination, *J. Am. Chem. Soc*. **138**, 6020, 2016.
[63] C. Hassan *et al*., Structure and Applications of Poly(vinyl alcohol) hydrogels produced by conventional crosslinking or by freezing/thawing methods, *Adv. Polym. Sci*. **153**, 37, 2000.
[64] M. Nambu *et al*., *Japanese Patent Kokai* **59**, 56446, 1984.
[65] F. Yokoyama *et al*., Morphology and structure of highly elastic poly(vinyl alcohol) hydrogel prepared by repeated freezing-and-melting, *Colloid & Polymer Sci*. **264**, 595, 1986.
[66] Y. Dan *et al*., Viscosity enhancement of complexed solutions formed through the complexation of nonionic water-soluble polymers with chemically complementary structures in aqueous media. *J. Polymer Sci. Polym. Phys. Ed.* **38**, 1069, 2000.
[67] J. W. Rhim *et al*., Pervaporation separation of MTBE–methanol mixtures using cross-linked PVA membranes. *J. Appl. Polym. Sci.* **75**, 1699, 2000.
[68] K.-F. Arndt *et al*., Poly(vinyl alcohol)/poly(acrylic acid) hydrogels: FT-IR spectroscopic characterization of crosslinking reaction and work at transition point. *Acta Polym.* **50**, 383, 1999.
[69] N. Chen *et al*., The role of hydrogen-bonding interaction in poly(vinyl alcohol)/poly(acrylic acid) blending solutions and their films. *Chinese Journal of Polymer Science* **28**, 903, 2010.
[70] I. M. Jipa *et al*., Potassium sorbate release from poly(vinyl alcohol)-bacterial cellulose films, *Chemical Papers* **66**, 138, 2012.
[71] A. Kharazmi *et al*., Structural, optical, opto-thermal and thermal properties of ZnS–PVA nanofluids synthesized through a radiolytic approach, *Beilstein J. Nanotechnol.* **6**, 529, 2015.
[72] Y. Gan *et al*., Reaction mechanism of thermally-induced electric conduction of poly(vinyl alcohol)–silver nitrate hybrid films, *RSC Adv.* **6**, 56728, 2016.
[73] Y. J. Jung *et al*., Morphology and conducting property of Ag/poly(pyrrole) composite nanoparticles: Effect of polymeric stabilizers, *Synth. Met.* **161**, 1991, 2011.
[74] E. Yildirim *et al*., Thermal Transitions in Polyelectrolyte Assemblies Occur via a Dehydration Mechanism, *ACD Macro Lett*. 4, 1017, 2015.
[75] B. Liu et al., Synthesis of ZnO nano-powders via a novel PVA-assisted freeze-drying process, *RSC. Adv.* **6**, 110349, 2016.
[76] M. Stoia *et al*., Synthesis of nanosized zinc and magnesium chromites starting from PVA–metal nitrate solutions, *J Therm Anal Calorim*. **110**, 85, 2012.
[77] A. Pathak *et al*., Nano-particles of oxides through chemical methods, *PINSA* **67**, 47, 2001.
[78] Y. Zhang *et al*., Effect of water on the thermal transition observed in poly(allylamine hydrochloride)–poly(acrylic acid) complexes, *Macromolecules*. **49**, 7563, 2016.

[79] G. Świderski *et al*., Thermal, spectroscopic, X-ray and theoretical studies of metal complexes (sodium, manganese, copper, nickel, cobalt and zinc) with pyrimidine-5-carboxylic and pyrimidine-2-carboxylic acids, *J. Therm. Anal. Calorim*. **138**, 2813, 2019.

[80] L. V. Ababei *et al*., Synthesis and characterization of new complexes of some divalent transition metals with N-isonicotinamido-4-chlorobenzalaldimine, *J. Serb. Chem. Soc.* **76**, 1103, 2011.

[81] J. Tie *et al*., Multi-responsive, self-healing and adhesive PVA based hydrogels induced by the ultrafast complexation of Fe^{3+} ions. *Soft Matter* **15**, 7404, 2019.

[82] J. Kubo *et al*., Improvement of poly(vinyl alcohol) properties by the addition of magnesium nitrate, *J. Appl. Polym. Sci.,* **112**, 1647, 2009).

[83] X. C. Jiang *et al*., Modification of poly(vinyl alcohol) films by the addition of magnesium chloride hexahydrate, *Polym. Eng. Sci.* **52**, 1565, 2012

[84] X. C. Jiang *et al*., Melt processing of poly(vinyl alcohol) through adding of magnesium chloride hexahydrate and ethylene glycol as a complex plasticizer, *Polym. Eng. Sci.* **52**, 2245, 2012.

[85] M. J. Adams *et al*., Friction and lubrication of human skin, *Tribology Letters*, **26**, 239, 2007.

[86] C. Pailler-Mattéi, *et al*., Analysis of adhesive behaviour of human skin in vivo by an indentation test, *Tribology International*, **39**, 12, 2006.

[87] P. Sacco *et al*., Concepts for developing physical gels of chitosan and of chitosan derivatives, *Gels*. **4**, 67, 2018.

[88] S. Fujii *et al*., "Pressure-sensitive adhesive powder," *Mater. Horiz.*, **3**, 47, 2016.

[89] S. H. Lee *et al*., "Scalable and continuous fabrication of bio-inspired dry adhesives with a thermosetting polymer," *Soft Matter*, **14**, 2586, 2018.

[90] M. Tupy *et al*., Effect of water and acid-base reactants on adhesive properties of various plasticized poly(vinyl butyral) sheet, *J. Appl. Polym. Sci.* **127**, 3474, 2013.

[91] J. Tang *et al*., Strong and efficient self-healing adhesives based on dynamic quaternization cross-links, *J. Mater. Chem. A.* **5**, 21169, 2017.

[92] A. Khan, A liquid water model: Density variation from supercooled to superheated states, prediction of H-bonds, and temperature limits, *Journal of Physical Chemistry*, **104**, 11268, 2000.

[93] V. P. Voloshin *et al*., Proper and improper hydrogen bonds in liquid water, *J. Struct. Chem*. **57**, 497, 2016.

[94] U. Keller *et al*., Adhesion in laminated safety glass – What makes it work?, *Glass Processing Days*, 13-16 June, 1999.

[95] P. A. Hooper *et al*., The mechanical behaviour of poly(vinyl butyral) at different strain magnitudes and strain rates, *J. Mater. Sci.* **47**, 3564, 2012.

[96] S. L. Swisher *et al*., Impedance sensing device enables early detection of pressure ulcers in vivo, *Nat. Commun.* **6**, 6575, 2015.

[97] S. Wang *et al*., Skin electronics from scalable fabrication of an intrinsically stretchable transistor array, *Nature* **555**, 83, 2018.

[98] S. Gong *et al.*, A wearable and highly sensitive pressure sensor with ultrathin gold nanowires. *Nat. Commun.* **5**, 3132, 2014.

[99] J. Kim *et al*., Stretchable silicon nanoribbon electronics for skin prosthesis. *Nat. Commun.* **5**, 5747, 2014.

[100] M. F. Farooqui *et al*., Low cost inkjet printed smart bandage for wireless monitoring of chronic wounds. *Sci. Rep.* **6**, 28949, 2016.
[101] D. Rus *et al.*, Design, fabrication and control of soft robots. Nature, **521**, 467, 2015.
[102] H. Yuk *et al.,* Hydraulic hydrogel actuators and robots optically and sonically camouflaged in water, *Nat. Commun.* **8**, 14230, 2017.
[103] H. Yuk *et al*., Skin-inspired hydrogel-elastomer hybrids with robust interfaces and functional microstructures, *Nat. Commun.* **7**, 12028, 2016.
[104] D. Stauffer & A. Aharony, *Introduction to Percolation Theory,* 2nd Ed., Taylor & Francis, 1994.
[105] W. H. Meyer, Polymer electrolytes for lithium-ion batteries, *Adv. Mater.* **10**, 439, 1998
[106] M. A. Ratner *et al*., Ion transport in solvent-free polymers, *Chem. Rev.* **88**, 109, 1988.
[107] Theodor Grotthuss, *Theory of decomposition of liquids by electrical currents*, 1806.
[108] S. Neyertz *et al*., Local structure and mobility of ions in polymer electrolytes: A molecular dynamics simulation study of the amorphous PEO_xNaI system, *J. Chem. Phys.* **104**, 3797, 1996.
[109] Y. Shi *et al*., Nanostructured conductive polymer gels as a general framework material to improve electrochemical performance of cathode materials in Li-ion batteries. *Nano Lett.* **17**, 1906, 2017.
[110] M. Liao *et al.*, Wearable, healable, and adhesive epidermal sensors assembled from mussel-inspired conductive hybrid hydrogel framework, *Adv. Funct. Mater.* **27**, 1703852, 2017.
[111] A. A. Barlian *et al.*, Semiconductor piezoresistance for microsystems, *Proc. IEEE* **97**, 513, 2009.
[112] D. Kang *et al.*, Ultrasensitive mechanical crack-based sensor inspired by the spider sensory system, *Nature* **516**, 222, 2014
[113] K. Takei *et al.*, A highly sensitive electronic whiskers based on patterned carbon nanotube and silver nanoparticle composite films, *PNAS.* **111**, 1703, 2014.
[114] M. Hempel *et al.*, A novel class of strain gauges based on layered percolative films of 2D materials, *Nano Lett.* **12**, 5714, 2012.
[115] K. Lim *et al.*, High-sensitive strain sensor using nano-crack and the process of that and the strain sensing system comprising that, *Korean Patent, KR101737525B1*, 2017.
[116] Y. Lin *et al.*, A highly stretchable and sensitive strain sensor based on graphene–elastomer composites with a novel double-interconnected network, *J. Mater. Chem. C* **4**, 6345, 2016.
[117] H.-J. Kim *et al.*, Highly sensitive and very stretchable strain sensor based on a rubbery semiconductor, *ACS Appl. Mater. Interfaces* **10**, 5000 (2018).
[118] D. Y. Choi *et al.*, Highly stretchable, hysteresis-free ionic liquid-based strain sensor for precise human motion monitoring, *ACS Appl. Mater. Interfaces* **9**, 1770, 2017.

[119] X. Fang *et al*.,High-performance wearable strain sensors based on fragmented carbonized melamine sponges for human motion detection, *Nanoscale* **9**, 17948, 2017.
[120] K. Suzuki *et al*., Rapid-response, widely stretchable sensor of aligned MWCNT/elastomer composites for human motion detection, *ACS Sensors* **1**, 817, 2016.
[121] L. Cai *et al*., Highly transparent and conductive stretchable conductors based on hierarchical reticulate single-walled carbon nanotube architecture, *Adv. Funct. Mater.* **22**, 5238, 2012.
[122] Y. Wu *et al.*, Piezoresistive stretchable strain sensors with human machine interface demonstrations, *Sensors and Actuators A* **279**, 46, 2018.
[123] S. Wang *et al.*, Network cracks-based wearable strain sensors for subtle and large strain detection of human motions, *J. Mater. Chem. C* **6**, 5140, 2018.
[124] H.-J. Kim *et al.*, Rubbery electronics and sensors from intrinsically stretchable elastomeric composites of semiconductors and conductors, *Sci. Adv.* **3**, 701114, 2017.
[125] H. Souri *et al.*, Wearable strain sensors based on electrically conductive natural fiber yarns, *Materials and Design* **154**, 217, 2018.
[126] J. J. Park *et al.*, Highly stretchable and wearable graphene strain sensors with controllable sensitivity for human motion monitoring, *ACS Appl. Mater. Interfaces* **7**, 6317, 2015.
[127] X. Guo *et al.*, Highly stretchable strain sensor based on SWCNTs/CB synergistic conductive network for wearable human-activity monitoring and recognition, *Smart Mater. Struct.* **26**, 095017, 2017.
[128] S. R. Larimi *et al.*, Low-cost ultra-stretchable strain sensors for monitoring human motion and bio-signals, *Sensors and Actuators A.* **271**,182, 2018.
[129] S. Chen *et al.*, Acid-Interface Engineering of Carbon Nanotube/Elastomers with Enhanced Sensitivity for Stretchable Strain Sensors, *ACS Appl. Mater. Interfaces* **10**, 37760, 2018.
[130] S. Han *et al.*, Multiscale nanowire-microfluidic hybrid strain sensors with high sensitivity and stretchability, *npj Flexible Electronics* **16**, 2018.
[131] X. Xiao *et al.*, High-strain sensors based on ZnO nanowire/polystyrene hybridized flexible films, *Adv. Mater.* **23**, 5440, 2011.
[132] M. Amjadi *et al.*, Ultra-stretchable and skin-mountable strain sensors using carbon nanotubes-Ecoflex nanocomposites, *Nanotechnology* **26**, 375501, 2015.
[133] T. Yamada *et al.*, A stretchable carbon nanotube strain sensor for human-motion detection, *Nat. Nanotechnol*. **6**, 296, 2011.
[134] C. Mattmann *et al.*, Sensor for measuring strain in textile, *Sensors* **8**, 3719, 2008.
[135] *L. Cai et al.*, Super-stretchable, transparent carbon nanotube-based capacitive strain sensors for human motion detection*, Sci. Rep.* **3**, 3048, 2013.
[136] E. Roh *et al.*, Stretchable, transparent, ultrasensitive, and patchable strain sensor for human-machine interfaces comprising a nanohybrid of carbon nanotubes and conductive elastomers, *ACS Nano* **9**, 6252, 2015.
[137] D. J. Cohen *et al.*, A highly elastic, capacitive strain gauge based on percolating nanotube networks, *Nano Lett.* **12**, 1821, 2012.

[138] N, Lu *et al.*, Highly sensitive skin-mountable strain gauges based entirely on elastomers, *Adv. Funct. Mater.* **22**, 4044, 2012.
[139] J.-H. Kong *et al.*, Simple and rapid micropatterning of conductive carbon composites and its application to elastic strain sensors, *Carbon* **77**, 199, 2014.
[140] S. Yao *et al.*, Wearable multifunctional sensors using printed stretchable conductors made of silver nanowires, *Nanoscale* **6**, 2345, 2014.
[141] S. Gong *et al.*, Highly stretchy black gold E-skin nanopatches as highly sensitive wearable biomedical sensors, *Adv. Electron. Mater*. **1**, 1400063, 2015.
[142] K. K. Kim *et al.*, Highly sensitive and stretchable multidimensional strain sensor with prestrained anisotropic metal nanowire percolation networks, *Nano Lett.* **15**, 5240, 2015.
[143] Y. R. Jeong *et al.*, Highly stretchable and sensitive strain sensors using fragmentized graphene foam, *Adv. Funct. Mater*. **25**, 4228, 2015.
[144] M. Amjadi *et al.*, Highly stretchable and sensitive strain sensor based on silver nanowire–elastomer nanocomposite, *ACS Nano* **8**, 5154, 2014.
[145] U.-H. Shin *et al.,*Highly stretchable conductors and piezocapacitive strain gauges based on simple contact-transfer patterning of carbon nanotube forests, *Carbon* **80**, 396, 2014.
[146] M. Li *et al.*, Stretchable conductive polypyrrole/polyurethane (PPy/PU) strain sensor with netlike microcracks for human breath detection, *ACS Appl. Mater. Interfaces* **6**, 1313, 2014.
[147] C. Yan *et al.*, Highly stretchable piezoresistive graphene–nanocellulose nanopaper for strain sensors, *Adv. Mater.* **26**, 2022, 2014.
[148] C. Wang *et al.*, Carbonized silk fabric for ultrastretchable, highly sensitive, and wearable strain sensors, *Adv. Mater.* **28,** 6640, 2016.
[149] Y. Tang *et al.*, Highly stretchable and ultrasensitive strain sensor based on reduced graphene oxide microtubes–elastomer composite, *ACS Appl. Mater. Interfaces* **7**, 27432, 2015.
[150] M. Zhang *et al.,* Sheath–Ccre graphite/silk fiber made by dry-Meyer-rod-coating for wearable strain sensors, *ACS Appl. Mater. Interfaces* **8**, 20894, 2016.
[151] J. Shintake *et al.*, Ultrastretchable strain sensors using carbon black-filled elastomer composites and comparison of capacitive versus resistive sensors, *Adv. Mater. Technol.* **3**, 1700284, 2018.
[152] R. Rahimi *et al.*, Highly stretchable and sensitive unidirectional strain sensor via laser carbonization, *ACS Appl. Mater. Interfaces* **7**, 4463, 2015.
[153] J. T. Muth *et al.*, Embedded 3D printing of strain sensors within highly stretchable elastomers, *Adv.Mater.* **26**, 6307, 2014.
[154] A. Frutiger *et al.*, Capacitive soft strain sensors via multicore–shell fiber printing, *Adv. Mater.* **27,** 2440, 2015.
[155] J. Tolvanen *et al.*, Stretchable and washable strain sensor based on cracking structure for human motion monitoring, *Sci. Rep*. **8**, 13241, 2018.
[156] Y. Lu *et al.*, Ultrastretchable conductive polymer complex as a strain sensor with a repeatable autonomous self-healing ability, *ACS Appl. Mater. Interfaces* **11**, 20453, 2019.

[157] G. Cai *et al.*, Extremely stretchable strain sensors based on conductive self-healing dynamic cross-links hydrogels for human-motion detection, *Adv.Sci*. **4**, 1600190, 2017.
[158] S. Liu *et al.*, Ultrastretchable and self-healing double-network hydrogel for 3D printing and strain sensor, *ACS Appl. Mater. Interfaces* **9**, 26429, 2017.
[159] Y.-J. Liu *et al.*, Ultrasensitive wearable soft strain sensors of conductive, self-healing, and elastic hydrogels with synergistic "soft and hard" hybrid networks, *ACS Appl. Mater. Interfaces* **9**, 25559, 2017.
[160] X. Liu *et al.*, Self-healing strain sensors based on nanostructured supramolecular conductive elastomers, *J. Mater. Chem. A.* 5, 9824, 2017.
[161] Y. Tang *et al.*, Scalable manufactured self-healing strain sensors based on ion-intercalated graphene nanosheets and interfacial coordination, *ACS Appl. Mater. Interfaces* **11**, 23527, 2019.
[162] C. Zheng *et al.*, Highly stretchable and self-healing strain sensors based on nanocellulose-supported graphene dispersed in electro-conductive hydrogels, *Nanomaterials* **9**, 937, 2019.
[163] M. Wang *et al.*, A fast self-healing and conductive nanocomposite hydrogel as soft strain sensor, *Colloids and Surfaces A.* **567**, 139, 2019.
[164] D. Wu *et al*., A rapid ammonia sensor based on lysine nanogel-sensitized PANI/PAN nanofibers, *J. Mater. Chem. B*, **4**, 1520, 2016.
[165] K. P. Yoo *et al*., Immediate exposure to 300 ppm NH_3 is considered to be dangerous to health, *Sensors and Actuators B: Chemical*, **143**, 333, 2009.
[166] *Acute Exposure Guideline Levels for Selected Airborne Chemicals: Volume 6*.
[167] A. Pathak *et al*., Fiber-optic ammonia sensor using Ag/SnO_2 thin optimization of thickness of SnO_2 film using electric field distribution and reaction factor, *Appl. Opt*. **54**, 8712, 2015.
[168] *https://www.chicagotribune.com/suburbs/elgin-courier-news/news/ct-streamwood-hazmat-0607-20170606-story.html*.
[169] A. L. Khalaf *et al.*, Room temperature ammonia sensor using side-polished optical fiber coated with graphene/polyaniline nanocomposite, *Opt. Mater. Exp*. **7**, 1858, 2017.
[170] T. Zhang *et al*., Recent progress in carbon nanotube-based gas sensors, *Nanotechnology* **19**, 332001, 2008.
[171] M. Penza *et al*., Enhancement of sensitivity in gas chemiresistors based on carbon nanotube surface functionalized with noble metal (Au, Pt) nanoclusters, *Appl. Phys. Lett*. **90**, 173123, 2007.
[172] K. Lee *et al*., Highly sensitive, transparent, and flexible gas sensors based on gold nanoparticle decorated carbon nanotubes, *Sensors and Actuators B: Chemical*, **188**, 571, 2013.
[173] C. Hua *et al*., A flexible gas sensor based on single-walled carbon nanotube-Fe_2O_3 composite film, *Applied Surface Science*, **405**, 405, 2017.
[174] J. Paek *et al*., Stretchable electronic devices using graphene and its hybrid nanostructures, *FlatChem* **3**, 71, 2017.
[175] K. Dunst *et al*., Nitrogen dioxide sensing properties of PEDOT polymer films, *Sensors and Actuators B: Chemical*, **247**, 108, 2017

[176] S. Li *et al*., Flexible ammonia sensor based on PEDOT:PSS/Silver nanowire composite film for meat freshness monitoring, *IEEE Electron Device Letters*, **38**, 7, 2017.
[177] Y. Zhang *et al*., Cotton-based wearable PEDOT:PSS electronic sensor for detecting acetone vapor, *Flexible and Printed Electronics*, **2**, 042001, 2017
[178] M. Nikolou *et al*., Applications of poly(3,4-ethylenedioxythiophene) doped with poly(styrene sulfonic acid) transistors in chemical and biological sensors, *The Chemical Record*, **8**, 13, 2008.
[179] Y. Seekaew *et al*., Low-cost and flexible printed graphene–PEDOT:PSS gas sensor for ammonia detection, *Organic Electronics* **15**, 2971, 2014.
[180] K. H. Won *et al*., Highly stretchable polymer composite microtube chemical sensors produced by the meniscus-guided approach, *Current Applied Physics*, **17**, 339, 2017.
[181] H. Yan *et al*., Stretchable electronic sensors of nanocomposite network films for ultrasensitive chemical vapor sensing, *Small* **13**, 1701697, 2017.
[182] M. Kugishima *et al*., Development of SnO2-based gas sensor sensitive to dilute ethylene oxide in air, *Sensors and Actuators B: Chemical* **108**, 130, 2005.
[183] C. S. Rout *et al*., Ammonia sensors based on metal oxide nanostructures, *Nanotechnology* **18**, 205504, 2007.
[184] G. Korotcenkov *et al.*, Conductometric gas sensors based on metal oxides modified with gold nanoparticles: a review, *Microchimica Acta* **183**, 1033, 2016.
[185] B. Timmer *et al*., Ammonia sensors and their applications - a review, *Sensors and Actuators B: Chemical*, **107**, 666, 2005.
[186] J. Komiyama *et al*., Conductance in water-poly(vinyl alcohol) mixtures, *PNAS.* **69**, 829, 1972.
[187] M. A. Vargas *et al*., New proton conducting membranes based on PVAL/H_3PO_2/H_2O, *Electrochimica Acta* **44**, 4227, 1999.
[188] R. Soares *et al*., Glycerol as a source for fuels and chemicals by low-temperature catalytic processing, *Angew. Chem*. **45**, 3982, 2006.
[189] G. Ayala *et al.*, Effect of glycerol on the electrical properties and phase behavior of cassava starch biopolymers, *Dyna* **171**, 138, 2012.
[190] M. N. Chai *et al*., Novel proton conducting solid bio-polymer electrolytes based on carboxymethyl cellulose doped with oleic acid and plasticized with glycerol, *Sci. Rep*. **6**, 27328, 2016.
[191] M. Allam *et al*., Physical properties of PVA doped with algal glycerol, *J. Appl. Polym. Sci*. **130**, 4482, 2013.
[192] A. L. Gopalan *et al*., Development of electrospun PVdF–PAN membrane-based polymer electrolytes for lithium batteries, *J. Membr. Sci*. **325**, 683, 2008.
[193] B. Natesan *et al*., Segmental relaxation and ion transport in polymer electrolyte films by dielectric spectroscopy, *J. Non-Crystalline Solids*, **352**, 5205, 2006.
[194] J. Lee *et al*., Very long Ag nanowire synthesis and its application in a highly transparent, conductive and flexible metal electrode touch panel, *Nanoscale*, **4**, 6408, 2012.
[195] E. Akbari *et al*., Analytical calculation of sensing parameters on carbon nanotube based gas sensors, *Sensor* **14**, 5502, 2014.

[196] M. R. Nimlos *et al*., Mechanisms of glycerol dehydration, *J. Phys. Chem. A*, **110**, 6145, 2006.
[197] I. V. Zaporotskova *et al*., Carbon nanotubes: Sensor properties. A review, *Modern Electronic Materials*, **2**, 95, 2016.
[198] B. Kirchner *et al.*, Eigen or Zundel Ion: News from calculated and experimental photoelectron spectroscopy, *ChemPhysChem.* **8**, 41, 2007.
[199] *Handbook of Solubility Parameters*, Allan F. M. Barton. Ph.D., CRC Press, 1983, page 153-157.
[200] O. Markovitch *et al.*, Structure and energetics of the hydronium hydration shells, *J. Phys. Chem. A*, **111**, 2253, 2007.
[201] A. Haaland *et al.*, Covalent versus dative bonds to main group metals, a useful distinction, *Angew. Chem.* **28**, 992, 1989.
[202] Y. Lee *et al.*, Wearable sensing systems with mechanically soft assemblies of nanoscale materials, *Adv. Mater. Technol.* **2**, 1700053, 2017.
[203] C. Jiang *et al.*, Nearly isotropic piezoresistive response due to charge detour conduction in nanoparticle thin films, *Sci. Rep.* **5**, 11939, 2015.
[204] Z. Zheng *et al.*, Light-controlling, flexible and transparent ethanol gas sensor based on ZnO nanoparticles for wearable devices, *Sci. Rep.* **5**, 11070, 2015.
[205] M. Park *et al.*, MoS2-based tactile sensor for electronic skin applications, *Adv. Mater.* **28**, 2556, 2016.
[206] S. J. Benight *et al.*, Stretchable and self-healing polymers and devices for electronic skin, *Progress in polymer science.* **38**, 1961, 2013.
[207] K. Urdl *et al.*, Self-healing of densely crosslinked thermoset polymers - a critical review, *Progress in Organic Coatings.* **104**, 232, 2017.
[208] G. Liang *et al.*, Self-healable electroluminescent devices, *Light: Science & Applications* **7**, 102, 2018.
[209] C. Wang *et al.*, Self-healing chemistry enables the stable operation of silicon microparticle anodes for high-energy lithium-ion batteries, *Nature Chem.* **5**, 1042, 2013.
[210] V. C. Li *et al.*, Bendable concrete, *Proc. in Innovation in Construction,* 11, 2015.
[211] T. Horikoshi *et al.*, Properties of polyvinyl alcohol fiber as reinforcing materials for cementitious composites, *Proc. in International Union of Laboratories and Experts in Construction Materials, Systems and Structures,* 145, 2006.
[212] Anon *et al.*, *Focus on Powder Coat.* **8**, 6, 2015.
[213] Ramezanzadeh *et al.*, A new approach to investigate scratch morphology and appearance of an automotive coating containing nano-SiO_2 and polysiloxane additives, *Progress in Organic Coatings,* **72**, 541, 2011.
[214] U. Lafont *et al.*, Self-healing thermally conductive adhesives, *J. of Intelligent Material Systems and Structures,* **25**, 67, 2014.
[215] Y. Yao *et al.*, Highly thermally conductive composite papers prepared based on the thought of bioinspired engineering, *ACS Appl. Mater. Interfaces,* **8**, 15645, 2016.